



HAL
open science

Bone extracellular matrix modifications under pathological and environmental conditions: characterization and impact on bone cells

Tatiana Gritsaenko

► **To cite this version:**

Tatiana Gritsaenko. Bone extracellular matrix modifications under pathological and environmental conditions: characterization and impact on bone cells. Molecular biology. COMUE Université Côte d'Azur (2015 - 2019), 2019. English. NNT: 2019AZUR6034 . tel-04837889

HAL Id: tel-04837889

<https://theses.hal.science/tel-04837889v1>

Submitted on 14 Dec 2024

HAL is a multi-disciplinary open access archive for the deposit and dissemination of scientific research documents, whether they are published or not. The documents may come from teaching and research institutions in France or abroad, or from public or private research centers.

L'archive ouverte pluridisciplinaire **HAL**, est destinée au dépôt et à la diffusion de documents scientifiques de niveau recherche, publiés ou non, émanant des établissements d'enseignement et de recherche français ou étrangers, des laboratoires publics ou privés.

THÈSE DE DOCTORAT

Modifications de la matrice
extracellulaire osseuse dans des
conditions pathologiques ou
environnementales : caractérisation et
conséquences sur les cellules
osseuses.

Tatiana GRITSAENKO

TIRO-MATOS UMR E4320

**Présentée en vue de l'obtention
du grade de docteur en** Sciences de la
vie et de la Santé
Mention Interactions moléculaires et
cellulaires
de l'Université Côte d'Azur

Dirigée par : Dr. Georges Carle
Soutenue le : 13 Décembre 2019

Devant le jury, composé de :

Tim Arnett, Professeur, University College
London
Georges Carle, Directeur de Recherche, CNRS
Luc Malaval, Chargé de Recherche, INSERM
Frédéric Marin, Directeur de Recherche, CNRS
Sabine Santucci, Chargé de Recherche, CNRS
Sylvie Tambutté, Directrice de Recherche, CSM

Modifications de la matrice extracellulaire osseuse dans des conditions pathologiques ou environnementales : caractérisation et conséquences sur les cellules osseuses.

Soutenance publique le 13 Décembre 2019

Devant le jury composé de :

Président du jury

Sylvie Tambutté, Directrice de Recherche, Centre Scientifique de Monaco

Rapporteurs

Tim Arnett, Professeur, University College London
Frédéric Marin, Directeur de Recherche, Université de Bourgogne, Dijon

Examineurs

Luc Malaval, Docteur, Université Jean Monnet, St-Etienne
Sabine Santucci, Docteur, Université de Nice-Sophia Antipolis

Directeur de thèse

Georges Carle, Directeur de Recherche, Université de Nice-Sophia Antipolis

Modifications de la matrice extracellulaire osseuse dans des conditions pathologiques ou environnementales : caractérisation et conséquences sur les cellules osseuses.

RÉSUMÉ

Le tissu osseux est soumis à un remodelage constant au cours duquel les ostéocytes font office de mécanorécepteurs et coordonnent l'activité des ostéoclastes (OCL) qui résorbent le tissu osseux, et des ostéoblastes (OB) qui synthétisent la matrice extracellulaire (MEC) minéralisée. L'objectif de mon projet de thèse était d'étudier les altérations des matrices osseuses induites par certaines conditions physiopathologiques ou environnementales et d'explorer leurs effets sur le comportement des cellules osseuses et sur le tissu osseux.

Dans la première partie du projet, j'ai étudié en tant que modèle de pathologie osseuse, des souris dont le gène *Recql4*, une ADN-hélicase, a été inactivé. Chez l'homme, les mutations du gène *RECQL4* sont responsables du syndrome Rothmund-Thomson de type II associé à différentes anomalies squelettiques dont une perte osseuse prématurée. Dans un premier temps, j'ai caractérisé le phénotype osseux des souris *Recql4*^{-/-} et constaté un vieillissement osseux prématuré chez ces animaux. Ensuite, j'ai analysé *ex vivo* le comportement des OB et OCL primaires isolés de souris *Recql4*^{-/-}. Nous avons observé que la MEC produite par les OB *Recql4*^{-/-} tend à être moins minéralisée et est significativement plus rigide que la MEC synthétisée par les OB témoins. La perte d'élasticité de la MEC dans le cas du tissu osseux serait associée à une stimulation de la résorption. Ceci corrobore nos analyses histologiques qui révèlent une augmentation de la surface osseuse couverte par les OCL chez les souris mutantes. L'analyse protéomique de matrices synthétisées *ex-vivo* par des OB *Recql4*^{-/-} ou des OB contrôles, a permis l'identification de 204 protéines différenciellement exprimées. Ces résultats étayaient l'hypothèse selon laquelle les OB *Recql4*^{-/-} synthétisent une matrice osseuse modifiée. Parmi ces protéines, je me suis focalisée sur celles connues pour être impliquées dans l'organisation de la matrice et/ou la communication cellule-matrice. Ces travaux serviront de point de départ à des études à venir visant à explorer l'implication de ces protéines candidates dans la perte osseuse provoquée par la perte de RECQL4 et à examiner le comportement des cellules osseuses sur la MEC modifiée *Recql4*^{-/-}.

La deuxième partie de ma thèse concerne l'effet de l'uranium naturel (U) piégé dans la matrice sur les cellules osseuses. L'U est un métal lourd naturellement présent dans l'environnement, qui possède un faible niveau de radioactivité mais une toxicité chimique importante. La matrice osseuse est le principal site de rétention de l'U à long terme dans l'organisme. Cet actinide perturbe le métabolisme de l'os, mais son mode d'action et ses effets sur les cellules osseuses, notamment les OCL, n'est pas connu. J'ai d'abord montré que la présence d'U dans le milieu de culture des OCL stimule ou inhibe la fonction de ces cellules, selon la concentration. J'ai ensuite examiné l'effet de l'U incorporé à la matrice sur les OCL. À cette fin, nous avons développé deux systèmes modèles : une surface osseuse synthétique biomimétique sur laquelle l'U a été adsorbé, et des matrices « biologiques » synthétisées par des OB cultivés en présence d'U. À l'aide de ces modèles, nous démontrons pour la première fois que l'U intégré à la matrice peut être remobilisé par la résorption ostéoclastique. De plus, nos données suggèrent que l'U libéré par résorption pourrait stimuler l'ostéoclastogenèse.

En conclusion, mes travaux ont conduit à la caractérisation d'un nouveau modèle murin de vieillissement prématuré des os et à la première démonstration de l'effet de l'uranium sur le comportement des ostéoclastes. Ce travail illustre l'importance que peuvent avoir les altérations de la MEC osseuse sur la fonction des cellules osseuses. En outre, la mise au point de systèmes de culture 3D de cellules osseuses qui miment les microenvironnements osseux normaux ou défectueux sera utile pour identifier de nouveaux mécanismes de la physiopathologie osseuse.

Mots clés : os, matrice extracellulaire, RECQL4, vieillissement, uranium

Bone extracellular matrix modifications under pathological and environmental conditions: characterization and impact on bone cells.

ABSTRACT

Bone tissue undergoes constant remodeling during which osteocytes, cells acting as mechanosensors, coordinate the function of osteoclasts (OCL), resorbing old and damaged bone, and of osteoblasts (OB), synthesizing new mineralized extracellular matrix (ECM). In addition to serving as a support for mineral deposits, the protein network of bone ECM is involved in regulating the behavior of bone cells by modulating their proliferation, differentiation and/or function. The aim of my thesis project was to study bone matrix alterations induced by various pathological or environmental conditions and to explore their consequences on bone cell behavior and/or on bone health.

In the first part of my project, RECQL4-deficient mice were used as a model of bone pathology. In humans, bi-allelic mutations in the RECQL4 gene, a DNA helicase, are responsible for type II Rothmund-Thomson syndrome (RTS-II), a rare progeroid disorder associated with a range of skeletal anomalies, including premature bone loss. We first characterized the bone phenotype of *Recql4*^{-/-} mice. We found that bone loss associated with normal aging is accelerated and more pronounced in *Recql4*^{-/-} animals. Next, we performed *ex-vivo* experiments using primary bone cells (OCL and OB) from elderly mice. ECM produced by *Recql4*^{-/-} OB tends to be less mineralized and is significantly stiffer compared to control ECM, suggesting osteoblast dysfunction. Stiffening of ECM is a general feature of aging tissue and is believed to promote bone resorption. This is consistent with our histological data, which show increase in bone surface covered by the OCL in *Recql4*^{-/-} mice compared to control. Proteomic analysis of ECM-enriched extracts derived from *Recql4*^{-/-} and *Recql4*^{+/-} primary OB identified 204 differentially expressed proteins, supporting the hypothesis that *Recql4*^{-/-} OB synthesize a modified bone matrix. Among these proteins, we focused in particular on those important for matrix organization as well as for cell-matrix communication. Additional studies are now necessary to explore their possible implication in the accelerated bone loss seen in RECQL4-deficient mice and to examine the behavior of bone cells on *Recql4*^{-/-} bone ECM.

A second part of my thesis work was aimed at evaluating the effect of natural uranium trapped in the bone matrix on bone cells. Uranium (U) is a naturally occurring heavy metal widespread in the environment. While its radioactive activity is low, uranium exhibits a strong chemical toxicity. The bone matrix is the main site of U long-term retention. *In vivo* and epidemiological studies have shown that natural U impairs bone metabolism. However, the mechanism of its action and its effects on bone cells, in particular on osteoclasts, remain largely unexplored. We examined for the first time *in vitro* the effects of natural U on osteoclasts. We first showed that the presence of U in the culture medium stimulates or inhibits osteoclastic function, depending on the U concentrations used. We then examined the effect of U immobilized in bone-like matrices on OCL. For this purpose, we developed two model systems: a bone synthetic biomimetic surface onto which U has been adsorbed and “biological” matrices synthesized by OB cultured in the presence of U. By using these models, we demonstrated for the first time that embedded U can be remobilized from the matrix through osteoclastic resorption. Moreover, our data suggest that U released by resorption could stimulate osteoclastogenesis.

In conclusion, my work led to the characterization of a new mouse model of premature bone aging, and provided the first evidence of the effect of uranium on osteoclast behavior. In doing so, this work illustrates the importance of bone matrix alterations on bone cell function. In addition, the development of three-dimensional bone cell culture systems that mimic normal or defective bone microenvironments will be useful in identifying new mechanisms essential to bone health.

Keywords: bone, ECM, RECQL4, aging, Uranium

Remerciements

J'aimerais remercier tous les membres de l'équipe MATOs pour le soutien qu'ils m'ont apporté tout au long de ma thèse : Georges Carle, Valérie Pierrefite-Carle, Michel Samson, Chantal Cros, Olivier Camuzard, Lucile Hurault et surtout Sabine Santucci.

Merci Sabine, de tout mon cœur, pour ton dévouement, ta rigueur scientifique, tes conseils avisés et ton ouverture d'esprit. Sans toi et ton incroyable investissement personnel, je n'aurais jamais réussi à mener à bien ce projet.

Je suis reconnaissante envers toute l'équipe TIRO. Je remercie particulièrement Thierry Pourcher de m'avoir accueillie dans son laboratoire et Colette Ricort qui a toujours fait son maximum pour me faciliter la vie !

Je tiens également à remercier les membres du jury, MM. Tim Arnett et Frédéric Marin, d'avoir accepté d'évaluer mon travail en tant que rapporteurs, ainsi que M^{me} Sylvie Tambutté et M. Luc Malaval, en tant qu'examinatrice et examinateur. J'exprime ma gratitude à Luc Malaval et à Ellen Van Obberghen qui m'ont conseillée au cours de ces trois années dans le cadre du comité de suivi de thèse.

Un grand merci à tous mes collaborateurs : Jean-Marie Guigonis de la plateforme de protéomique, Sabrina Pisano et Laurence Cailleteau de la plateforme PICMI, François Orange et Sophie Pagnotta du CCMA, Gaëlle Creff et Christophe Den Auwer de l'ICN, Claude Vidaud du CEA, et Agnès Hagège de l'ISA.

Enfin, je souhaite adresser un immense merci à mon mari, Philippe Couture, pour son soutien indéfectible et pour avoir supporté pendant près de trois ans mes interminables descriptions des travaux en cours et, ces quatre derniers mois, ma quasi-absence.

TABLE OF CONTENTS

Table of contents	1
Abbreviations	5
List of tables and illustrations	9
Introduction	10
Chapter 1: Bone. General background	10
I. Bone organization	10
1. Bone anatomy and development.....	10
2. Bone tissue composition	14
A. Blood vessels	14
B. Nerves.....	16
3. Hierarchical bone structure	16
II. Bone functions.....	19
Chapter 2: Bone cells and remodeling.....	22
I. Osteoblastic cells	22
1. Lineage and stages of differentiation	22
2. Molecular regulation of osteoblast activity.....	24
3. Osteocytes	27
II. Osteoclasts.....	28
1. Differentiation: genetic regulation, role of the surrounding cells and of cytokines	28
2. Osteoclast activation and function.....	31
III. Bone remodeling	33
1. Steps of the remodeling cycle	33
2. Recruitment of the osteoclasts and the osteoblasts and coupling factors	35
3. Age-related remodeling imbalance and bone alterations	37
Chapter 3: Bone extracellular matrix	38
I. A very brief history of the extracellular matrix.....	38
II. Components of the mineralized ECM.....	39
1. Water	39
2. The organic bone matrix	41
A. Collagen	41
B. Noncollagenous proteins (NCP).....	46
3. Mineral phase.....	51

III. ECM regulation of remodeling	52
Chapter 4: Bone ECM alterations	54
I. Bone Matrix-associated diseases	54
II. Modification of bone ECM with aging.	55
1. Inorganic matix.....	55
2. Collagen.....	56
3. Noncollagenous proteins.....	57
III. Bone ECM modification and environmental pollution by metals	58
Chapter 5: Study models	60
I. RECQL4 and the type II Rothmund-Thomson syndrome	60
1. Type II Rothmund-Thomson Syndrome	60
2. The RECQL4 helicase	62
3. Mouse models.....	65
II. Uranium and Bone	66
1. Uranium: physicochemical properties	66
2. Uranium exposure and bone.....	67
3. Effects of Uranium on bone and bone cells.....	69
Results part 1	71
Bone and bone ECM alterations induced by RECQL4 deficiency.	71
I. Submitted manuscript.....	72
1. Summary.....	73
2. Introduction	74
3. Results	77
4. Discussion.....	86
5. Experimental procedures	92
6. Acknowledgements.....	95
7. Figures	96
8. Supplementary figures.	108
9. Supporting Information.....	112
10. References.....	121
II. Characterization of the mineralized ecm produced by RECQL4-deficient osteoblasts.	124
1. Summary.....	124
2. Materials and methods.....	125
A. Cell culture media	125
B. Long bone cell culture and mineralization	125
C. MLO-A5 culture and mineralization.....	126

D. Development of the protocol for protein extraction from mineralized matrices	126
E. Protein extraction from primary cell-produced mineralized matrix.....	128
F. Sample processing for LC-MS/MS analysis	129
G. Liquid Chromatography Tandem Mass spectrometry (LC-MS/MS).....	130
H. Protein extraction tests: protein identification and proteomic data analysis from MLO-A5 mineralized matrices	131
I. Protein identification and differential proteomic analysis by label-free quantitation.....	131
J. Western Blot.....	133
K. Quantitative RT-PCR	134
3. Results and Discussion.....	135
A. Development of the extracellular matrix protein-enriched extraction protocol.....	135
B. Quantitative Label-free proteomic analysis of bone extracellular matrix produced by RECQL4-deficient osteoblasts	144
C. Validation of selected proteins by western blotting	158
D. RT-qPCR	166
III. Discussion	173
Results Part 2.....	180
The effect of natural uranium on the osteoclasts.....	180
I. Publication.....	181
II. Manuscript in preparation “The effect of uranium-modified extracellular matrix on osteoclasts”	192
1. Summary.....	192
2. Introduction	193
3. Materials and methods.....	196
A. Uranium exposure.....	196
B. Cell culture	196
C. Biomimetic matrices.....	196
D. Osteoclast generation, TRAP staining and pit resorption assays.....	197
E. Scanning electron microscopy	197
F. Transmission Electron Microscopy.....	198
G. ICP/MS analysis	198
H. Extended X-Ray Absorption Fine Structure Analysis	199

I. Statistical analysis	200
4. Results	201
5. Figures	209
6. Supplementary data	224
7. Discussion.....	226
8. References.....	234
Conclusion.....	239
References	241

ABBREVIATIONS

Ab	Antibody
AFM	Atomic Force Microscopy
AGEs	Advanced glycation end-products
Ahsg	Alpha-2-HS-glycoprotein
AKT	Protein kinase B
ALP	Alkaline phosphatase
ASARM	Acidic-Serine-Aspartate Rich MEPE associated
ATP	Adenosine triphosphate
Atp6v0d2	d2 isoform of vacuolar ATPase V0 domain
Bglap	Osteocalcin
BMD	Bone mineral density
BMP2	Bone Morphogenic Protein 2
BMPs	Bone Morphogenetic Proteins
BMU	Basic multicellular unit
BSP	Bone sialoprotein
BV/TV	Bone volume / total volume
Ca	Calcium
CCL	C-C motif chemokine ligand
Cd	Cadmium
Co	Cobalt
Col14a1	Collagen type IV, alpha 1 chain
Col1a1	Collagen type I, alpha 1 chain
Col1a2	Collagen type I, alpha 2 chain
Col5a3	Collagen type V, alpha 3 chain
CPC	Cetyl-pyridinium chloride
Cr	Chromium
CTHRC1	Collagen Triple Helix Repeat Containing 1
CTx	C-Terminal Telopeptides Type I collagen
CXCL	C-X-C motif chemokine ligand
Dcn	Decorin
DC-STAMP	Dendritic cell-specific Transmembrane protein
Dkk1	Dickkopf-related protein 1
DMEM	Dulbecco's modified eagle medium
DMP-1	Dentin Matrix Protein 1
DMP1	Dentin Matrix Protein 1
DNA	Deoxyribonucleic acid
ECM	Extracellular matrix
EDTA	Ethylenediaminetetraacetic acid
EDX	Energy-dispersive X-ray spectroscopy
EGF	Epidermal growth factor
Enpp2	Ectonucleotide pyrophosphatase/phosphodiesterase family member 2

EXAFS	Extented x-ray absorption fine structure
FBN	Fibrillin
FC	Fold change
FGF23	Fibroblast Growth Factor 23
FN	Fibronectin
Fzd	Frizzled co-receptors
GAG	Glycosaminoglycans
GO	Gene onthology
HA	Hydroxyapatite
Hh	Hedgehog
Hist1h1a	Histone H1.1
Hmga1	High mobility group protein HMG-I/HMG-Y
Hmgb1	High Mobility Group Box 1
HSC	Hematopoietic stem cell
Ibsp	Bone sialoprotein 2
ICP-MS	Inductively coupled plasma mass spectrometry
IFN	Interferons
IGF	Insulin-like growth factors
Igfbp5	Insulin-like growth factor-binding protein 5
IL	Interleukine
Itga5	Integrin alpha-5
LC	Liquid chromatography
LEF	Lymphoid enhancer-binding factor
LOX	Lysyl oxidase
Lox14	Lysyl oxidase homolog 4
LRP5/6	Low-density lipoprotein Receptor-related Protein 5 or 6
Ltbp1	Latent-transforming growth factor beta-binding protein 1
μCT	Microcomputed tomography
MCF	Mineralized collagen fibril
MCS-F	Macrophage colony-stimulating factor
MEM	Minimal essential medium
MEPE	Matrix Extracellular Phosphoglycoprotein
Mg	Magnesium
MLO-A5	Murine like osteocyte clone A5
MMP	Matrix metalloproteinase
MS	Mass spectroscopy
MSC	Mesenchymal Stem/Stromal cells
MTT	3-(4,5-dimethylthiazol-2-yl)-2,5-diphenyltetrazolium bromide) tetrazolium
Na	Sodium
NCP	Noncollagenous proteins
NFATc1	Nuclear Factor of Activated T cells c1
NFκB	Nuclear Factor kappa-B
NO	Nitric Oxyde / Oxide Nitrique

OB	Osteoblast
OCL	Osteoclast
OCN	Osteocalcin
OI	Osteogenesis imperfecta
OPG	Osteoprotegerin
OPN	Osteopontin
Osx	Osterix
Pb	Lead
PG	Prostaglandin
PHEX	Phosphate-regulating neutral Endopeptidase, X linked
P_i	Inorganic phosphate
POC	Primary ossification center
Pp_i	Pyrophosphate
PTH	Parathyroid hormone
PTH1R	Parathyroid Hormone type 1 Receptor
PTM	Post-translational modifications
Ptn	Pleiotrophin
RAGE	AGE-specific receptor
RANKL	Receptor Activator of Nuclear Factor kappa-B Ligand
RECQL4	ATP-dependent DNA helicase Q4
RGD	ArgGlyAsp amino-acid motifs
RNA	Ribonucleic acid
ROS	Reactive Oxygen Species
RT-qPCR	Reverse transcriptase- quantitative polymerase chain reaction
RTS-II	Rothmund-Thomson syndrome type II
RUNX2	Runt-related transcription factor 2
SEM	Scanning electron microscopy
SEMA4D	Semaphorin 4D
SIBLINGs	Small Integrin-Binding Ligands with N-linked Glycosylation
Slit3	Slit homolog 3 protein
SLRP	Small Leucine-rich Repeat-containing Proteoglycans
Sost	Sclerostin
SPARC	Osteonectin
Spp1	Osteopontin
Tb.N	Trabecular number
Tb.Pf	Trabecular pattern factor
Tb.Sp	Trabecular spacing
Tb.Th.	Trabecular thickness
TCV	Transcortical vessels
TEM	Transmission electron microscopy
TFG-β	Transforming Growth Factor -β
THBS	Thrombospondin

TNF	Tumor Necrosis Factor
TRAP	Tartrate-resistant acid phosphatase
TRPV5	Transient Receptor Potential Vanilloide 5
Tubb6	Tubulin beta-6 chain
U	Uranium
U(VI)	Hexavalente Uranium
VEGF	Vascular endothelial growth factor
VEGF	Vascular Endothelial Growth Factor
Ybx1	Y-box-binding protein 1
Zn	Zinc

LIST OF TABLES AND ILLUSTRATIONS IN THE INTRODUCTION

Figure 1: Endochondral ossification.....	11
Figure 2: Long bone structure.....	12
Figure 3: Bone composition	14
Figure 4: Bone vascular system	15
Figure 5: Bone hierarchical structure	18
Figure 6: Osteoblast differentiation and fate	23
Figure 7: Wnt signaling pathways	24
Figure 8: BMP signaling in osteoblasts.....	26
Figure 9: Osteoclast differentiation and function.....	29
Figure 10: Five phases of bone remodeling in humans	34
Figure 11: Water compartment in the mineralized ECM	40
Figure 12: Collagen synthesis	42
Figure 13: Cross-linking in bone collagen.....	45
Figure 14: AGE formation	46
Figure 15: Bone microenvironmental changes induced by RAGE signaling	56
Figure 16: Human syndromes associated with <i>RECQL4</i> mutations	61
Figure 17: <i>RECQL4</i> structure and functions.	63
Table 1: Functions of the noncollagenous proteins in bone	49

INTRODUCTION

INTRODUCTION

CHAPTER 1: BONE. GENERAL BACKGROUND

I. BONE ORGANIZATION

1. Bone anatomy and development

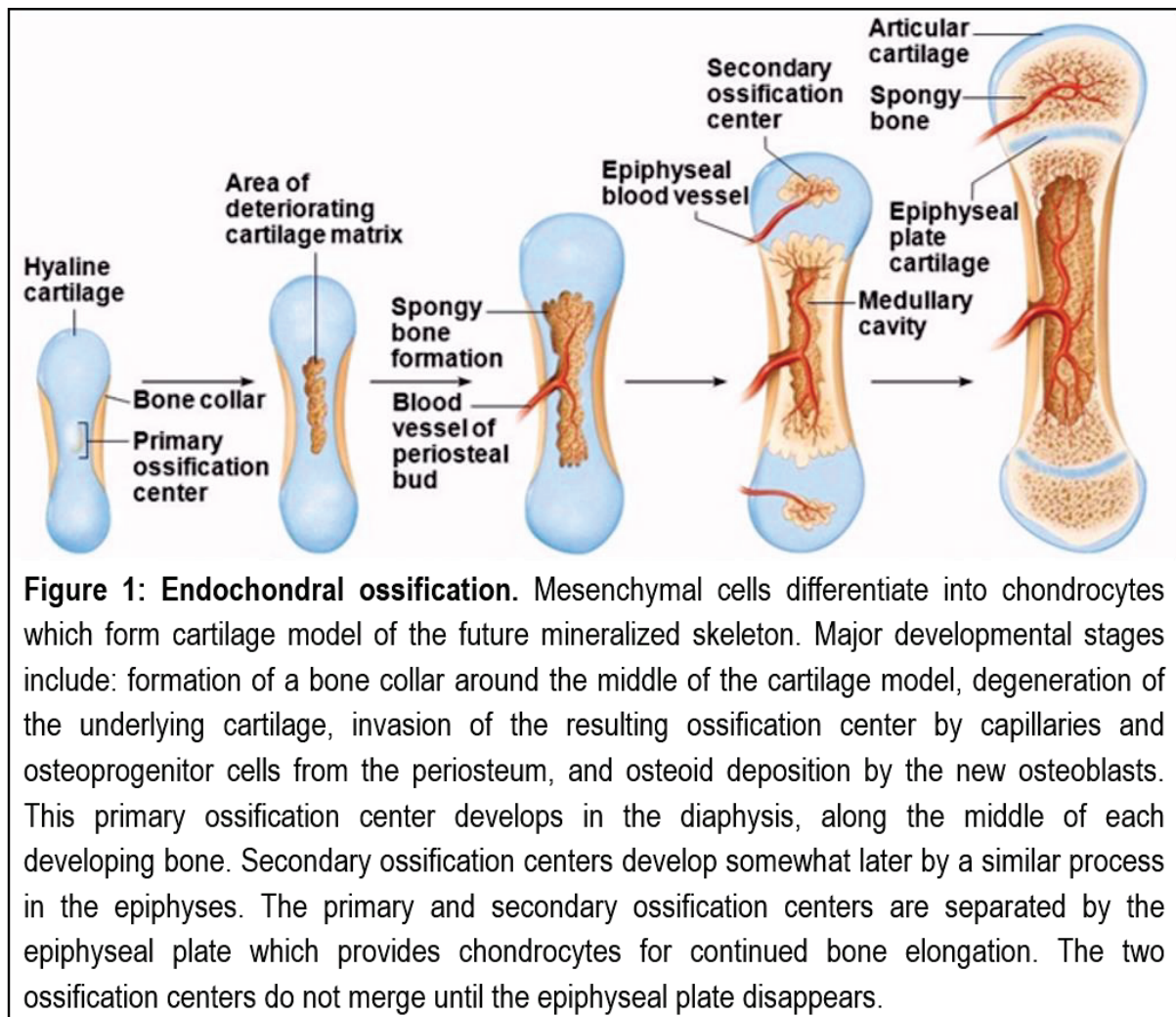
Bone is a hard, mineralized connective tissue forming a major part of the skeleton (the other part being cartilage). There are multiple but interconnected ways to classify bones. From an anatomical point of view, bones can be divided into two types: those belonging to the axial skeleton – the skull, the vertebral column and the thoracic cage – and those belonging to the appendicular skeleton – limbs and the bones that attach limbs to the axial skeleton¹.

From a developmental point of view, the bones are distinguished by the type of ossification that takes place during skeletal development. Membranous bones are produced by intramembranous ossification, a process in which embryonic mesenchymal cells differentiate directly into osteoblasts that deposit mineralized extracellular matrix (ECM). Most of the cranial and facial bones, and part of clavicles are formed through this ossification process².

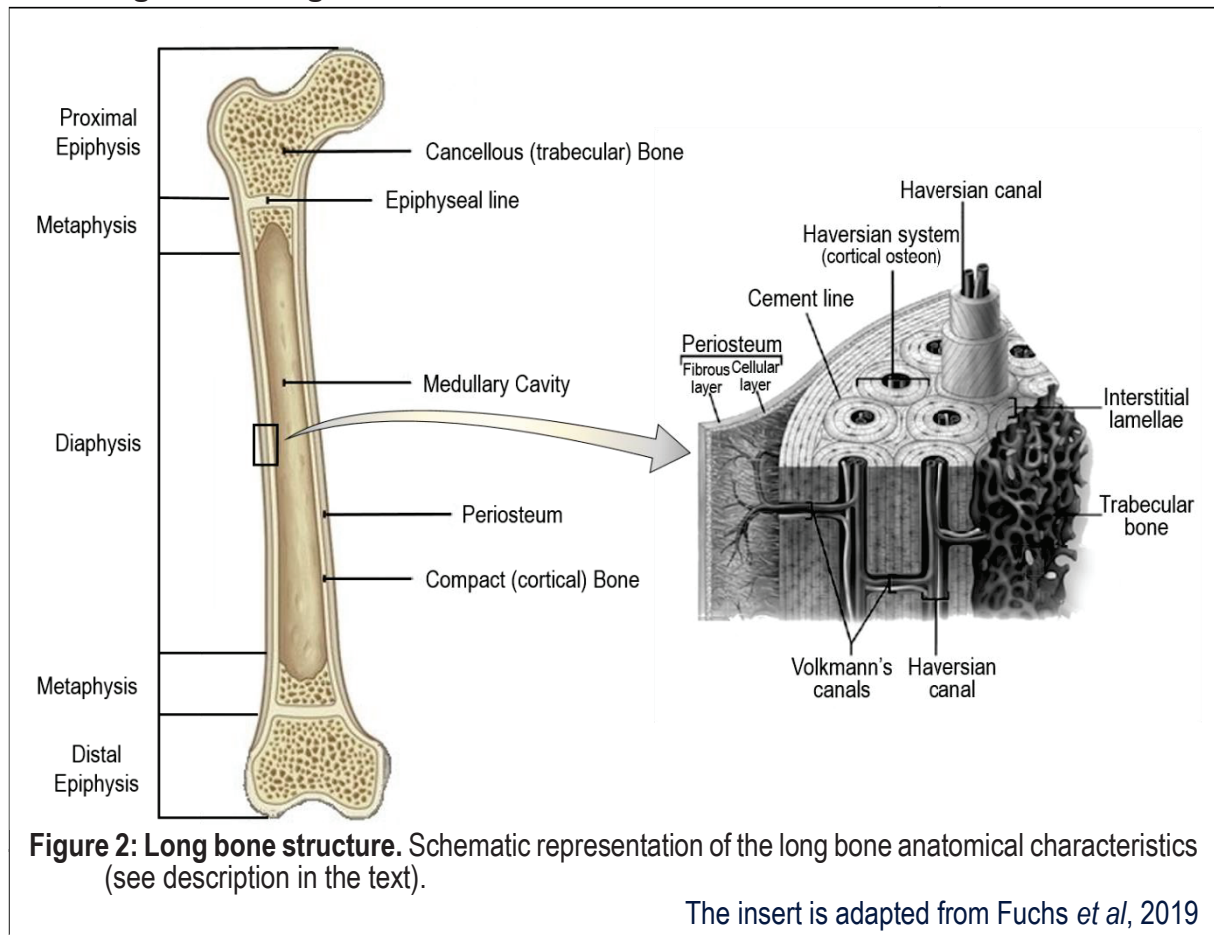
Most of the other bones, including the long bones of the limbs, are so-called cartilaginous bones and are the result of endochondral ossification, a process that involves several steps detailed in Figure 1. The first stages of this process include the condensation of mesenchymal cells, their differentiation into chondroblasts, proliferation and maturation into chondrocytes. Chondrocytes synthesize collagen II-rich cartilaginous matrix that will serve as a model (anlage) for the future bone. Thereafter, the cells in the middle of the anlage stop proliferating, become hypertrophic, and secrete an extracellular matrix enriched in collagen X that undergoes some mineralization. Mesenchymal cells outside of the cartilage differentiate into

osteoblasts and deposit a mineralized matrix around the cartilage template which will become cortical bone.

Figure 1: Endochondral ossification



Concomitantly, primary ossification centers (POC) are formed: blood vessels and nerves invade the hypertrophic cartilage core, providing access to osteoprogenitors and osteoclasts. Hypertrophic chondrocytes die by apoptosis, leaving behind extensive lacunae, further enlarged by osteoclasts and matrix metalloproteinases which digest partially mineralized cartilaginous matrix. What is left of the cartilage serves as a scaffold for the new collagen I-based mineralized matrix secreted by osteoblasts. Newly formed bone takes the shape of interconnected rods and plates called trabeculae.

Figure 2: Long bone structure

The process of ossification propagates along the initial cartilage template creating an elongated shaft, the diaphysis (Figure 1 and 2). Meanwhile, secondary ossification centers (SOC) form at the ends of the anlage, or epiphyses. From there, the replacement of the cartilage by bone proceeds towards the bone midline and recapture the steps described above³.

Finally, between the primary and secondary ossification centers, there remains only a narrow disk of non-mineralized cartilage, referred to as the growth plate. Postnatally, this growth plate serves as a source of chondrocytes for the elongation process occurring during long bone growth⁴, where new cartilage is produced and replaced by trabeculae on the diaphysis side of the long bone.

The actively elongating part of the bone below the growth plate is called the metaphysis (Figure 2). When bones reach their adult length, the growth plate is

"closed", that is to say mineralized. The epiphysis and metaphysis are fused and their blood supply is unified. However, in murine long bones, as opposed to human ones, the growth plate never completely fuses and bones do not altogether stop growing – their growth simply slow-down considerably after 8 month of age⁵. Since mouse metaphysis is the site where a low-level osteogenic activity continues throughout the life of the individual, it is the recommended site for the analysis of trabecular bone architecture by microcomputed tomography and histomorphometry⁶.

The dense and hard outer surface of the bone is made of compact, or cortical, bone covered with a non-mineralized layer called periosteum⁷. Periosteum is divided into an outer fibrous layer, mostly made of collagen and elastin fibers, and an inner cellular layer (cambium) containing mesenchymal precursor cells and mature osteoblasts⁸. Another non-mineralized layer – endosteum – lines the inner surface of the cortical bone and covers all trabeculae.

Human cortical bone contains cylindrical channels (Haversian canals) made by lamellar structures (cortical osteons) running at 10-17° with respect to the long axis of the bone (this angle is not represented in the simplified representation of the figure 1) and interconnected by transversal Volkmann's canals⁹. Osteons are separated from the interstitial lamellae by cement lines, a boundary structure with a different degree of mineralization¹⁰.

Trabecular (or cancellous) bone lies inside the diaphysis, partially fills the metaphysis and completely fills the epiphysis. The trabeculae are also composed of lamellae. In humans they are crescent-shaped and called hemi-osteons or trabecular packets¹¹.

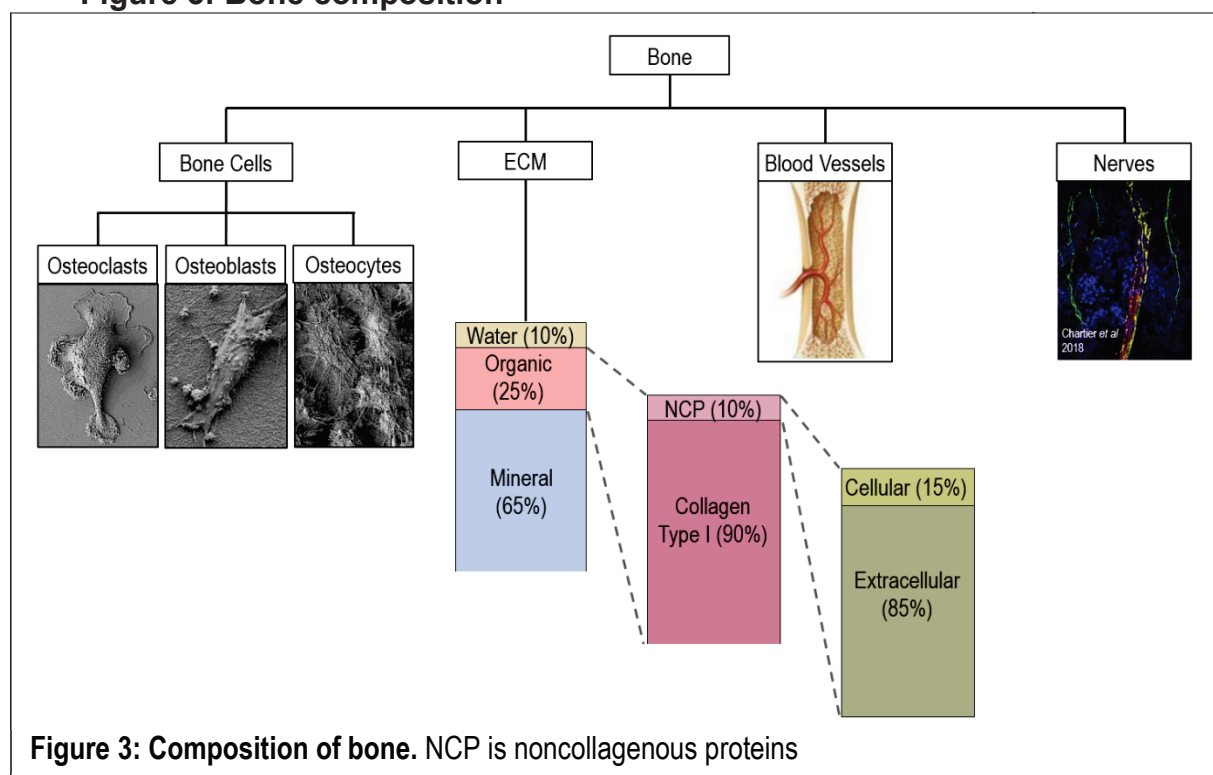
Bone marrow, a site of hematopoiesis, fills the medullary cavity and intratrabecular space⁷.

Both in cortical and in trabecular bone, the osteocytic lacunae lie between the lamellae. The lacunae are interconnected by canaliculi, micro-canals containing osteocytic processes.

2. Bone tissue composition

Bone tissue contains mineralized et non-mineralized ECM, blood vessels, nerves, and three specialized cell types – osteoclasts that resorb bone matrix, osteoblasts that synthesize it and mechanosensing osteocytes (Figure 3).

Figure 3: Bone composition



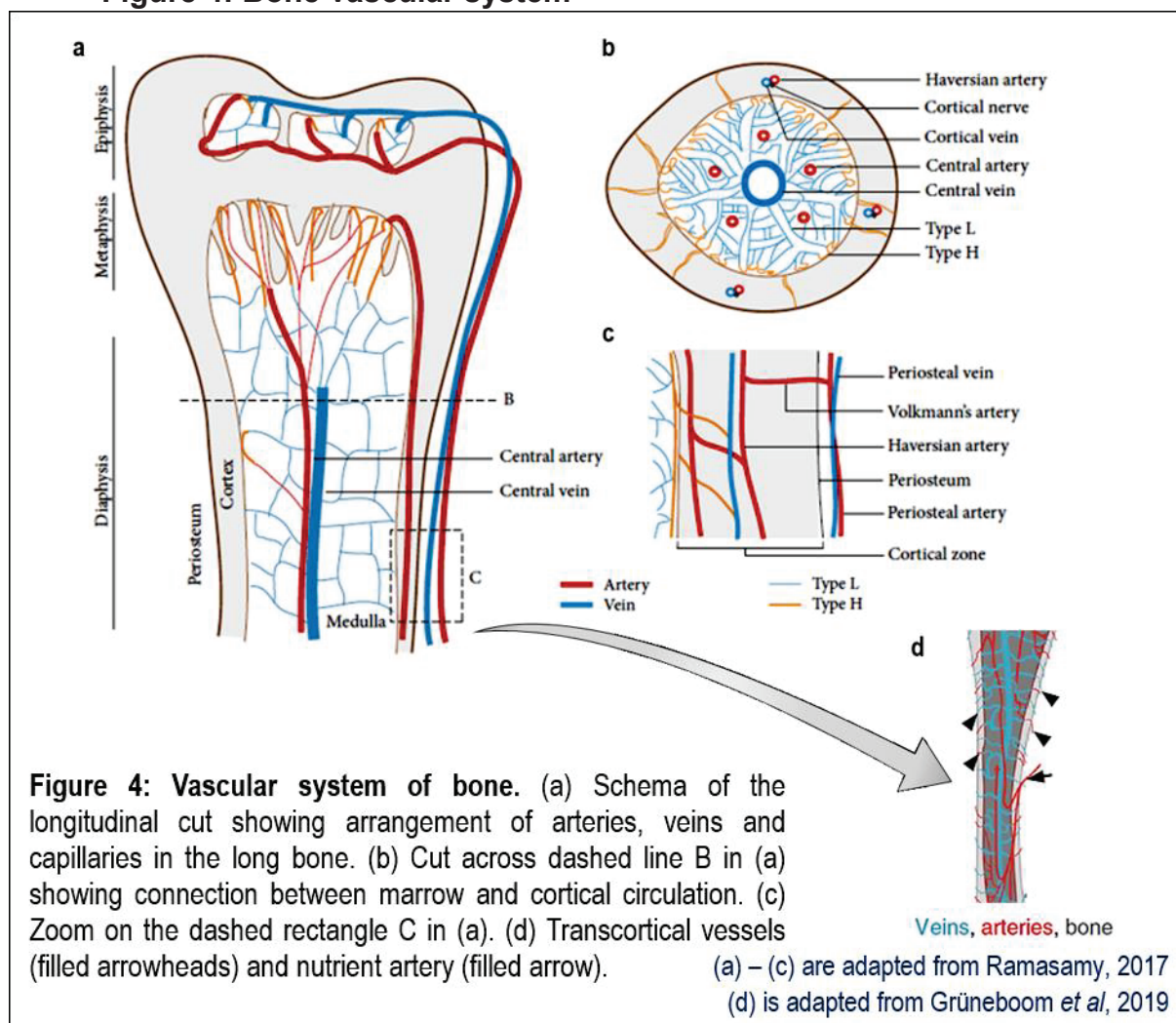
Bone cells and mineralized ECM will be described more extensively further in the manuscript. Here I will give a brief overview of the two other often neglected bone tissue components: blood vessels and nerves.

A. Blood vessels

Until 2019, the blood supply of the bone was considered to come from two sources (Figure 4). Nutrient arteries pass through the cortical bone in the epiphysis and mid-diaphysis regions, branch into capillaries (type H capillaries) in the metaphysis

and endosteum, which connect via medullary capillaries (type L) to a central vein. The second source is periosteal arteries connected to the Haversian system which also converges in metaphyseal capillaries to be drained away by the central vein¹².

Figure 4: Bone vascular system



However, in the beginning of 2019 a new vascular system was discovered in mouse and human long bones (Figure 4d) – transcortical vessels (TCV) – including both arteries and veins that originate in the marrow cavity, run through cortical bone and connect to periosteal circulation¹³. TCV are extremely thin (10–15 μm) and have only recently been detected by using new imaging techniques including bone transparency¹⁴. TCVs are responsible for 80% of arterial and 59% of venous blood flow, so are evidently important for the nutrition and oxygen supply of osteocytes that

lie in close proximity, as well as for rapid dissemination of blood-carried factors in and out of the bone. Since it was also shown that TCV number was significantly lower in aged mice¹³, the decline of TCV network could be associated with (if not being a direct underlying cause of) other deleterious age-dependent bone phenomena, such as reduction in osteocytes^{15,16} and osteoprogenitor cells¹⁷⁻¹⁹.

B. Nerves

There are two types of nerves in the bone: sensory fibers, that belong to somatic (voluntary) peripheral nervous system (PNS), and sympathetic fibers (fight-or-flight reflex) of the autonomous (regulating physiological functions) PNS²⁰. Both types of nerves densely innervate periosteum, then enter cortical bone with blood vessels through nutrient canals in mice and through Volkmann's canals and Haversian system in other large vertebrates. Multiple studies have suggested that both sensory and sympathetic fibers play a role, sometimes opposite, in bone metabolism. For example, in rats, chemical depletion of sympathetic fibers resulted in 45% increase in the osteoclast number at the remodeling site in the mandible, while chemical depletion of sensory fibers produced 21% reduction in the osteoclast number at the comparable site²¹. The mechanisms by which nerves effect changes on the bone are still under investigation, although it has been demonstrated (*in vitro*) that they release neuropeptides affecting bone cells²²⁻²⁴. Even more interesting, at least two molecules initially identified as axonal guidance molecules, Semaphorin 3A and SLIT3, have recently been shown to simultaneously increase osteoblastic bone formation and decrease osteoclastic bone resorption^{25,26}.

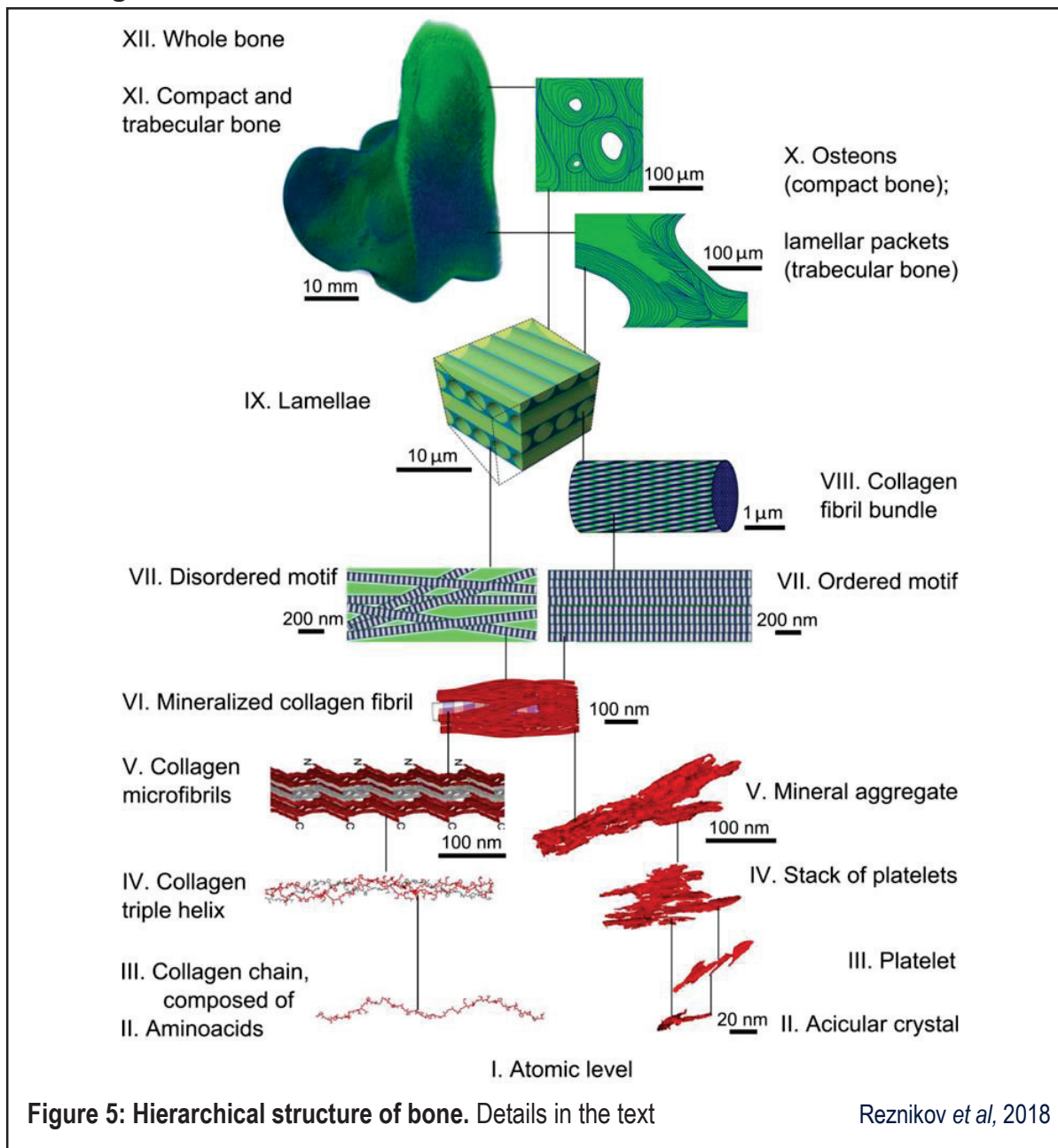
3. Hierarchical bone structure

Bone is a composite material in which the organic and mineral phases are intertwined. Therefore, its global structural properties depend on the characteristics of

each component and how they are assembled. The initial hierarchical bone model was proposed by Weiner and Wagner in 1998 and included 7 levels²⁷. Recently, aided by more powerful instruments and techniques, Reznikov and her colleagues have expanded it to 12 levels^{28,29}. Their scheme represents bone as hierarchical arrangement of progressively smaller and smaller elements, down to atomic level. Components of lower level combine to become components of the higher level. However, organic and minerals elements between the first (atoms) and the sixth (mineralized fibril) levels have to be described separately, since at this scale they have not yet merged and exist as separate entities.

From bottom to top, these levels are (Figure 5):

1. Constitutive atoms.
2. Organic phase: amino acids. Mineral phase: acicular (needle-like) slightly curved crystals.
3. Organic phase: separate α chains of collagen molecule. Mineral phase: mineral platelets, meaning lateral (side by side) aggregates of crystals.
4. Organic phase: collagen triple helix, a supercoil of 3 individual chains (two $\alpha 1$ and one $\alpha 2$). Mineral phase: stacked arrangements of 2 to 4 mineral platelets on the other side. Similarly to collagen, mineral stacks display a twist along the long axis²⁹.
5. Organic phase: collagen microfibrils, a staggered and rope-like packing of a minimum 5 collagen molecules producing a typical gap-overlap repeat called D band every 67 nm³⁰. Mineral phase: large aggregates of mineral stacks and platelets.
6. Mineralized collagen fibril (MCF), a blend of organic and inorganic components and water, in which mineral aggregates from level V are stabilized by water and are present both inside and outside of collagen microfibrils, connecting neighboring microfibrils²⁹.

Figure 5: Bone hierarchical structure

7. Two types of higher-scale organization of MCFs: an ordered motif, *i.e.* arrays of aligned MCFs that could on higher levels form different plywood-like structures by changing directions either continuously or in discrete steps^{31,32}; and a disordered motif – short, randomly aligned individual mineralized fibrils that are loosely packed and are embedded in a large quantity of ground matter^{28,33–36}.

8. Collagen bundles – unidirectionally aligned and tightly packed MCFs oriented almost parallel to one another but with a long-pitch twist around the bundle axis. These structures are shaped like 2-3 μm thick cylinders^{28,37} and separated by disorganized material.

9. Lamellae, layers of aligned collagen bundles enclosed inside disorganized material. The bundles inside the same layer are parallel but those in adjacent layers are angled 45-80° relative to each other. The narrow spaces between the bundles and thicker space between layers is filled with disorganized material which constitutes thus a continuous phase. It is worth noting that osteocytic lacunae and canaliculi are found exclusively in the disorganized phase²⁸.

10. Osteons in cortical bone and trabecular packets in the cancellous bone, both composed of lamellae. This level is not present in rodent bone.

11. Compact and trabecular bone constructed either of osteons and trabecular packets respectively in humans, or from lamellae in mice.

12. Whole bone.

II. BONE FUNCTIONS

Bone is a multifunctional organ. Being part of a skeleton, the earliest roles recognized for the bone were mechanical: upholding body, providing protection for internal organs and giving structural support for the movement. The structural organization of the different types of bone reflects these functions. Bones that serve a protective role, such as skull and ribs, are constructed in a way that allows them to absorb and dissipate maximum energy without damage. They are made of two layers of dense cortical bone completely separated by a thin layer of porous trabecular bone. A cortical bone provides necessary strength and stiffness, whereas a trabecular bone allows an even distribution of the impact load and an absorption of energy³⁸. In the case of the ribs, their curved shape increases even more their ability to withstand a

shock. Limb bones, on the other hand, have to support the weight of the body, while amplifying the effect of muscle contraction for the locomotion. For the latter effect, they need to be being as long as possible, which inevitably increases their weight. These conflicting demands on the long bones are resolved by their design: long and mostly hollow cylinders (*i.e.* light), but with the cortical bone being thicker in the middle of the diaphysis, an area where most of the load is transferred⁹.

Bone marrow is a site of hematopoiesis³⁹ and of hematopoietic stem cell (HSC) niche^{40,41}. Again, bone structure is well adapted for those functions, as it is very well vascularized. Therefore, newly produced cells can rapidly enter general blood circulation and be distributed. At the same time, HSC themselves are kept quiescent and multipotent in the marrow by osteoblasts lining endosteal surface of the bone^{42,43}.

Trabecular bone, with its large surface area available for remodeling, is also well adapted for the maintenance of the calcium and phosphate homeostasis through rapid bone turnover⁴⁴. Parathyroid hormone (PTH) and 1,25-dihydroxyvitamin D₃ (1,25-D), a vitamin D metabolite, are the main regulators of Ca²⁺ homeostasis, while fibroblast growth factor 23 (FGF23) regulates phosphate. Skeletal effects of PTH are mediated by the osteoblasts. At low concentrations, PTH directly stimulates osteoblast differentiation and promotes bone formation⁴⁵, but at high concentrations, it increases bone resorption via the release, from the osteoblastic cell surfaces, of the soluble RANKL (receptor activator of nuclear factor κ B ligand), a major osteoclastogenic factor. Levels of PTH are in turn regulated through a feed-back loop by serum in which an increase in serum calcium inhibits PTH secretion⁴⁶. The effect of 1,25-D on bone is similar to that of PTH: stimulation of bone formation at low doses and promotion of bone resorption at high doses⁴⁷.

Additionally, recent findings have identified bone as an endocrine organ. It is a known source of at least two hormones: (FGF23) and osteocalcin⁴⁸.

FGF23 is produced by osteocytes^{49,50} and transported by blood^{51,52} to the site of its action – kidney – where it inhibits phosphate reabsorption both directly, by reducing expression of sodium-phosphate (Na/P_i) co-transporters⁵³, and indirectly. For the latter, FGF23 suppresses the synthesis of 1,25-dihydroxyvitamin D₃^{54–56}, the active form of vitamin D that otherwise stimulates renal absorption of P_i⁵⁷. Since the decrease in active vitamin D leads as well to a lower absorption of the P_i in the intestine, cumulative effect of the FGF23 action is to depress serum phosphate levels. Additionally, FGF23 directly promotes renal reabsorption of calcium⁵⁸ and sodium⁵⁹, and appears thus to be one of the major regulators of systemic mineral metabolism.

Osteocalcin (OCN), another bone-derived hormone, is synthesized by osteoblasts, carboxylated post-translationally on three glutamic acid residues and embedded in the bone matrix during mineralization⁶⁰. To become an active hormone, OCN has to be decarboxylated⁶¹. Physiologically, this is achieved during bone resorption by osteoclasts^{62,63}, due to the low pH in the resorption pit. It is now established that bioactive OCN fulfills multiple hormonal functions. It stimulates body's energy metabolism by increasing β -cell proliferation, insulin production and secretion in pancreas, as well as by promoting insulin sensitivity in adipose tissue, muscle and liver⁶¹. It regulates male fertility by enhancing testosterone synthesis in testes⁶⁴; it is also capable to cross blood-brain barrier and is implicated in the fetal brain development and adult cognitive performance⁶⁵.

CHAPTER 2: BONE CELLS AND REMODELING

I. OSTEOLASTIC CELLS

1. *Lineage and stages of differentiation*

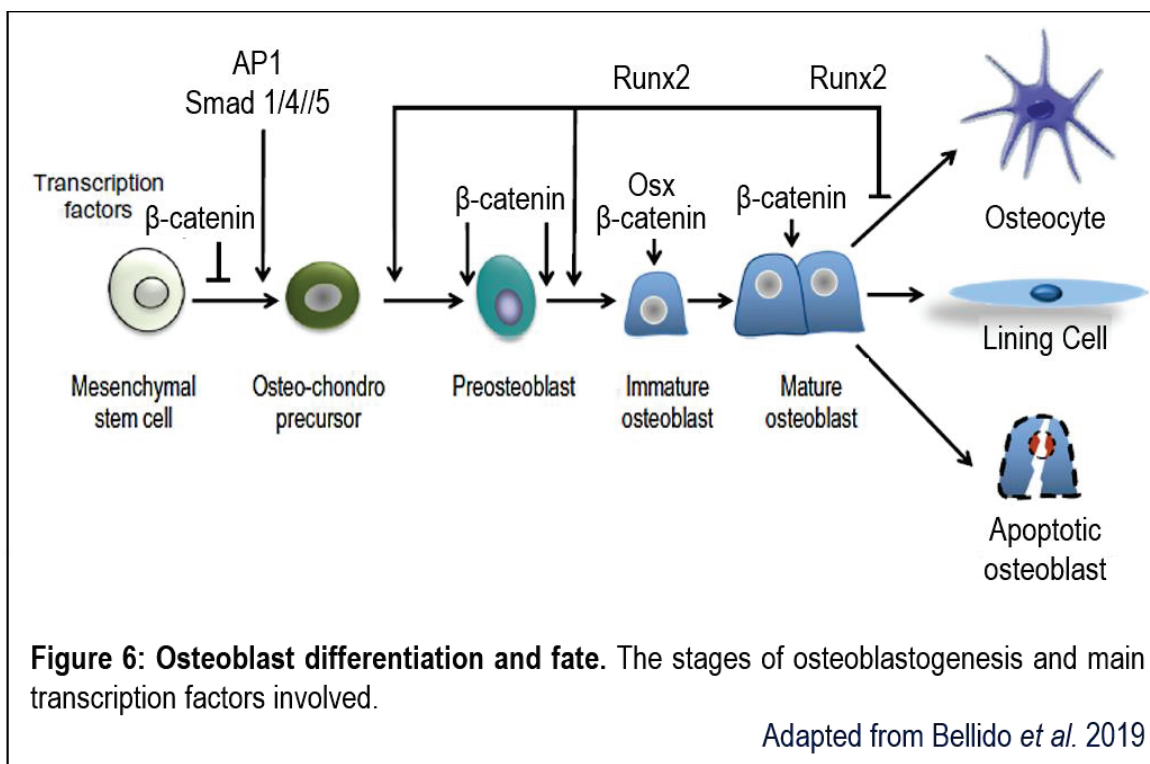
Osteoblasts are the post-mitotic cells that secrete and mineralize bone extracellular matrix. They are derived from the multipotent mesenchymal stromal/stem cells (MSC), which also give rise to chondrocytes and adipocytes^{66–69}. MSCs are found in bone marrow⁶⁹, but they have been isolated as well from other tissues including, compact bone⁷⁰, periosteum^{71–73} and adipose tissue⁷⁴. However, even when derived from the same tissue, MSC are heterogeneous in size, morphology, and differentiation potential⁷⁵. Only some of the MSC are multipotent stem cells or primitive progenitors whereas others are more restricted^{76–78}. For example, there is evidence for the existence of bipotential osteoblast-adipocyte⁷⁹ and osteoblast-chondrocyte⁸⁰ precursors.

During osteoblastogenesis, several stages of maturation can be observed (Figure 6). Progression through the differentiation process depends on interactions with other cells^{81–83}, mechanical signals⁸⁴ and extracellular signaling factors^{78,85}.

Osteoblast progenitors are proliferating spindle-shaped cells that express Runx2 (**Runt**-related transcription factor 2 or Cbfa1), the master regulator of the osteoblastic lineage⁸⁶. This transcription factor is required for osteoblast commitment and differentiation as first revealed by the complete lack of ossification and the depletion of mature osteoblasts in Runx2-null mice⁸⁷. Runx2 has many target genes including the bone matrix genes Col1a1 (Collagen I alpha-1 chain), Col1a2 (Collagen I alpha-2 chain), Spp1 (coding for Osteopontin) and Bglap (coding for Osteocalcin)⁸⁸. Runx2 positively influences early stages of osteoblast differentiation but it also

maintains osteoblastic cells in an immature stage, for this reason its expression has to be down-regulated during latter stages of differentiation^{89–92}.

Figure 6: Osteoblast differentiation and fate



At the next differentiation stage, the cells (pre-osteoblasts) acquire a typical cuboid shape and continue to proliferate. They secrete an extracellular matrix and express osteopontin, high levels of ALP, BSP^{93–95} and Osx (Osterix)⁹⁶ a transcription factor that, with Runx2, controls the expression of osteoblast-specific genes⁹⁷.

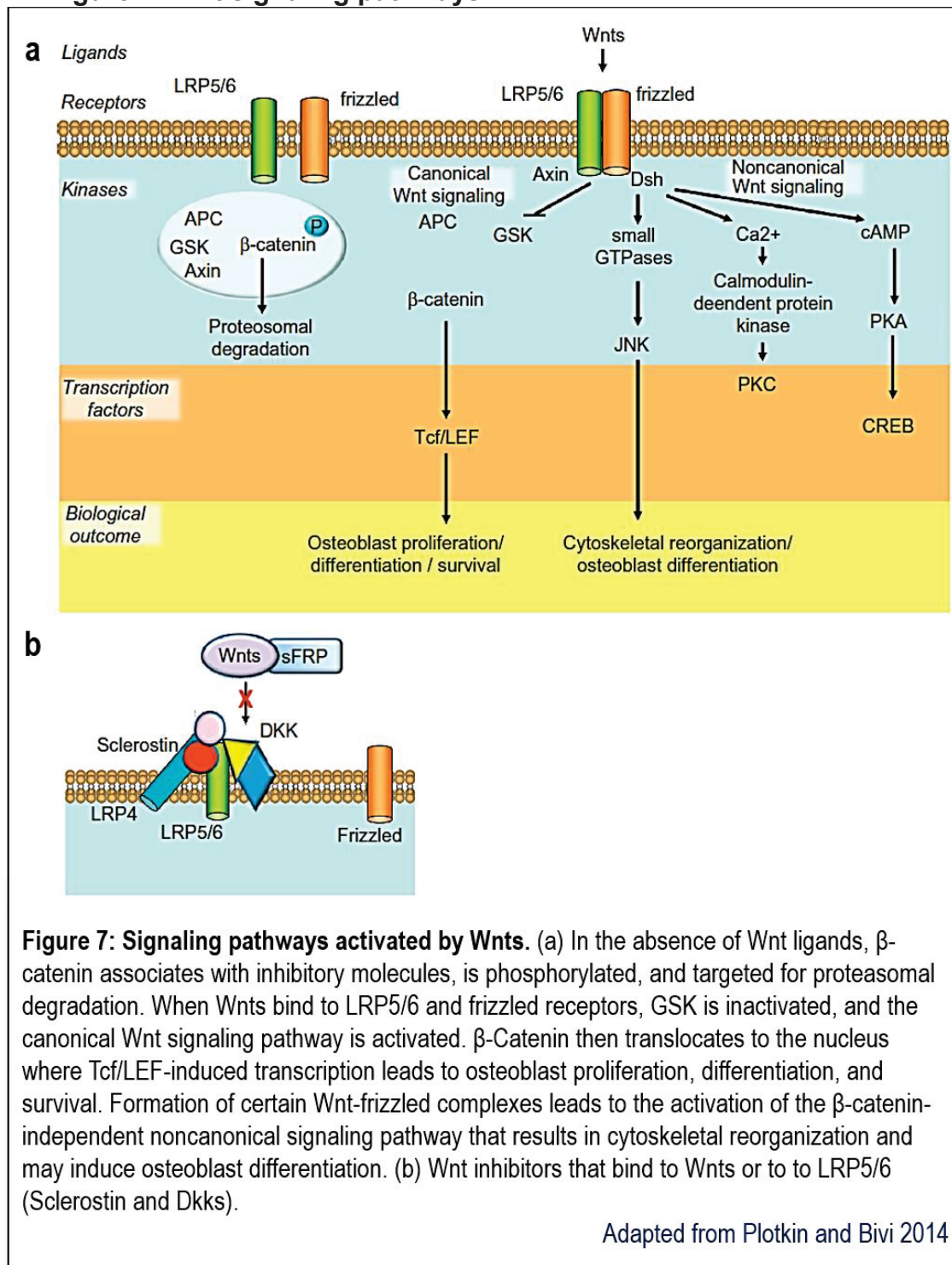
Finally, mature osteoblasts enter a post-mitotic state. They have high ALP activity, secrete large amounts of ECM proteins (including collagen I, osteopontin, BSP and osteocalcin) and engage in mineralization⁹⁸.

At the end of the bone formation phase, 65% of osteoblasts die by apoptosis⁹⁹, 10 to 15% surround themselves with the mineralized matrix and differentiate into osteocytes and the remainder are transformed into lining cells that cover the quiescent bone surfaces¹⁰⁰.

2. Molecular regulation of osteoblast activity

Two of the main signaling pathways involved in the regulation of osteoblastogenesis are those activated by Wnts glycoproteins and BMPs (**B**one **M**orphogenetic **P**roteins).

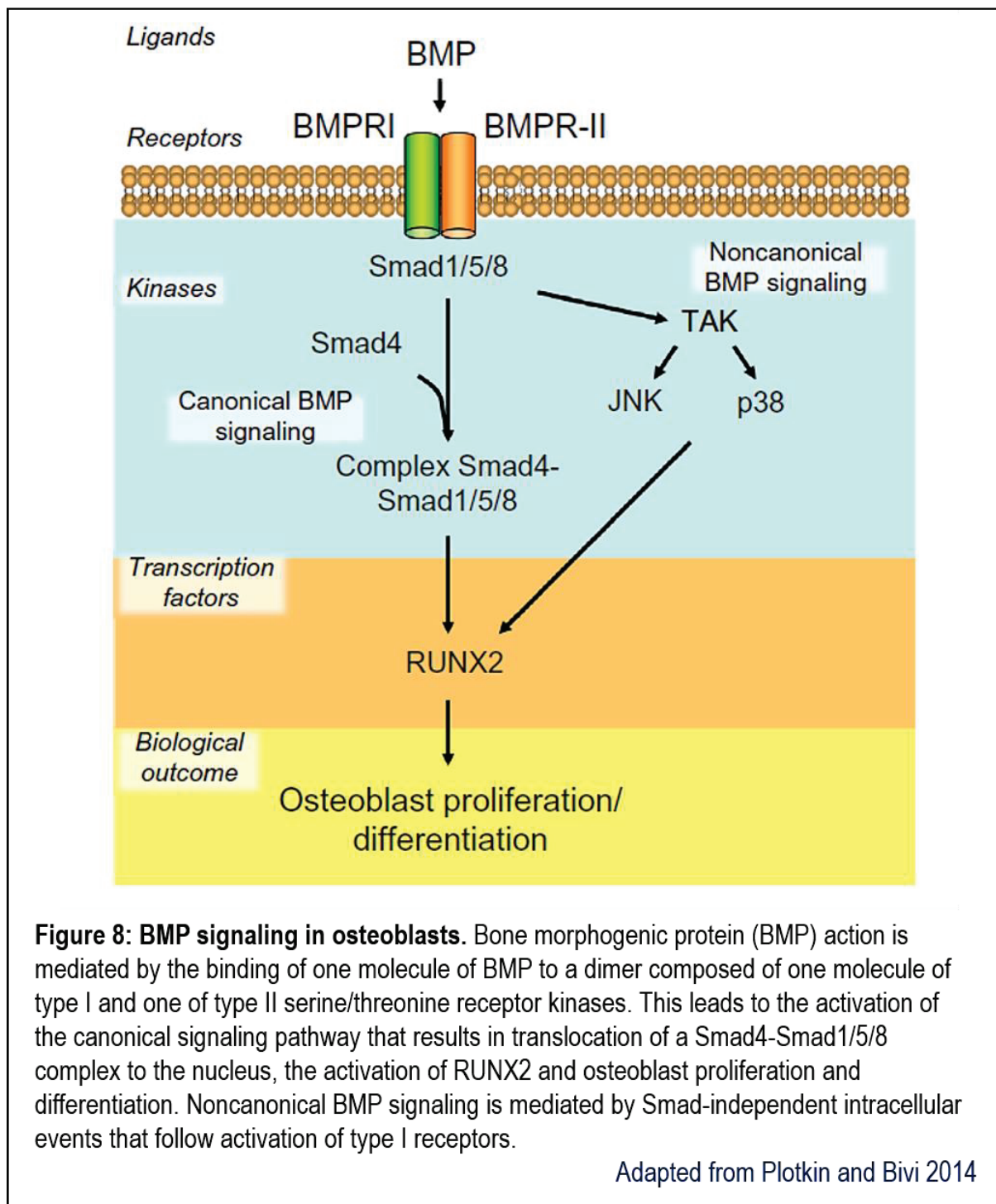
Figure 7: Wnt signaling pathways



Wnt proteins are involved in several signaling cascades (Figure 7), one of which called "Wnt/ β -catenin canonical" is particularly important for osteoblast differentiation. In this pathway, Wnt proteins bind to LRP5/6 (Low-density lipoprotein Receptor-related Protein 5 or 6) and Frizzled (Fzd) co-receptors¹⁰¹, forming a trimeric complex. This binding triggers an intracellular signaling cascade that results in the stabilization of β -catenin and its translocation into the nucleus where, in association with TCF/LEF transcription factors, it induces the expression of Runx2, as well as other pro-osteogenic genes¹⁰². Osteoblasts, osteocytes, chondrocytes and bone marrow cells have been reported to secrete various Wnt ligands¹⁰³. Bone cells also secrete Wnt antagonists. The sclerostin (SOST), expressed in particular by osteocytes¹⁰⁴, and the Dickkopfs proteins (DKKs) bind to LRP5/6 and inhibit the canonical Wnt pathway^{105,106}, allowing to fine tune the signaling.

The effect of Wnt canonical signaling on osteogenesis is influenced by the differentiation step. Overall, this pathway seems to stimulate the differentiation of MCS committed into the osteogenic lineage, while it inhibits the terminal differentiation of mature osteoblasts. In addition, Wnt signaling inhibits apoptosis of osteoblasts and mature osteocytes¹⁰⁷. Conversely, Wnt antagonists induce osteoblastic apoptosis¹⁰⁸. As an example, the decrease in sclerostin levels caused by the action of PTH or mechanical loading leads to a stimulation of osteoblastic differentiation and an extension of their lifespan.

The second important pathway for osteoblast differentiation is activated by the members of the TGF β (**T**ransforming **G**rowth **F**actor beta) superfamily, the BMPs, which includes at least 30 members involved in several functions, such as embryonic development, cell proliferation, and differentiation¹⁰⁹. BMP ligands activate signaling by binding to transmembrane receptor serine/threonine kinases (Figure 8). BMPs are

Figure 8: BMP signaling in osteoblasts

mainly involved in the earliest phases of osteoblast differentiation, favoring the commitment of bone marrow MSCs toward an osteochondral precursor stage¹¹⁰. Osteoblast conditional knockout for BMP-2 and BMP-4 inhibits *Osx* expression and impairs osteoblast maturation which severely affects embryonic bone formation¹¹¹. Another BMP involved in osteoblast differentiation is BMP-7, which enhances the

expression of osteopontin, osteocalcin and osterix, ALP activity and nodule formation in *in vitro* MSC culture¹¹².

Recent studies show that during osteoblastogenesis, Wnt and BMP pathways engage an active cross-talk. For example, BMPs are the negative regulators of the Wnt signaling in osteoblasts, since both SOST and Dkk1 are down-regulated in mice null for BMP receptor IA¹¹³. On the other hand, BMP-9 induces osteoblast differentiation through β -catenin¹¹⁴.

3. Osteocytes

Osteocytes are the most abundant (90–95%) and long-lived cells in the bone, with a lifespan of up to 25 years¹¹⁵. They have a stellate shape due to multiple (from 40 to 100 per cell) cytoplasmic processes running along the canaliculi in the mineralized matrix^{116–118}. Through the process called osteocytic osteolysis, osteocytes are capable to deposit and resorb bone around the lacuna in which they are housed, thus changing its shape^{119–121}

Osteocyte formation follows different phases, during which the osteoblast goes through the phases of (1) type I pre-osteocyte stage (osteoblastic osteocyte), (2) a type II pre-osteocyte, which is encased in the osteoid, (3) a type III pre-osteocyte, that is partly surrounded by mineralized matrix, (4) a young osteocyte and (5) an old osteocyte¹²². The latter two are fully embedded in a mineralized matrix, but the old osteocyte has fewer cellular processes¹¹⁵. Although osteocytes express almost all osteoblastic markers, their level of expression changes. For example, ALP and type I collagen expression are lower¹²³, whereas osteocalcin¹²⁴ and PTH receptor expression are higher in osteocytes¹²⁵ compared to osteoblast. On the other hand, the expression of the osteocytes specific markers, such as E11¹²⁶, PHEX (**Phosphate-regulating gene with homologies to Endopeptidases on the X chromosome**)¹²⁷, sclerostin¹²⁸ and DMP-1

(Dentin Matrix Protein 1)^{129,130} are either induced or greatly upregulated. However, great heterogeneity remains in the expression profiles of some lineage markers, which reflects the same heterogeneity as in osteoblasts⁸⁶.

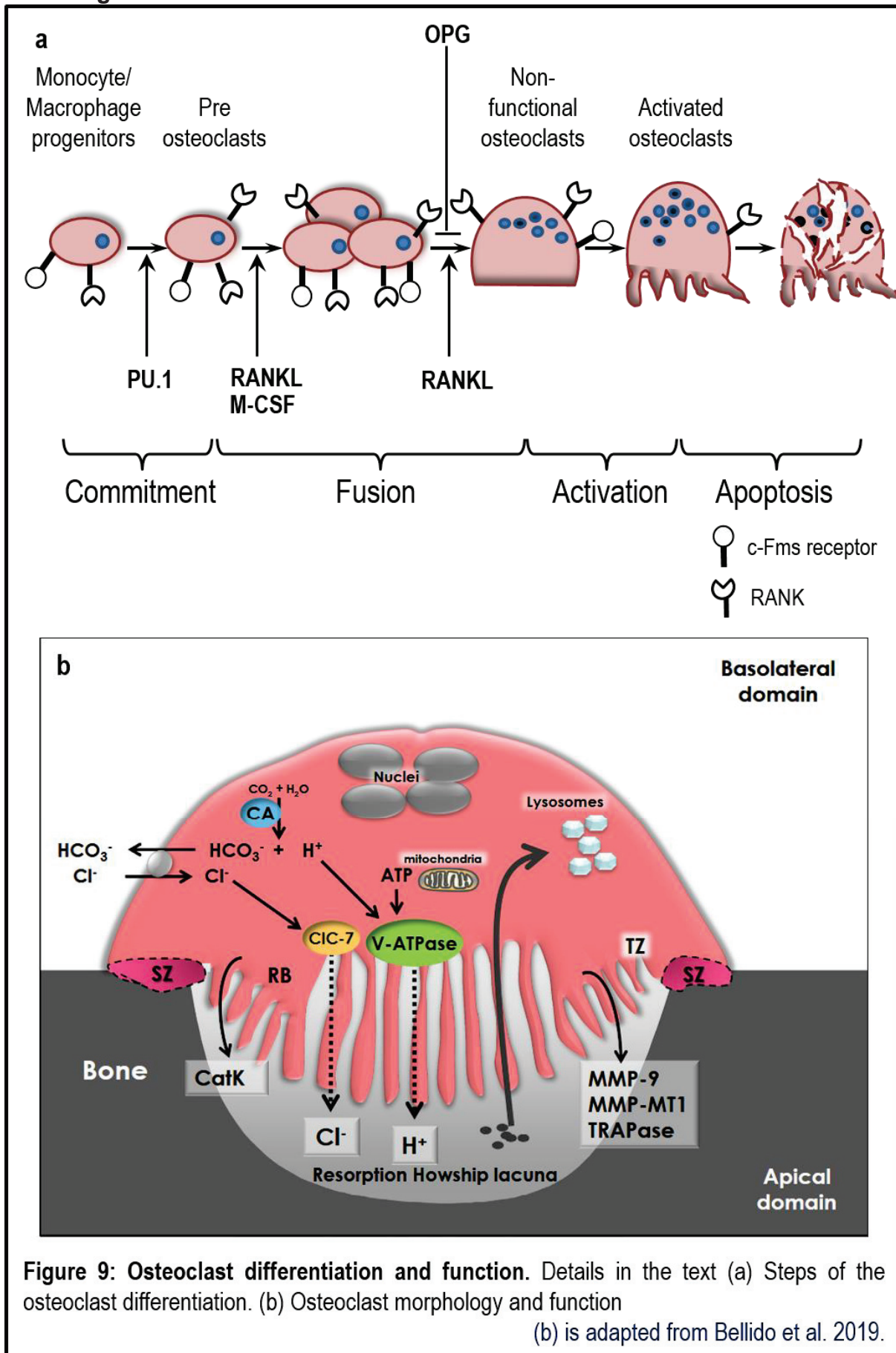
Osteocytes communicate between themselves and with other bone cells through gap junctions at the end of their the cell processes^{122,131}. This allows them to coordinate the function of osteoblasts and osteoclasts in response to both mechanical and hormonal stimuli. Osteocytes sense the stress and the strain of the surrounding bone and transmit them as biochemical signals to other cells^{132,133}. In normal physiological conditions, the osteocytes maintain the balance between bone resorption and bone synthesis through the secretion of osteoprotegerin¹³⁴ and sclerostin¹⁰⁴, decreasing osteoclast or osteoblast differentiation respectively. In the case of bone fatigue, extreme microdamage accumulation or menopause, osteocytes undergo apoptosis^{135–138}, and their death markedly enhances bone resorption¹³⁹.

II. OSTEOCLASTS

1. *Differentiation: genetic regulation, role of the surrounding cells and of cytokines*

Osteoclasts are giant multinucleated cells capable to resorb bone. They are of hematopoietic origin and generated from myeloid precursors (MP) in several steps (Figure 9a). The first identifiable marker of the OC/macrophage lineage is the transcription factor PU.1 which is essential for the commitment of myeloid precursors towards osteoclastic differentiation¹⁴⁰. PU.1 is involved in the regulation of the expression of c-Fms and RANK, the receptors of the two key osteoclastogenic cytokines, M-CSF (**M**acrophage **C**olony-**S**timulating **F**actor) and RANKL (**R**eceptor

Figure 9: Osteoclast differentiation and function



Activator of the nuclear factor **NF-κB**) respectively¹⁴¹. In the bone microenvironment, M-CSF and RANKL are expressed by bone marrow stromal cells, osteoblasts, lining cells and osteocytes, which are, as recently demonstrated, an important source of these two cytokines¹⁴²⁻¹⁴⁴.

The main effect of M-CSF binding to its tyrosine kinase receptor, c-Fms, is the stimulation of the proliferation and survival of osteoclast precursors through the activation of key transducers such as ERK and Akt¹⁴⁵. M-CSF also upregulates the expression of the C/EBPα (**C**CAAT/**E**nhancer **B**inding **P**rotein α), a transcription factor that reinforces osteoclast lineage commitment^{146,147}. Furthermore, M-CSF increases the expression of RANK and therefore augments the effect of RANKL on osteoclastogenesis.

Some other cytokines, such as IL-34^{148,149}, HGF (hepatocyte growth factor)¹⁵⁰, FL (FLT3 ligand)¹⁵¹, PlGF (placental growth factor), and VEGF-A (vascular endothelial growth factor-A)¹⁵², are capable to replace M-CSF in the promotion of the osteoclastogenesis in the presence of RANKL. However, it seems likely that they do it mostly in pathological conditions such as rheumatoid arthritis or cancer-associated osteolytic lesions^{153,154}.

Binding of RANKL to its receptor RANK promotes differentiation of osteoclast precursors into osteoclasts and mediates osteoclast activation¹⁵⁵. OPG (osteoprotegerin) which is produced by osteoblasts and osteocytes is a soluble decoy receptor for RANKL that prevents the RANKL/RANK association and thus exerts a negative effect on osteoclastogenesis^{134,156}. RANKL/RANK interaction leads to the recruitment of TRAF6 (TNF receptor-associated factor 6) and the formation of a protein complex that subsequently activates NF-κB (**N**uclear **F**actor **κB**), JNK, ERK, p38 and AKT pathways¹⁵⁴ and induces transcription factors such as c-FOS¹⁵⁷ and NFATc1

(Nuclear Factor of Activated T cells c1), the master regulator of osteoclastogenesis^{158,159}. A second pathway (ITAM receptor mediated pathway) acts in synergy with RANKL signaling to induce the expression of NFATc1¹⁶⁰.

NFATc1 in turn induces the expression of the proteins necessary for osteoclast fusion, DC-STAMP (**D**endritic **C**ell-**S**pecific **T**rans**M**embrane **P**rotein) and the Atp6v0d2 (d2 isoform of vacuolar ATPase V₀ domain)¹⁶¹. NFATc1 also regulates osteoclast activation by switching on the transcription of c-Src, CIC7 (**C**hloride **C**hannel 7), cathepsin K, LTBP3 (**L**atent **T**ransforming growth factor beta **B**inding **P**rotein 3), and MMP9 (**M**atrix **M**etallo**p**eptidase 9)¹⁶², proteins necessary for resorption.

2. Osteoclast activation and function

The osteoclast develops in three steps (Figure 9a). First, monocyte/macrophage precursors proliferate and differentiate into preosteoclasts. Second, mononuclear preosteoclasts fuse together to become nonfunctional multinucleated osteoclasts that cannot yet resorb bone. Third, the osteoclasts are activated and become functional.

Recent studies identified at least nine proteins required for the preosteoclast fusion¹⁶³, most important being DC-STAMP¹⁶⁴, OC-STAMP (**O**steoclast **S**timulatory **T**rans**m**embrane **P**rotein)¹⁶⁵ and Atp6v0d2¹⁶⁶. However, it is still unclear mechanistically how they participate in the fusion process. Nevertheless, a mechanism of action has been proposed recently for DC-STAMP. This protein has been shown to regulate a non-apoptotic transfer of phosphatidylserine (PS) to the surface of osteoclast precursors. Exposure of PS then triggers the assembly of an extracellular molecular complex that assembles and fuses cell membranes¹⁶³.

Osteoclast maturation is a complex process including the formation of a bone resorption compartment that depends in part on integrin $\alpha_v\beta_3$ which mediates bone-cell interaction^{167,168}. Integrin $\alpha_v\beta_3$ forms a transmembrane bridge between intracellular

actin filaments and matrix proteins containing ArgGlyAsp (RGD) amino-acid motifs, particularly osteopontin and bone sialoprotein¹⁶⁸. The interaction of integrin $\alpha_v\beta_3$ with matrix proteins results in a cytoskeleton rearrangement leading to the formation of an actin ring. This process involves activation of the Src kinase family members^{169,170} and results in the osteoclast polarization¹⁷¹. The apical membrane is in contact with the bone (Figure 9b). It is composed of a ruffled border surrounded by the acting ring¹⁷². The basolateral membrane is on the opposing side, and contains the functional secretory domain (FSD) in its center¹⁷³.

Sealing zone made of the acting ring firmly attaches the osteoclast to the matrix and creates a hermetic compartment for the resorption¹⁷⁴. The ruffled border consists of multiple folds of the cell membrane and contains the machinery required for the resorption. It is formed by the fusion of lysosomal secretory vesicles with the apical membrane¹⁷⁵.

Bone resorption (Figure 9b) starts with the dissolution of the mineral by H^+ and Cl^- ions and is followed by the protease-mediated degradation of the organic matrix¹⁷⁶. H^+ and Cl^- are transported in the resorption lacuna by the ATP-driven proton pump called vacuolar ATP-ase (V-ATPase)^{177–179} and chloride-specific ion channel 7 (ClC-7)¹⁸⁰ respectively (Figure 9b). The source of H^+ in the cell is carbonic acid (H_2CO_3), which is synthesized in the cytoplasm from carbon dioxide and water by carbonic anhydrase II (CA II)^{181,182}. To avoid alkalization of the cytoplasm, the bicarbonate (HCO_3^-) left in the cell after the secretion of protons is removed through the basolateral membrane by a passive chloride-bicarbonate exchanger SLC4A2^{183–185}.

After demineralization, exposed organic matrix is digested by the MMP-9 that releases a cross-linked C-terminal part of collagen I¹⁸⁶, and by cathepsin K^{187–189}, the unique enzyme capable of cleaving the insoluble collagen I^{190–192}. Byproducts of the

resorption are endocytosed at the ruffled border membrane, transported through the osteoclast in vesicles and released at the functional secretory domain on the basolateral site^{173,193}, a process called transcytosis. Organic molecules are further degraded in the transcytotic vesicles by TRAP-generated reactive oxygen species (ROS)¹⁹⁴.

At the end of the resorption process, the osteoclasts die by apoptosis¹⁹⁵

III. BONE REMODELING

1. Steps of the remodeling cycle

Bone remodeling is a process that, replacing old bone with new, serves to repair microdamage and to maintain calcium and phosphate homeostasis^{196,197}. Remodeling is performed by bone-resorbing osteoclasts and bone-forming osteoblasts functioning as a unit called “basic multicellular unit” (BMU)¹⁹⁸.

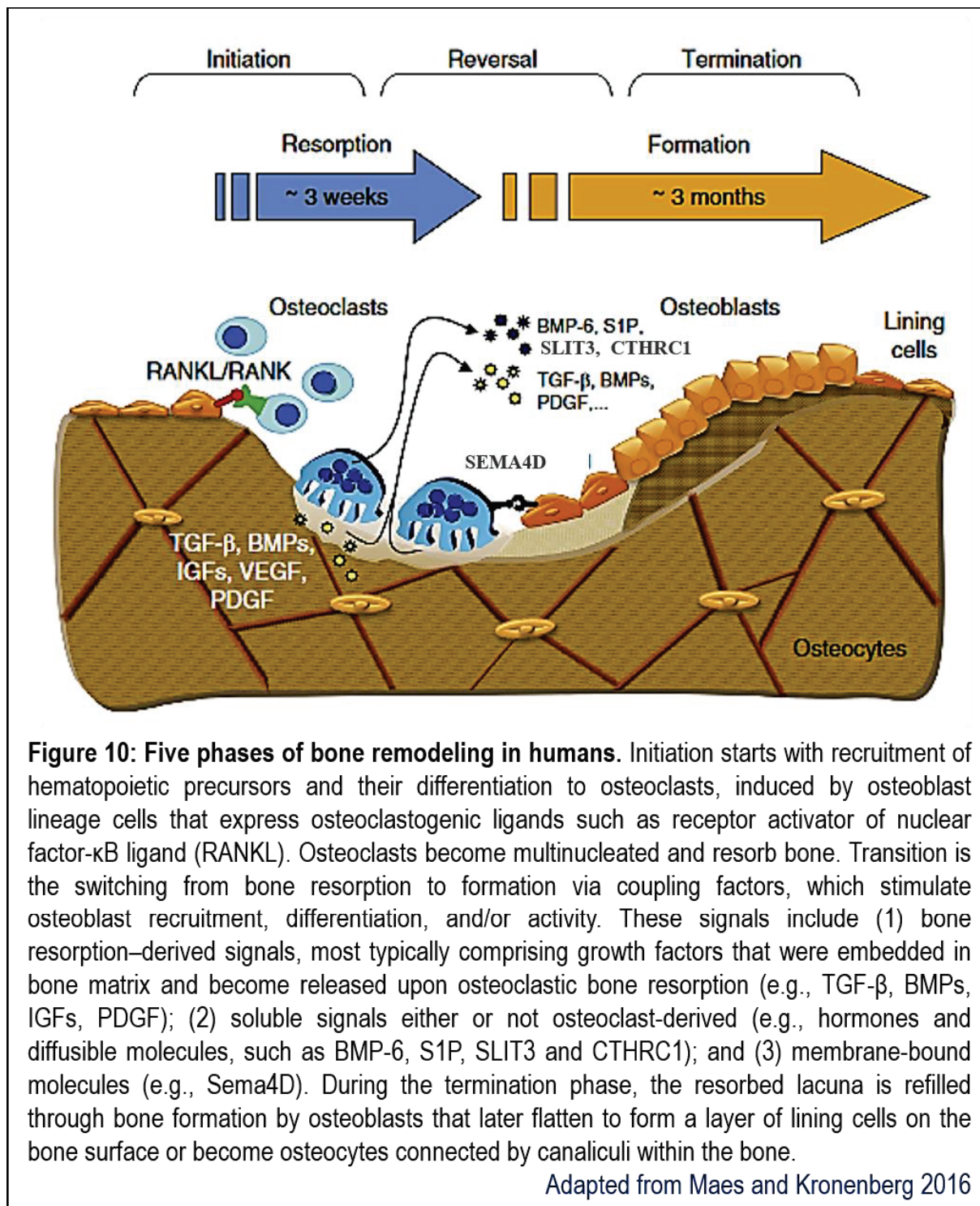
In humans, bone remodeling takes place both in the cortical and trabecular bone. The cellular mechanism is similar in both types of bone but the three-dimensional outcome is different. In trabecular bone the BMU is located on the surface where a volume of bone in the form of a ‘trench’, called Howship’s lacunae, is resorbed then refilled. In cortical bone, the osteoclasts excavate a tunnel in the cortex. New bone is then laid down concentrically on the tunnel walls by osteoblasts to leave a vascular canal in the center of the new osteon¹⁹⁹. The complete cycle of remodeling takes 120 - 200 days in cortical and trabecular bone respectively²⁰⁰. In mice, the remodeling occurs only in the trabecular bone⁵ and takes 2 weeks²⁰¹.

The remodeling cycle is composed of five sequential steps: initiation, resorption, reversal, formation and termination (Figure 10).

In the initiation phase, osteoclast precursors are recruited from the circulation^{202,203} and activated. Preosteoclasts cause lining cells to detach from the

underlying bone^{204,205}. Detached cells form as a raised canopy above the future resorption site, establishing a bone remodeling compartment (BRC) separated from the bone marrow²⁰⁶.

Figure 10: Five phases of bone remodeling in humans



Until the end of resorption phase new osteoclasts can be recruited to the remodeling site to replace those that die. However, it is still unclear what mechanism regulates the extent of remodeling²⁰⁷.

The reversal phase is a transition between bone resorption and formation. Immediately after the departure of the osteoclasts, the resorbed bone surface is colonized by the bone lining cells which remove undigested demineralized collagen left by the osteoclasts²⁰⁸. They then deposit a non-collagenous mineralized matrix rich in osteopontin, called a cement-line, which improves osteoblastic adhesion^{209,210}. Finally, clastokines released by osteoclasts²¹¹ and/or hormones or cytokines released by the matrix^{212–214} promote the migration and differentiation of osteoprogenitors.

During bone formation, osteoblasts first synthesize an unmineralized organic matrix (osteoid), which is mainly composed of type I collagen serving as a scaffold for mineralization^{215,216}. Then osteoid is mineralized²⁰⁷. Mineralization is regulated by local inhibitors and enhancers, such as pyrophosphate (PP_i) and non-collagenous proteins, and by extracellular concentration of calcium and phosphate (P_i)²¹⁷. The ratio P_i/PP_i is critical for the mineralization, since PP_i inhibits the initiation of mineral precipitation²¹⁸. ALP, an enzyme bound to the osteoblast cell membrane and present inside extracellular matrix vesicles, cleaves PP_i to generate P_i and alters the local P_i to PP_i ratio to favor mineralization²¹⁹. Noncollagenous matrix proteins serve as mineral nucleation sites and regulate crystal growth and maturation^{220–223}.

At the end of a remodeling cycle, part of the osteoblasts become the bone lining cells and cover the new bone.

2. Recruitment of the osteoclasts and the osteoblasts and coupling factors

The mechanisms that regulate the initial recruitment of the hematopoietic osteoclast precursors to the remodeling sites are not very clear, although recent

findings indicate that the sphingosine-1-phosphate (S1P)^{224–226}, and chemokines such as CCL2²²⁷, CCL9²²⁸, CXCL1²²⁹, and CXCL12²³⁰ may be implicated.

Coupling mechanism is a direct and an indirect crosstalk between osteoclasts and osteoblasts during remodeling cycle that allows spatial and temporal coordination of bone resorption with bone formation²³¹. As was described in previous section, osteoblastic cells control osteoclast activation and differentiation (Figure 10). Osteoclasts themselves were believed to participate in the coupling through their primary function, by releasing growth factors and cytokines from the matrix during resorption^{212–214}. However, emerging evidence suggests that osteoclasts can recruit and affect osteoblasts directly²¹¹. First, the conditioned media from the osteoclasts grown on plastic dose-dependently stimulates mineralization *in vitro*²³². Second, the inhibition of Cathepsin K which blocks resorption without affecting osteoclast viability does not alter bone formation, suggesting that factors released from the matrix by resorption are not essential for osteoblast function²³³. Finally, several regulatory molecules derived from the osteoclasts, called clastokines, have been recently discovered²¹¹.

Among them, SLIT3 was initially identified as an axonal guidance molecule²³⁴. However, it is also secreted by the osteoclasts and its synthesis is upregulated during osteoclast differentiation. More importantly, SLIT3 stimulates pre-osteoblast migration and proliferation while inhibiting osteoclastogenesis in an autocrine way²⁶.

CTHRC1 (**C**ollagen **T**riple **H**elix **R**epeat **C**ontaining 1) is also a protein secreted by mature bone-resorbing osteoclasts. It suppresses adipocytic differentiation of marrow stromal cells and increases osteoblastogenesis^{235,236}.

SEMA4D (Semaphorin 4D) is another axonal guidance molecule²³⁷ produced by osteoclasts. Unlike SLIT3 and CTHRC1, it reduces bone formation²³⁸. Therefore,

SEMA4D could not be considered as a coupling factor. However, it may play a role in remodeling by inhibiting osteoblast differentiation until the completion of the resorption phase²³⁹.

3. Age-related remodeling imbalance and bone alterations

In aging men and women, bone mineral density, cortical bone thickness and trabecular bone volume decrease with increasing age and there is a substantial increase in cortical bone porosity²⁴⁰, which is more prominent in post-menopausal women²⁴¹. Mice show analogous changes²⁴²⁻²⁴⁵. Several causes have been discovered for the loss of bone mass. First, estrogen's withdrawal in women or declining levels in men lead to a shortening in the bone formation period and an increase in the resorptive period²⁴⁶, resulting in the net loss of bone mass. Second, age-related osteocyte loss through apoptosis^{201,247,248} and consecutive disappearance of osteocyte-secreted signaling factors also tips bone remodeling balance in favor of bone resorption²⁴⁹. Finally, possible depletion of the bone marrow osteoblast progenitors^{17,250,251}, their increased bias toward adipogenic differentiation²⁵²⁻²⁵⁴ and/or osteoblast senescence²⁵⁵⁻²⁵⁷ impair the osteoblastogenesis and therefore new bone formation.

Age-associated modifications described above contribute to the increased risk of bone fracture. Currently, the assessment of the fracture risk is based principally on bone mineral density (BMD)²⁵⁸ which is thought to be correlated with the loss of bone mass and alterations to skeletal architecture, especially after the menopause in women. However, these changes contribute to only about 75% of the increased risk of fracture^{259,260}. The remaining 25% could be engendered by age-related modifications of bone matrix properties. The discussion regarding changes observable in bone ECM components with age is presented in chapter IV.

CHAPTER 3: BONE EXTRACELLULAR MATRIX

I. A VERY BRIEF HISTORY OF THE EXTRACELLULAR MATRIX.

In a sense, humans have known about the existence of the extracellular matrix (ECM) since the beginning of their history, considering that they used a variety of objects made from bone and skin. Thus, when the first theories of life were developed in the middle ages, living organisms were described as being composed of fibers that were somehow alive. These fibers were given primordial importance, since, under the right conditions, life could arise from them by spontaneous generation. Those theories were reinforced in the early 1700s, when some living tissues were first studied with light microscopy, and fibers were observed. Later on, the fibers were collectively named “connective tissue” (in German, “bindegewebe”, by Johannes Müller in 1830), a term that we still use today. Nevertheless, with the discovery of cells in the mid-nineteenth century, a new theory emerged and was gradually accepted: cells are the basis of life and produce all intercellular substances, which started to be called extracellular matrix (ECM) in the 1930s²⁶¹.

However, as it so often happens during a change of paradigm, ECM was relegated to a role of a structural support and nothing more. Only in the last 10-20 years it has started to be recognized that matrix plays a far more active role. ECM not only constitutes the microenvironment in which cells reside, but it also regulates their fate, behavior and function. ECM has been shown to direct the stem cell differentiation along different pathways or, conversely, to retain their stemness²⁶²⁻²⁶⁴; to promote or inhibit cell adhesion^{265,266}, cell migration^{267,268} and proliferation^{269,270}; and to regulate apoptosis and survival^{271,272}. Not surprisingly, it is currently a very dynamic field of research. However, bone ECM presents a particular challenge, being mineralized and

therefore hard, compact and difficult to study in its entirety. What follows below is a brief review of what is currently known about the composition of the bone matrix.

II. COMPONENTS OF THE MINERALIZED ECM.

Mineralized bone ECM (Figure 2 in the chapter I) is composed of approximately 65 % of mineral phase (carbonated apatite), 25 % organic phase and 10 % water⁴⁴. The organic phase contains about 90 % of collagens, mostly collagen I, with some collagen III and V, and 10 % of noncollagenous proteins (NCP)²⁷³. These proportions could vary depending on the bone type, the age of the mineralized tissue and even the location inside the lamella, where disordered phase seems to have more NCP^{28,215}.

1. Water

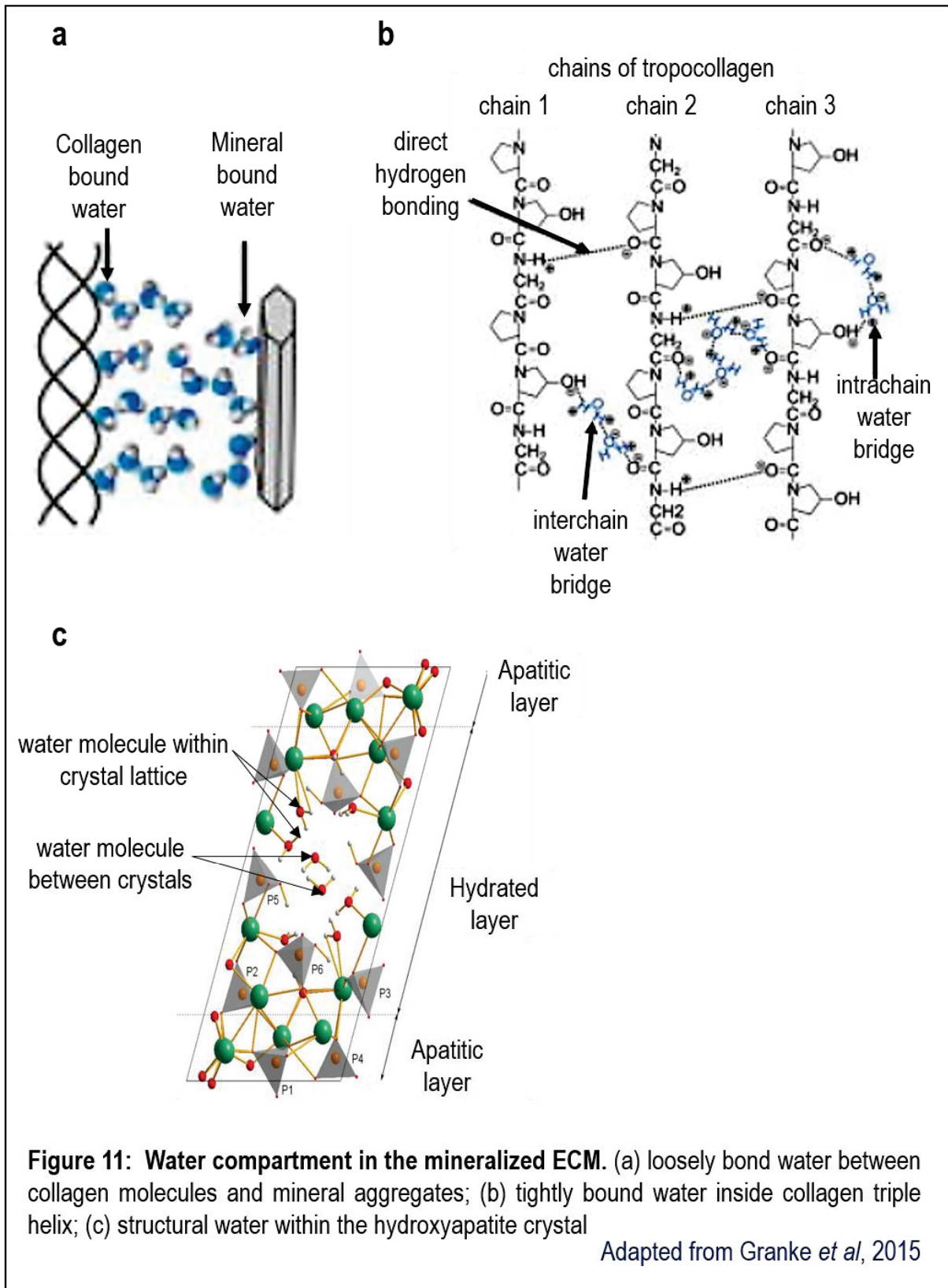
Water exists in two different states in the mineralized matrix: free in the lacuno-canalicular and vascular spaces, and bound inside and around mineralized collagen fibrils. It can therefore affect mechanical behavior of bone differently depending on its location. Free water is a macrostructural feature of the bone and reflects intra-cortical porosity comprising Haversian and Volkmann's canals, lacuno-canalicular network and resorption lacunae^{274,275}. Several studies have shown that an increase in porosity, and thus in free water content of the bone, is inversely proportional to the fracture toughness, *i.e.* the ability to resist fracture^{276–278}.

Bound water exists in three different configurations (Figure 11).

The tightly bound water forms inter- and intra-chain hydrogen bonds between hydrophilic sites of collagen (Figure 11b)^{279,280}, and thus contributes to the structuring and the stabilization of the tropomolecule^{281,282}. It should be noted that during mineralization water in the collagen is exchanged on 1:1 basis with mineral⁴⁴. Therefore, the more collagen fibril is mineralized, the less water it contains. Removal

of the tightly bound water was shown to increase matrix's hardness and stiffness (elastic modulus), but also brittleness²⁸³.

Figure 11: Water compartment in the mineralized ECM



The so-called structural water, is trapped in the bone's mineral phase, both inside²⁸⁴ and in-between²⁸⁵ hydroxyapatite crystals (Figure 11c). Structural water molecules form hydrogen-bonding bridges between surrounding ions, thus stabilizing the crystals²⁸⁶.

Finally, there is an organized layer of water between collagen molecules and mineral crystals^{284,287,288}, and between adjoining mineral platelets^{289,290} (Figure 11a). This loosely bound water is one of the major factors responsible for bone's ductility – the capacity for non-elastic (permanent) deformation preventing complete fracture. Indeed, when load exciding yield point is applied to the bone, loosely bound water allows hydroxyapatite platelets to slide over each other instead of separating²⁸⁸. Removal of loosely bound water is thought to lead to a higher accumulation of the micro-cracks^{291,292}.

Given its importance to the bone mechanical performance, water remains an ECM component that is not very well investigated, probably because its study requires a combination of biochemical and mechanical knowledge.

2. The organic bone matrix

A. Collagen

Collagen I is a major determinant of bone mechanical qualities (Chapter I). It also has a direct effect on bone cell function: inducing apoptosis of osteoblasts and osteocytes when mutated in a murine model²⁹³, stimulating proliferation and function of osteoblasts derived from rat calvaria²⁹⁴ and modifying intracellular signaling²⁹⁵.

Collagen I is a heterotrimeric molecule ~300 nm long and ~1,5 nm thick, formed of two $\alpha 1$ chains and one $\alpha 2$ chain. A minor homotrimeric form assembled from three $\alpha 1$ chains is also found in bone (Figure 11). Each chain is about 1000 amino acid long, almost entirely made up of repeating Gly-X-Y triplets, where Gly is glycine and X and

Figure 12: Collagen synthesis

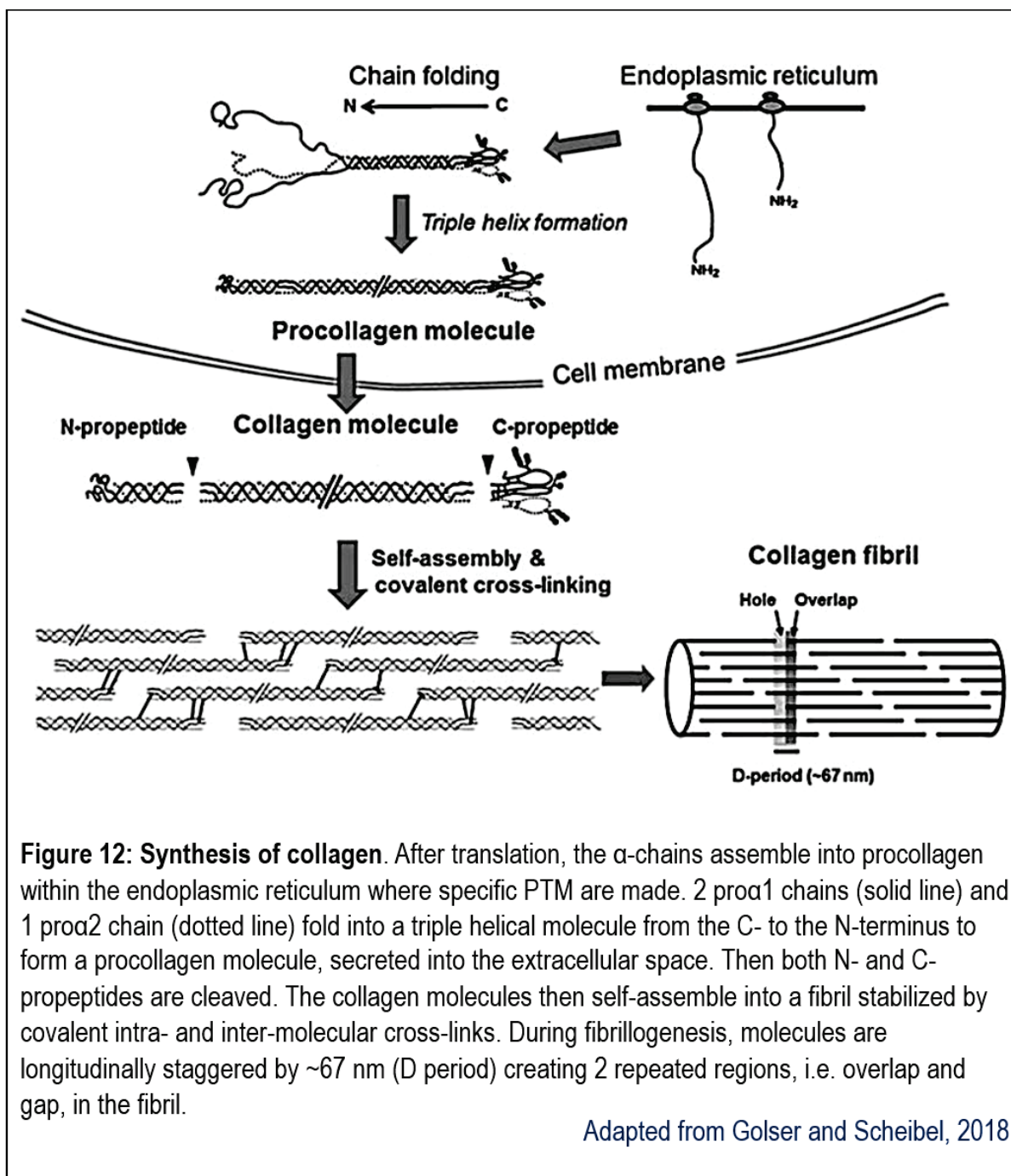


Figure 12: Synthesis of collagen. After translation, the α -chains assemble into procollagen within the endoplasmic reticulum where specific PTM are made. 2 $\text{pro}\alpha 1$ chains (solid line) and 1 $\text{pro}\alpha 2$ chain (dotted line) fold into a triple helical molecule from the C- to the N-terminus to form a procollagen molecule, secreted into the extracellular space. Then both N- and C-propeptides are cleaved. The collagen molecules then self-assemble into a fibril stabilized by covalent intra- and inter-molecular cross-links. During fibrillogenesis, molecules are longitudinally staggered by ~ 67 nm (D period) creating 2 repeated regions, i.e. overlap and gap, in the fibril.

Adapted from Golser and Scheibel, 2018

Y are often proline and 3- or 4-hydroxyprolines. Repetition of the glycine residues is essential for the formation of helical structure, since it allows the helix to turn at every third position without suffering from steric hindrances that would have been created by any other, bulkier residue^{296,297}. The helix is further stabilized by hydrogen bonds between OH of hydroxyproline and interchain water²⁹⁸.

Collagen biosynthesis is a very complex and tightly regulated process involving post-translational modifications (PTM), folding, secretion, extracellular procollagen processing, microfibril assembly and gradual cross-linking (Figure 11).

During collagen synthesis in the endoplasmic reticulum (ER), the nascent polypeptide chains are post-translationally modified – hydroxylated on proline and lysine residues. Some of the resulting hydroxylysines are then glycosylated. After the synthesis, three α chains associate at their carboxy termini and assemble into a triple helix in a zipper-like fashion. The resultant procollagen molecule consists of 5 domains: the central triple helical domain (about 95% of the total length²⁹⁹), N- and C-terminal non triple helical domains (called N- and C- telopeptides respectively), and N- and C-terminal propeptides. The propeptides stabilize procollagen by sulfur cross-links⁴⁴. It should be noted that lysine PTMs in bone present special characteristics. In collagen I of bone, only 50% of telopeptide lysines are hydroxylated, compared with 100% in the cartilage and 0% in the skin³⁰⁰. As described below, lysine hydroxylation during collagen synthesis determines subsequent tissue-specific cross-linking patterns.

After formation of the triple helix, the procollagen molecule is secreted to the extracellular space, where N- and C-terminal propeptides are cleaved by ADAMTS (**A** Disintegrin **A**nd **M**etalloproteinase with **T**hrombospondin motifs) and BMP1 (**B**one **M**orphogenetic **P**rotein 1) respectively. Then, the resulting tropocollagen molecules self-assemble into collagen fibrils, via a mechanism that remains controversial.

The currently accepted scheme of the collagen I fibril structure was proposed in 1963 by Hodge and Petruska, based on transmission electron microscopy observations: tropocollagen molecules are aligned in several parallel layers with a regular space between two adjacent molecules of the same layer. Moreover, each molecule is shifted relative to the molecules of the other layers by ~67 nm or D period.

This arrangement creates repeated zones of high and low packing density, i.e. overlap and hole zones respectively as shown in Figure 12, resulting in a characteristic banding pattern of collagen fibrils.

Because this model proved to be difficult to adapt to a three-dimensional structure of the collagen fiber as observed by X-ray diffraction, several 3D models of collagen packing into fibers have been proposed in the last 50 years such as liquid crystalline assemblies³⁰¹ or fiber assembly directly from collagen monomers^{302,303}. However, recent advances in crystallographic techniques have shown that fibrils are indeed the building blocks of collagen fibers^{30,304,305}. Tropocollagen molecules assembled in a fibril rotate around the central axis and interlace with each other, leading to a rope-like structure.

Concomitantly with fibril assembly, intra- and intermolecular and interfibrillar cross-links of the collagen are initiated by the lysyl oxidase (LOX) that catalyzes the conversion of lysine molecules into highly reactive aldehydes. In the collagen I, there are only five Lys or hydroxylysines in the telopeptides, giving a total of 5 possible cross-linking sites, since LOX cannot catalyze reactions in the helical domain²⁹⁹. Once the lysines and hydroxylysine of telopeptides are converted to reactive aldehydes, they non-enzymatically condense with amine groups of lysine or hydroxylysine residues in the triple helical domain to form bivalent (initial) cross-links (Figure 13). These links can further develop into trivalent (mature) links: pyridinolines and pyrroles. In normal bone, pyridinolines and pyrroles are present in equal amounts³⁰⁶, but the latter can only be generated from non-hydroxylated telopeptide lysines. Change in this proportion has been shown to lead to bone pathologies. For example, higher than normal content of pyrroles due to higher number of non-hydroxylated telopeptide lysine residues (under-hydroxylation) during collagen intracellular processing results in brittle bones

both in Bruck syndrome and in osteogenesis imperfecta^{307,308}; however, lower amount of pyrroles due to over-hydroxylation of telopeptide lysine also leads to osteogenesis imperfecta³⁰⁹.

Figure 13: Cross-linking in bone collagen

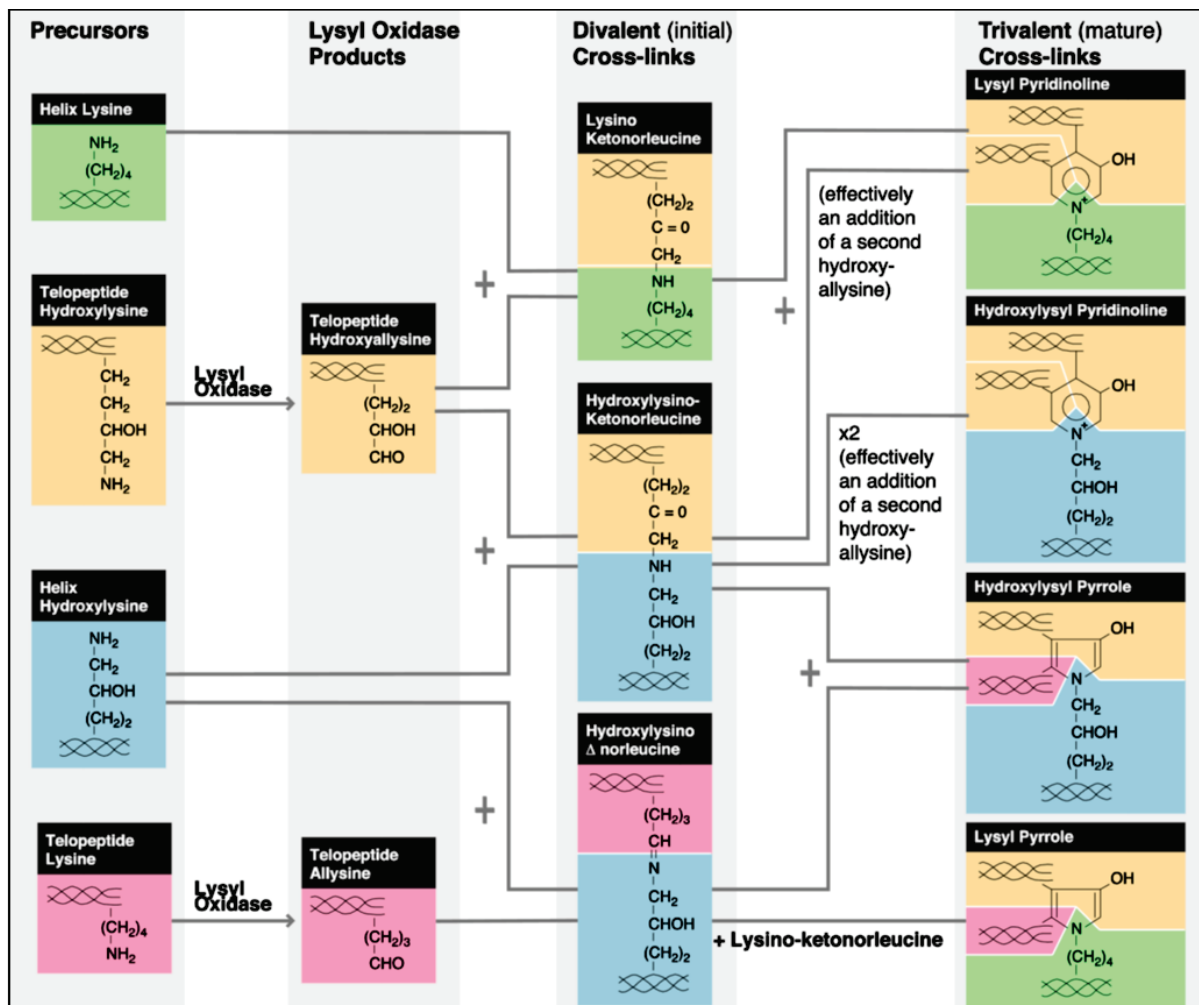


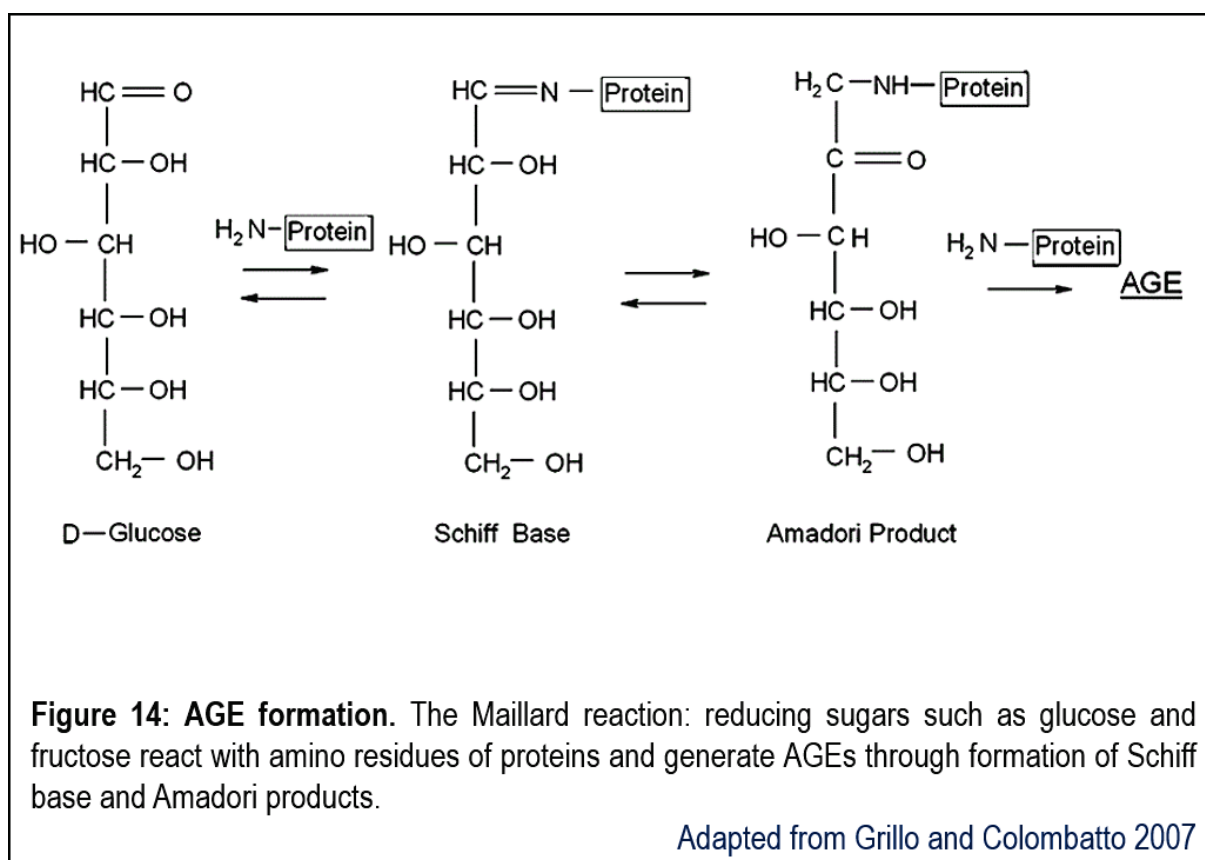
Figure 13: Cross-linking in bone collagen. Summary of various pathways of collagen cross-linking in bone collagen I. After lysyl oxidase produces aldehydes from lysine and hydroxylysine in telopeptides, divalent reducible (immature) cross-links spontaneously occur between these aldehydes and Lys or Hyl in the triple helix. With time, the divalent cross-links mature into trivalent non-reducible cross-links

From Eyre and Weis, 2013

Being a long-lived protein, bone collagen is susceptible to the accumulation of the advanced glycation end-products (AGEs) resulting from a spontaneous non-enzymatic glycation (Figure 14). In this process, called Maillard reaction, glucose reacts with free amino-groups, such as lysine and arginine, to form unstable Schiff

bases^{310,311}, which undergo further modifications to form Amadori products and then AGEs³¹². Some AGEs, such as pentosidine, form crosslinks between two residues (Figure 14, upper right panel), others, such as CEL (carboxyethyl lysine) are attached to single residue³¹³. The former change collagen structural properties and decrease bone mechanical performance^{314–316}. The latter mostly act through a cellular receptor, RAGE, and negatively affect bone cell function^{317–320}.

Figure 14: AGE formation



B. Noncollagenous proteins (NCP)

The term noncollagenous proteins (NCP) encompasses a wide variety of proteins with very different functions that could however be divided in several broad categories. These are:

- 1) structural NCP, participating in regulation of collagen assembly and of matrix mineralization,

- 2) chemotaxic molecules, acting as homing signals for bone cells during bone remodeling,
 - 3) matrix-degrading enzymes, such as matrix metalloproteinases (MMPs)
- and
- 4) matrix-bound growth factors, affecting bone cell proliferation and differentiation.

Since there is a very abundant literature on NCPs and their role in bone, my experimental results prompt me, after a brief description of structural NCP, to focus on proteins that are of interest for further discussion.

Structural NCP could be classified on the basis of their biochemical composition as (1) glycoproteins, (2) γ -glutamic acid containing proteins (Gla-proteins) and (3) proteoglycans. Although they all play some role in the organization of the bone ECM, some of them, which have recently been labeled as matricellular proteins, modulate cell functions³²¹. Table 1 summarizes both structural and matricellular (if known) roles of the most abundant NCP.

(1) Glycoproteins are characterized by polysaccharides that are post-translationally added to either serinyl or asparaginyl residues (O- or N-linked glycosylation respectively). With some exceptions [alkaline phosphatase (ALP), osteonectin and tenascin C], they also contain RGD (Arg-Gly-Asp) sequence that mediates cell-matrix interactions through binding to integrin receptors on the cell surface³²². The list of RGD-containing matrix glycoproteins is very long (and getting longer each year), but in bone the best characterized examples are fibronectin, vitronectin and thrombospondins. They can bind both collagen and cell membrane receptors and therefore serve as an intermediary in the cell-ECM signaling.

A part of the RGD-containing proteins forms a family known as SIBLINGs (**S**mall **I**ntegrin-**B**inding **L**igand, **N**-linked **G**lycoprotein) which is characterized by the N-linked

oligosaccharides containing large amount of sialic acid and by the long poly-acidic sequences in the core protein, that also incorporates many phosphorylation sites. The family includes osteopontin (OPN), bone sialoprotein 2 (BSP), dentin matrix protein 1 (DMP1), matrix extracellular glycoprotein (MEPE), dentin phosphoprotein (DPP) and enamelin (ENAM). In humans, these proteins are clustered on chromosome 4 and thought to have appeared by the duplication of a single gene³²³. Carrying a high negative charge which has a strong affinity for the Ca^{2+} ions, the members of this family are the major regulators of mineralization³²⁴.

(2) Gla-proteins are post-translationally carboxylated on the γ -carbon of the glutamic acid residues by vitamin K-dependent enzymes. There are three Gla-containing proteins in the bone matrix: osteocalcin³²⁵ with 3 Gla, matrix Gla protein³²⁶ with 5 Gla, and protein S³²⁷ with 11 Gla. Similar to SIBLINGs, they bear a high negative charge that confers them an affinity for calcium ions, but in the case of Gla-proteins, the charge is carried by the di-carboxylic glutamyl residues. The functions of Gla-proteins are therefore dependent on their ability to sequester Ca^{2+} but specific to each protein (Table 1): while matrix Gla protein inhibits soft tissue mineralization^{328,329}, osteocalcin controls hydroxyapatite crystal growth³³⁰.

(3) Proteoglycans are defined by the covalent attachment of long chains of repeated disaccharide units, often sulfated, termed glycosaminoglycans (GAG) to a core protein. Four types of GAG could be bound to the proteoglycan core (Figure C): chondroitin sulfate (CS), dermatan sulfate (DS), keratan sulfate (KS) and heparan sulfate (HS). Hyaluronic acid (HA), another GAG found in bone, is not sulfated and exists as a separate entity not linked to a core protein. Most of the bone proteoglycans belong to the family of **S**mall **L**eucine-rich **R**epeat-containing **P**roteoglycans (SLRP), characterized by a small protein core containing 10-12 repeats of peptide sequence

rich in leucine residues³³¹. All bone SLRP can bind collagen, but with varying degree of affinity. Collectively, they play a crucial role in collagen fibrillogenesis, matrix assembly³³² and spacio-temporal control of the matrix mineralization³³³.

Decorin (DCN) is the best characterized SLRP, however its role in mineralized ECM is still under study as most of the research has been performed in soft tissues. Nevertheless, as a first indication, numerous histological examinations of normal bone performed mostly in the 1970s showed that the amount of proteoglycans is inversely proportional to the degree of bone mineralization²¹⁵ and that 45 % of proteoglycans were removed during bone calcification³³⁴. In agreement with these observations, Hoshi *et al.* later showed that bone mineralization is preceded by the elimination of DCN³³⁵. Moreover, overexpression of the DCN in MC3T3-E1 osteoblastic cells induced a delay in the mineralization³³⁶. Combined evidence therefore suggests that DCN inhibits mineralization. However, the fact that it is expressed by osteoblasts at the onset of matrix synthesis³³⁷ implies that it could play a role in bone formation. Mouse Knock-out models and *in vitro* studies established that DCN limits side-to-side fusion of collagen fibrils, thus maintaining them thinner and uniform^{338–340}. Taken together, the role of DCN in bone seems to be to regulate collagen fibril diameter and to prevent premature calcification of the osteon³⁴¹.

Table 1: Functions of the noncollagenous proteins in bone

Protein name / type	Gene name	Structural function	Matricellular function
Alkaline phosphatase / <i>glycoprotein</i>	ALPL	Promotes mineralization by hydrolysis of pyrophosphates ³⁴²	
Osteonectin / <i>glycoprotein</i>	SPARC	Synthesis and assembly of collagen I containing ECM ³⁴³	Promotes OB differentiation and survival, inhibits adipogenesis ³⁴⁴

Protein name / type	Gene name	Structural function	Matricellular function
Tenascin C / glycoprotein	TN-C	Affects initial matrix synthesis through control of fibronectin deposition and turn-over ³⁴⁵	Promotes OB differentiation ³⁴⁶
Fibronectin / RGD glycoprotein	FN1	Regulates collagen I matrix assembly ³⁴⁷ and stability ³⁴⁸	Important for OB differentiation ^{349,350} and function ³⁵¹
Vitronectin / RGD glycoprotein	VTN	Inhibits HA nucleation <i>in vitro</i> ³⁵²	Promotes OB ³⁵³ and OCL ³⁵⁴ attachment
Thrombospondin 1 / RGD glycoprotein	THBS1		Promotes OSC function ³⁵⁵ , modulates cell migration ³⁵⁶ , antiangiogenic ³⁵⁷
Thrombospondin 2 / RGD glycoprotein	THBS2	Possibly modulates collagen fibrillogenesis ³⁵⁸	Promotes OB differentiation, inhibits adipogenesis, inhibits MSC proliferation ^{359,360}
Osteopontin / acidic SIBLING glycoprotein	SPP1	Inhibits mineralization <i>in vitro</i> ³⁶¹ ; modulates HA crystal growth ³⁶² ; inhibits soft tissue calcification ³⁶³ ; increases bone toughness through sacrificial bond formation ³⁶⁴	Promotes OCL migration, fusion and resorption activity ^{365,366}
Bone sialoprotein / acidic SIBLING glycoprotein	IBSP	Nucleation of hydroxyapatite ^{367,368} ; implication in primary bone formation and modeling ³⁶⁹	Promotes OB differentiation and function ³⁷⁰ ; promotes OCL adhesion, proliferation and function ^{371,372}
Dentin matrix protein 1 /acidic SIBLING glycoprotein	DMP1	Participates in bone response to mechanical stress ³⁷³	Controls systemic phosphorus homeostasis through negative regulation of the FGF23 synthesis in osteocytes ^{49,374}
Osteocalcin /acidic Gla protein	BGLAP	Controls the growth of hydroxyapatite crystals and regulates their maturation ^{330,375}	Acts as systemic hormone (chapter I); promotes OCL differentiation ³⁷⁶
Matrix Gla protein / acidic Gla protein	MGP	Inhibits calcification in soft tissues ³²⁸	
Versican / proteoglycan	VCAN	May define space destined to become bone ³⁷⁷	May inhibit pre-OB proliferation ³⁷⁸

Protein name / type	Gene name	Structural function	Matricellular function
Fibromodulin / SLRP proteoglycan	FMOD	Binds collagen ³⁷⁹ and may modulate collagen fibrillogenesis ^{380,381}	
Biglycan / SLRP proteoglycan	BGN	Modulates in dose-dependent manner HA crystal growth <i>in vitro</i> ³⁸² ; controls collagen I fiber diameter ³⁸³	Promotes OB differentiation ^{384,385}
Decorin / SLRP proteoglycan	DCN	Controls collagen I fiber diameter and matrix mineralization ^{339,340} ; prevents premature bone calcification ³⁴¹	Inhibits angiogenesis ³⁸⁶ ; inhibits multiple growth factor receptors ³³¹

3. Mineral phase

The inorganic phase of bone is best described as impure hydroxyapatite (HA)³⁸⁷. Pure geological hydroxyapatite has the formula $\text{Ca}_{10}(\text{PO}_4)_6(\text{OH})_2$ ³⁸⁸, but bone mineral contains 5–8 % of carbonate (CO_3^{2-}), which substitutes phosphate (PO_4^{3-}) and hydroxide (OH^-)^{387,389}. Moreover, calcium (Ca^{2+}) in HA crystal lattices is often replaced by sodium (Na^+), potassium (K^+), magnesium (Mg^{2+}), and zinc (Zn^{2+}) as well as being simply absent (calcium vacancies). Despite high level of crystal defects, mineral phase integrity is maintained via hydrogen bonds created by structural water in and around crystals²⁸⁶ and, possibly, through HA interactions with NCP³⁶⁴. Specific effect of each ion substitution in the bone matrix is still not well understood, but it is established that the composition of HA lattice can affect the function of bone cells. For example, higher levels of Mg stimulate osteoblast differentiation³⁹⁰ while its depletion causes bone loss³⁹¹. Besides above-mentioned physiological substitutions, in case of intoxication, phosphate in HA can be replaced by arsenic³⁹², and calcium, substituted by aluminum^{393,394}, lead³⁹⁵ and uranium³⁹⁶. This creates a long-term internal reservoir of these toxic substances, and extends their deleterious effect.

The long axis of the HA crystals in bone is aligned with collagen fibrils. Individual crystals are long and thin platelets (~20-80 nm in length, 15-30 nm in width and 2-8 nm in thickness)³⁹⁷. These dimensions are important for optimal mechanical performance of the bone. Increase in the crystal size was observed in osteogenesis imperfecta³⁹⁸ and osteoporosis patients²¹⁶, as well as in normal bone with aging^{399,400}. Moreover, small size of crystals confers them their unique biological properties. The smaller the size of a substance, the greater is its surface area, meaning that more of its constituent ions are available for rapid mobilization in order to maintain ion homeostasis. However, the size and the shape of the crystals are affected by the composition of the matrix. That is the case in the osteocalcin and osteopontin knock-out mouse models, where crystals are thinner, smaller and less aligned along collagen fibrils³³⁰. Nonetheless, much remains to be learned about how the nanoscale mineral properties are regulated.

III. ECM REGULATION OF REMODELING

To describe how bone matrix regulates remodeling means to show how ECM affects the behavior of the osteoclasts, the osteoblasts and the osteocytes, the actors of the remodeling. Many examples of this regulation were presented throughout this chapter, particularly in the section of noncollagenous proteins (table 1). Here, I will describe some cases that were left out.

Multiple studies have demonstrated that the nature of the ECM, such as topology, stiffness and mineral composition, affects both osteoclasts and osteoblasts. As an example, the mineral phase of bone matrix is required for the resorptive activity of osteoclasts because, when osteoclasts are cultured on demineralized dentin or bone, they fail to form a proper actin ring structure or resorption pit⁴⁰¹⁻⁴⁰³. Osteoclasts also form bigger and more stable sealing zones when cultured on surfaces with rough topologies^{404,405}. Furthermore, presence of small cracks can stimulate actin ring

formation around these cracks⁴⁰⁴, while steep-sloped barriers prevents sealing zone expansion⁴⁰⁶. Osteoblasts are also sensitive to the surface topology, since pre-osteoblasts grow and differentiate better on surfaces with microgrooves⁴⁰⁷ or inside small steeply-angled concavities^{408,409}.

There is now enough evidence identifying ECM as an active player in osteoblast differentiation. First, matrix stiffness [expressed as elastic (Young's) modulus and measured in pascals (Pa); the higher the modulus, the stiffer the material], specify lineage commitment of mesenchymal stem cells towards neurons (0,1-1 kPa), myoblasts (8-17 kPa), or osteoblasts (25-40kPa)⁴¹⁰. Then, collagen I-rich extracellular matrix is required for initial⁴¹¹⁻⁴¹³ and terminal osteoblast differentiation steps⁴¹⁴. The regulation passes through the binding of the osteoblast integrin $\alpha 2\beta 1$ receptor to collagen I^{415,416}. Finally, matrix-bound growth factors stimulate osteoblast function, as does, for example, IGF-1⁴¹⁷.

Growth factors embedded in ECM directly participate in the remodeling process. When released from the matrix by osteoclastic resorption, TGF β recruits mesenchymal progenitors cells to the site of remodeling²¹⁴ and IGF-1 induces their differentiation⁴¹⁸.

Exogenous factors incorporated into the bone matrix also affect bone cell functions and thus influence remodeling. Gallium, for example, impairs osteoclast differentiation and resorptive activity⁴¹⁹ and bisphosphonates induce osteoclast apoptosis⁴²⁰ and drastically reduces remodeling⁴²¹.

These examples are far from exhaustive, but illustrate the many mechanisms by which ECM can affect remodeling and thus contribute to the development of bone pathologies.

CHAPTER 4: BONE ECM ALTERATIONS

I. BONE MATRIX-ASSOCIATED DISEASES

Mutations in genes associated with the extracellular matrix affect various tissue organization and/or functions and can therefore lead to disorders with a wide range of clinical phenotypes. Here are some examples of genetic disorders related to the bone matrix.

Osteogenesis imperfecta (OI), also called “brittle bone disease”, is a group of genetic disorder of variable severity, characterized by increased bone fragility and susceptibility to bone fracture, bone deformity, osteopenia, dental problems, and hearing loss⁴²². About 90% of OI cases are autosomal dominant disorders caused by monoallelic mutations in one of the two genes encoding type I collagen (COL1A1 and COL1A2) that affect either the amount or the structure of the collagen matrix⁴²³. The remaining 10% of OI cases are mostly autosomal recessive diseases caused by mutations in genes related to collagen I biosynthesis and organization. Among mutations affecting COL1A1 or COL1A2, those resulting in a premature stop codon lead to collagen I haploinsufficiency through nonsense-mediated mRNA decay. Mutations leading to structural abnormalities, such as missense mutations, have different consequences, depending on the position of the mutation and/or the type of amino acid substitution. These consequences include:

- (i) the secretion of structurally abnormal triple helices that interfere with fibrillogenesis, collagen-NCP or collagen-cell interactions, or mineralization⁴²⁴;
- (ii) a delay in helix propagation during the formation of the triple helix which allows increased hydroxylation and glycosylation in the unfolded part of collagen chains⁴²⁵. This increase in post-translational modifications may

lead to a shift from pyrrole to pyridinoline cross-links in collagen³⁰⁹, a known cause of impaired trabecular bone formation⁴²⁶.

- (iii) the impaired assembly of the triple helix which triggers the intracellular degradation of the misfolded collagen via the ER-associated proteasomal degradation (ERAD) and consequently decreased collagen secretion^{427,428}. The triple helix misfolding can also initiate an ER-stress response with deleterious cellular consequences up to apoptosis⁴²⁹.

Another group of diseases are those caused by mutations in Fibrillin-1 (*FBN1*) and -2 (*FBN2*) genes that cause serious skeletal abnormalities in patients with Marfan syndrome (MFS) and congenital contracture arachnodactyly (CCA)⁴³⁰. Fibrillin-1 and Fibrillin-2 are glycoproteins that assemble as microfibrils and elastic fibers and play a structural role in the ECM of most tissues, including bones^{431,432}. However, several studies have shown that these proteins play an important role in bone formation and metabolism by regulating the bioavailability of TGF β and BMP proteins, which are crucial regulators of bone cell differentiation (OB and OCL)^{433,434}.

II. MODIFICATION OF BONE ECM WITH AGING.

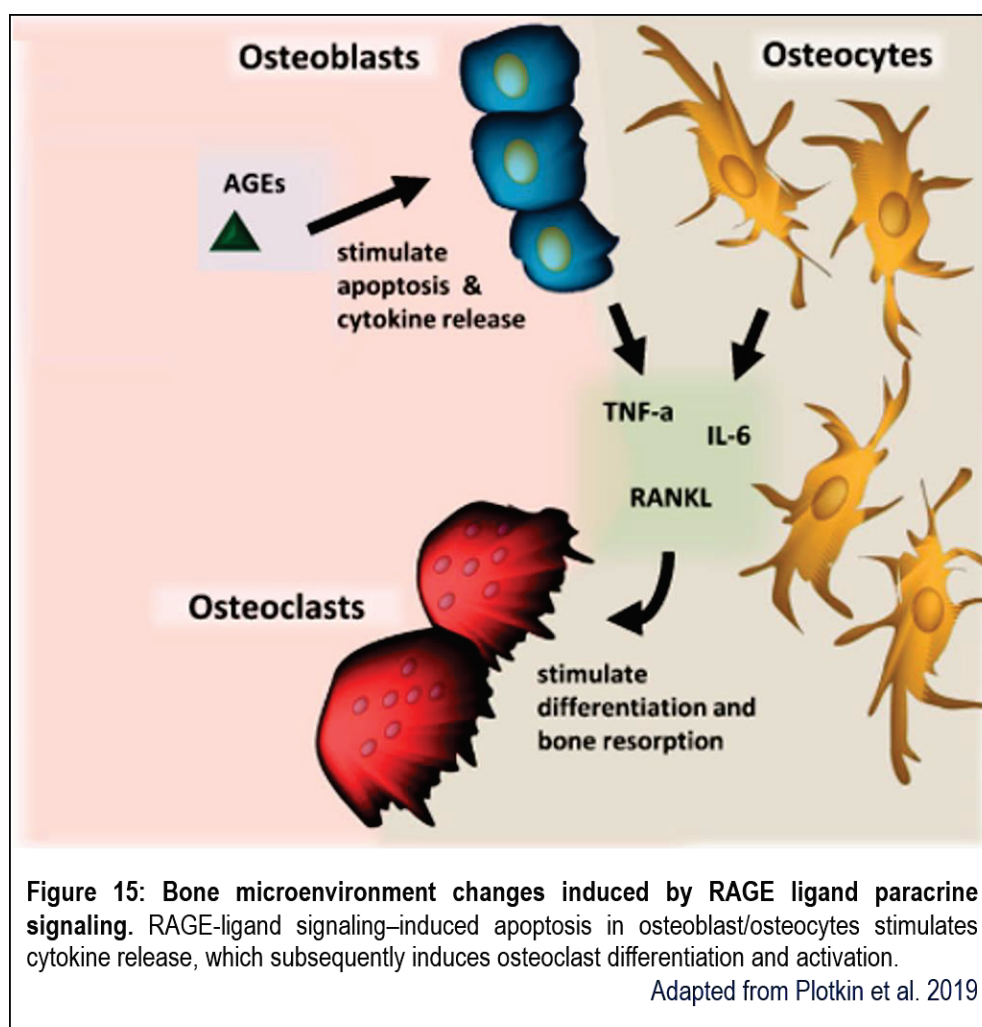
1. *Inorganic matrix*

General level of bone mineralization remains stable over the lifetime^{259,277,435}, *i.e.* the amount of hydroxyapatite per volume of bone remains the same. However, as the bone ages, the mineral crystals lengthen⁴³⁶, most likely due to the increased substitution of carbonate ions (CO_3^{2-}) for the phosphate ions (PO_4^{3-}) in the hydroxyapatite^{437,438}. This change in mineral conformation may increase stiffness⁴³⁹, but reduces the toughness of the bone as a result of the inverse relationship between toughness and stiffness⁴⁴⁰, thus leading to more fragile bone.

2. Collagen

Both collagen content and the extent and nature of its cross-linking have a significant effect on bone mechanical properties. The bulk of mature enzymatic crosslinks does not change with age, with the exception of pyrroles, which are known to decrease with loss of bone mass^{441,442}. This decrease could be detrimental since there is some evidence that pyrroles have a positive effect on bone strength^{441,443,444}. Proteins with long half-lives, such as collagen, can accumulate substantial amounts of AGEs^{445–447}, achieving levels 3-10 times those in younger bone⁴⁴⁸. AGEs form in the middle of the collagen fibrils, and restrict deformation (plasticity) of the collagen fibers⁴⁴⁹, reducing bone strength and toughness by making the tissue more brittle^{450,451}.

Figure 15: Bone microenvironmental changes induced by RAGE signaling



The accumulation of AGEs in bone ECM also has important effects on cell behavior. AGEs can impair the proliferation and differentiation of osteoblasts^{317,452} through interaction with the AGE-specific receptor (RAGE)^{453,454}. Binding of AGE to its receptor reduces osteocalcin secretion (which regulates mineral crystal size), causes disruptions in cell-matrix interaction and cell adhesion⁴⁵⁵, and increased osteoblast apoptosis³¹⁷, that affect bone formation⁴⁵². Moreover, AGE-mediated RAGE signaling activates NF- κ B in osteoblasts and stimulates the production of osteoclast-stimulating cytokines such as IL-1 β , IL-6, and TGF- α or β ^{456,457}. The AGE-RAGE binding interaction also induces the production of reactive oxygen species (ROS)²⁴⁷ and heightens inflammation in the bone microenvironment that can lead to bone loss⁴⁵⁸. ROS are known to antagonize Wnt signaling in pre-osteoblasts^{459,460} and promote osteoclastic differentiation (Figure 15)^{454,461,462}. The AGE-RAGE interaction should therefore promote resorption and reduce bone formation, which are characteristics of bone aging.

3. Noncollagenous proteins

Very little is known about age-related changes in bone NCP. One exception is proteoglycans such as biglycan and their hydrophilic GAGs side-chains, that are known to decline with aging⁴⁶³. This loss is accompanied by reduction in loosely bound water which correlates with the age-related deterioration of bone toughness⁴⁶⁴. In addition, a recent study has shown that sulfated GAGs bind sclerostin and can therefore regulate its bioavailability⁴⁶⁵. Therefore, a reduction in GAG content that occurs with aging could negatively affect Wnt signaling leading to lower bone formation. There is also some evidence that phosphorylation of bone NCP declines with aging, in particular that of osteopontin⁴⁶⁶. Such reduction of osteopontin negative

charge may interfere with its regulatory role during the mineralization process³³⁰ and with its biomechanical role in energy dissipation under stress^{364,467}.

III. BONE ECM MODIFICATION AND ENVIRONMENTAL POLLUTION BY METALS

Metals are present in the natural environment, but also could be found in a highly purified form in the medical devices and in the manufactured products, such as batteries and dyes. In case of metal intoxication, bulk of the dose is rapidly eliminated by excretion, but some part of it is incorporated in the bone in the course of mineral deposition. The rate of metal uptake in bone tissue depends on the affinity of the given metal for the mineral or organic phase of the matrix, on the chemical similarity with calcium or phosphate ions and on its serum concentration⁴⁶⁸.

Therefore, metals could generate two problems: their direct toxicity on bone cells and their accumulation in the bone matrix which may cause its pathological modification. Their direct toxicity mainly affects osteoblasts, inhibiting osteoblast differentiation, synthesis activity and mineralization of the extracellular matrix^{469–474}. Their effect on osteoclasts differs according to the metal, increasing or decreasing TRAP enzyme activity and inhibiting maturation of precursors^{471,475–480}.

The ability of metals to accumulate in the extracellular bone matrix also leads to an increase in the half-life of the metal in the body. This is the case of Uranium⁴⁸¹, the subject of my thesis project that will be described in detail later.

Some metals were shown to modify bone ECM⁴⁸². Here are some examples.

Aluminum (Al) is present in drinking water and food. Through inhalation and/or ingestion it may enter the body, and 60% of the part that is not eliminated is stored in bones⁴⁸³. Al enters skeletal tissue with calcium, competing with it, and fixes phosphates in the bone mineral⁴⁸⁴. Al delays the formation and growth of hydroxyapatite crystals^{484,485} and alters the shape of newly formed mineral⁴⁸⁶. Thus, without affecting

cellular function, aluminum has a direct negative effect on the mineralization, which can partially explain osteomalacia observed in case of Al poisoning⁴⁸⁷.

Cadmium (Cd) intoxication is principally the result of heavy metal mining, where it is a contaminant⁴⁶⁸. Like aluminum, Cd poisoning causes osteomalacia⁴⁸⁸, partially through modifications of bone ECM, disturbing both mineral and organic part of the matrix. In the mineral phase, Cd has an inhibitory effect on hydroxyapatite nucleation and growth and decreases crystal size *in vitro*⁴⁸⁹. In the organic phase, Cd diminishes collagen crosslinking through inhibition of lysyl oxidase^{490,491}. It also affects GAG (glycosaminoglycan) content. In rat bones, total amount of GAGs was decreased and their relative composition and sulphation pattern altered after Cd exposure⁴⁹².

Lead (Pb) contamination of the environment is due to its former widespread use in paints and in gasoline⁴⁶⁸. Bone accounts for 75% of total body lead⁴⁹³ and can serve as an endogenous source for many years⁴⁹⁴. Much as Al and Cd, Pb was shown to induce alterations in bone matrix: diminished hydroxyapatite crystal size and increased amount of immature collagen crosslinks, both detrimental to bone strength⁴⁹⁵. Surprisingly, Pb also enhances osteocalcin binding to hydroxyapatite⁴⁹⁶. Since osteocalcin both inhibits mineralization and regulates crystal growth³³⁰, the increase of osteocalcin bound to mineral could play a role in the smaller hydroxyapatite crystal size⁴⁹⁵, the low bone formation rates⁴⁹⁷ and decreased bone density observed in Pb-intoxicated animals⁴⁹⁸.

All metals discussed in this chapter appear to have an effect on the skeleton, but though I have described how they affect ECM, there is no clear distinction between cellular effects and effects due to accumulation in the bone mineral and/or the ECM. The study of the mechanism of metals' bioaccumulation may reveal not only the details

of their action on the bone cells and the changes that they bring to bone matrix, but also give new insights into the process of biomineralization.

CHAPTER 5: STUDY MODELS

During my thesis, I have explored alterations of the bone matrix and their consequences in two different contexts presented in this chapter. The first one is a murine model of bone pathology corresponding to a rare human progeroid syndrome called the type II Rothmund-Thomson syndrome that is due to bi-allelic mutations in the *RECQL4* gene. The second deals with bone matrices exposed to a heavy metal pollutant, natural uranium.

I. **RECQL4 AND THE TYPE II ROTHMUND-THOMSON SYNDROME**

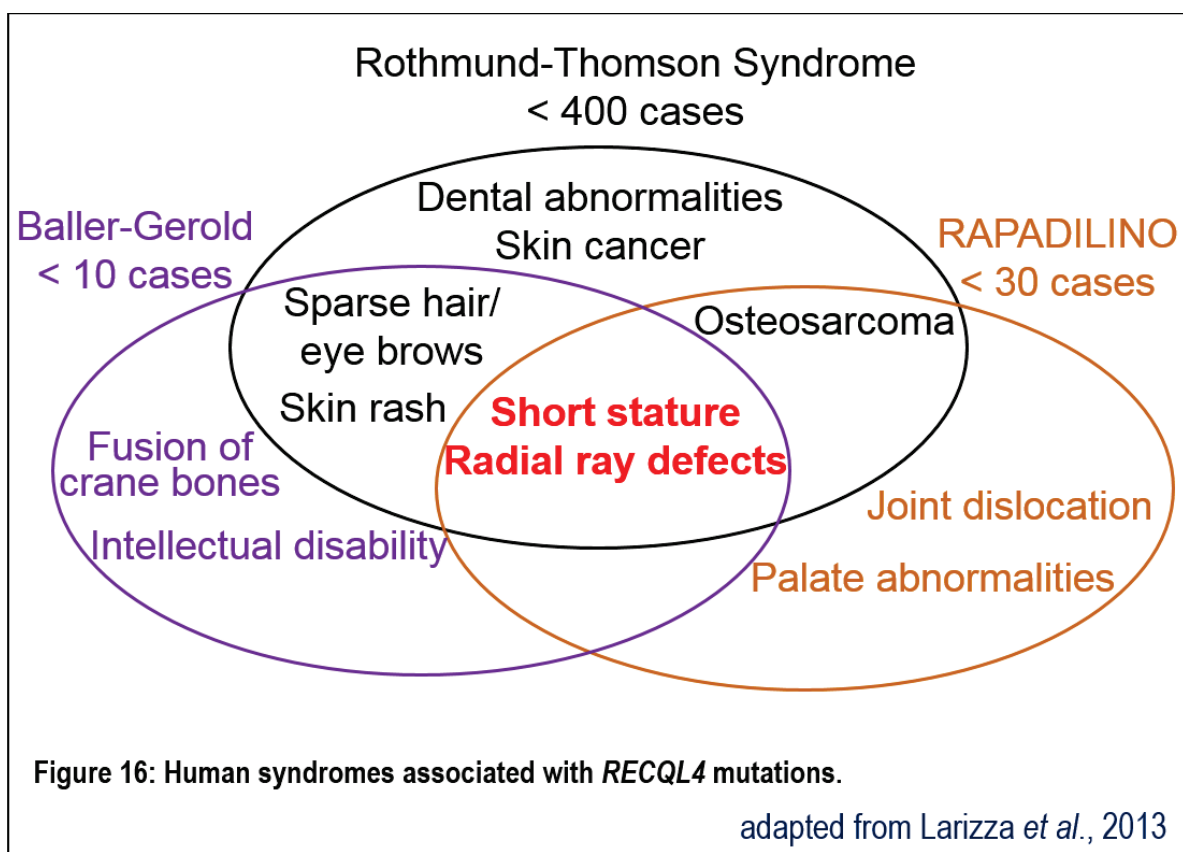
1. *Type II Rothmund-Thomson Syndrome*

RECQL4 is a DNA helicase (an enzyme that catalyzes ATP-dependent DNA unwinding), member of the RecQ helicase family which contains highly conserved proteins homologous to the RecQ helicase of *Escherichia coli*. In mammals, five RecQ helicase genes are involved in several DNA metabolism processes and mutations in three of them are linked to human autosomal recessive disorders. Loss-of-function mutations in the BLM gene give rise to a syndrome (Bloom's syndrome) characterized by growth deficiency and a pronounced predisposition to almost all types of cancer⁴⁹⁹. The absence of a functional WRN protein results in segmental progeroid syndrome (Werner's syndrome) associated with the premature onset of features associated with normal aging and increased incidence of various cancers^{500,501}.

Bi-allelic mutations in the *RECQL4* gene are associated with three rare recessive disorders: type II Rothmund-Thomson (RTS-II)⁵⁰², RAPADILINO⁵⁰³ and Baller-Gerold (BGS)⁵⁰⁴ syndromes. BGS represents less than 40 cases in the literature. This disorder is characterized by premature fusion of cranial bones

(craniosynostosis), radial ray malformations, growth retardation and poikiloderma (skin abnormalities including erythema, atrophy, telangiectasia)⁵⁰⁴. Patients with RAPADILINO are fewer and predominantly Finnish. They exhibit a short stature, radial abnormalities and other bone malformations, in addition to infantile diarrhea⁵⁰³. Approximately 200 Type II Rothmund-Thomson syndrome (RTS-II) patients have been reported. These patients present poikiloderma, skeletal abnormalities, predisposition to osteosarcomas and premature aging⁵⁰⁵. The three *RECQL4*-related syndromes are therefore associated with specific clinical signs but share common skeletal defects, which indicate a particularly important role of the *RECQL4* protein in bone tissue⁵⁰⁶.

Figure 16: Human syndromes associated with *RECQL4* mutations



Clinical examinations of RTS-II patients revealed various congenital bone deformities, including frontal bossing, saddle nose, absent or malformed radii and thumbs, fused fingers and toes, clubfoot and abnormal ulna⁵⁰⁷. Subsequent studies,

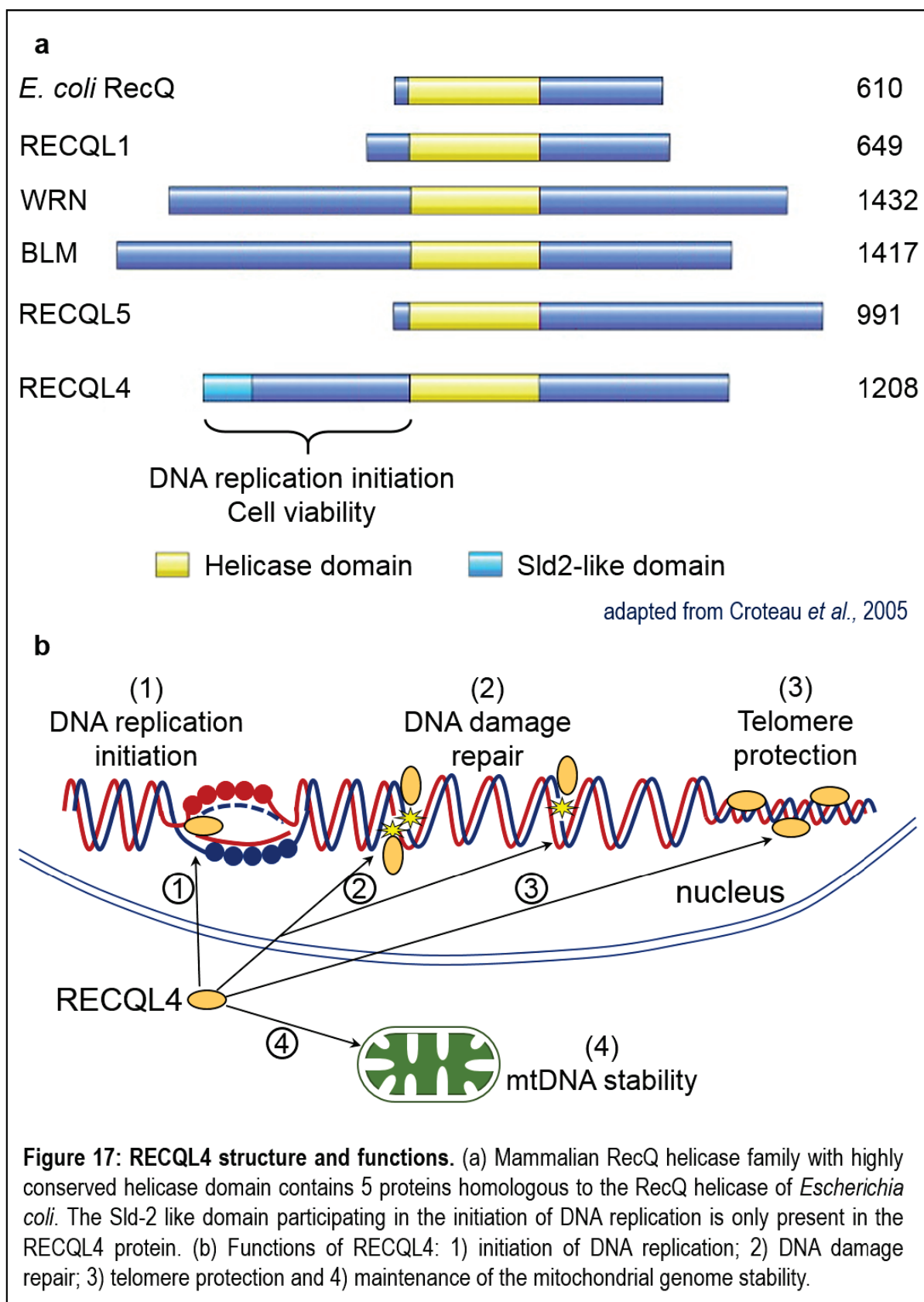
reporting radiological follow-up of RTS-II patients have revealed other bone defects that could not be detected by clinical examinations alone^{508,509}. These are mainly abnormal metaphyseal trabeculation, osteopenia and osteolytic lesions. In line with these radiological data, it was recently reported that more than 50% of RTS-II patients examined have a high incidence of bone fractures⁵¹⁰. Together, these observations indicate that RTS-II is associated with bone remodeling dysfunction and premature aging of bone tissue.

Approximately 30% of RTS-II patients develop osteosarcoma⁵¹¹ which present characteristics very similar to those of sporadic osteosarcomas. These tumors are mainly of osteoblastic origin, located in the femur or tibia and exhibit a high degree of genetic instability. However, the median age at diagnosis (11 years) is slightly younger than that observed for sporadic tumors (14-17 years)⁵¹¹.

Nearly 70 mutations have been described for the three *RECQL4* syndromes, about 50 of which are found in RTS-II patients⁵⁰⁵. Most of these are frameshift or nonsense mutations or other mutations that can interfere with the splicing of pre-mRNA^{502,511,512}. These compound heterozygous mutations of the *RECQL4* gene alleles are expected to lead to the production of truncated RECQL4 proteins which do not have all or part of the conserved helicase domain but retain the N-terminal region⁵¹³.

2. The *RECQL4* helicase

The human *RECQL4* gene mapped to chromosome 8q24.3, consists of 21 exons⁵¹⁴ and has a specific tissue expression pattern, with the highest level of *RECQL4*

Figure 17: RECQL4 structure and functions.

mRNA detected in testis and lymphoid tissues (thymus, bone marrow)⁵¹⁴. *RECQL4* transcription is also regulated according to the cell cycle with a peak of expression in S-phase⁵¹⁴. p53 and the Rb family have been shown to partially repress *RECQL4* transcription^{515,516}. This could explain why *RECQL4* is found overexpressed in many cancers^{517–520}, since p53 and RB pathway disruptions are common oncogenic mutations.

RECQL4 is the only RecQ helicase present in both the nucleus and mitochondria. This protein plays many roles in DNA metabolism and genome stability, probably through its interactions with multiple partners⁵²¹.

Several studies have focused on the role of *RECQL4* in initiating replication^{522–524}. This function involves the N-terminal part of *RECQL4* that is homologous to the yeast *Saccharomyces cerevisiae* replication factor Sld2, required for the assembly of the replication initiation complex⁵²⁵. The *RECQL4* N-terminus has also been shown to be essential for the viability of vertebrate cells⁵²⁶ and is almost never affected by mutations in *RECQL4* patients^{527,528}. The crucial role of *RECQL4* in replication has led to the proposition that mutations in *RECQL4* could result in replication stress, a phenomenon that seems to favor chromosomal abnormalities and aging⁵²⁹. Consistent with this proposal, chromosomal abnormalities in RTS-II patient cells⁵⁰⁹ and in primary cells of *Recq14*-deficient mice have been reported⁵³⁰.

Another important region of *RECQL4* is the helicase domain that catalyzes ATP-dependent DNA unwinding^{531–534} and has been implicated in the repair of different types of DNA lesions, in particular double-stranded DNA breaks (DBSs)^{535,536}. *RECQL4* also contributes to telomere protection^{537,538}; to mitochondrial genome stability^{539,540} and consequently to mitochondrial function⁵⁴¹. Finally, mitotic functions

of this helicase have recently emerged^{542,543}. Notably, RECQL4 seems required for proper alignment of mitotic chromosomes⁵⁴³.

Some *in vitro* and *in vivo* studies have also reported that RECQL4 dysfunction may lead an increased senescence^{529,544,545}. Since the accumulation of DNA damage is known to promote senescence, it has been proposed that an increase in senescence could be the consequence of unrepaired DNA damage in cells lacking functional RECQL4⁵⁴⁵.

3. Mouse models

Mouse *Recql4* gene shares 63.4% identity and 85.8% homology with the human *RECQL4* gene⁵⁴⁶. Thus, to investigate the role of RECQL4 in the pathophysiology of RECQL4-related diseases several mouse models with global or conditional inactivation of the *Recql4* gene have been developed.

Targeted deletion of *Recql4* in the mesenchyme of developing limbs leads to limb abnormalities, craniosynostosis (premature fusion of cranial sutures) and developmental bone abnormalities, as well as reduced femoral bone mass in 3-month-old mice^{547,548}. A very close phenotype has been described for mice with *Recql4* conditional deletion at a downstream stage of osteoblastic differentiation⁵⁴⁹.

The knockout mouse model chosen for this thesis project carries a germline deletion of helicase domain (exons 9-13)⁵³⁰ and it is known to express aberrant transcripts that could allow the production of *Recql4* polypeptides with an intact N-terminal region⁵³⁰. These mice are known to exhibit genomic instability, skin abnormalities (hypo-/hyper-pigmentation on their tails) and birth defects of the skeletal system reminiscent of those found in RTS-II patients (Mann *et al.*, 2005). However, this mouse model had never been explored regarding bone remodeling and aging before my thesis.

In conclusion, evidence that RECQL4 participates in a large number of cellular processes has been accumulating in recent years thanks to *in vitro* studies and also mouse models characterization. However, the mechanisms by which RECQL4 deficiency affects bone remodeling remain elusive. Bone homeostasis and remodeling do not solely rely on osteoblasts but depend on the coordinated action of various cell types and on systemic factors^{550,551}, this model with the constitutive gene knock-out allows a more comprehensive analysis of the mechanisms underlying RECQL4 deficiency-induced bone pathology. Several factors have prompted us to analyze in particular the bone ECM in this model. As have already been mentioned, fibroblasts and bone marrow cells derived from RECQL4-deficient mice showed signs of premature senescence^{544,545}. Senescent cells have been demonstrated to have an altered secretome⁵⁵² that may lead to ECM modifications^{553–555}. We decided to investigate if RECQL4-deficient osteoblasts indeed produce an altered bone matrix and, that being the case, to characterize these modified ECM with the view to explore their possible implication in the accelerated bone loss.

II. URANIUM AND BONE

The following section briefly presents the uranium and summarizes the known effects of the uranium toxicity on bone and bone cells.

1. *Uranium: physicochemical properties*

Natural uranium (U), the 92nd element of the periodic table, is the heaviest of the two naturally occurring actinide elements and is a silvery-white metal. Natural U consists of a mixture of three radioactive isotopes ²³⁸U (99.27%), ²³⁵U (0.72%) and ²³⁴U (0.0054%). The half-lives (time for the radioactivity to decay to half its original value) of the uranium radio-isotopes are very long, 244 000 years for ²³⁴U, 710 million

years for ^{235}U and 4500 million years for ^{238}U ⁵⁵⁶. The longer the half-life the less radioactive is a material.

The chemical properties of U resemble those of the rare earth elements: U oxides are insoluble in water and alkalis, but dissolve in acids. U solubility in water – and hence its potential for water pollution – is strongly dependent on the oxidation state which ranges from +II to +VI. In aqueous solution and in the body, the most stable form of U is its oxygen-containing cation $\{\text{UO}_2^{2+}\}$ with the oxidation state +VI (called uranyl and referred to as U(VI) in the following text). U(VI) has a much higher solubility than U(IV). As a hard Lewis acid, U(VI) mainly reacts with hard bases such as oxygen-containing groups like carboxylate and phosphate groups. Thus, U(VI) does not appear as a “free” uranyl cation in biological media, but forms various organic or inorganic complexes. This is in agreement with the experimentally determined uranium speciation, *i.e.* complexes that it forms, showing that in the physiological pH range approximately 50% of U(VI) is found in carbonate complexes⁵⁵⁷. The rest of U(VI) may be bound to proteins (~30%) and to red blood cells (~20%)⁵⁵⁸. Another type of study, the thermodynamic computational modeling, add a nuance to these results predicting that uranium speciation in human fluids (blood, plasma, bile, saliva, sweat, urine *etc.*) could vary between each biological fluid due to differences in composition, ionic strength, and pH⁵⁵⁹. The latter results need to be developed further, since several groups have demonstrated that uranium bioavailability and cytotoxicity strongly depend on its speciation^{560–562}.

2. Uranium exposure and bone

Uranium is both naturally present and released into the environment through human activities. Typical abundance of U in seawater is 1-3 $\mu\text{g}/\text{kg}$, and in bedrock, 1-15 mg/kg , with the highest concentration in granite⁵⁶³. Most natural U is mined to

produce highly enriched ^{235}U for use in nuclear power plants and nuclear weapons. U that remains after removal of the enriched fraction, called depleted uranium, and natural U are employed for armor-piercing shells, ship ballast, radiation shields in medical equipment or as a negative contrast in electron microscopy⁵⁶³. This extensive use of U in civil and military activities has led to an increased risk of exposure. Moreover, despite its poor solubility and the generally low concentrations, natural U in the Earth's crust may also lead to significant exposures, for example in Finland through drinking water from wells in granite⁵⁶⁴.

Exposure to uranium may occur by inhalation of airborne particles, ingestion of food and water and/or through skin uptake⁵⁶³. Natural U is weakly radioactive⁵⁵⁶. Therefore, the main health risk of uranium exposure is associated with its chemical toxicity⁵⁶⁵.

Approximately 95% of U entering the body is eliminated in feces and only a small part reaches the bloodstream⁵⁵⁶. Then 80 to 90% of the uranium present in the blood is filtered through the kidneys and cleared within a few days in urine⁵⁶³. On average, approximately 90 μg of accumulated U exist in the human body from normal intakes of water, food and air. Approximately 66% is found in the skeleton, 16% in the liver, 8% in the kidneys and 10% in other tissues⁵⁵⁶.

U(VI) shows a great affinity for bone. According to the biokinetic model established by the International Commission on Radiological Protection (ICRP), a few hours after intoxication, around 20% of uranium is found in bone where it can stay for several years⁵⁶⁶. The precise mechanism of uranium incorporation into the bone is still not completely clarified. Early *in vitro* studies have demonstrated that U can be adsorbed to the bone passively, possibly by exchange with calcium ions⁵⁶⁷ and that U has a greater affinity to the newly formed bone⁵⁶⁸. Further research provided some

evidence that the rate of U incorporation may correlate with the rate of the remodeling of the particular bone⁵⁶⁹. Analysis of the spatiotemporal kinetics of the uranium deposition into the rat bones showed that the uranium appeared initially on the bone surfaces before diffusing in the whole bone⁵⁷⁰. Furthermore, several studies have shown that U distribution pattern is remarkably like that of calcium, with intense hot spots over the growth regions and on the calcifying zones of skeletal cartilage^{481,570,571}. Taken together, these results suggest that the mechanism of U(VI) accumulation in bone does not simply follow a chemical pathway, but may rely on its incorporation by the osteoblasts.

3. Effects of Uranium on bone and bone cells

Uranium has been shown to interfere with bone physiology by several groups. Indeed, *in vivo*, uranium alters the structure of the trabecular zone, seems to promote bone resorption, and inhibits bone formation⁵⁷². Depleted uranium particles were subcutaneously implanted in rats⁵⁷³. The results revealed that the particles caused a diminution of height and length of the bones, probably caused by a slow delivery of soluble species from uranium particles. The authors observed a depletion of active osteoblasts replaced by a large increase in bone-lining cells at the trabecular surface. Cytoplasmic and nuclear alterations of rat OBs were also observed after intra-peritoneal injections of U(VI) nitrate⁵⁷⁴. Chronic exposure of rats just after birth decreased significantly the cortical bone diameter and significantly reduced mRNA expression of genes involved in OB differentiation, bone remodeling and bone mineralization⁵⁷⁵. In humans, Kurttio *et al.* observed some evidence for an association between increased bone turnover and exposure to natural U(VI) through drinking water⁵⁷⁶. Taken together, these data suggest that U(VI) is able to perturb bone metabolism.

In vitro, the effect of U(VI) on OBs and OCs is poorly documented. OBs have been shown to accumulate 10 times more U(VI) than kidney cells, suggesting a facilitated internalization or the capacity to transform U(VI) into a non-toxic form in this cell type⁵⁷⁷. Moreover, a concentration threshold, below which no toxicity and no accumulation could be measured, has been observed for U(VI) exposure in OBs. Above this threshold concentration, which is highly dependent on metal speciation, cytotoxicity correlates with metal accumulation⁵⁷⁷. After a 24 h exposure to low doses of U(VI) bicarbonate, culture in metal-free medium allowed a decrease of intracellular U(VI) concentration associated with a growth recovery, suggesting the existence of a detoxification mechanism. Finally, Tasat *et al.* demonstrated that sub-toxic concentrations of U(VI) nitrate induced the production of reactive oxygen species and decreased alkaline phosphatase (ALP) activity in human fetal OBs⁵⁷⁴. Previous work of our team demonstrated that sub-toxic concentrations of U(VI) reduces mineralization capacity of OB cells and trigger the induction of autophagy, a survival process induced by various stresses⁵⁷⁸. In addition, our results suggest that U(VI) exerts its toxicity in osteoblasts in part through the inhibition of autophagy, a major cellular catabolic process⁵⁷⁸.

While a number of studies have focused on the effect of U(VI) on bone formation and osteoblasts⁵⁷⁹, the impact of U(VI) on bone resorption has been poorly explored. Ubios *et al.* have observed an increase in bone resorption of the alveolar bone after intraperitoneal injection of uranyl nitrate in Wistar rats⁵⁸⁰. Analysis of histomorphometric parameters of mouse metaphyseal bone, after oral administration of a lethal dose of uranyl nitrate, has also revealed an extension of resorption surfaces compared to untreated animals⁵⁸¹. These results are not confirmed by those of Fukuda *et al.*⁵⁸². Indeed, after an intramuscular injection of depleted uranium to rats, the

authors have failed to detect any significant modification in bone resorption of proximal tibial metaphyses⁵⁸². Besides animal studies, several epidemiological investigations have addressed the question of the health effects of naturally occurring uranium in drinking water⁵⁸³. Among them, the study from Kurttio *et al.*⁵⁷⁶ provided some evidence of a positive association (only in males) between uranium exposure and serum levels of carboxy-terminal telopeptide, an indicator of bone resorption. The aforementioned *in vivo* studies have led to the proposal that U(VI) could promote bone resorption. Nonetheless, as far as we know, the cellular and molecular mechanisms underlying this possible effect of uranium have never been explored.

Despite several experimental studies on uranium chemical toxicity in animals and a few epidemiological studies, the data are still too sparse to derive the precise cellular and molecular mechanism of uranium toxicity. Moreover, the effects of uranium on skeletal tissue where it accumulates remain an open question. Indeed, the observations that are available are mostly derived from *in vivo* studies where the form and doses of U(VI), as well as the administration ways are very different. It is still difficult to clearly assess which mechanism is affected upon U(VI) exposure and to discern how uranium affects each type of bone cells. Our team has previously examined uranium effect on osteoblasts. In continuation of this effort, my project was designed to analyze how mineralized matrix alteration due to uranium exposure would affect the osteoclasts.

Our approach in this project was to start with a model where we can control most of the variables: the exposure of the osteoclasts to the uranium present in the culture medium at a range of concentrations. Having analyzed the osteoclast behavior in that condition, we proceeded to a more physiological systems of uranium incorporated in the mineralized matrix.

RESULTS

RESULTS PART 1

BONE AND BONE ECM ALTERATIONS INDUCED BY RECQL4 DEFICIENCY.

I.	Submitted manuscript	
	“Premature bone aging in a RECQL4-deficient mouse model”	72 – 123
II.	Characterization of the mineralized ECM produced by RECQL4-deficient osteoblasts.....	124 – 172
III.	Discussion.....	173 - 179

I. SUBMITTED MANUSCRIPT

Premature bone aging in a RECQL4-deficient mouse model

Tatiana Gritsaenko^a, Valérie Pierrefite-Carle^a, Sabrina Pisano^b, Thomas Lorivel^c,
Hélène Follet^d, Séverine Battaglia^e, Jérôme Amiaud^e, Chantal Cros^a, Laurence
Cailleteau^b, Véronique Breuil^{a,f}, Georges F. Carle^a and Sabine Santucci-Darmanin^a.

a. CEA/DRF/BIAM, UMR E-4320, TIRO-MATOs, Université Côte d'Azur, 06107 Nice, France

b. Université Côte d'Azur, INSERM, U 1081, CNRS UMR 7284, IRCAN, Nice, 06107, France.

c. Université Côte d'Azur, CNRS UMR 7275, IPMC, Sophia Antipolis, 06560 Valbonne, France.

d. Univ Lyon, Université Claude Bernard Lyon 1, INSERM, LYOS UMR1033, F69008, Lyon, France.

e. INSERM, U 1238, Université de Nantes, Faculté de Médecine, F-44035, Nantes, France

f. Université Côte d'Azur, Service de Rhumatologie, CHU DE NICE, 06001 Nice Cedex 1, France

Correspondance to:

Dr Sabine Santucci-Darmanin, CEA/DRF/BIAM, UMR E-4320 TIRO-MATOs, Faculté de Médecine, Université Côte d'Azur, 28 Avenue de Valombrose, 06107 Nice CEDEX 2, France.

Phone : +33 493 377 629

Fax : +33 493 377 717

Email : santucci@unice.fr,

Email addresses:

Tatiana Gritsaenko : Tatiana.Gritsaenko@unice.fr - Valérie Pierrefite-Carle : pierrefi@unice.fr

Sabrina Pisano : Sabrina.Pisano@unice.fr - Thomas Lorivel : lorivel@ipmc.cnrs.fr

Hélène Follet : helene.follet@inserm.fr - Séverine Battaglia : severine.battaglia@univ-nantes.fr

Jérôme Amiaud : jerome.amiaud@univ-nantes.fr - Chantal Cros : chantal.cros@unice.fr

Laurence Cailleteau : laurence.cailleteau@unice.fr - Véronique Breuil : breuil.v@chu-nice.fr

Georges F. Carle : Georges.Carle@unice.fr

Running title: Premature bone aging in a RECQL4-deficient mouse model

Key words: Accelerated aging, RECQL4, Bone, Rothmund-Thomson, mouse model, extracellular matrix

1. Summary

Bi-allelic mutations in the *RECQL4* helicase gene are responsible for type II Rothmund-Thomson syndrome, a rare progeroid disorder associated with a range of skeletal anomalies, including premature bone loss. While the physiological role of *RECQL4* in bone development has been the subject of recent studies, its involvement in bone aging remains uncharacterized. To investigate the physiological function of *RECQL4* in bone maintenance, we characterized age-related skeletal changes in a global *Recq4* knockout mouse model. By using X-ray micro-computed tomography to assess bone architecture at different bone sites (femur and caudal vertebrae), we found that bone loss associated with normal aging is accelerated and more pronounced in *Recq4*-deficient animals of both sexes. *Ex-vivo* experiments using primary cells from elderly mice suggest that *RECQL4*-deficiency leads to osteoblast dysfunction, as evidenced by the production of an altered bone extracellular matrix (ECM), which is stiffer and less mineralized compared to control ECM. Stiffening of ECM is a general feature of aging tissue and is believed to promote bone resorption, which is consistent with our histological data. Collectively, our results reveal that this *Recq4* knockout model is relevant for studying accelerated bone aging and that osteoblast dysfunction could be a prominent feature of precocious bone loss caused by *RECQL4*-deficiency.

2. Introduction

The role of DNA damage in age-related bone decline has not yet been fully explored although several arguments suggest that genome stability is an important factor in bone quality. In particular, loss-of-function mutations in human genes implicated in DNA metabolism or DNA damage response are related to decreased bone mass and altered bone microarchitecture (Schumacher *et al.*, 2008). This is the case for bi-allelic mutations of the *RECQL4* gene (Cao *et al.* 2017), a member of the *RecQ* family of DNA helicase genes, that result in three rare recessive disorders: type II Rothmund-Thomson (RTS-II) (Kitao *et al.*, 1999), RAPADILINO (Siitonen *et al.*, 2003) and Baller-Gerold (BGS) (Van Maldergem *et al.*, 2006) syndromes which occur with specific clinical signs but share common skeletal defects, suggesting a particularly important role of *RECQL4* in bone tissue.

Approximately 200 patients have been reported with RTS-II that are suffering from poikiloderma, skeletal abnormalities, predisposition to osteosarcomas and premature aging (Larizza *et al.*, 2010). In addition to congenital bone abnormalities, such as radial hypoplasia, malformed or absent thumbs, patellar abnormalities (Vennos *et al.*, 1992), studies reporting radiological follow-up of RTS-II patients, revealed other bone anomalies (Mehollin-Ray *et al.*, 2008). These are mainly abnormal trabeculation in metaphyseal bone and diffuse or localized decreases in bone density. In addition, more than 50% of RTS-II patients included in a recent study had a high incidence of bone fractures (Cao *et al.*, 2017). Together, these findings suggest that RTS-II is associated with bone remodeling dysfunction and bone tissue premature aging.

Nearly 70 mutations have been described for the three *RECQL4* syndromes (Larizza *et al.*, 2010). Most of these are frameshift or nonsense mutations or other mutations that can interfere with the splicing of pre-mRNA (Siitonen *et al.* 2009) and are expected

to lead to the production of truncated proteins which do not have all or part of the conserved helicase domain, but retain the N-terminal region (Jin *et al.*, 2008).

RECQL4 plays many roles in DNA metabolism and genome stability, probably through its interactions with multiple partners (Mo *et al.*, 2018). Several studies have focused on its crucial role in initiating replication (Capp *et al.*, 2010). This function involves the N-terminal part of RECQL4 that shares similarity with the Sld2 protein of *Saccharomyces cerevisiae* involved in the assembly of the replication initiation complex (Bruck and Kaplan, 2014). Consistently, the RECQL4 N-terminus has been shown to be essential for the viability of vertebrate cells (Abe *et al.*, 2011) and is never affected by mutations in RECQL4 patients (Siitonen *et al.*, 2009). Another important region of RECQL4 is the helicase domain that catalyzes ATP-dependent DNA unwinding (Xu and Liu, 2009) and has been implicated in the repair of different types of DNA lesions (Croteau *et al.*, 2012). The contribution of RECQL4 to telomere protection has also been documented (Ghosh *et al.*, 2012) as well as its role in mitochondrial genome stability (Gupta *et al.*, 2014) and in mitochondrial function (Kumari *et al.*, 2016). Finally, evidence for a mitotic role of RECQL4 has recently emerged (Yokoyama *et al.* 2019).

Although evidence that RECQL4 participates in many cellular processes has been accumulating in recent years, the mechanisms by which RECQL4-deficiency affect patient bone tissue remain elusive. To get a better understanding of the pathophysiology of RECQL4-related diseases, several mouse models with global or conditional *Recql4* inactivation have been developed. Targeted deletion of *Recql4* in the mesenchyme of developing limbs results in skeletal development abnormalities and reduced femoral bone mass in 3-month-old mice (Cao *et al.*, 2017; Lu *et al.*, 2015). A very close phenotype has been described for mice with *Recql4* conditional deletion

at a later stage of osteoblastic differentiation (Ng *et al.*, 2015). Because bone homeostasis and remodeling do not solely rely on osteoblasts but depend on the coordinated action of various cell types and on systemic factors, we decided to analyze the bone phenotype of a constitutive knockout mice carrying a germ-line deletion spanning from part of exon 9 through exon 13 and encoding the helicase domain of RECQL4 (Mann *et al.*, 2005). These mice are known to exhibit skin abnormalities and birth defects of the skeletal system (Mann *et al.*, 2005). Here, we report a detailed investigation of sex-specific and age-related evolution of bone density and microarchitecture in this murine model. In addition, we conducted *ex-vivo* investigations of *Recql4*^{-/-} osteoblast and osteoclast function to understand the involvement of RECQL4 in bone physiology.

3. Results

The *Recql4* knockout mouse model

RT-PCR experiments confirmed that cells from *Recql4*^{-/-} mice do not express a full-length *Recql4* cDNA, unlike cells from wild-type or heterozygous mice (*Recql4*^{+/-}) (Fig. 1A). As previously reported (Mann *et al.*, 2005), we observed that *Recql4*^{+/-} were indistinguishable from their wild-type littermates (data not shown) and that 100% of *Recql4*^{-/-} mice develop with age a skin pigmentation defect that becomes visible on their tails from the age of 6 months (Fig. 1B). Since most RTS-II patients exhibit short stature, we examined mice long bone lengths. No differences were found in the femur and tibia length of 3-month-old *Recql4*^{-/-} males and females compared to heterozygous control mice of the same sex, excluding a developmental delay in the growth of *Recql4*^{-/-} animals (Fig. 1C). Although the body weight of *Recql4*^{-/-} mice was similar to that of heterozygous mice at 3 weeks and 3 months of age, they were significantly underweight compared to controls at 13 months of age (Fig. 1D).

Accelerated bone loss in long bones of *Recql4*^{-/-} mice

In order to characterize the aging process of bone in control and *Recql4*^{-/-} mice, we conducted a cohort study consisting of 5 to 10 mice per age group per genotype and per sex, for which trabecular architecture of the metaphyseal femoral bone was examined using microcomputed tomography (μ CT). As previously described for wild-type C57BL/6J male mice (Glatt *et al.*, 2007), the trabecular bone volume fraction (BV/TV) showed downward trend (10,8%) between 6 and 13 months in control males. In *Recql4*^{-/-} males, BV/TV decreased from 3 months of age and severely dropped (51.8%) between the age of 6 and 13 months (Fig. 2B). Consequently, 13-month-old *Recql4*^{-/-} males had a significantly reduced BV/TV compared to control males of the same age (5.47% vs 12.08%, $p = 0.0003$) (Fig. 2A and 2B). Females of both genotypes

had a lower BV/TV than male counterparts at all ages tested and showed a gradual and significant decrease in BV/TV as they aged (Fig. 2B). At all time points analyzed, *Recq14*^{-/-} females had a lower amount of trabecular bone compared to age-matched *Recq14*^{+/-} females, with a statistical significance reached for the 13-month-old group (0.83% vs. 1.7%, $p = 0.0004$). Trabecular number (Tb.N) showed a pattern of age-related changes very similar to that of BV/TV in both sexes and genotypes, leading in older animals to a significantly lower number of trabeculae in *Recq14*^{-/-} male (0.8 vs. 1.58/mm, $p = 0.0002$) and female (0.12 vs. 0.22/mm, $p = 0.0002$) compared to controls (Fig. 2C). Consistent with this, trabecular spacing (Tb.Sp) increased with age in both sexes and genotypes, with a greater increase in females (Fig. 2D). In older individuals, the Tb.Sp. was higher in mutants than in controls, with a difference observed in both sexes and significant in males (0.28 vs. 0.34 mm, $p = 0.038$). The trabecular thickness (Tb.Th.) increased progressively and significantly with age in males of both genotypes (Fig. 2E), this increase being less marked in mutant males compared to heterozygous littermates (20% vs. 52% increase between 3 and 13 months of age, respectively). Thereby, at the age of 13 months, the Tb.Th. was lower in *Recq14*^{-/-} than in control males, although this did not reach statistical significance. In females of both genotypes, the Tb.Th. remained stable between 3 and 6 months and then evolved in older animals in a manner similar to that observed in males. The bi-allelic deletion of the *Recq14* gene had also an effect on the trabecular pattern factor (Tb.Pf). This parameter reflects the connectivity of the trabecular network, the low values of Tb.Pf corresponding to a well-connected network (Hahn *et al.*, 1992). For all ages analyzed and regardless of genotype, Tb.Pf values were higher in females indicating a gender effect on trabecular connectivity (Fig. S1). We also noticed that both 13-month-old *Recq14*^{-/-} male (27.5 vs. 15.4, $p = 0.0016$) and female (40.5 vs. 31.9, $p = 0.0353$) had increased Tb.Pf compared

to heterozygous control mice suggesting that aged mutant mice exhibited a more disconnected trabecular structure than control ones (Fig. S1).

Cortical thickness (Cort.Th.) of the femoral mid-diaphysis was also evaluated. While this parameter fluctuated only slightly in *Recql4*^{+/-} males as a function of age (Fig. 2F), it dropped significantly in mutant males between 6 and 13 months of age (0.186 vs. 0.208 mm, $p=0.0072$). Consequently, 13-month-old *Recql4*^{-/-} males exhibited thinner cortical bone than the age-matched controls (0.206 vs. 0.186 mm, $p= 0.0172$). In females, the evolution of cortical thickness was different from that observed in males in that it increased gradually and significantly between 3 and 13 months for both *Recql4*^{+/-} (0.215 vs. 0.240 mm $p= 0.0134$) and *Recql4*^{-/-} (0.209 vs. 0.224 mm, $p= 0.0371$) mice (Fig. 2F). However, at all ages analyzed, the Cort.Th. was lower in mutant females, this difference being statistically significant in 6-month-old animals (0.212 vs. 0.230, $p= 0,0279$) and close to the significance at 13 months of age (0.224 vs. 0.240 mm, $p= 0.0722$).

In summary, we showed a significant age-by-sex interaction in age-related changes of trabecular bone architecture and femoral cortical thickness for both genotypes, as revealed by statistical two-way ANOVA analysis. More importantly, our results demonstrated that age-related alterations of trabecular and cortical femoral bone were more pronounced in the absence of RECQL4, in both sexes. This observation was supported by statistical analysis showing a significant age X genotype interaction for most parameters. Thereby, our data revealed that *Recql4*^{-/-} mice are a relevant model of premature bone aging.

Reduced bone mass in non-weight bearing bone sites in *Recql4*^{-/-} mice

As bone decline due to aging or pathological conditions may be dependent on the skeleton site considered (Glatt *et al.*, 2007; Willinghamm *et al.*, 2010), we also

examined a non-weight bearing site such as tail vertebrae of 6- and 13-month-old *Recql4*^{+/-} and *Recql4*^{-/-} male. For both age groups, an X-ray examination showed a notable difference in bone density between the two genotypes (Fig. 3A). Accordingly, μ Ct evaluation revealed strong differences between *Recql4*^{+/-} and *Recql4*^{-/-} mice from the age of 6 months and for all measured parameters (Fig. 3C to 3G), indicating that bi-allelic deletion of the *Recql4* gene had an important deleterious effect on vertebral trabecular bone volume and architecture, as illustrated by μ CT 3D reconstruction of the 12th caudal vertebra (Fig. 3B).

Unlike what we observed for long bones, BV/TV (Fig. 3C), Tb.N. (Fig. 3D) and Tb.Th. (Fig. 3E) did not decrease in caudal vertebrae of control mice between 6 and 13 months of age. Instead, these parameters tended to increase during this period and the Tb.Sp. decreased significantly at the same time (0.281 vs. 0.422 mm, $p=0.0152$) (Fig. 3F). These observations are consistent with studies showing that the evolution of trabecular bone volume over time is different in long bones compared to caudal vertebrae, with an earlier onset of decline in long bones (discussed in Lambers *et al.* 2012). In contrast to control mice, *Recql4*^{-/-} animals failed to show an increase in caudal vertebral BV/TV and Tb.Th. between 6 and 13 months (Fig. 3C and 3E) and displayed an increase in Tb.N. smaller than the one observed for control mice (7.3 % vs. 10%, Fig. 3D). In line with this, their Tb.Sp. declined during this same period of life but to a lesser extent compared to *Recql4*^{+/-} mice (14.7% vs. 21.7%). These data showed that RECQL4 dysfunction modifies the trabecular bone architecture in the caudal vertebrae.

Table 1: Summary of bone parameters evaluated by micro computed tomography

Site	Parameter	median value males						median value females					
		3 months-old		6 months-old		13 months-old		3 months-old		6 months-old		13 months-old	
		<i>recql4^{+/+}</i>	<i>recql4^{-/-}</i>										
distal femoral metaphysis	BV/TV (%)	8,54	11,22	12,77	9,77	12,45	5,64*	6,28	4,98	2,85	1,75	1,89	0,91*
	Tb. N. (1/mm)	1,86	2,11	2,12	1,60	1,59	0,83*	1,08	0,95	0,49	0,37	0,22	0,13*
	Tb. Th. (mm)	0,049	0,055	0,061	0,063	0,074	0,066	0,060	0,054	0,056	0,053	0,079	0,071
	Tb. Sp. (mm)	0,217	0,221	0,240	0,246	0,284	0,313*	0,316	0,297	0,392	0,387	0,547	0,611
	Tb. Pf (1/mm)	26,27	20,47	16,18	22,50	13,86	29,63*	27,99	31,79	34,25	43,62	30,49	39,38*
	Cort. Th. (mm)	0,198	0,212	0,210	0,210	0,208	0,189*	0,213	0,211	0,230	0,209*	0,240	0,227
12th caudal vertebra	BV/TV (%)			45,52	19,00*	50,57	20,14*						
	Tb. N. (1/mm)			3,36	1,95*	3,88	2,06*						
	Tb. Th. (mm)			0,127	0,100*	0,141	0,091*						
	Tb. Sp. (mm)			0,284	0,416*	0,230	0,352*						
	Tb. Pf (1/mm)			4,54	13,87*	4,89	16,62*						

Key: BV/TV Bone Volume to Total Volume = bone volume fraction
Tb. N. Trabecular Number
Tb. Th. Trabecular Thickness
Tb. Sp. Trabecular Spacing
Tb. Pf Trabecular Pattern factor
Cort. Th. Cortical Thickness
* Significant difference with the control of the same age group

The bone perimeter covered by osteoclasts increases in older *Recql4^{-/-}* mice

To understand the cellular basis of *Recql4^{-/-}* mice bone phenotype, we performed bone histomorphometric analysis of femoral trabecular bone, for animals aged 12 months and older. Both the mineral apposition rate (MAR, Fig. 4A) and the numbers of osteoblasts per unit of bone perimeter (N.Ob./B.Pm, Fig. 4B) showed a weak decreasing trend in *Recql4^{-/-}* mice compared to controls, without reaching significance. The percentage of bone perimeter covered by osteoclasts (Oc Pm/B.Pm) was slightly and significantly higher in mutant mice than in control littermates (11.72 vs. 8.68 %, $p=0,0185$) (Fig. 4C), raising the possibility that RECQL4 dysfunction could be associated with higher bone resorption. This prompted us to seek whether RECQL4 deficiency

has a direct or indirect effect on osteoclast differentiation and function.

RECQL4 deficiency does not activate osteoclast formation and function through osteoclast-autonomous mechanisms nor via paracrine action of osteoblasts

Since osteoclasts are of hematopoietic origin, we first checked the total cellularity of the bone marrow of *Recql4*^{-/-} mice, in order to rule out the possibility of a major hematopoietic defect in these animals. We did not observe a significant difference in the number of cells in the bone marrow of *Recql4*^{+/-} and *Recql4*^{-/-} mice of either sex (Fig. 5A). Because reactive oxygen species (ROS) are crucial for osteoclast differentiation (Domazetovic *et al.*, 2017), and are known to be increased in fibroblasts of RTS-II patients (Kumari *et al.*, 2016), we evaluated the levels of ROS in osteoclast precursors isolated from *Recql4*^{+/-} or *Recql4*^{-/-} mice. As shown in Fig. 5B, the levels of ROS in bone marrow-derived macrophages (BMM) were similar irrespective of the genotype. To explore the effect of RECQL4 dysfunction on osteoclast differentiation and resorption, primary BMM isolated from control or mutant mice were cultured on synthetic bone substrate in the presence of M-CSF (macrophage colony-stimulating factor) and RANKL (Receptor activator of nuclear factor-kappa B ligand), two critical factors for osteoclast formation and function. At the end of the culture, cells positive for tartrate-resistant acid phosphatase (TRAP) staining and containing more than 3 nuclei were counted as osteoclasts (Fig. 5C) and the area of matrix resorbed per osteoclast was quantified (Fig. 5D). *Recql4*^{+/-} and *Recql4*^{-/-} BMM produced a similar number of osteoclasts with comparable resorption ability, indicating that RECQL4 dysfunction affects neither the formation nor the function of osteoclasts, through cell-autonomous mechanisms.

Osteoblasts contribute to the regulation of osteoclast differentiation through the production of signaling molecules involved in osteoclastogenesis (Han *et al.*, 2018). In

order to determine whether *Recql4*^{-/-} osteoblasts enhanced osteoclast differentiation, calvaria explant cultures were used as an osteoblast/osteoclast co-culture system (Nollet *et al.*, 2014). TRAP staining was used to detect osteoclasts formed after 10 days of culture of calvaria explants, each prepared from an individual mouse. We found no difference in the number of osteoclasts obtained in *Recql4*^{-/-} cultures compared to the control ones (Fig. 5E), suggesting that the deficiency of RECQL4 in osteoblasts does not result in an increased stimulation of osteoclastogenesis through direct or paracrine cellular interaction.

Recql4 deficiency leads to the production of an altered extracellular matrix

Because our histological data showed a slight decrease in the number of osteoblasts in femoral cancellous bone of *Recql4*^{-/-} mice (Fig. 4B), we next investigated the potential consequence of RECQL4 deficiency on cells of the osteoblastic lineage. We first examined the frequency of mesenchymal progenitor cells (CFU-F) in bone marrow from either *Recql4*^{+/-} or *Recql4*^{-/-} animals. By using colony-forming assays in bone marrow stromal cell cultures isolated from males aged 13 months and over, we found that the numbers of small and large colonies were not significantly different between *Recql4*^{+/-} and *Recql4*^{-/-} cultures (Fig. 6A). This suggested that neither the frequency, nor the proliferation ability of mesenchymal progenitors, is altered in *Recql4*^{-/-} mice. In addition, the number of mature osteoblast colonies (colonies positive for mineral deposition) was unchanged between the two genotypes (data not shown). We next assessed the proliferation of primary osteoblastic cells from long bones and found that *Recql4*^{-/-} cell growth was not slowed down compared to that of control cells (Fig. 6B). In order to determine if RECQL4 deficiency affects osteoblast differentiation and function we examined ECM produced *ex-vivo* by *Recql4*^{+/-} and *Recql4*^{-/-} primary osteoblasts. Primary long bone cells isolated from 13-month-old individual mouse (6

mice per genotype) were grown to confluence and then placed under differentiation conditions for 21 days. ECM mineralization was assessed by quantification of Alizarin Red S staining. Although the results were not significant due to a high inter-individual variability in control mice, we observed a 50% mineralization decrease in *Recql4*^{-/-} cultures compared to *Recql4*^{+/-} cells (Fig. S2). By comparing mineralization in cultures of primary bone cells pooled from 3 to 4 mice per genotype, we also found a 50% mineralization decrease in mutant cultures, although the difference compared to control cultures did not reach significance (Fig. 6C). Collagen matrix deposition was also examined in cultures of these pooled primary osteoblastic cells by Picrosirius Red staining, the quantification of which indicated that equivalent amounts of collagen was deposited in ECM synthesized by osteoblasts regardless of their genotype (Fig. 6D). These results were consistent with the ECM thickness measurements made using atomic force microscopy (AFM), which showed that the height of the *Recql4*^{+/-} and *Recql4*^{-/-} ECM was similar (Fig. 6E, Fig. S3). It should be noted that these measurements were made in matrix areas without mineralization and therefore reflected the amount of deposited collagen. Thus, Picrosirius red assays and matrix height measurements suggested that there was no difference between the extracellular collagen levels present in *Recql4*^{+/-} and *Recql4*^{-/-} cultures. Despite this, the organic part of ECM derived from *Recql4*^{-/-} osteoblasts exhibited a significantly increased stiffness compared to *Recql4*^{+/-} cell-derived ECM (x 1.3) as revealed by Young's modulus measurements performed by using AFM (Fig. 6E and Fig. S3). By contrast, no difference was found between the control and mutant ECMs when elasticity was evaluated in mineralized regions (Fig. S3). Our *ex-vivo* data suggest that RECQL4 deficiency in cells of osteoblastic lineage results in the production of an altered extracellular matrix with fewer mineral but also increased stiffness of the

organic matrix, which is a well-known characteristic of tissue aging (Lampi and Reinhart-King, 2018).

4. Discussion

Our understanding of the relationship between age-related bone loss and impaired DNA metabolism is based only on the study of a few mouse models (Jilka, 2013). RECQL4 belongs to a family of DNA helicases critical for the maintenance of genome stability and, accordingly, mice with a global knockout of the *Recql4* gene display genomic instability (Mann *et al.*, 2005). Here, we show for the first time that these *Recql4*^{-/-} mice exhibit accelerated bone aging in both sexes, which underlines the relevance of this model to assess the relationship between DNA instability and bone aging. *Recql4*^{-/-} mice exhibit other signs of aging, including uneven skin pigmentation (Mann *et al.* 2005 and here). The skin and skeleton being the two organs affected by abnormal aging in patients with bi-allelic mutations of *RECQL4* (RTS-II patients), this mouse model thereby represents an interesting tool for studying this human disorder. We also noticed that, as *Recql4*^{-/-} mice aged, their body weight becomes significantly lower than that of control mice. This could be interpreted as a further sign of accelerated aging since the body weight in wild-type C57BL/6J mice is known to increase until 15 to 20 months and decreases beyond 24 months of age (Fahlström *et al.*, 2011).

Femoral trabecular and cortical bone parameters show age-related changes in control (*Recql4*^{+/-}) male and female mice that are in line with those presented by others (Glatt *et al.*, 2007; Halloran *et al.*, 2002) and that are overall similar to those seen in human aging (Jilka, 2013; Riggs *et al.*, 2004), with especially a strong gender effect. For instance, BV/TV and Tb.N. parameters of femoral metaphysis decrease from the age of 3 months in females, while this decrease only appears from 6 months in males. Besides, the cortical thickness of the femoral mid-diaphyseal region does not vary between 3 and 13 months in control males but whilst it increases in control females.

Interestingly, this cortical thickening could be a phenomenon driven by mechanical loading that compensate for the decrease in metaphyseal trabecular bone volume, which is dramatic in females. The effect of RECQL4 deficiency on the architecture of the femoral trabecular bone is observed as early as 3 months and worsens with age. Both BV/TV and Tb.N. peak at 3 months in the femur of mutant males instead of 6 months in controls, indicating an accelerated evolution of trabecular bone architecture in the former. In mutant females, most of bone architecture parameters are altered compared to control females from the age of 3 months even if these differences reach statistical significance at 13 months of age.

Trabecular bone was analyzed in the caudal vertebrae, which is also a valid model for studying bone loss (Lambers *et al.*, 2012). By first examining the control animals, we found that overall age-related changes are less severe in the trabecular bone of the tail vertebrae compared to the femoral metaphysis. Although this same observation has been made by others (Glatt *et al.*, 2007; Lambers *et al.*, 2012; Willingham *et al.*, 2010), it is nevertheless surprising: since the caudal vertebrae are not weight-bearing bones, they do not benefit from the stimulating effect of mechanical loading on bone mass and should therefore be more sensitive to aging. At the moment, this paradox is not clearly understood albeit some proposals have been put forward, such as a different responsiveness to systemic factor between non-weight and weight bearing bones (Willingham *et al.*, 2010). The effect of RECQL4 dysfunction on the trabecular bone of the tail vertebrae is stronger and earlier than in the case of long bones. The reason why vertebral trabecular bone, which seems less sensitive to aging than femoral trabecular bone, is more sensitive to RECQL4 deficiency remains to be determined. We cannot exclude that the phenotypic variations between the two bone sites are due to the differences in loads supported by these skeletal regions. In this

case, a more severe phenotype in the caudal vertebrae may be due to less compensation for the impact of the *Recql4* mutation by the beneficial effects of mechanical loading.

We found a significant association between age and genotype with respect to trabecular bone changes in femoral metaphysis, which supports an accelerated bone aging phenotype in *Recql4*^{-/-} mice. The same conclusions cannot be formally drawn from the examination of the vertebral trabecular bone, since only two age groups were analyzed for this bone site. However, our data support the hypothesis that RECQL4 deficiency leads to the premature cessation of the increase in BV/TV observed during normal vertebral bone aging, which also reflects a premature aging phenotype.

Even if we cannot exclude the existence of bone development disorders in our model, this seems very unlikely because neither body size (not shown), nor body weight or long bone length are affected in young *Recql4*^{-/-} mice. More generally, we did not detect any bone abnormalities other than low bone mass in these mice. Thus, all our data suggest that the skeletal phenotype observed in *Recql4*^{-/-} mice reflects accelerated bone aging rather than developmental disorders. This contrasts with the study by Mann *et al.* (2005) which found, using the same model, congenital polydactyly in 5,7 % of mutant animals and palatal defects in 100% of them. The reason for this discrepancy is not known at this time but may be due to differences in genetic backgrounds. Mann *et al.* used mice with a mixed genetic background (75% B6 / 25% 129S7) while we analyzed animals with more than 95% B6 background, as assessed by microsatellite analysis (not shown).

Two conditional models of *Recql4* knockout mice with a deletion of the *Recql4* gene in osteoprogenitors have been described with abnormalities in bone development, mainly characterized by reduced skeletal growth leading to decreased body size and

shortened limbs (Lu *et al.*, 2015; Ng *et al.*, 2015). These mutants show significant bone loss as early as 9 or 12 weeks of age, the evolution of which at an older age has not been documented (Cao *et al.*, 2017; Ng *et al.*, 2015). Thus, these phenotypes are more severe bone phenotype than that observed in the global *Recq14* knockout model studied by Mann *et al.* (2005) and ourselves. This observation could be explained by differences in *Recq14* mutant alleles considered. While *Recq14* conditional knockout mice are believed to bear null alleles of *Recq14* (Ng *et al.*, 2015), global mutant mice, carrying homozygous germ-line deletion of exons 9-13, are known to express aberrant transcripts that could allow the production of RECQL4 polypeptides with an intact N-terminal region (Mann *et al.*, 2005). This part of RECQL4, that shares homology with yeast DNA replication initiation factor Sld2, is essential for the initiation of DNA replication and cell viability (Sangrithi *et al.* 2005). Global *Recq14* mutant allele could be a hypomorphic allele that retains some functions of RECQL4, a situation similar to most of mutant alleles in RTS-II patients, that are expected to be translated into truncated proteins conserving the N-terminal Sld2-domain (Siitonen *et al.*, 2009). This hypothesis is supported by the comparison of histomorphometric data from the different models. Whereas conditional deletion of *Recq14* in osteoblastic progenitors leads to a sharp decrease in either the mineral apposition rate (MAR) (Ng *et al.*, 2015) or the number of osteoblasts (N.Ob/B.Pm) (Cao *et al.*, 2017), we found only a slight diminution of these parameters in *Recq14*^{-/-} mice. Moreover, our *ex-vivo* experiments suggest that the *Recq14* mutant allele has retained some RECQL4 functions regarding cell proliferation and viability, since neither the bone marrow cellularity, nor the frequency of mesenchymal progenitors, nor the proliferation rate of primary osteoblastic cells, are affected in *Recq14*^{-/-} mice.

The perimeter of femoral trabecular bone covered by osteoclast appears greater in *Recql4*^{-/-} older mice than in *Recql4*^{+/-} controls of the same age. This is not due to a change in the intrinsic behavior of *Recql4*^{-/-} osteoclasts, nor to a paracrine effect of mutant osteoblasts. A recent study has suggested that age-related changes in the bone ECM influence the number and activity of osteoclasts (Panwar *et al.*, 2015). By analyzing ECM produced *ex-vivo* by *Recql4*^{-/-} primary osteoblasts, we found that they synthesize less mineralized matrices than those produced by *Recql4*^{+/-} osteoblasts. Moreover, whereas RECQL4 deficiency does not quantitatively impact collagen production, the organic part of the *Recql4*^{-/-} ECM displays modified mechanical properties with an increased stiffness compared to control ECM. Stiffening of organic ECM is considered as a feature of tissue aging, the age-related loss of collagen flexibility being mainly attributed to its non-enzymatic glycation that leads to excessive cross-linking of this major ECM component (Lampi and Reinhart-King, 2018). In bone, an increase of the stiffness of collagen fibrils and fibers with aging has been reported (Zimmermann *et al.* 2011) and the study of Panwar *et al.* (2015) suggests that these collagen modifications could promote excessive osteoclast bone resorption.

Results from our *ex-vivo* experiments support *in-vivo* analyses by revealing a further sign of accelerated aging associated with *Recql4*^{-/-} mice. More importantly, they suggest that the main mechanism of bone loss in *Recql4*^{-/-} animals is independent of cell proliferation but might be related to osteoblastic dysfunction, as illustrated by the production of a modified ECM showing features which could potentially promote osteoclastic resorption. Besides its role in the initiation of DNA replication, RECQL4 has several functions essential to genomic stability and whose loss could lead to cellular attrition (Mo *et al.*, 2018). Further studies are therefore required to elucidate the role of the *Recql4* allele studied here, in osteoblast dysfunction.

Collectively, this study shows that mice with a homozygous germ-line deletion of the entire *Recq14* helicase domain display an accelerated bone aging phenotype that summarizes both the bone loss associated with normal human aging (Parfitt, 1984) and the premature bone aging observed in RTS-II patients (Cao *et al.*, 2017). We believe that this mouse model is complementary to the conditional *Recq14* knockout mouse models for providing new insights on the RTS-II pathophysiology, which is a disorder associated with both congenital skeletal anomalies and accelerated bone aging. Moreover, comparing the different *Recq14* murine models could help to better understand the role of the different RECQL4 domains in the function of this protein, a subject on which much remains to be learned.

5. Experimental procedures

Mice

Heterozygous males carrying the *Recq14* mutant allele were received from Guangbin Luo (Case Western Reserve University, Cleveland, OH), quarantined and mated with C57BL/6J females. Resulting embryos were transferred to surrogate dams. Offsprings were PCR-genotyped and homozygous mutant males (*Recq14*^{-/-}) males were backcrossed with C57BL/6J females. The mice were housed and bred in the Faculty of Medicine animal facility, University of Nice, France. The procedures for the care and sacrifice of the animals were in accordance with the EU Directive 2010/63/EU for animal experiments and approved by the local experimentation committee.

Micro-CT analysis

The femoral mice samples were imaged using the Skyscan1174 micro-CT system (Bruker, Kontich, Belgium). After scanning, the images were reconstructed using a filtered back-projection algorithm (NRecon reconstruction software, V1.6.4.8). A core of 200 sections, each 10 µm thick was used for trabecular bone morphometry evaluations with SkyScan CtAn software V1.13.

For tail vertebrae analysis, each tail was scanned at a pixel size of 18µm using the SkyScan1076 system (Bruker). 3D microstructural image data was reconstructed using the same NRecon software used for femoral samples. The bone parameters were calculated on the 12th caudal vertebrae, as the volume of interest for trabecular microarchitectural variables. Analyze of 3D morphometric parameters was done using SkyScan CtAn software V1.13. Scanning conditions and bone parameters measurements of femoral and vertebral samples are detailed in Appendix S1.

Atomic Force Microscopy analyses

Primary long-bone cells pooled from 4 mice per genotype were grown in 50 mm glass bottom dishes (Willco Wells, Amsterdam, NL) and subjected to osteogenic differentiation. After 28 days, cells were removed by incubation with PBS containing 20 mM NH₄OH and 0.5% Triton X-100 for 5 min at 37°C. The mechanical properties of the resulting decellularized matrices were studied using a BioScope Catalyst atomic force microscope (Bruker Nano Surfaces, Santa Barbara, CA, USA) equipped with a Nanoscope V controller and coupled with an optical microscope (Leica DMI6000B, Leica Microsystems Ltd., UK). The experiments were performed using a probe having a Borosilicate Glass spherical tip (5 µm diameter) and a cantilever with a nominal spring constant $k=0.06$ N/m (Novascan Technologies, Ames, IA, USA). Force-distance curves were collected using a velocity of 2 µm/s, in relative trigger mode and by setting the trigger threshold to 2 nN. The apparent Young's modulus was calculated using the NanoScope Analysis 1.80 software (Bruker Nano Surfaces, Santa Barbara, CA, USA). For the detailed procedure and data normalization see (Appendix S1).

The thickness of extracellular matrices was evaluated as previously described⁵⁸⁴ with minor modifications (Appendix S1).

Statistical analyses

Our results were submitted to parametric or non-parametric analysis depending on the compliance of data with the statistical assumptions. The normality of residuals was assessed using normal probability plots. Variances homogeneity was checked by comparing the externally studentized residuals of groups to each other. The difference of means between two groups was evaluated by two-sample t-test, when possible. In case the assumptions were not met, Mann-Whitney test was chosen. If several factors had to be considered in the statistical model, we applied either two-way (Genotype X Age) or three-way (Genotype X Age X Sexe) ANOVA. Post-hoc analysis was achieved

by using t-test with Holm (two-way ANOVA) or Benjamini-Hochberg (three-way ANOVA) corrections for multiple comparisons. In order to comply with the normality and variances homogeneity assumptions, some data were log₁₀ transformed before analysis. Statistical analyses specific to AFM experiments are in Appendix S1.

The experimental procedures for bone histomorphometry, primary cell cultures, X-ray imaging, RT-PCR, oxidative stress analysis and MTT assays are described in Appendix S1.

6. Acknowledgements

The authors thank Jérôme Henriquez for his help in automated image analysis, and Colette Ricort for technical assistance. The authors acknowledge the IRCAN PICMI, and Animal core facilities which are supported by grants from the Conseil Général 06, the FEDER, GIS IBISA, the Ministère de l'Enseignement Supérieur, the Région PACA, the Canceropole PACA, the foundation ARC and INSERM. This study was supported by grants from the Société Française de Rhumatologie (SFR).

Conflict of interest

The authors have no conflict of interest to declare

7. Figures

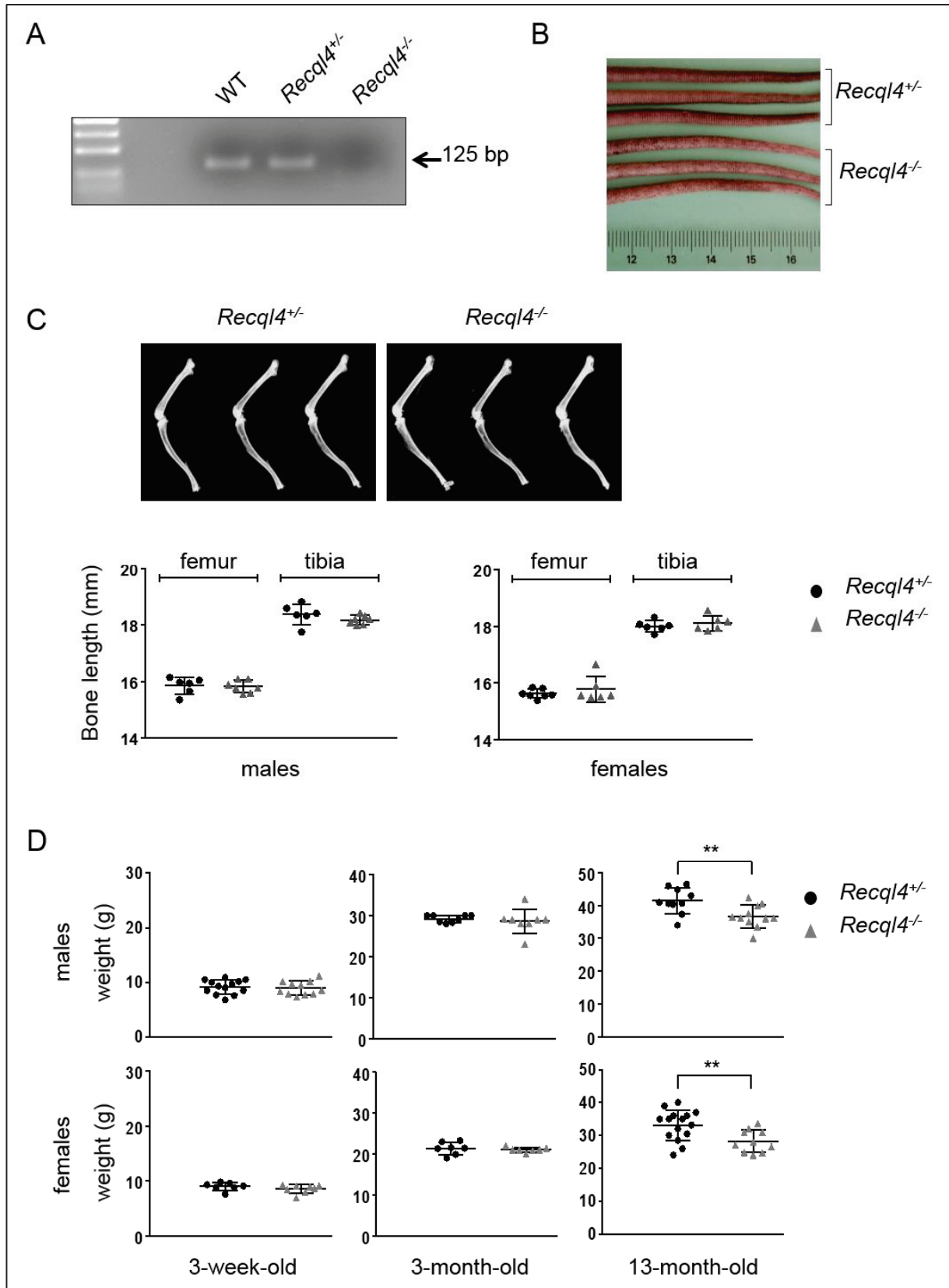


Figure 1

Figure 1: The Recql4 knock-out mouse model

(A) Gel electrophoresis analysis of RT-PCR amplification products. Total RNA prepared from wild-type (WT), *recql4*^{+/-} or *recql4*^{-/-} mouse bone marrow were subjected to RT-PCR amplification by using a forward primer located at the junction between exons 9 and 10 and a reverse primer placed in exon 10 of the *recql4* gene. (B) Photograph of representative 6-month-old *recql4*^{+/-} and a *recql4*^{-/-} mouse tails. (C) Representative X-ray radiographs of left femur and tibia of 3-month-old *recql4*^{+/-} or *Recql4*^{-/-} males are shown at the top. Evaluation of femur and tibia lengths of 3-month-old males and females of both genotypes is presented at the bottom as a dot plot with mean \pm SD (D) Comparative evolution of total body weight for both sexes and genotypes. Data are mean \pm SD (** p <0.01, t-test).

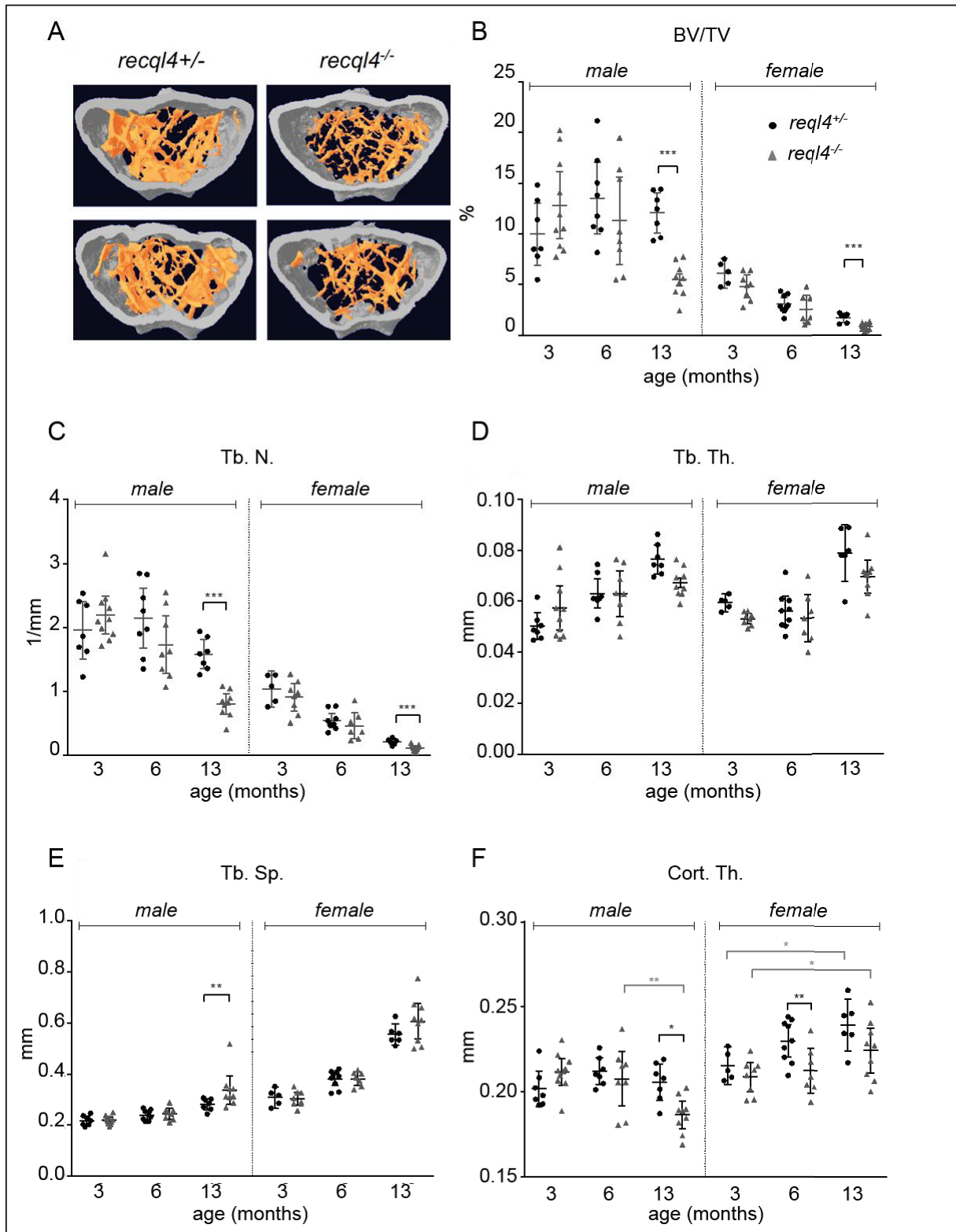


Figure 2

Figure 2: Age dependent loss of trabecular and cortical long bone in *Recql4*^{-/-} mice

(A) Representative 3D μ CT images of distal femurs from *recql4*^{+/-} and *recql4*^{-/-} 13-month-old male mice. (B to F) μ CT analyses of distal femoral trabecular bone and cortical bone of *recql4*^{+/-} (black circles) and *recql4*^{-/-} (grey triangles) mice of each sex and three age groups (3, 6 and 13 months) (B) BV/TV for trabecular bone volume fraction, (C) Tb.N. for trabecular number, (D) Tb.Th. for trabecular thickness, (E) Tb.Sp. for trabecular separation, (F) Ct.Th. for cortical thickness. n = 5 to 10 per group. For all parameters data are expressed as dot plots with mean \pm 95% CI ; (*p < 0.05, **p < 0.01, ***p < 0.001, two-way ANOVA test).

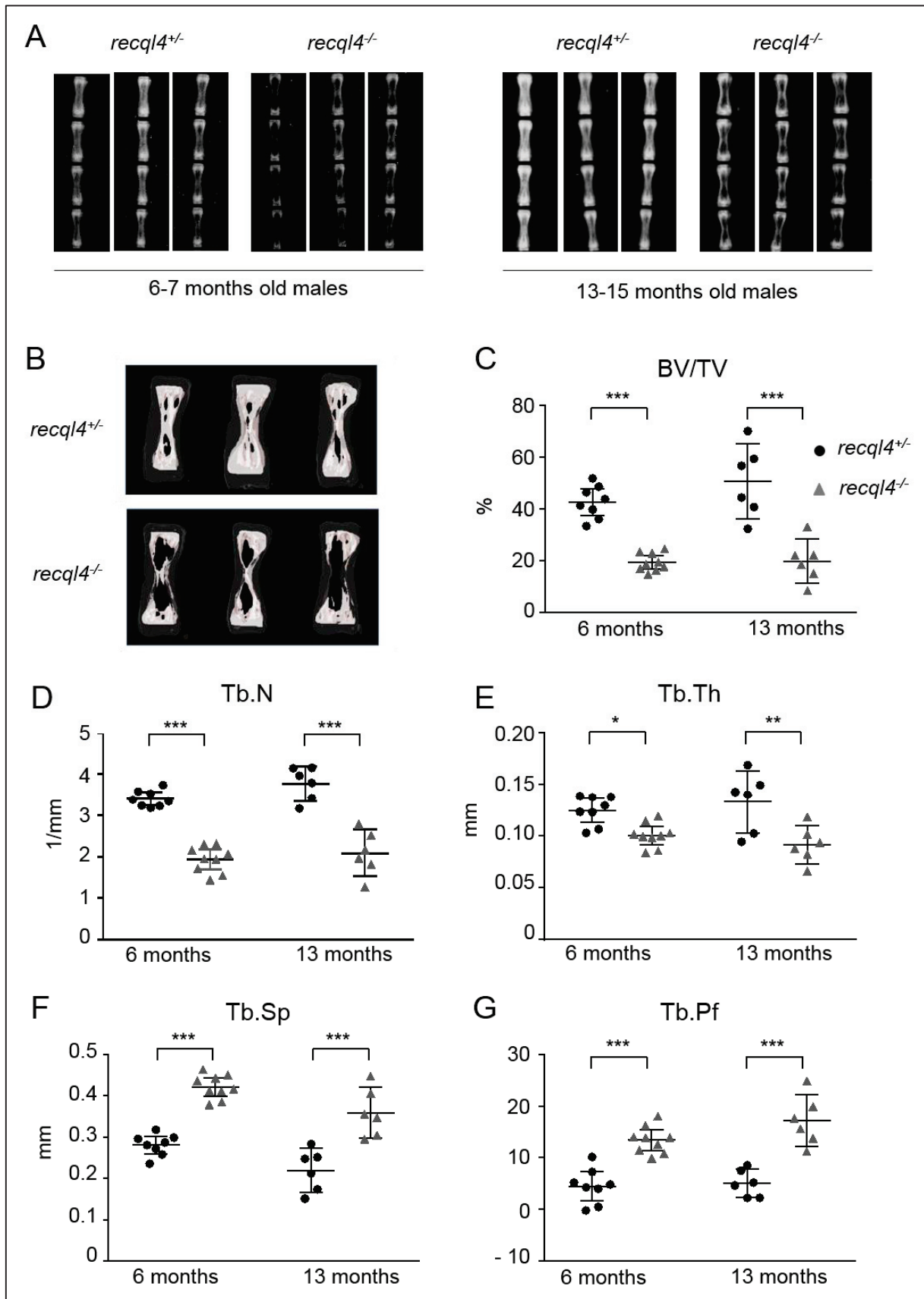


Figure 3

Figure 3: Bone loss in the caudal vertebrae of *Recql4*^{-/-} mice

X-ray radiographs showing tail vertebrae of *recql4*^{+/-} and *recql4*^{-/-} male mice of two groups of age. (B) 3D μ CT reconstruction of the 12th caudal vertebra of male mice. Representative examples are shown. (C to G) μ CT analyses of the 12th caudal vertebra from *recql4*^{+/-} (black circles) and *recql4*^{-/-} (grey triangles) male mice of two age groups (6 and 13 months). The following parameters BV/TV (C), Tb.N. (D), Tb.Th. (E), Tb.Sp. (F) and Tb.Pf for Trabecular Pattern Factor, are presented as dot plots with mean \pm 95% CI. n= 6 to 9 per group. (*p < 0.05, **p < 0.01, ***p < 0.001, two-way ANOVA test).

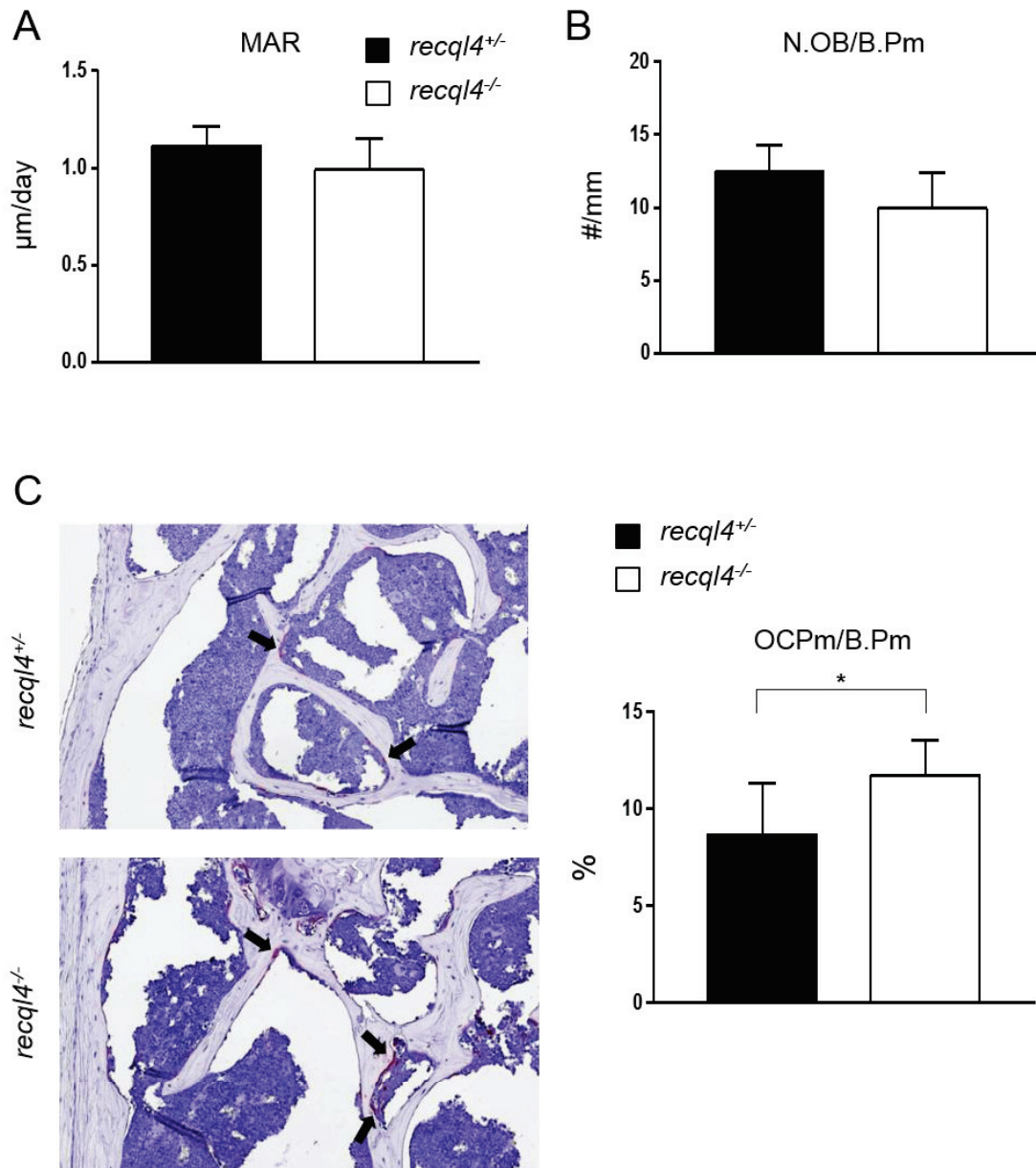


Figure 4: Histological analysis of distal femoral trabecular sections

(A) Mineralization apposition rate (MAR) visualized after calcein double labelling was measured for males aged 12 months and older. $n=6$ per genotype, data are means \pm SD (B) The number of osteoblasts per bone perimeter (N.OB/B.Pm) was evaluated after Osterix labeling. $n=3$ males per genotype aged 12 months, data are means \pm SD. (C) Representative photos showing osteoclasts (arrows) in a femur section stained with toluidine blue and TRAP. Quantification of the percent of bone perimeter covered by osteoclast (OC.Pm/B.Pm) was performed on femoral section from *recq14*^{+/-} ($n=7$) and *recq14*^{-/-} ($n=10$) males aged 17 months or older. The bar graph shows mean \pm SD. (* $p<0.05$, Mann-Whitney U-test).

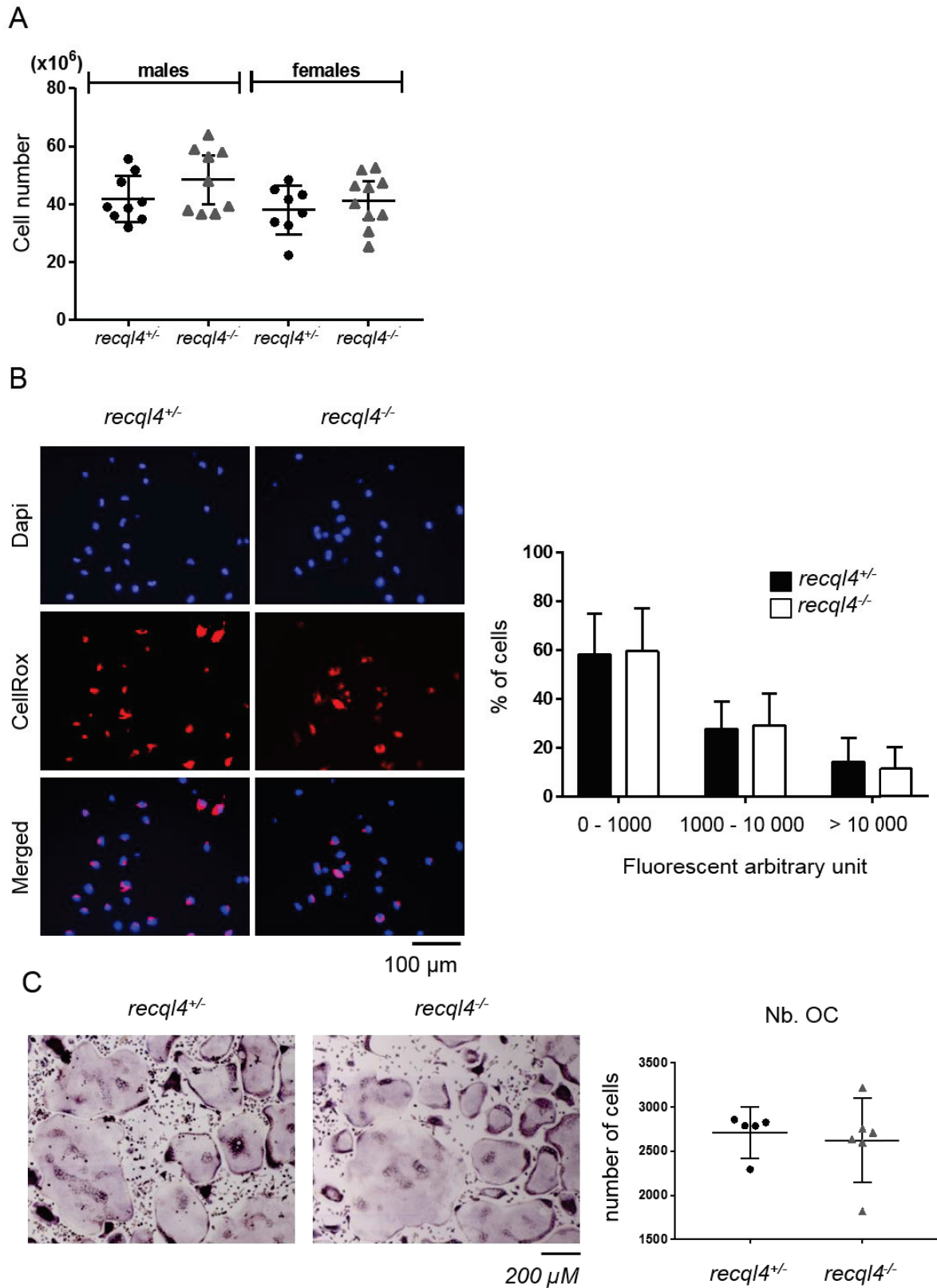


Figure 5

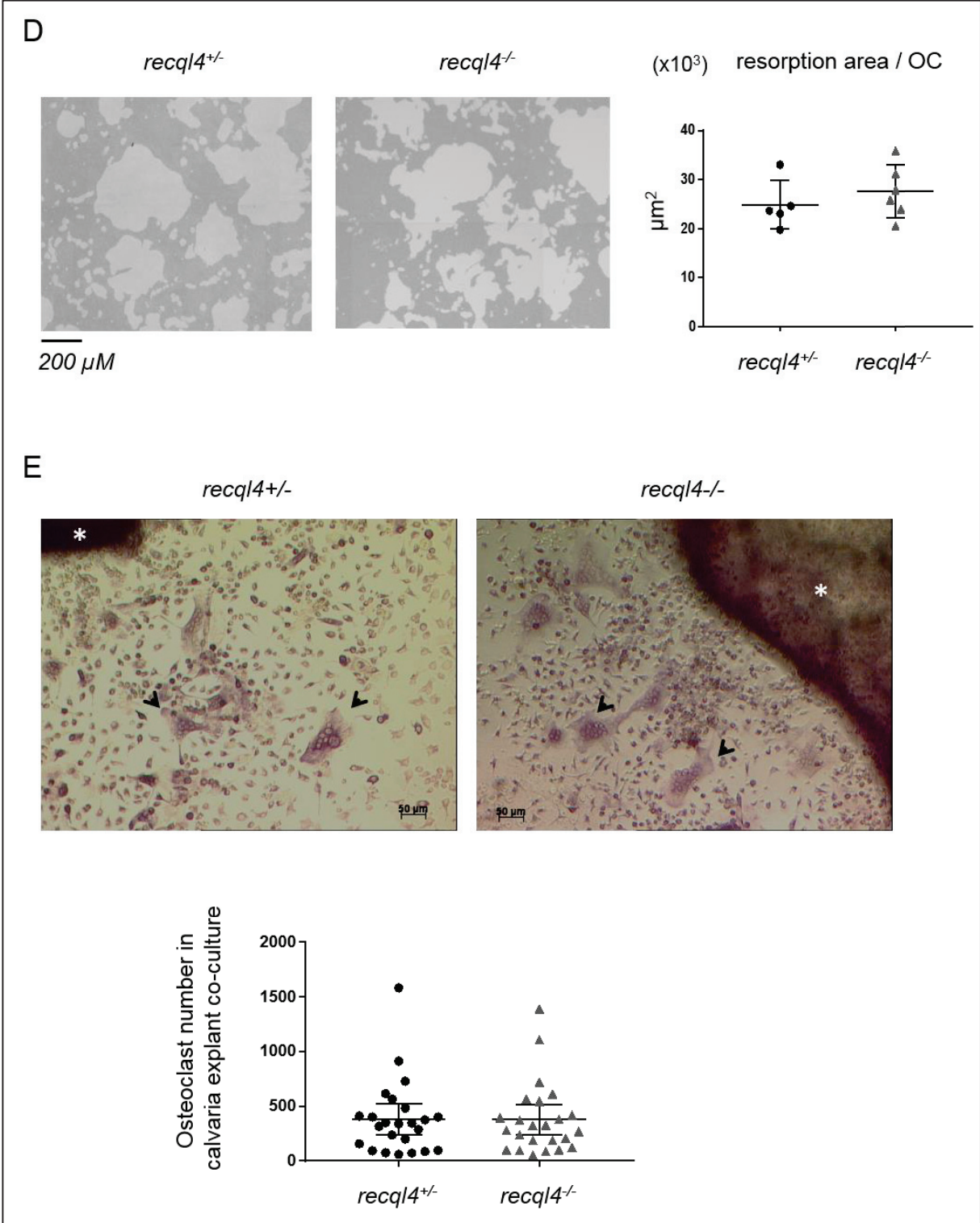


Figure 5 (suite)

Figure 5: *Recq14*^{-/-} osteoclast differentiation and function

(A) The numbers of bone marrow cells per mouse tibiae and femurs are shown as dot plots with mean \pm 95% CI (n= 8 to 10, 13-month-old mice per genotype). (B) ROS levels were evaluated in BMM from 13-month-old mice (n=9 mice per genotype). Photos of DAPI and Cell-ROX staining are shown. The percentage of cells with different levels of fluorescent intensity is presented as a bar graph showing the means \pm SD. (C and D) BMM from individual *recq14*^{+/-} (n=5) and *recq14*^{-/-} (n=6) mice were cultured on an inorganic bone mimetic surface in differentiation conditions. Multinucleated (\geq 3 nuclei) and TRAP⁺ cells were considered as osteoclasts. (C) Micrographs of osteoclasts obtained after 5 days of culture are shown. The numbers of osteoclasts in each culture are presented as dot plots with means \pm 95%CI. (D) Representative resorbed matrices are shown. Quantification of the resorbed area per osteoclast is shown as means \pm 95% CI. (E) Calvaria from individual mouse (n= 24 per genotype) were cut into small fragments (white asterisk), cultured for 10 days and subjected to TRAP staining (black arrowheads indicate examples of osteoclasts). TRAP⁺ multinucleated cells were counted. Data are presented as dot plots with mean \pm 95% CI.

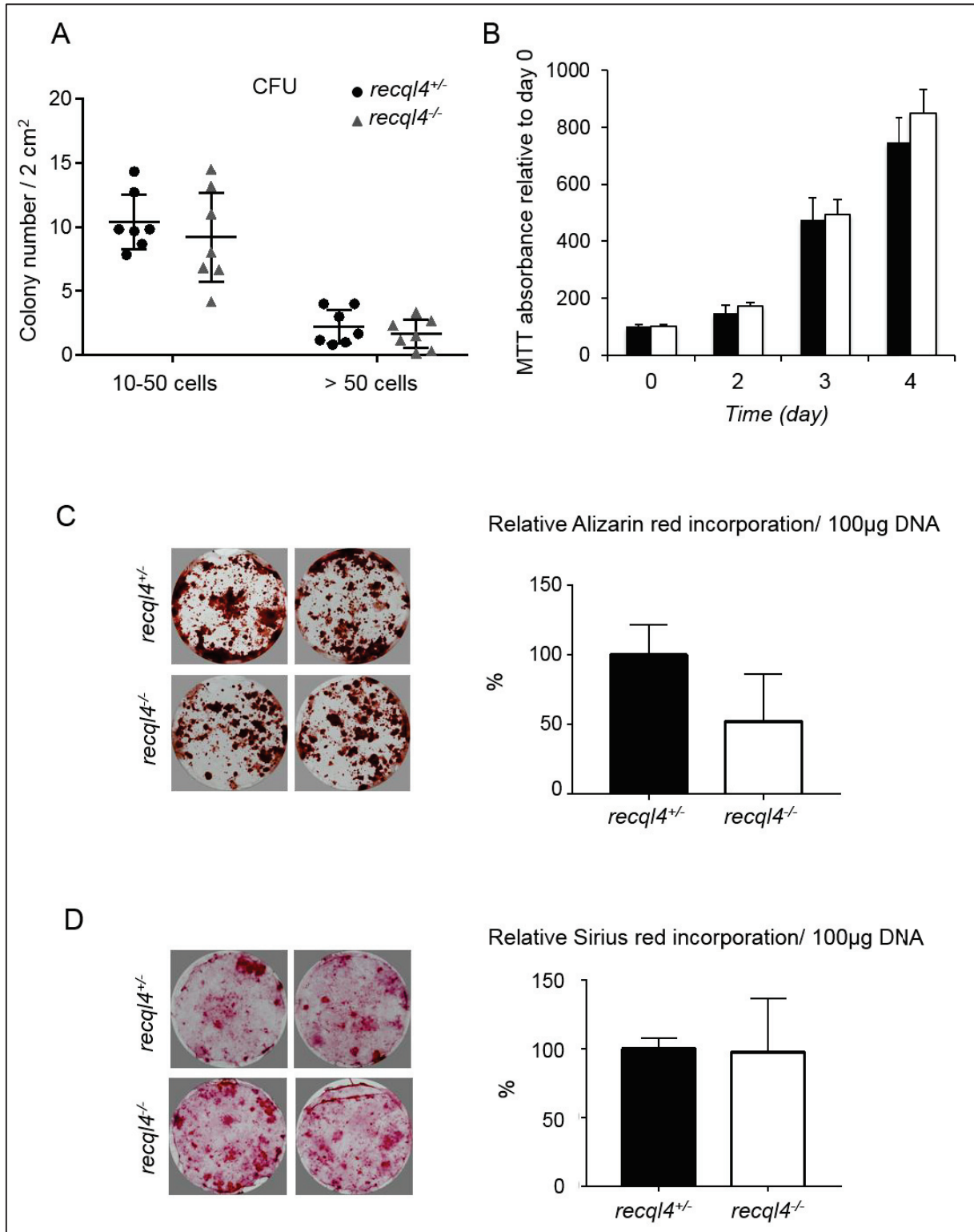


Figure 6

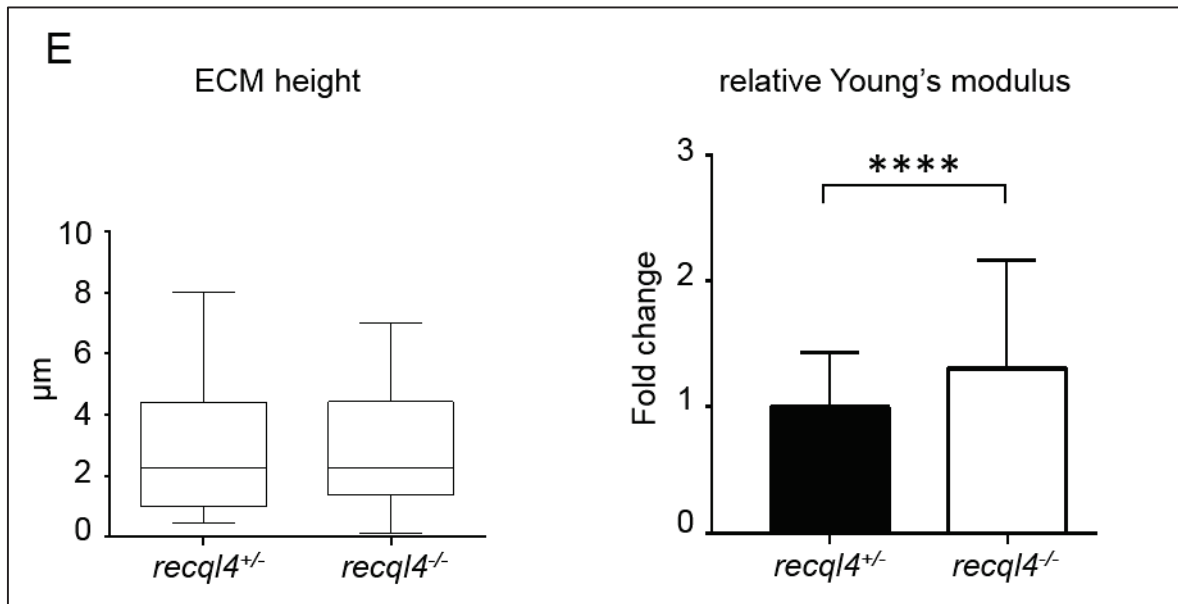
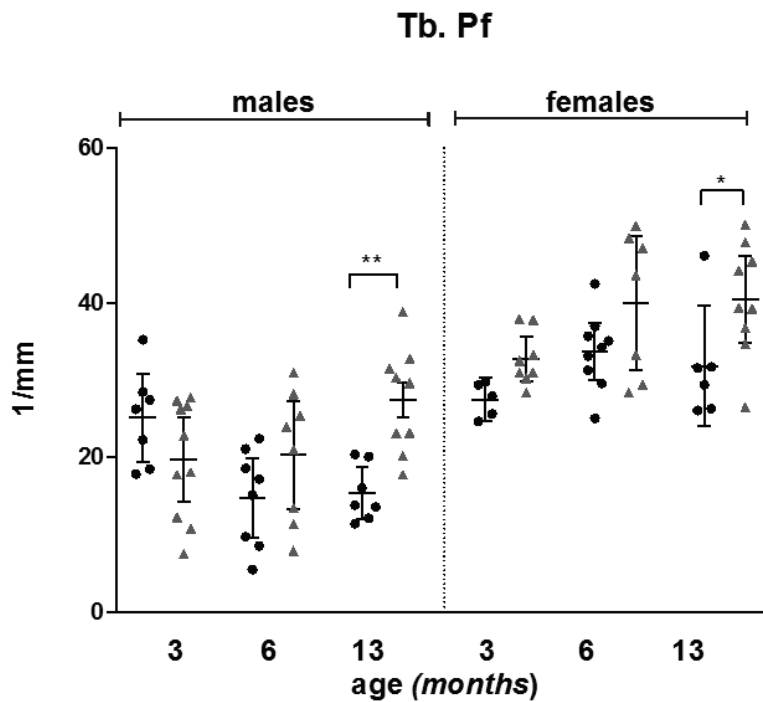
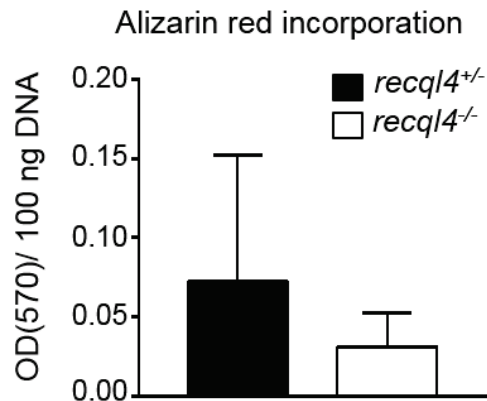


Figure 6: *Recq14*^{-/-} osteoblast differentiation and function

(A) Quantification of total colony forming unit (CFU) in bone marrow stromal cells from *recq14*^{+/-} and *recq14*^{-/-} mice (n=7 mice of 13 month of age and older per genotype). (B) Time-course of *in-vitro* cell growth in *recq14*^{+/-} and *recq14*^{-/-} long bone cells culture (n=4 13-month-old mice per genotype). Data are mean \pm SD. (C) Primary long-bone cells pooled from 3 to 4 mice per genotype were cultured 21 to 28 days. Photographs show mineralization as assessed by Alizarin red staining. Bound alizarin red was dissolved, measured by absorbance (570 nm) and related to total DNA content. Relative Alizarin red staining was then calculated as a % of the *recq14*^{+/-} condition. (D) Cultures were stained with Picrosirius red to visualize collagen deposition. Bar graph shows relative Picrosirius staining as a % of the *recq14*^{+/-} condition. (C) et (D) Data are mean \pm SD from 4 experiments with 3 to 4 mice/genotype/experiment. All mice were 13-month-old. (E) (Left panel) The organic matrix thickness was calculated from the AFM image height profiles. n=5 independent experiments in which 3 to 12 height profiles were analyzed per sample. Data are presented as box-and-whisker (Tukey) plots. (Right panel) Apparent Young's modulus values of organic matrix samples were normalized against the median value of the *recq14*^{+/-} matrix sample in each experiment and are presented as a fold change relative to the *recq14*^{+/-} condition. Data presented as a bar graph are median values with interquartile range. n=5 independent experiments, (**** p < 0.0001, Mann-Whitney U test).

8. Supplementary figures.**Figure S1: Trabecular Pattern factor**

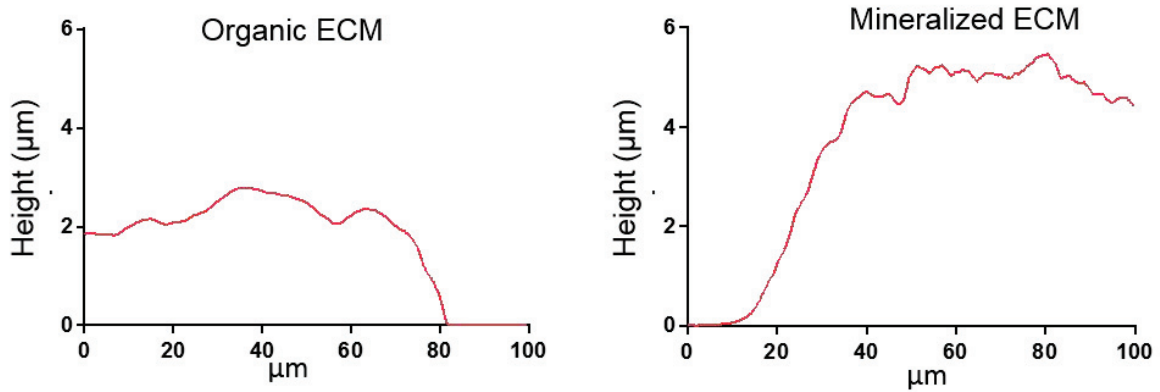
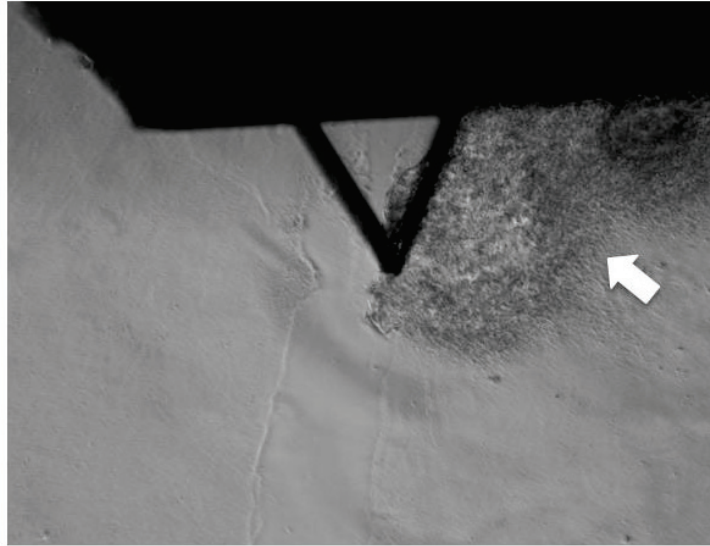
Trabecular Pattern Factor (Tb. Pf.) based on μ CT analyses of distal femoral trabecular bone are shown for Recq14^{+/-} (black circles) and Recq14^{-/-} (grey triangles) mice of each sex and three age groups (3, 6 and 13 months). For all parameters data are expressed as mean \pm 95% CI. ** $p < 0.01$, *** $p < 0.001$, (two-way ANOVA).

Figure S2 : Extracellular matrix mineralization

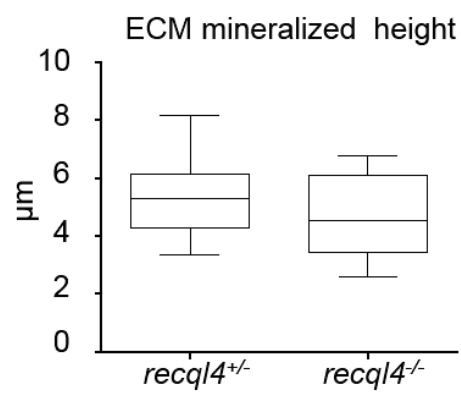
Primary long-bone cells isolated from 13-month-old individual mouse (6 mice per genotype) were cultured in differentiation conditions for 21 days. Extracellular matrix mineralization was assessed by alizarin red S staining. Bound alizarin red was dissolved, measure by absorbance (570 nm) and related to total DNA content. Data are presented as means \pm SD.

Figure S3 : AFM analysis

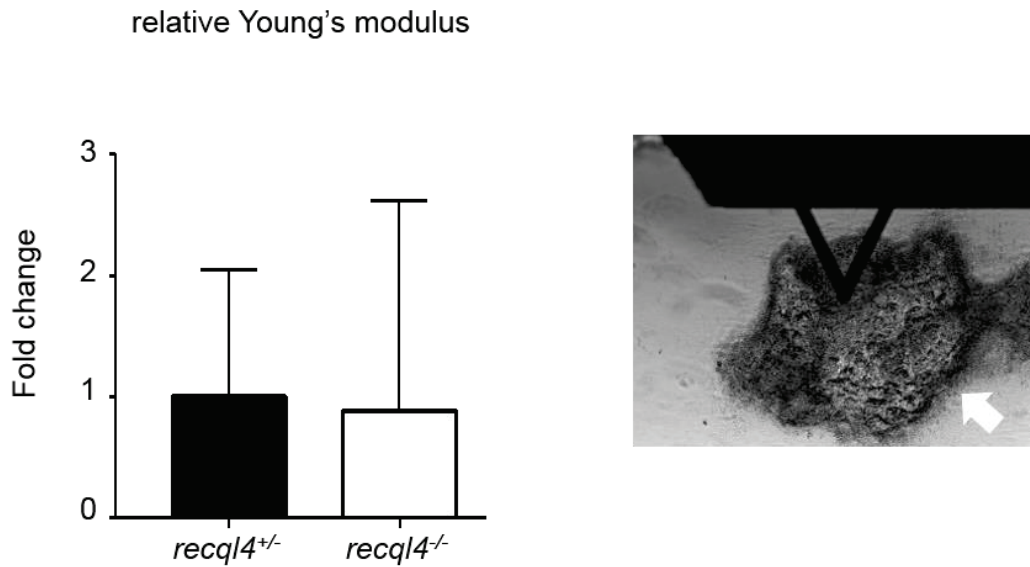
A.



B.



C.



- A. Phase contrast micrograph showing the AFM probe and a scratch across an extracellular matrix performed in order to evaluate matrix thickness. Two examples of AFM height profiles are shown corresponding to ECM areas without (on the left) or with (on the right) mineralization. A mineralization nodule is shown (white arrow)
- B. The thickness of ECM in mineralized areas was calculated from the AFM image height profiles. $n=5$ independent experiments in which 3 to 12 height profiles were analyzed per sample. Data are presented as box-and-whisker (Tukey) plots.
- C. Apparent Young's modulus values of mineralized matrix samples were normalized against the median value of the *RecqL4*^{+/-} matrix sample in each experiment and are presented as a fold change relative to the *RecqL4*^{+/-} condition. Data presented as a bar graph are median values with interquartile range. $n=5$ independent experiments. A Phase contrast micrograph showing the AFM probe over a mineralization nodule (white arrow) is shown.

9. Supporting Information

Supplementary experimental procedures and authors contributions

Mice

In the mutant allele, a PGKHprt mini-gene cassette replaced a genomic fragment of the *Recq14* gene spanning from exon 9 to exon 13 and encoding the conserved helicase domain (Mann *et al.*, 2005).

For all experiments, *Recq14*^{+/-} littermates were used as controls as these mice were indistinguishable from wild-type mice and did not exhibit any observable phenotype.

Micro-CT analysis

Scanning of femoral mouse samples was done with the bone specimen immersed in distilled water in a 6 mm inner diameter plastic tube and held in place thanks to gauze. Sample axial axis (i.e., femur long axis principal orientation) was aligned to the rotation axis of the sample holder. Scans were performed with a field of view of 1024x1024 pixels, a source voltage of 50 kV, a current of 800 μ A, a rotation step of 0.6° over a 180° rotation and a 0.5mm-thick aluminum filter for beam hardening reduction. An isotropic voxel size of 10.44 μ m was used with an exposure time of 4 seconds, 2 frames averaging leading to a total scan time of 41 minutes for each sample.

After image reconstruction, a core of 200 sections was used to measure the following factors by using SkyScan CtAn software V1.13: total volume, bone volume (BV) and the BV/tissue volume (TV) ratio. Trabecular BV and cortical BV were evaluated separately and the ratio of these two volumes was calculated. Trabecular bone thickness (Tb.Th.), trabecular number (Tb.N.) and separation (Tb.Sp.) were measured with a semi-automating morphing procedure, from total BV. Cortical thickness (Cort.Th.) was evaluated on 150 sections at mid shaft of diaphysis.

For tail vertebrae analysis, scanning conditions were as follows: X-ray tube potential was 50kV and the X-ray intensity was 200 μ A. An aluminum filter was used to remove image noise. The ring artifact correction was 6, and the beam hardening correction was 20%. To analyze 3D morphometric parameters with the SkyScan CtAn software, an upper threshold of 255 and a lower threshold of 55 were used to delineate each pixel as “bone” or “non-bone”.

X-Ray Imaging

Radiographic images of bone specimens were obtained by exposing them for 12 seconds to an 18 keV radiation using a Faxitron X-ray cabinet (Faxitron, Tucson, AZ, USA).

Bone histomorphometry

Distal femoral metaphyses were used for histomorphometric analyses. Femurs were decalcified before embedding in paraffin. Two 3 μ m-thick serial sections (Leica Microsystems, Wetzlar, Germany) were deparaffinized and subjected to tartrate-resistant acid phosphatase (TRAP) staining to identify osteoclasts or Osterix immunostaining to detect osteoblasts.

For TRAP staining, slides were stained for 1 hour at 37°C in a pH 5.2 acetate buffer containing 100 mmol/L sodium tartrate, 1 mg/mL of Naphthol AS-TR phosphate, 60 mmol/L *N,N*-dimethylformamide, and 1 mg/mL Fast Red TR Salt (all from Sigma-Aldrich, Darmstadt, Germany), and counterstained with hematoxylin (Sigma-Aldrich). For immunohistochemistry, after quenching of endogenous peroxidase activity, sections were blocked (2% of normal goat serum and 1% BSA in TBS Tween 0.05%) and incubated with anti-Osterix primary antibodies (ab22552, 1/1000, Abcam, Cambridge, UK). The revelation was performed using a standard ABC method (Agilent, Santa Clara, CA, USA) and the signal visualized using

3,3'-diaminobenzidine (Microm Microtech, Brignais, France). Histological images were acquired using a NanoZoomer 2.0-RS slide scanner (Hamamatsu, Hamamatsu, Japan). Quantifications of osteoclasts (osteoclast perimeter/bone perimeter) and of osteoblasts (osteoblast number/bone perimeter) in a calibrated region of interest (ROI) were done using ImageJ software (NIH, Bethesda, MD, USA). For dynamic histomorphometry, *in vivo* labeling of bone formation was performed with intra-peritoneal injection of 13-month-old male mice with calcein (Sigma-Aldrich) 7 days and 2 days respectively before tissue collection. Femurs were dissected and embedded in glycol methacrylate and 3 sections per sample were used to measure the mineralization apposition rate (MAR).

Bone marrow cell cultures

Bone marrow cells were flushed-out from both femurs and tibias of each mouse with Dulbecco's phosphate buffered saline modified (DPBS) (Sigma-Aldrich) dispensed by a 2.5 ml syringe with a 26-gauge needle. After centrifugation, cells were treated for 5 min with 3 ml of ACK buffer (0.01 mM EDTA, 0.011 M KHCO₃, and 0.155 M NH₄Cl, pH 7.3) in order to lyse red blood cells. The ACK lysis reaction was stopped by the addition of 27 ml of DPBS and the resulting 30 ml were filtered with a 70 µm mesh filter. Cells were centrifuged, suspended in suitable complete culture medium and counted.

For stromal colony count assays (CFU assays), nucleated bone marrow cells, flushed-out from mouse femurs and tibias, were suspended in α MEM (Lonza, Basel, Switzerland) complemented with 15% HyClone fetal bovine serum (Thermo Scientific, Logan, UT, USA), 2 mM L-Glutamine, 1000 U/ml Penicillin and 1 mg/ml Streptomycin (all from Sigma-Aldrich) and directly seeded at 1×10^6 cells/well in 6-well plates (3 wells/mouse). The medium was changed rapidly to eliminate non-adherent cells and

then every two or three days. After 14 days, the cells were stained with crystal violet dye.

For the preparation of bone marrow-derived macrophages (BMM), bone marrow cells were suspended in α MEM containing 10% HyClone fetal bovine serum complemented with 2 mM L-Glutamine and the penicillin-streptomycin mixture (α M10 medium) and cultured for 24 h in the presence of 10 ng/ml M-CSF (PeproTech, Rocky Hill, NJ, USA). The non-adherent cells were carefully collected and used as BMM.

Osteoclast formation and function analysis

BMM were seeded at a density of 10^5 cells/cm² in osteo assay plates that provide a synthetic inorganic bone mimetic surface (Corning Life Science, Tewksbury, MA, USA) and were cultured in α M10 medium complemented with 25 ng/ml of M-CSF and 50 ng/ml of GST-RANKL (Gritsaenko *et al.* 2017). On day 3, media were changed and on day 5 the cultures were stopped. 3 wells per mouse were subjected to TRAP staining as previously described (Gritsaenko *et al.* 2017) and multinucleated (≥ 3 nuclei) TRAP-positive cells were considered as differentiated osteoclasts. 3 other wells of the same plate were used to measure resorbed areas as was done before (Gritsaenko *et al.* 2017). Subsequently, we determined for each mouse the average surface resorbed per osteoclast. 5 to 6 mice per genotype were analyzed.

Primary long-bone cell cultures, mineralization and collagen deposition assays

Osteoblasts from mouse long bone were isolated as previously described (Bakker & Klein-Nulend 2012). Briefly, cleaned and flushed femoral and tibial diaphyses of each mouse were cut into small pieces, washed in DPBS and incubated in 6 ml of α MEM containing 2 mg/ml of collagenase II (Gibco, ThermoFisher Scientific) at 37°C in a shaking water bath. After 2 h, the bone pieces were washed in α MEM and then

resuspended in α M10 medium before being transferred to a 25 cm² flask. After 10 to 15 days of culture, cells were trypsinized, counted and seeded in α M10 medium, under conditions adapted to the different types of assays: 3 x 10³ cells/cm² in 24-well plates for MTT assays, 12.5 x 10³ cells/cm² in 6-well plates for mineralization and collagen deposition assays and 20 x 10³ cells/cm² in glass bottom dishes (WillCo Wells, Amsterdam, The Netherlands) used for Atomic Force Microscopy (AFM) analysis.

For mineralization and collagen deposition assays, primary long-bone cells from a single mouse or pooled from 3 to 4 mice of the same genotype, were seeded in 6 well plates and cultured in α M10 medium until reaching subconfluency, upon which the medium was changed for alpha-MEM containing 10% heat-inactivated HyClone fetal bovine serum, 2 mM L-Glutamine, the penicillin-streptomycin cocktail, 50 μ g/ml ascorbic acid (Sigma-Aldrich) and 10 mM beta-glycerophosphate (Sigma-Aldrich). This osteogenic medium was changed every two or three days for 21 or 28 days. For mineralization evaluation, cultures in 4 of the 6 wells were then fixed with 4% formaldehyde solution (Sigma-Aldrich), rinsed with deionized water and stained with 1% Alizarin red S solution (Alfa Aesar, ThermoFisher Scientific) for 5 min to assess calcium deposition. Extensive washes with deionized water were performed prior to solubilization of Alizarin Red S dye with 10% Cetylpyridinium chloride in PBS (Sigma-Aldrich) and absorbance reading at 570 nm. The two remaining wells were used to extract DNA by using QIAamp DNA mini kit (QIAGEN, Hilden, Germany) in order to normalize Alizarin staining to DNA content.

For collagen deposition assessment, cultures in 4 of the 6 wells were decellularized as previously described (Sun *et al.* 2018), fixed for 1 hour in 2% formaldehyde/ 2.5% glutaraldehyde (Sigma Aldrich) solution, washed in PBS prior to staining for 1 hour with 0.1% Picrosirius Red (Sigma Aldrich) in saturated picric acid solution (Sigma Aldrich).

Then, the non-specific staining was removed by extensive washes with 0.01 N hydrochloric acid (Sigma Aldrich) and the specifically bound dye was dissolved for 30 min at 37°C in 0.6 N sodium hydroxide and quantified by reading absorbance at 546 nm (Tullberg-Reinert & Jundt 1999). The two remaining wells were used for DNA quantification as described above.

Calvaria explant co-cultures

Explant culture from mouse calvaria was performed as previously described (Nollet *et al.*, 2014). Briefly, calvarial bone (cleaned of soft tissue) was cut into 1 to 2 mm² fragments that were cultured into 12-well plates in α M10 medium (1 calvaria per well). Osteoclasts obtained after 10 days of culture were stained for TRAP and counted.

Atomic Force Microscopy analysis

Elastic modulus measurement

The decellularized matrices were rinsed 3 times and covered with 3 ml of PBS. After thermal stabilization of the sample and AFM probe, at least three different areas per sample were analyzed using the “Point and Shoot” method, collecting a minimum of 100 force-distance curves at as many discrete points spaced at least 20 μ m apart. For each set of experiments, the calibration was performed by determining the deflection sensitivity of the system in PBS, using a clean Willco glass bottom dish and the spring constant of the cantilever, by the thermal tune method.

The apparent Young's modulus was calculated using the NanoScope Analysis 1.80 software, applying to the force curves, after the baseline correction, the Hertz spherical indentation model using a Poisson's ratio of 0.5. For the analysis, only the force curves with a maximum value at 2 nN were considered and to avoid large indentation, the force fit boundary chosen to perform the fit was between 5% and 25% of the whole

force curve. Among all the obtained data, only the apparent Young's modulus values corresponding to a fit with $R^2 > 0.80$ were considered.

Data normalization

For each set of experiments, the median value of the apparent Young's modulus (YM) of the control sample (*Recq14*^{+/-} matrix) was calculated. For each set of samples (*Recq14*^{+/-} and *Recq14*^{-/-} matrices) belonging to the same experiment, the ratios between every single calculated apparent YM value and the median value of the control sample were determined. Data from both genotypes were compared by non-parametric two-tailed Mann-Whitney statistical test.

ECM thickness measurement

ECM samples were washed 3 times with deionized water and dried with a gentle N₂ flux. Using a scalpel, four radial scratches were made across matrices. Then, the samples were covered with PBS to allow the re-hydration and their AFM height profiles were obtained using a Borosilicate Glass spherical tip of 5 μm of diameter and a cantilever with a nominal spring constant of $k=0.06$ N/m. The height profile analyses were performed on images obtained by peak force QNM (Bruker Nano Surfaces, Santa Barbara, CA, USA) and having a scan area of 100 x 2 μm (corresponding to 512 x 10 pixels) and perpendicular to the scratch. These images were acquired with a scan rate of 0.1 Hz and a peak force setpoint of 6 nN. Matrix thickness evaluation was performed using the Step Analysis (NanoScope Analysis 1.80 software) in which 10 height profiles corresponding to 10 scan lines of 2 microns were averaged.

RT-PCR of the *Recq14* RNA

Total RNA samples were prepared using TRIzol reagent (Thermo Fisher Scientific) following manufacturer's instructions. Reverse transcription (RT) was performed using

SuperScript II reverse transcriptase (Thermo Fisher scientific), 1 µg of RNA and random hexamer primers. A 10-fold dilution of resulting cDNAs was then subjected to PCR amplification with primers located at the junction between exons 9 and 10 (5'-CGG ATT CTT TCT GGC ATC TCT AC-3') and in exon 10 (5'-GGC GAG ACC ACG AGT GTG A-3') of the *Recq14* gene.

Oxidative stress analysis

For oxidative stress analysis, BMM cells prepared from each mouse (n= 9 per genotype) were cultured for 30 min at 37°C with 3 µM of the fluorescent indicator probe, Cell-ROX orange reagent (Molecular Probes, ThermoFisher Scientific, Illkirch-Graffenstaden, France). A cell-permeant nuclear counterstain (Hoechst® 33342 dye, Molecular Probes, ThermoFisher Scientific) was also added to the medium for the last 15 min. The cells were washed two times in PBS and fluorescence images from at least 6 different microscopic fields per culture were acquired at magnification x 20, using an Axio Observer Z1 motorized inverted microscope. The pictures were taken under fixed exposure conditions and fluorescence quantification was done by using CellQuant, a freely available ImageJ plugin developed in our laboratory (<http://biophytiro.unice.fr/tiro/>). All mice used to prepare BMM cultures were at least 13-month-old.

MTT assay

The growth of primary long-bone cells, from day 1 to day 4 after seeding, was established using MTT (3-(4,5-Dimethylthiazol-2-yl)-2,5-diphenyltetrazolium bromide) viability assay as described previously⁶²⁶. In brief, the cells were washed in DPBS before incubation at 37°C with 0.5 mg/ml MTT solution (400 µl/well). After 2.5 h, intracellular formazan crystals were dissolved in DMSO (Sigma-Aldrich) and absorbance was read at 570 nm (test wavelength) and 690 nm (reference wavelength).

The 690 nm background absorbance was subtracted from the 570 nm measurement to obtain corrected absorbance values. 3 wells/time point/mouse were analyzed. n = 4 13-month-old mice per genotype.

References

Bakker AD & Klein-Nulend J (2012) Osteoblast isolation from murine calvaria and long bones. *Methods Mol. Biol.* 816, 19–29.

Gritsaenko T, Pierrefite-Carle V, Lorivel T, Breuil V, Carle GF & Santucci-Darmanin S (2017) Natural uranium impairs the differentiation and the resorbing function of osteoclasts. *Biochim Biophys Acta Gen Subj* 1861, 715–726.

Sun Y, Yan L, Chen S & Pei M (2018) Functionality of decellularized matrix in cartilage regeneration: A comparison of tissue versus cell sources. *Acta Biomaterialia* 74, 56–73.

Tullberg-Reinert H & Jundt G (1999) In situ measurement of collagen synthesis by human bone cells with a sirius red-based colorimetric microassay: effects of transforming growth factor beta2 and ascorbic acid 2-phosphate. *Histochem. Cell Biol.* 112, 271–276.

Authors contributions

T.G. performed *ex-vivo* experiments and analysed data; V.P.-C. and G.F.C. co-supervised parts of the study and edited the manuscript; S.P. established and analysed AFM experiments; T.L. performed statistical analyses; H.F. and S.B. carried on μ CT acquisition, J.F. performed histologic and histomorphometric experiments, C.R. did the mouse genotyping and contributed to *ex-vivo* experiments, L.C. performed image acquisitions, V.B. gave conceptual advice; S. S.D. supervised the study, analysed data and wrote the manuscript with detailed comments provided by all the authors.

10. References

- Abe T, Yoshimura A, Hosono Y, Tada S, Seki M & Enomoto T (2011) The N-terminal region of RECQL4 lacking the helicase domain is both essential and sufficient for the viability of vertebrate cells: Role of the N-terminal region of RECQL4 in cells. *Biochimica et Biophysica Acta (BBA) - Molecular Cell Research* 1813, 473–479.
- Bruck I & Kaplan DL (2014) The replication initiation protein Sld2 regulates helicase assembly. *J. Biol. Chem.* 289, 1948–1959.
- Cao F, Lu L, Abrams SA, Hawthorne KM, Tam A, Jin W, Wang LL (2017) Generalized metabolic bone disease and fracture risk in Rothmund-Thomson syndrome. *Hum. Mol. Genet.* 26, 3046–3055.
- Capp C, Wu J & Hsieh T-S (2010) RecQ4: the second replicative helicase? *Crit. Rev. Biochem. Mol. Biol.* 45, 233–242.
- Croteau DL, Singh DK, Ferrarelli LH, Lu H & Bohr VA (2012) RECQL4 in genomic instability and aging. *Trends Genet* 28, 624–631.
- Domazetovic V, Marcucci G, Iantomasi T, Brandi ML & Vincenzini MT (2017) Oxidative stress in bone remodeling: role of antioxidants. *Clin Cases Miner Bone Metab* 14, 209–216.
- Fahlström A, Yu Q & Ulfhake B (2011) Behavioral changes in aging female C57BL/6 mice. *Neurobiol. Aging* 32, 1868–1880.
- Ghosh AK, Rossi ML, Singh DK, Dunn C, Ramamoorthy M, Croteau DL, Liu Y & Bohr VA (2012) RECQL4, the Protein Mutated in Rothmund-Thomson Syndrome, Functions in Telomere Maintenance. *J. Biol. Chem.* 287, 196–209.
- Glatt V, Canalis E, Stadmeier L & Bouxsein ML (2007) Age-Related Changes in Trabecular Architecture Differ in Female and Male C57BL/6J Mice. *Journal of Bone and Mineral Research* 22, 1197–1207.
- Gupta S, De S, Srivastava V, Hussain M, Kumari J, Muniyappa K & Sengupta S (2014) RECQL4 and p53 potentiate the activity of polymerase γ and maintain the integrity of the human mitochondrial genome. *Carcinogenesis* 35, 34–45.
- Hahn M, Vogel M, Pompesius-Kempa M & Delling G (1992) Trabecular bone pattern factor—a new parameter for simple quantification of bone microarchitecture. *Bone* 13, 327–330.
- Halloran BP, Ferguson VL, Simske SJ, Burghardt A, Venton LL & Majumdar S (2002) Changes in Bone Structure and Mass with Advancing Age in the Male C57BL/6J Mouse. *Journal of Bone and Mineral Research* 17, 1044–1050.
- Han Y, You X, Xing W, Zhang Z & Zou W (2018) Paracrine and endocrine actions of bone—the functions of secretory proteins from osteoblasts, osteocytes, and osteoclasts. *Bone Res* 6.
- Jilka RL (2013) The Relevance of Mouse Models for Investigating Age-Related Bone Loss in Humans. *J Gerontol A Biol Sci Med Sci* 68, 1209–1217.
- Jin W, Liu H, Zhang Y, Otta SK, Plon SE & Wang LL (2008) Sensitivity of RECQL4-deficient fibroblasts from Rothmund-Thomson syndrome patients to genotoxic agents. *Hum. Genet.* 123, 643–653.

Kitao S, Lindor NM, Shiratori M, Furuichi Y & Shimamoto A (1999) Rothmund-thomson syndrome responsible gene, RECQL4: genomic structure and products. *Genomics* 61, 268–276.

Kumari J, Hussain M, De S, Chandra S, Modi P, Tikoo S, Singh A, Sagar C, Sepuri NBV & Sengupta S (2016) Mitochondrial functions of RECQL4 are required for the prevention of aerobic glycolysis-dependent cell invasion. *J. Cell. Sci.* 129, 1312–1318.

Lambers FM, Kuhn G, Schulte FA, Koch K & Müller R (2012) Longitudinal assessment of in vivo bone dynamics in a mouse tail model of postmenopausal osteoporosis. *Calcif. Tissue Int.* 90, 108–119.

Lampi MC & Reinhart-King CA (2018) Targeting extracellular matrix stiffness to attenuate disease: From molecular mechanisms to clinical trials. *Sci Transl Med* 10.

Larizza L, Roversi G & Volpi L (2010) Rothmund-Thomson syndrome. *Orphanet J Rare Dis* 5, 2.

Lu L, Harutyunyan K, Jin W, Wu J, Yang T, Chen Y, Joeng KS, ... Wang LL (2015) RECQL4 Regulates p53 Function In Vivo During Skeletogenesis. *J. Bone Miner. Res.* 30, 1077–1089.

Mann MB, Hodges CA, Barnes E, Vogel H, Hassold TJ & Luo G (2005) Defective sister-chromatid cohesion, aneuploidy and cancer predisposition in a mouse model of type II Rothmund-Thomson syndrome. *Hum. Mol. Genet.* 14, 813–825.

Mehollin-Ray AR, Kozinetz CA, Schlesinger AE, Guillerman RP & Wang LL (2008) Radiographic abnormalities in Rothmund-Thomson syndrome and genotype-phenotype correlation with RECQL4 mutation status. *AJR Am J Roentgenol* 191, W62-66.

Mo D, Zhao Y & Balajee AS (2018) Human RecQL4 helicase plays multifaceted roles in the genomic stability of normal and cancer cells. *Cancer Lett.* 413, 1–10.

Ng AJM, Walia MK, Smeets MF, Mutsaers AJ, Sims NA, Purton LE, ... Walkley CR (2015) The DNA helicase recql4 is required for normal osteoblast expansion and osteosarcoma formation. *PLoS Genet.* 11, e1005160.

Nollet M, Santucci-Darmanin S, Breuil V, Al-Sahlanee R, Cros C, Topi M, ... Pierrefite-Carle V (2014) Autophagy in osteoblasts is involved in mineralization and bone homeostasis. *Autophagy* 10, 1965–1977.

Panwar P, Lamour G, Mackenzie NCW, Yang H, Ko F, Li H & Brömme D (2015) Changes in Structural-Mechanical Properties and Degradability of Collagen during Aging-associated Modifications. *J Biol Chem* 290, 23291–23306.

Parfitt AM (1984) Age-related structural changes in trabecular and cortical bone: cellular mechanisms and biomechanical consequences. *Calcif. Tissue Int.* 36 Suppl 1, S123-128.

Prewitz MC, Seib FP, von Bonin M, Friedrichs J, Stißel A, Niehage C, ... Werner C (2013) Tightly anchored tissue-mimetic matrices as instructive stem cell microenvironments. *Nat. Methods* 10, 788–794.

Riggs BL, Melton Iii LJ, Robb RA, Camp JJ, Atkinson EJ, Peterson JM, ... Khosla S (2004) Population-based study of age and sex differences in bone volumetric

density, size, geometry, and structure at different skeletal sites. *J. Bone Miner. Res.* 19, 1945–1954.

Sangrithi MN, Bernal JA, Madine M, Philpott A, Lee J, Dunphy WG & Venkitaraman AR (2005) Initiation of DNA replication requires the RECQL4 protein mutated in Rothmund-Thomson syndrome. *Cell* 121, 887–898.

Schumacher B, Garinis GA & Hoeijmakers JHJ (2008) Age to survive: DNA damage and aging. *Trends Genet.* 24, 77–85.

Siitonen HA, Kopra O, Kääriäinen H, Haravuori H, Winter RM, Säämänen A-M, ... Kestilä M (2003) Molecular defect of RAPADILINO syndrome expands the phenotype spectrum of RECQL diseases. *Hum. Mol. Genet.* 12, 2837–2844.

Siitonen HA, Sotkasiira J, Biervliet M, Benmansour A, Capri Y, Cormier-Daire V, ... Kestilä M (2009) The mutation spectrum in RECQL4 diseases. *Eur. J. Hum. Genet.* 17, 151–158.

Van Maldergem L, Siitonen HA, Jalkh N, Chouery E, De Roy M, Delague V, ... Verloes A (2006) Revisiting the craniosynostosis-radial ray hypoplasia association: Baller-Gerold syndrome caused by mutations in the RECQL4 gene. *J. Med. Genet.* 43, 148–152.

Vennos EM, Collins M & James WD (1992) Rothmund-Thomson syndrome: review of the world literature. *J. Am. Acad. Dermatol.* 27, 750–762.

Willingham MD, Brodt MD, Lee KL, Stephens AL, Ye J & Silva MJ (2010) Age-related changes in bone structure and strength in female and male BALB/c mice. *Calcif. Tissue Int.* 86, 470–483.

Xu X & Liu Y (2009) Dual DNA unwinding activities of the Rothmund–Thomson syndrome protein, RECQ4. *The EMBO Journal* 28, 568–577.

Yokoyama H, Moreno-Andres D, Astrinidis SA, Hao Y, Weberruss M, Schellhaus AK, ... Antonin W (2019) *Life Sci Alliance* 2. Chromosome alignment maintenance requires the MAP RECQL4, mutated in the Rothmund-Thomson syndrome.

Zimmermann EA, Schaible E, Bale H, Barth HD, Tang SY, Reichert P, ... Ritchie RO (2011) Age-related changes in the plasticity and toughness of human cortical bone at multiple length scales. *PNAS* 108, 14416–14421.

[dataset] Gritsaenko *et al.* 2019, Premature bone aging in a RECQL4-deficient mouse

model dataset, Figshare, 10.6084/m9.figshare.9425318

II. CHARACTERIZATION OF THE MINERALIZED ECM PRODUCED BY RECQL4-DEFICIENT OSTEOBLASTS.

1. Summary

In the previous study we have characterized the bone phenotype of RECQL4-deficient mice. By performing micro-CT analysis of bearing (distal femoral metaphysis) and non-bearing (caudal vertebrae) skeletal sites, we demonstrated that *recql4*^{-/-} animals of both sexes have accelerated bone loss reminiscent of the premature osteopenia seen in RTS-II patients. All the *ex vivo* experiments we have carried out suggest that the observed bone loss could be linked to modifications in the extracellular matrix of *recql4*^{-/-} animals. Indeed, the organic part of the bone matrix synthesized by *recql4*^{-/-} osteoblasts was found to be more rigid, whereas its mineral content tends to be lower than that of the control matrix.

In the following study we continued to characterize the mineralized ECM produced *ex vivo* by *recql4*^{-/-} and *recql4*^{+/-} osteoblasts. As a first step, we developed a method for extracting proteins from mineralized matrices, that provided samples enriched in ECM proteins and suitable for LS-MS/MS analysis. Next, we performed a proteomic analysis that identified 204 proteins with differential expression, which added support to the hypothesis that RECQL4-deficient osteoblasts synthesize an altered bone matrix. We focused on 4 of these proteins, based on their role in bone tissue biology or DNA metabolism. Two of them were found overexpressed in mutant matrices: Decorin, a structural proteoglycan involved in collagen fibrillogenesis and YB1, a transcription factor interacting with RECQL4. The other two candidates, Pleiotrophin and SLIT3, under-represented in *recql4*^{-/-} matrices, are proteins known mainly as axonal guidance molecules. The expression of these candidates was further studied using Western Blot and RT-qPCR. Taken together, our data lead us to propose the following working hypotheses concerning *recql4*^{-/-} mice bone loss. Accumulation of Decorin in the mutant bone ECM, could stiffen the organic matrix, thereby enhancing osteoclastic resorption. At the same time, the decrease in Pleiotrophin and SLIT3 level, two chemoattractant molecules of osteoblasts, could affect the recruitment of these cells at remodeling sites, and thus decrease mineralization.

These hypotheses remain to be investigated, nevertheless all the work carried out has made it possible to characterize a model that offers interesting prospects for studying the complex relationship between DNA metabolism, bone cells and bone matrix and its role in bone aging.

2. *Materials and methods*

A. Cell culture media

Following culture media were used:

- α MEM: alpha modified Minimum Essential Medium (Lonza, #BE12-169F)
- α M10-AA, long bone amplification culture medium: α MEM with nucleosides (Lonza, #BE02-002F) supplemented with 10% HyClone fetal bovine serum (ThermoFisher Scientific, #SH30071.03), antibiotics (100 IU/ml penicillin and 100 μ g/ml streptomycin, Sigma-Aldrich, #P4333) and 50 μ g/ml ascorbic acid (Sigma Aldrich, #A8960)
- α M5, MLO-A5 cell line culture medium: α MEM with nucleotides supplemented with 1% penicillin/streptomycin, 5% heat-inactivated HyClone fetal bovine serum (GE Healthcare, #SH30071.03), and 5% heat-inactivated Hyclone calf serum (GE Healthcare, #SH30072.03)
- MM, long bone mineralization medium: α MEM with nucleosides supplemented with 10% heat-inactivated HyClone fetal bovine serum, 1% penicillin/streptomycin, 50 μ g/ml ascorbic acid and 10 mM beta-glycerophosphate (Sigma-Aldrich, #G9422)

B. Long bone cell culture and mineralization

Three to four mice of each genotype [*Recq4*^{+/-} (control, ctr) and *Recq4*^{-/-} (mutant, mut)] were used for each experiment. Osteoblasts from mouse long bone (LB) were isolated as previously described (Bakker and Klein-Nulend, 2012). Briefly, cleaned and flushed femoral and tibial diaphyses of each mouse were cut into small pieces, washed in DPBS and incubated in 6 ml of α MEM containing 2 mg/ml of collagenase II (Gibco, #17101-015), at 37°C in a shaking waterbath (Gibco, ThermoFisher Scientific). After 2 h, the bone pieces were washed in α MEM and then resuspended in the α M10-AA medium before being transferred to a 25 cm² flask. After

10 to 15 days of culture, cells were trypsinized (Trypsin-EDTA 0,25%, Sigma-Aldrich, #59429C), pooled according to genotype, counted and seeded in α M10-AA medium, under conditions adapted to the different experiments: 1.5×10^4 cells/cm² in 24-well plates and 1.2×10^4 cells/cm² in 6-well plates. 24-well plates were used as is for TEM (transmission electron microscopy); containing plastic coverslips (Thermanox, ThermoFisher Scientific, #174950), for SEM (scanning electron microscopy); and containing glass coverslips, for immunofluorescence staining. 6-well plates were used for RNA and protein extraction. At confluence, the medium was changed for MM. This osteogenic medium was changed every two to three days during 28 days.

C. MLO-A5 culture and mineralization

The MLO-A5 cell line was maintained subconfluent at 37°C, 5% CO₂ in rat-tail collagen I (Sigma-Aldrich) coated flasks, in α M5 medium. Cells were used within a maximum of 4 passages after thawing. For mineralized matrix synthesis, MLO-A5 cells were plated at 35 000 cells/cm² on rat-tail collagen I coated 6-well plates in α M5 medium. At confluence, the media was replaced with nucleotide-containing α MEM supplemented with 1% antibiotics, 10% heat-inactivated HyClone FBS, 4 mM β -glycerophosphate and 100 μ g/ml ascorbic acid. This mineralization medium was changed every 2–3 days for 10 days.

D. Development of the protocol for protein extraction from mineralized matrices

Four protein extraction methods were tried on the mineralized matrices produces by MLO-A5 cell line. After 10 days of mineralization in 6-well plates and prior to protein extraction, cells were removed from the mineralized ECM by incubation in PBS containing 20 mM NH₄OH and 0.5% Triton X-100 for 5 min at 37°C. Three wells of the 6-well plate were used for each protocol.

1. Method 1 (M1) is based on the protocol of Xiao *et al.* (Xiao *et al.* 2007). Decellularized ECM were incubated with magnesium-enriched PBS (Sigma-Aldrich, #D8662) containing 1 mg/ml DNase I (Roche Diagnostic, #10104159001) for 30 min at 37°C to remove DNA. After 3 washes in PBS, the matrices were incubated for 30 min at 37°C with mixture of collagenase/dispase (Sigma-Aldrich, #10269638001). The supernatants were pooled, concentrated with centrifugal filter units (Amicon Ultra-2, Sigma Aldrich, #Z740163-24EA) and quantified by absorbance at 280 nm. After addition of 4x NuPAGE LDS buffer (see following method) and of DTT to 50 mM, the sample was heated to 80°C, rapidly cooled on ice and frozen at -80°C until LC-MS/MS analysis.

2. Method 2 (M2) is based on the protocol of Swift *et al.* (Swift *et al.* 2013). After removing DNA as above, cell plate was placed on ice where mineralized matrices were mechanically scraped from wells in the ice-cold PBS containing a protease inhibitors cocktail (Roche Diagnostic, #11836170001). The extracts were pooled and centrifuged at 4000 rpm for 10 min at 4°C. The pellet was suspended in 6 volumes of ice-cold lysis buffer [1x RIPA buffer (50 mM Tris HCl pH8,0; 150 mM NaCl; 1% NP-40; 0.5% DOC (Deoxycholate); 0.1% SDS), 1x NuPAGE LDS buffer (106 mM Tris HCl; 141 mM Tris Base; 2% LDS; 10% Glycerol; 0.51 mM EDTA; 0.22 mM SERVA Blue G250; 0.175 mM Phenol Red, pH 8.5), protease inhibitor cocktail]. After 30 min incubation at 4°C, sample was homogenized by sonication using Bioruptor (Next Gen, Diagenode) for 5 cycles: 20 sec ON / 30 sec OFF. Dithiothreitol (DTT), a reducing agent, was added to 50mM and the sample was heated to 80°C for 10 minutes before ultra-centrifugation at 4°C for 1 hour at 90,000 rpm in a TLA100 rotor (Beckman). The sample was frozen at -80°C until LC-MS/MS analysis.

3. Method 3 (M3) is based on the protocol of Sroga *et al.* (Sroga *et al.* 2011). The matrices were recovered from the well bottoms as in M2, pooled in the pre-weighed tube and centrifuged at 4000 rpm for 10 min at 4°C. The pellet was weighed and suspended in 0.5 ml of the following lysis buffer (5 mM EDTA; 4 M Guanidine hydrochloride; 30 mM Tris-HCl; 15% Glycerol; protease inhibitor cocktail) for every 20 to 50 mg of extract. The suspension was incubated overnight at 4°C in the rotary mixer, then sonicated for 45 cycles at 4°C (15 sec ON / 30 sec OFF) and centrifuged at 4 000 rpm for 10 min at 4°C. The recovered supernatant was dialyzed for 24 h at 4°C against 3 changes of PBS in the MAXI GeBaFlex-tube with 3.5 kDa cut-off membrane (Gene Bio-Application, #D035). Following concentration with centrifugal filter units (Amicon), the extract was quantified by absorbance at 280 nm. After addition of 4x NuPAGE LDS buffer and of DTT to 50 mM, the sample was heated to 80°C, rapidly cooled on ice and frozen at -80°C until LC-MS/MS analysis.

4. Method 4 (M4) is based on the protocol of Prewitz *et al.* (Prewitz *et al.* 2013b) and is similar to M3 in all points, except that a mechanical homogenization step using Ultra-Turrax T8 (IKA-Werke) was added before dialysis.

E. Protein extraction from primary cell-produced mineralized matrix

LB cells derived from *Recql4^{+/-}* and *Recql4^{-/-}* mice were differentiated in 6-well plates for 28 days. The synthesized mineralized ECM were decellularized, and proteins were extracted with Method 3 as described in previous section with one modification: after concentration, the extracts were quantified with Lowry-based detergent-compatible protein assay (Bio-Rad, #5000112). 3 wells per genotype were pooled during extraction. Samples were stored at -80°C in 90 µg aliquots.

F. Sample processing for LC-MS/MS analysis

The same sample preparation protocol was used for the MLO-A5 trial samples and for the extracts of the mineralized matrix produced by primary cells.

After thawing and heating to 80°C for 10 min, 120 µg of each protein extract were shortly electrophoresed by SDS PAGE in 10% polyacrylamide gel to obtain approximately 1 cm-long protein lanes. Gels were stained with SimplyBlue SafeStain (Invitrogen), then washed overnight on the rocking mixer in the MS quality-grade water (Sigma-Aldrich, #1.15333) to eliminate all traces of the detergent. Next, protein-containing lanes were excised, cut into small pieces (~1-2 mm²), transferred to an eppendorf tube and destained with three 15 min washes in 1:1 v/v mixture of ACN (Acetonitrile, Sigma-Aldrich, #1.00029) / 50 mM ABC (Ammonium Bicarbonate, ThermoFisher Scientific, #40867). Protein extracts were incubated for 10 min at 56°C in 25 mM DTT (Sigma-Aldrich, #646563) / 50 mM ABC for reduction. Next, alkylation was carried out by incubating the samples for 10 min at room temperature in the dark in 25 mM IAM (Iodoacetamide, Sigma-Aldrich, #16125) diluted in a 50 mM ABC solution. After two 15 min washes in ACN / 50 mM ABC, the gel pieces were mechanically homogenized in ACN, dried in a speedvac and trypsin digestion was performed overnight at 37°C with Sequencing Grade Modified Trypsin (Promega, #V5111) diluted in 50 mM ABC at enzyme-to-protein ratio 1:40 w/w. The reaction was stopped with formic acid (Fisher, #A117) added to 5% final volume. The peptides were extracted with ACN and centrifuged 5 min at 8 000 rpm. Supernatants were dried in a speedvac, reconstituted in 20 µl of 19% ACN / 76% MS grade water / 5% formic acid to a final concentration of 6 µg/ml and centrifuged 10 min at 14 000 rpm. The resultant supernatants containing extracted peptides mixtures were stored at 4°C until LC-MS/MS analysis.

G. Liquid Chromatography Tandem Mass spectrometry (LC-MS/MS)

Shotgun label-free tandem mass spectrometry was performed by Jean-Marie Guigonis (Bernard Rossi platform, UMR E4320 TIRO-MATOs, CEA / Université Nice-Sophia Antipolis).

The peptides (10 μ L at 6 μ g/ μ l) were analyzed using an ESI-Q Exactive Plus mass spectrometer (ThermoFisher Scientific) incorporating a high-field Orbitrap analyzer and coupled to an Ultimate 3000 RSL Capillary LC System (ThermoFisher Scientific).

For capillary-liquid chromatography, the system was set up for a pre-concentration step using a 300 μ m x 5 mm trap column in back-flush configuration at 40°C (P/N 6720.0315). An EASY-Spray 15 cm x 150 μ m column (P/N ES806) was connected to the system and coupled with an EASY-Spray source (P/N ES081) operating at 40°C.

The flow rate was 2 μ L/min with a 5-45% gradient of solvent B (80% acetonitrile, 20% water, 0.1% formic acid) against solvent A (0.1% formic acid, 100% water) for 180 min.

Full-scan (MS) spectra were obtained from 350 to 1500 m/z with an Automatic Gain Control Target set at 3×10^6 ions and a resolution of 70,000. For each full-scan, the most intense ions (top 15) were fragmented for MS/MS spectrum acquisition. MS/MS scan was initiated at a resolution of 17,500 for ions with potential charge of 2+, 3+ and 4+ with a dynamic exclusion of 20 s. MS/MS were recorded with an Automatic Gain Control Target set at 5×10^4 ions.

H. Protein extraction tests: protein identification and proteomic data analysis from MLO-A5 mineralized matrices

All MS/MS raw data files were analyzed by Proteome Discoverer software 1.4 (ThermoFisher, France) using the Sequest HT search engine against a database of protein sequences (Uniprot version 2015_2). X corr confidence was held higher than 0.7 for all parameters. Precursor mass tolerance was set to 10 ppm and fragment ion tolerance was 0.02 Da. Two missed cleavages were allowed in the trypsin digests. To ensure the reliability of the identified proteins, the Percolator algorithm within the Proteome Discoverer suite calculated the false discovery rate (FDR) using a decoy database search strategy. A 1% target FDR as strict criteria and a 5% target FDR as relaxed criteria were required for peptide validation. At least two peptides were required for protein identification. The strict maximum parsimony principle was imposed, and only peptide spectra with at least medium confidence were considered for protein grouping. Carbamidomethylation on cysteine was set as static modification and oxidized Methionine as dynamic modification.

Cellular compartment enrichment analysis was performed with PANTHER software (Protein Analysis Through Evolutionary Relationships; (Mi *et al.* 2019)) that categorizes proteins using a highly controlled vocabulary (Gene Ontology (GO) terms) and calculates FDR (false discovery rate) that provides evaluation of the enrichment significance. Raw p-values for GO enriched terms were calculated with Fisher's exact test and FDR, with Benjamini-Hochberg correction (Benjamini and Hochberg 1995).

I. Protein identification and differential proteomic analysis by label-free quantitation

The raw data obtained from mass spectrometry analysis were processed in MaxQuant 1.5.5.1 (Cox *et al.* 2014; Tyanova *et al.* 2016). Spectra were searched using the reverted decoy mode of the Andromeda search engine implemented in MaxQuant

against the mouse proteome database downloaded from UniprotKB (The UniProt Consortium 2019) on April 4th 2018 (UP000000589, taxonomy ID 10090, *Mus musculus*) and the MaxQuant embedded database of frequently observed contaminants. MS tolerance was set to 20 ppm. A maximum number of 2 missed cleavages was accepted, and carbamidomethylation of cysteine residues was set as fixed modification, while acetylation of protein N-termini and oxidation of methionine residues were set as variable modifications. False discovery rates (FDR) were set to 1% for peptide spectrum matches (minimum length of 7 amino acids). All other MaxQuant parameters were set as default.

The resulted peptide list with corresponding ion peak intensities values was loaded into ProStaR (Wieczorek *et al.*, 2017) for statistical analysis. Contaminant and reverse proteins were removed and only the proteins with five quantified values (including the values the duplicate runs) in at least one condition (control or mutant) were taken into account. After the peptide peak intensities were normalized by summed intensity of the sample and \log_2 transformed, missing values were imputed by using imp4p algorithm (Gianetto 2019) with 10 iterations. The intensities were assumed to follow beta-distribution, and the upper limit on the values completely absent in one condition was set at 2.5%. Protein abundance value was calculated as a sum of top 4 peptide intensities. Statistical testing of the proteins was conducted using the limma t-test (Ritchie *et al.* 2015) implemented in the ProStaR. Then, p-values were adjusted for multiple testing with the “histo” method (Nettleton *et al.* 2006) to estimate the proportion of true null hypotheses among the set of statistical tests. The proteins with an adjusted p-value inferior to a FDR of 0.01% and with a \log_2 (fold-change) superior to 0,8 (corresponding to the 1.75 fold-change) have been considered as significantly differentially abundant proteins.

GO term enrichment analysis was conducted with online tools Panther (Mi *et al.* 2019), DAVID (The Database for Annotation, Visualization and Integrated Discovery; (Huang *et al.* 2009a)) and Gorilla (Gene Ontology Enrichment Analysis and Visualization Tool; (Eden *et al.* 2009)). In the latter, either differentially abundant proteins were compared separately (over- and under-represented in the *Recq14*^{-/-} ECM) against whole mouse proteome downloaded from UniprotKB on April 4th 2018, or all the identified proteins were presented as a ranked list for analysis (based on the modulus of fold change). Another online software package, IPA (Ingenuity Pathway Analysis (version 0.1-0.7; QIAGEN)) was used to explore affected molecular pathways and networks.

J. Western Blot

Protein samples were denatured at 80°C for 10 min in NuPAGE sample buffer, separated by electrophoresis on a SDS-polyacrylamide gel and electrotransferred to polyvinylidene difluoride membranes (Millipore, #IPVH00010). Blots were blocked for 1 h with Tris-buffered saline (TBS) supplemented with 0,05% Tween 20 (Sigma-Aldrich, #P1379 (TBS-T)), 3% or 5% nonfat milk or 5% BSA (Bovine Serum Albumin, Sigma-Aldrich, #A9647) depending on the primary antibody, and incubated overnight at 4°C with the primary antibodies diluted in blocking solution. Membranes were then washed in TBS-T, incubated for 1 h at room temperature with goat anti-rabbit secondary antibody conjugated to horseradish peroxidase (Santa Cruz Biotechnology, #sc-2004) at 1/20 000 dilution and washed again prior to detection of signal with ECL plus chemiluminescent detection kit (GE Healthcare, #RPN2232). Primary antibodies used in this study were rabbit polyclonal anti-Decorin Ab (Cohesion Biosciences, #CQA1927) at 1/400 in 5% BSA / TBS-T, rabbit polyclonal anti-Pleiotrophin Ab (Boster, #PA1414) at 1/1000 in 5% milk / TBS-T, rabbit polyclonal anti-YB1 Ab (Abcam,

#ab12148) at 1/500 in 3% milk / TBS-T, rabbit polyclonal anti-SLIT3 Ab (Abcam, #ab11018) at 1/500 in 5% milk / TBS-T and rabbit polyclonal anti-HSP90 α Ab (Abcam, #ab2928) at 1/5000 in 5% milk / TBS-T.

K. Quantitative RT-PCR

Total RNA was extracted with Trizol Reagent (Life Technologies, #15596-01) according to the manufacturer's instructions. Reverse transcription (RT) was performed using SuperScript IV reverse transcriptase (Invitrogen, #18090050), 0.5 μ g of RNA and random hexamer primers (Invitrogen, #48190-011). Triplicates of each 10-fold diluted cDNAs were subjected to real-time PCR analysis in an ABI PRISM 7000 system (Applied Biosystems). Reactions were performed in a 20 μ l final volume using 5 μ l of diluted cDNAs and MESA GREEN qPCR Mastermix Plus (Eurogentec, #RT-SY2X-03). Amplification conditions were: 95 $^{\circ}$ C, 2 min followed by (95 $^{\circ}$ C, 15 s, 60 $^{\circ}$ C, 1 min) cycled 40 times. Nucleotide sequences of PCR primers are shown in Table 1. Cycle thresholds (Ct) were obtained graphically (ABI PRISM7000 Sequence Detection System version 1.2.3). Δ Ct values were then calculated by subtracting the Ct value of the endogenous reference gene *Rplp0* (Acidic Ribosomal Phosphoprotein P0). Relative expression was calculated as $2^{-\Delta\Delta Ct}$, $\Delta\Delta Ct$ being the difference between Δ Ct of a target gene at any given point and Δ Ct of the same gene at day 0. Values presented are means \pm standard deviations from 3 experiments (*Ybx1*) or technical triplicate (*Slit3*).

Table 1: Primer sequences

Gene	Accession number	Forward primer	Reverse primer
<i>Rplp0</i>	NM_007475.5	5'-TCCAGGCTTTGGGCATCA-3'	5'-CTTTATCAGCTGCACATCACTCAGA-3'
<i>Slit3</i>	NM_011412.3	5' AGGTCATCGCAACGAAGGTTT 3'	5' CAGTCTCTCCATCGCCTACAC 3'
<i>Ybx1</i>	NM_011732.2	5' GAAGTGATGGAGGGTGCTGAC 3'	5' GATACCGACGTTGAGGTGGC 3'

3. Results and Discussion

A. Development of the extracellular matrix protein-enriched extraction protocol

Starting with the isolation of primary murine long bone (LB) cells, the process of mineralized matrices synthesis *in vitro* takes approximately 40-45 days, depending on the length of the cell amplification stage. As this process is much shorter, we have developed the protein extraction protocol by using mineralized ECM generated by a cell line. First, the mineralized ECM produced by the murine pre-osteocyte MLO-A5 and by the human osteosarcoma SAOS-2 cell lines were examined by SEM and compared with ECM synthesized by the primary LB cells (Figure 1). SAOS-2 cells produced very thin matrices with globular mineralization nodules dispersed over the matrix surface, either separately (two protruding spheres in the Figure 1c), or in clusters. MLO-A5 cells synthesize multilayered ECM (Figure 1b) with mineralization often hidden between layers. The structural aspects and the thickness of MLO-A5 matrices are more reminiscent to the ECM generated by primary cells (Figure 1a). Therefore, the ECM protein extraction protocols were assayed on MLO-A5 matrices.

Protein extraction from the mineralized ECM presents several particular difficulties. First, many bone proteins are tightly bound to the hydroxyapatite, therefore, the mineralized ECM has to be demineralized to release them. Moreover, this association with mineral is thought to protect proteins against enzymatic digestion (Collins *et al.* 2002), a step necessary for mass-spectroscopic analysis. Second, several of the bone proteins are large fibrous cross-linked or highly glycosylated molecules (collagens and proteoglycans respectively) which poses solubility problems during extraction and analysis. Third, collagen I is so abundant in the organic ECM synthesized by osteoblasts, that it could mask other proteins during analysis.

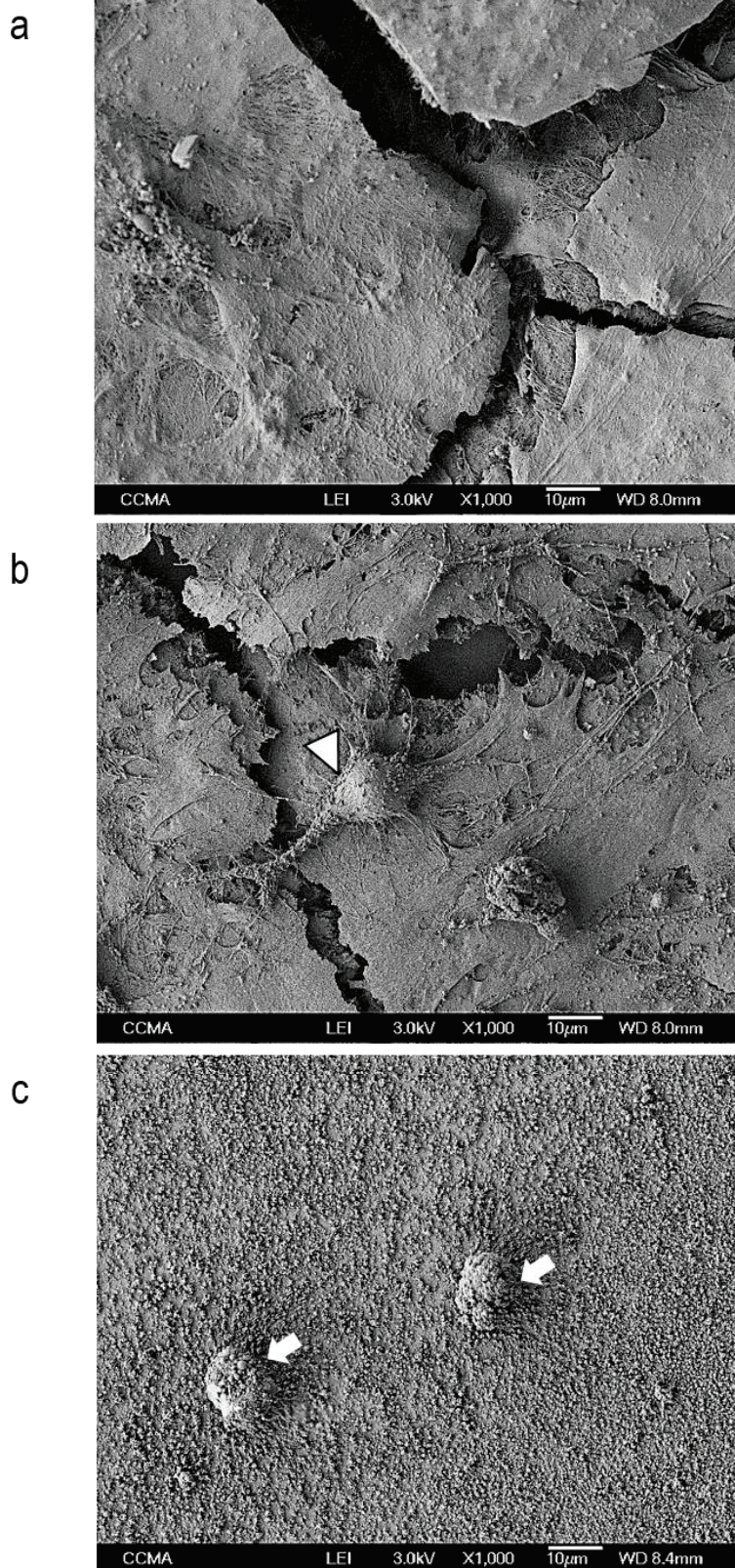


Figure 1: Scanning electron micrographs of the mineralized ECM. ECM was synthesized *in vitro* by (a) primary mouse long bone cells; (b) pre-osteocyte MLO-A5 murine cell line, white arrowhead indicates a cell; and (c) the SAOS-2 human osteosarcoma cell line, white arrows indicate mineralization nodules. Acquisition was done at x1000 magnification, scale bar corresponds to 10 µm.

Therefore, in order to make our future ECM composition analysis as complete as possible, we have tested four extraction protocols, each of them applied to the mineralized matrices either with cells or decellularized. The goal was to determine which method produced an extract containing the highest number of the extracellular matrix proteins.

Method 1 (M1), based on the protein extraction protocol of Xiao *et al.* (Xiao *et al.* 2007), uses a mixture of two extracellular matrix digesting enzymes – collagenase, that cleaves collagen I, and dispase, that cleaves fibronectin and collagen IV (Stenn *et al.* 1989). These proteases are supposed to release most of the ECM proteins in the medium, while leaving intact cells attached to the culture dishes. Additional advantage of this protocol is its brevity. Only two steps are necessary to complete the extraction: (1) 30-minutes incubation with enzymes and (2) 2-hours concentration of the extracts. Moreover, with this method, large molecules, such as fibronectin and collagen, are cleaved and solubilized in the first step of the protocol, avoiding future problems. This method interested us since the authors have successfully applied it to extract both ECM proteins and matrix vesicles from the mineralized matrix synthesized by MC3T3-E1 osteoblast-like cells – a workflow similar to the one we had in mind in our project.

Method 2 (M2), the extraction in RIPA-NuPAGE / LDC buffer, was adapted from Swift *et al.* (Swift *et al.* 2013). The slightly alkaline pH (8.5) of this buffer allows a higher reactivity of the usual reducing agents (*e.g.* DTT or β -mercaptoethanol) and therefore a more complete reduction of disulfide bonds (Lukesh *et al.* 2012). LDS (Lithium dodecyl sulfate) detergent that this buffer contains not only has a better solubility below room temperature than SDS (sodium dodecyl sulfate), but also permits to heat the sample at lower temperature (80°C instead of 95°C), which limits oxidation. Authors applied this protocol to a whole range of mouse tissues, including bone, in the project

exploring the relationship between matrix stiffness and the direction of stem cell differentiation. Since our results from atomic force microscopy revealed a difference between organic part of the *Recq14^{+/-}* and *Recq14^{-/-}* matrices (see submitted manuscript), we wanted to test this extraction method on the mineralized matrices produced *in vitro*.

The third method (M3), is adapted from the protocol of Sroga *et al.* (Sroga *et al.* 2011) and is based on several classical methods of protein extraction from bone (Termine *et al.* 1981; Wendel *et al.* 1998). The authors applied this protocol to very thin bone slices, which implies that the amount of extractable proteins was low, a situation similar to the *in vitro* produced mineralized matrices. This method employs EDTA (ethylenediaminetetraacetic acid) for demineralization, GuHCl (Guanidine Hydrochloride) for protein extraction, and dialysis for desalting. EDTA chelates calcium, removing it from the mineral and thereby releasing the phosphate into solution, which results in demineralization. GuHCl is a chaotropic agent that weakens hydrophobic interaction of the molecules, thus unwinding and solubilizing them (Greene and Pace 1974).

The last method (M4), based on the protocol of Prewitz *et al.* (Prewitz *et al.* 2013b), is the same as M3 with addition of mechanical homogenization before dialysis. In their project, the authors used proteomics to analyze protein composition of the anchored decellularized ECM synthesized *in vitro* in 10-day period by human marrow stromal cells undergoing osteogenic differentiation. On our part, we wanted to determine if adding mechanical homogenization to the protocol augment the number of identified ECM proteins.

All protocols were applied both to the whole cellular layers (indicated by “ ϕ ” next to the protocol number) and to the decellularized matrices (indicated by “de ϕ ”).

Protocols M1 and M2 took one day to complete; M3 and M4, three days. Methods M3 and M4 produced extracts that were viscous and cloudy, particularly these that were obtained from the samples containing cells. Given the incubation of the decellularized matrices with DNase I and 45 cycles of sonication, this effect is most likely due to the aggregates of undissolved fibrous molecules, particularly collagen. The final homogenization step in the M4 extraction engendered some loss of the sample due to the difficulty of transferring resultant foamy material. Processing of the extracts for the mass spectrometry was identical for all methods, and included in-gel reduction, alkylation and trypsin digestion. A total of 8 extracts were analyzed by LC-MS/MS.

The proteins were identified with Sequest HT search engine (Eng *et al.* 1994) implemented in Proteome Discoverer software (ThermoFisher, France). The lists of all the identified proteins can be found in Appendix 1.

The highest total number of identified proteins was obtained with M2 ϕ (2466), followed by M2 de ϕ (2130), and the lowest number, with M1 ϕ (759) and M1 de ϕ (1194) (Table 2). M3 and M4 gave intermediate numbers: 1969 for M4 de ϕ , 1834 for M3 de ϕ , 1510 for M3 ϕ and 1477 for M4 ϕ . For various reasons, these numbers are difficult to compare with what was obtained by the authors of protocols that we have adapted. Indeed, Swift *et al.* (M2) do not give the total number of proteins identified (Swift *et al.* 2013). Sroga *et al.* (M3) used a different mass spectrometry method, the MALDI-TOF/TOF, which is known to identify less proteins. Moreover, these authors do not specify the total number of proteins either, since they were interested in a limited number of specific bone proteins to the exclusion of all the others (Sroga *et al.* 2011). The authors of M4 (Prewitz *et al.* 2013b) did use the same MS/MS analysis as us, and identified 500 proteins, a lower number that we did, but after only 10 days of human MSC culture they probably had to work with less material than we did. Regarding the

M1 method (Xiao *et al.* 2007), authors employed the same type of MS/MS analysis as us and identified 1327 proteins, 1.75 times more than we did (759). On the other hand, they separated the extracts by SDS-PAGE and analyzed each of the 24 bands separately. This approach always gives a higher number of identifications, but it is considerably more time-consuming. The lowest number of the proteins in M1 ϕ is not surprising. It could be explained by the fact that without demineralization many proteins were protected from enzymatic digestion (Collins *et al.* 2002). The increase of the identified protein number after decellularization in M1de ϕ suggests that either enzymes got access to the proteins not previously accessible because of the cell layer, or that decellularization resulted in the release of intracellular proteins that were not removed in consequent washes, got attached to the matrix and were thus incorporated in the extract.

However, what interested us most was not the total number of identified proteins but specifically the number of the extracellular matrix proteins.

The lists of identified proteins were analyzed online with Panther (Mi *et al.* 2019). This is a software that categorizes proteins using a highly controlled vocabulary (Gene Ontology (GO) terms assigned to each protein in GO database (Ashburner *et al.* 2000; The Gene Ontology Consortium 2019)), compares input list (*i.e.* our identified proteins) to a reference list (*e.g.* total mouse proteome) and calculates GO term enrichment and FDR (false discovery rate). We have used “Cellular component” over-representation analysis, looking for the enrichment of the GO term “Extracellular Matrix”.

Over-representation analysis answers the following question: can a given term be found statistically more (or less) often in the input list, than expected by chance? For example, mouse reference proteome contains 22296 entries (The UniProt Consortium 2019), with 475 entries (interchangeably genes or proteins) assigned the

GO term “Extracellular Matrix” (The Gene Ontology Consortium 2019). Based on this, 2.13% (475 divided by 22296) of the genes in the reference list encode for ECM proteins. When we upload a list of, for example, 759 genes (the number of proteins identified with M1 ϕ), 16 genes in that list (2.13% of 759) are expected to belong to ECM. If, instead, our list has 67 genes that were assigned this term, the ECM category in the input list is enriched 4.1 times (67 divided by 16).

Next, a raw p-value, that represents a probability of observing such enrichment by pure chance, is calculated for each GO term. However, raw p-value (e.g. $p < 0,01$) implies that there is still a chance (though less than 1%) that the observation was in fact due to randomness. When multiple p-values are calculated during the same analysis, the chance of reporting at least one false positive increases quickly. When this is done thousands of times (like when comparing the input gene list to all “Cellular Component” GO terms), we are virtually guaranteed to have some terms that appear to be significant just by chance. Therefore, some multiple comparison correction must be applied. The FDR (False Discovery Rate) is the expected proportion of true null hypotheses rejected out of the total number of null hypotheses rejected. In other terms, it is the expected proportion of false positive results. Developed by Benjamini and Hochberg (Benjamini and Hochberg 1995), FDR correction implemented in Panther guarantees that the proportion of false positive tests will be smaller than the chosen significance threshold. FDR is not applied to genes (or proteins) belonging to each enriched term, but to the GO term itself.

The results of the “Extracellular Matrix” GO term enrichment analysis applied to the proteins identified with all extraction methods are summarized in Table 2.

Table 2: ECM enrichment of the proteins identified with each extraction protocol. Extracts from the samples with cells are marked in yellow, and decellularized are in blue. False Discovery Rate.

Method	Nb identified proteins	Nb ECM proteins	ECM protein Enrichment	FDR-corrected p-value
M1 with ϕ	759	67	4,1	2,5E-18
M1 decellul.	1194	67	2,59	8,4E-10
M2 with ϕ	2466	75	1,43	2,4E-02
M2 decellul.	2130	90	1,98	3,7E-07
M3 with ϕ	1510	49	1,52	4,0E-02
M3 decellul.	1834	88	2,24	2,0E-09
M4 with ϕ	1969	70	1,67	9,8E-04
M4 decellul.	1477	82	2,59	1,3E-11

Method 1 (M1) collagenase/ dispase
Method 2 (M2) RIPA/ NuPAGE
Method 3 (M3) EDTA/ Guanidine Chloride
Method 4 (M4) EDTA/ Guanidine Chloride with Ultra-Turrax T8 grinding

Consistently, the number of ECM proteins was greater or equal in the decellularized samples of the same extraction protocol, even when the total number of proteins was higher in the samples with cells. The latter case is illustrated by M2 (ECM proteins 90 de ϕ versus 75 ϕ , compared to the total proteins 2130 de ϕ versus 2466 ϕ) and M4 (ECM proteins 82 de ϕ versus 70 ϕ , compared to the total proteins 1477 de ϕ versus 1969 ϕ). Thus, with the exception of M1, the decellularization allows to identify more ECM proteins, probably because they are not obscured to the same degree by the highly expressed cellular proteins. However, the fold change values for the ECM enrichment, even in the protocols with decellularization, are rather low: 1.98 for M2, 2.24 for M3 and 2.59 for M1 and M4. These values indicate that we still have many non-matrix proteins in our extracts. These proteins could be due, as I have mentioned before, to the "contamination" with cellular proteins released during decellularization, or/and some of them could be actually present in the extracellular space. For example, Xiao *et al.* (Xiao *et al.* 2007) discovered many membrane and cytoskeletal proteins, as well as some cytoplasmic enzymes in the extracellular matrix vesicles. We can suppose that similar matrix vesicles are present in our extracts. Nevertheless, the ECM

enrichment in methods with decellularization is real, as indicated by the highly significant FDR-corrected p-values, ranging from 1.3×10^{-11} in M4, through 8.4×10^{-10} in M1 and 2×10^{-9} in M3 to 3.7×10^{-7} in M2.

M1 resulted in the highest enrichment (4.1 for M1 ϕ and 2.59 for M1 de ϕ), but the lowest matrix protein number (67), either when extracted with cells or after decellularization. This relatively high ECM enrichment could be attributed to the targeted action of the enzymes (collagenase and dispase) during extraction, which allowed to obtain high a proportion of ECM proteins in the otherwise shortest list of proteins. Nevertheless, these enzymes were probably hindered in their action by the hydroxyapatite, which would explain the lowest absolute number of the matrix proteins extracted with this method. While M4 de ϕ method achieved an ECM protein enrichment of 2.59, it only led to the identification of 82 ECM proteins, probably due to the considerable loss of material during the extraction process. Thus, M1 and M4 were not chosen as extraction methods, despite their higher enrichment rate, due to the low absolute number of ECM proteins extracted by these two methods and also due, in the case of M4, to the rather laborious extraction process which did not seem to provide any advantage.

The highest number of ECM proteins was obtained with M2 (90), followed very closely by M3 (88). However, M2 resulted in the lower ECM enrichment than M3 (1.98 versus 2.24), suggesting that the demineralization step prior to extraction contributes to increase the proportion of matrix-specific proteins in the extract. Based on this observation and almost equal numbers of ECM proteins extracted with M2 and M3, we have chosen M3 as the extraction method.

B. Quantitative Label-free proteomic analysis of bone extracellular matrix produced by RECQL4-deficient osteoblasts

Protein extracts for the proteomic analysis were prepared from the decellularized mineralized ECMs produced *in vitro* by the osteoblasts derived from long bones of either homozygous (ECM mut) or heterozygous (ECM ctr) RECQL4-deficient mice (Figure 2). Six independent experiments were performed over a period of more than two years because of the cell culture time required to obtain mineralized

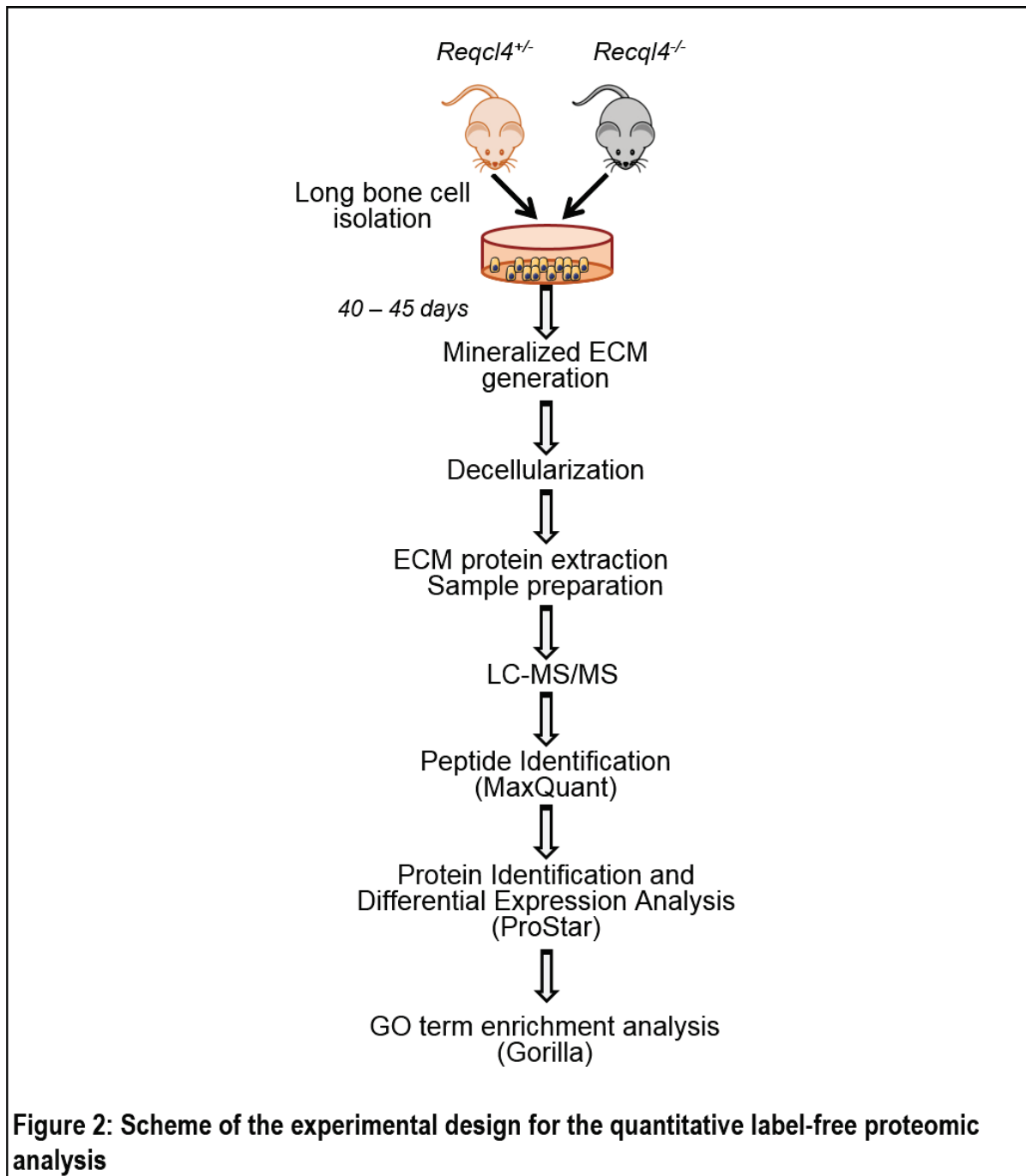


Figure 2: Scheme of the experimental design for the quantitative label-free proteomic analysis

extracellular matrix. In each experiment, in order to reduce the potential effect of inter-individual variation and to obtain a sufficient number of primary cells, osteoblasts from three to four elderly mice (approximately 60 weeks) were grouped by genotype. While we conducted 6 independent experiments, only 5 mutant extracts for 6 control extracts were analyzed due to the loss of a mutant matrix extract. Each extract was subjected twice to MS/MS analysis.

In every MS/MS run, more than 57 000 fragmentation spectra were acquired. To consolidate the data for further analysis, RAW files from all MS/MS runs (containing the unprocessed output of the mass spectrometer) were downloaded to the MaxQuant proteomic search engine (Cox *et al.* 2014; Tyanova *et al.* 2016), which combined and analyzed them, matching 11 549 spectra to peptides. Using MaxQuant confers two advantages. First, contrary to Sequest HT (Eng *et al.* 1994), it assigns the same unique peptide identifier throughout the experimental series, a condition necessary for the subsequent statistical treatment with other tools. Second, it can increase the number of peptide identifications: in the case where a peptide had been identified by MS/MS in some runs but not in others, MaxQuant can “look back” at the corresponding LC-MS data and perform a “match between runs” based on the LC retention time and MS mass/charge ratio, resulting in the addition of the missing peptide identification if the match is found.

MaxQuant’s results were uploaded online to the ProStaR (Wieczorek *et al.* 2017) proteomic analysis software, which has proven its performance in the statistical analysis applied to proteomic data (Stratton *et al.* 2019). ProStaR identified 1363 proteins (Appendix 2), performed their relative quantification and associated statistical evaluation. The totality of identified proteins was subjected to GO term enrichment analysis with Gorilla online tool (Eden *et al.* 2009), which, unlike Panther, is specialized

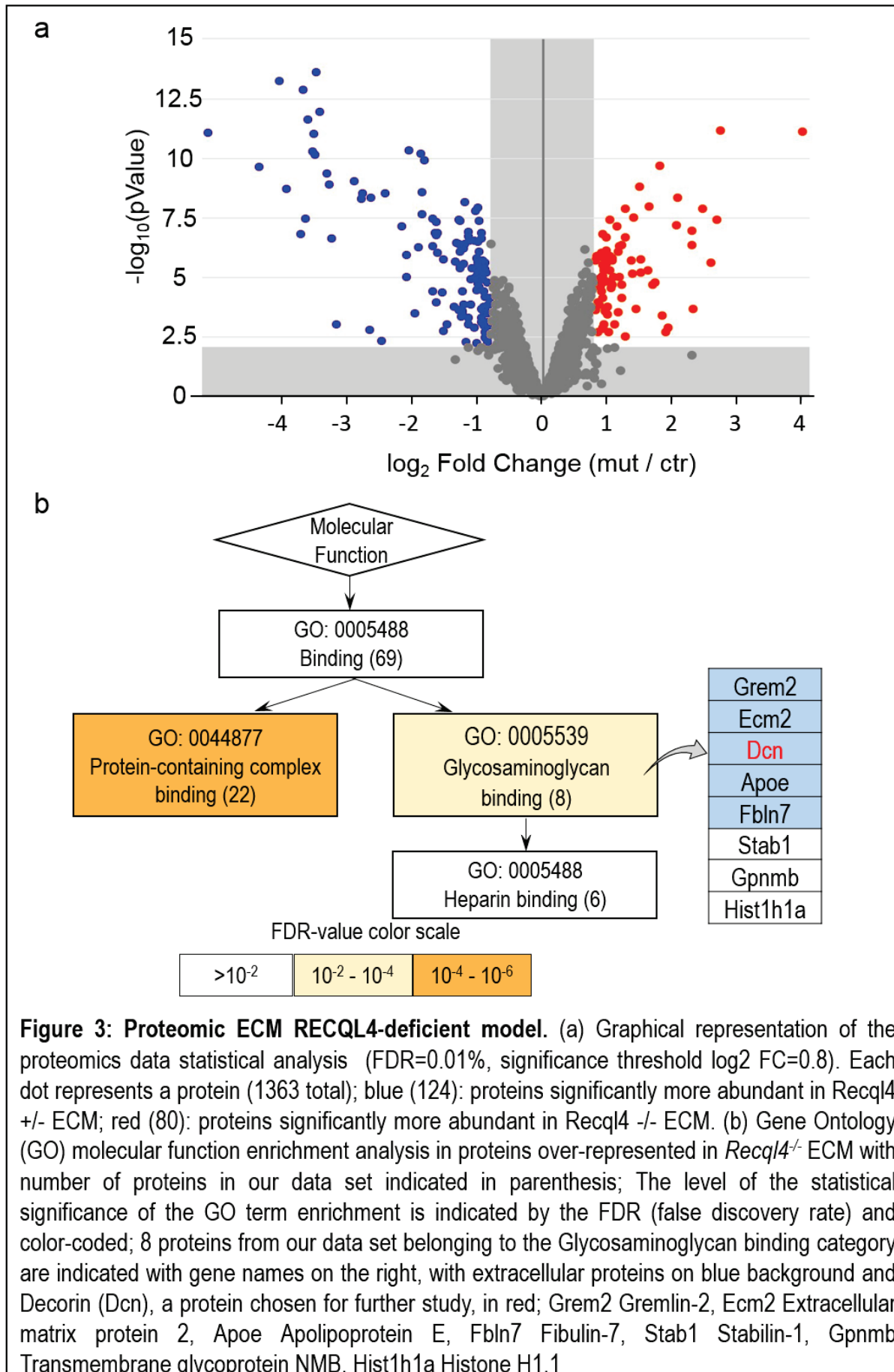
in the analysis of ranked lists. The results (Table 3) show that the term “extracellular region” was enriched 2.6 times in our data set (224 proteins or ~17% of the list), while the term “ECM” was enriched more than 5-fold (124 proteins).

The most enriched category of the analysis, the “Myelin sheath”, that contains 88 proteins, is a surprising result. The explanation could be in the fact that GO assigns multiple terms to the same gene. For example, if we analyze the list of proteins in “Myelin sheath” category with Panther, we’ll find that 13 of them are also classified as cytoskeletal proteins, 7 as chaperons and 4, including three ATPase subunits, as anion channels. Besides, 14 other proteins have oxydoreductase activity and another 17, hydrolase activity. Another possible explanation is that all these proteins were found to be present in myelin membranes by one proteomic study (Werner *et al.* 2007), that is referenced in GO. However, these 88 proteins are not oligodendrocyte cell-specific, and therefore could be found in or secreted by other cells types, including osteoblasts.

Table 3: Cellular Component Enrichment. All MS/MS identified proteins were analyzed with Gorilla online tool for cellular component enrichment. This table represents an excerpt of the total analysis showing 10 most significantly enriched categories. The level of the statistical significance of the Gene Ontology (GO) term enrichment is indicated by the FDR (false discovery rate). Categories containing extracellular proteins are highlighted in red.

GO term	Description	Enrichment	FDR q-value	Nb proteins in the target dataset
GO:0043209	myelin sheath	10	1,42E-63	88
GO:0062023	collagen-containing extracellular matrix	6,46	6,62E-55	107
GO:0044445	cytosolic part	6,35	5,06E-37	74
GO:0031012	extracellular matrix	5,69	5,17E-57	124
GO:1990904	ribonucleoprotein complex	3,44	2,20E-34	130
GO:0044421	extracellular region part	2,62	1,94E-41	224
GO:0005615	extracellular space	2,47	2,14E-28	176
GO:0005739	mitochondrion	2,41	1,04E-29	191
GO:0032991	protein-containing complex	2,03	7,20E-68	487
GO:0044444	cytoplasmic part	1,75	1,45E-81	664

More importantly, ProStaR analysis revealed 80 significantly over- and 124 significantly under-represented proteins in the *Recq4*^{-/-} ECM (Figure 3a, Tables 4 and



5 respectively). These lists include 25 and 32 extracellular proteins respectively in over- and under-represented categories (shown on the blue background in Tables 4 and 5). The proteins were considered to be significantly differentially abundant if they had a fold change of over 1.75 or under 0.57 with FDR set to 0.001.

Table 4: Proteins over-represented in *Recq14*^{-/-} ECM. The proteins chosen for further analysis are highlighted in red, blue background indicates extracellular proteins.

UniProt accession	Gene name	Protein names	log ₂ FC mut vs ctr	FC mut vs ctr	p-value mut vs ctr
Q9CQS8	Sec61b	Protein transport protein Sec61 subunit beta	4,02	16,24	7,48E-12
P26339	Chga	Chromogranin-A	2,74	6,68	7,18E-12
D3YYC2	Drap1	Dr1-associated corepressor	2,69	6,46	3,83E-08
Q9DCS9	Ndufb10	NADH dehydrogenase [ubiquinone] 1 beta subcomplex subunit 10	2,60	6,05	2,52E-06
O88273	Grem2	Gremlin-2	2,48	5,56	1,34E-08
O88952	Lin7c	Protein lin-7 homolog C	2,32	5,00	2,15E-04
Q92511	Atad3	ATPase family AAA domain-containing protein 3	2,31	4,95	1,13E-07
G3X973	Stab1	Stabilin-1	2,31	4,95	4,32E-07
Q3UGC7	Eif3j1	Eukaryotic translation initiation factor 3 subunit J-A	2,10	4,27	4,65E-09
E9Q7T7	Chadl	Chondroadherin-like protein	2,07	4,19	6,63E-08
P17095	Hmga1	High mobility group protein HMG-I/HMG-Y	1,94	3,84	1,30E-03
O09164	Sod3	Extracellular superoxide dismutase [Cu-Zn]	1,91	3,76	2,17E-03
Q6NSP9	Hmga2	High mobility group protein HMGI-C	1,86	3,63	4,08E-04
P62960	Ybx1	Y-box-binding protein 1	1,81	3,52	2,21E-10
Q3TW96	Uap111	UDP-N-acetylhexosamine pyrophosphorylase-like protein 1	1,74	3,33	1,63E-05
P51942	Matn1	Cartilage matrix protein	1,71	3,27	2,13E-05
Q3UDC3	Tom1	Target of Myb protein 1	1,64	3,12	1,05E-08
A0A0G2JG59	Nexn	Nexilin	1,63	3,09	5,06E-06
G3UXY9	Enpp2	Ectonucleotide pyrophosphatase/phosphodiesterase family member 2	1,53	2,88	1,80E-06
P12787	Cox5a	Cytochrome c oxidase subunit 5A, mitochondrial	1,51	2,85	6,83E-06
E9QQ18	Prg4	Proteoglycan 4;Proteoglycan 4 C-terminal part	1,50	2,84	1,62E-09
Q3U0V1	Khsrp	KH-Type Splicing Regulatory Protein	1,44	2,72	2,18E-04
Q9ERD7	Tubb6	Tubulin beta-6 chain	1,42	2,67	3,17E-08
P97379-2	G3bp2	Ras GTPase-activating protein-binding protein 2 isoform 2	1,38	2,61	6,97E-06
Q8C0E2	Vps26b	Vacuolar protein sorting-associated protein 26B	1,38	2,60	1,98E-06
P70699	Gaa	Lysosomal alpha-glucosidase	1,29	2,44	1,42E-08
P12382	Pfkl	ATP-dependent 6-phosphofructokinase, liver type	1,28	2,43	2,08E-07

Results: part 1-2 – Matrix characterization

UniProt accession	Gene name	Protein names	log ₂ FC mut vs ctr	FC mut vs ctr	p-value mut vs ctr
Q8BVA0	Gpmb	Transmembrane glycoprotein NMB	1,28	2,42	3,13E-03
Q9D8B3	Chmp4b	Charged multivesicular body protein 4b	1,23	2,35	4,69E-07
P51655	Gpc4	Glypican-4	1,23	2,35	2,11E-05
Q8R2K3	Ssbp1	Single-stranded DNA-binding protein	1,23	2,34	7,95E-05
Q8BVY0	Rsl1d1	Ribosomal L1 domain-containing protein 1	1,19	2,29	9,84E-06
Q02248	Ctnnb1	Catenin beta-1	1,19	2,28	4,92E-07
Q6PB66	Lrpprc	Leucine-rich PPR motif-containing protein, mitochondrial	1,17	2,25	3,10E-04
P09535	Igf2	Insulin-like growth factor II	1,17	2,25	8,85E-07
P17809	Slc2a1	Solute carrier family 2, facilitated glucose transporter member 1	1,16	2,23	7,28E-08
G3UZX6	Sumo3	Small ubiquitin-related modifier 3	1,11	2,16	9,71E-04
Q920A5	Scpep1	Retinoid-inducible serine carboxypeptidase	1,10	2,15	1,02E-05
P26040	Ezr	Ezrin	1,09	2,13	2,21E-05
Q8CG19-3	Ltbp1	Latent-transforming growth factor beta-binding protein 1 isoform 3	1,07	2,11	2,10E-06
Q07079	Igfbp5	Insulin-like growth factor-binding protein 5	1,07	2,10	1,57E-06
Q9D6J6	Ndufv2	NADH dehydrogenase [ubiquinone] flavoprotein 2, mitochondrial	1,06	2,09	2,84E-05
A0A0U1RPJ7	1110004F10Rik	Small acidic protein	1,05	2,07	1,33E-06
F6Q3W0	Wdr5	WD repeat-containing protein 5	1,04	2,05	3,86E-08
E9PYG9	Samhd1	Deoxynucleoside triphosphate triphosphohydrolase SAMHD1	1,04	2,05	5,20E-06
O88322	Nid2	Nidogen-2	1,03	2,04	1,77E-06
P43275	Hist1h1a	Histone H1.1	1,02	2,03	2,10E-03
Q5FW85	Ecm2	Extracellular matrix protein 2	1,01	2,02	1,78E-04
Q91YW3	Dnajc3	DnaJ homolog subfamily C member 3	1,01	2,01	2,31E-06
Q61711	Ibsp	Bone sialoprotein 2	1,00	2,00	3,81E-04
P26645	Marcks	Myristoylated alanine-rich C-kinase substrate	1,00	2,00	1,59E-05
A2ARA0	Tfpi	Tissue factor pathway inhibitor	0,99	1,98	2,66E-06
Q8BVF2	Pdcl3	Phosducin-like protein 3	0,98	1,97	2,19E-07
Q6ZWX6	Eif2s1	Eukaryotic translation initiation factor 2 subunit 1	0,98	1,97	7,61E-07
F6ZCF0	Agtpbp1	Cytosolic carboxypeptidase 1	0,97	1,96	2,22E-04
P30681	Hmgb2	High mobility group protein B2	0,97	1,96	2,81E-04
P16460	Ass1	Argininosuccinate synthase	0,95	1,94	5,32E-06
H3BKH6	Esd	S-formylglutathione hydrolase	0,95	1,93	1,70E-06
Q9CR51	Atp6v1g1	V-type proton ATPase subunit G 1	0,95	1,93	9,39E-04
P28654	Dcn	Decorin	0,95	1,93	4,13E-06
F8WIR1	Ctsd	Cathepsin D	0,94	1,92	3,17E-06

UniProt accession	Gene name	Protein names	log ₂ FC mut vs ctr	FC mut vs ctr	p-value mut vs ctr
P21278	Gna11	Guanine nucleotide-binding protein subunit alpha-11	0,94	1,91	1,45E-03
E9Q600	Loxl4	Lysyl oxidase homolog 4	0,94	1,91	1,65E-07
P48771	Cox7a2	Cytochrome c oxidase subunit 7A2, mitochondrial	0,93	1,91	1,41E-03
Q6ZWZ2	Ube2r2	Ubiquitin-conjugating enzyme E2 R2	0,93	1,90	7,21E-05
A0A1L1SV25	Actn4	Alpha-actinin-4	0,93	1,90	9,38E-06
P08226	Apoe	Apolipoprotein E	0,92	1,89	9,74E-07
Q3TCN2	Plbd2	Putative phospholipase B-like 2	0,91	1,88	1,88E-05
Q921L6	Ctnn	Src substrate cortactin	0,91	1,88	4,08E-05
Q791V5	Mtch2	Mitochondrial carrier homolog 2	0,90	1,86	2,54E-05
Q501P1	Fbln7	Fibulin-7	0,89	1,85	1,06E-05
S4R1W1	Gm3839	Glyceraldehyde-3-phosphate dehydrogenase	0,88	1,84	1,50E-04
Q9JM58	Crif1	Cytokine receptor-like factor 1	0,87	1,82	2,01E-03
P11688	Itga5	Integrin alpha-5	0,86	1,82	1,14E-04
Q91VK1	Bzw2	Basic leucine zipper and W2 domain-containing protein 2	0,83	1,78	1,27E-06
Q9R0N0	Galk1	Galactokinase	0,82	1,77	2,34E-05
S4R2M6	Rbm3	RNA-binding protein 3	0,82	1,76	2,43E-04
Q8BGD9	Eif4b	Eukaryotic translation initiation factor 4B	0,82	1,76	2,08E-06
P39876	Timp3	Metalloproteinase inhibitor 3	0,81	1,76	1,62E-05
P80314	Cct2	T-complex protein 1 subunit beta	0,81	1,75	1,75E-05

Similar to our test proteomics results, the list of the over-represented proteins in *Recq14*^{-/-} ECM contains several cytoskeletal proteins (α actinin 4, tubulin β 6 chain, nexilin), the integrin α -5 receptor and the Enpp2 (Ectonucleotide pyrophosphatase / phosphodiesterase family member 2) phosphatase, which were seen previously in the matrix vesicles isolated from femurs of chicken embryo (Balcerzak *et al.* 2008). Accumulation of the Enpp2 (Fold Change 2.9) is very interesting, because it produces the pyrophosphate (PP_i), an inhibitor of mineralization (Orriss *et al.* 2016). The build-up of extracellular PP_i could account for the lower mineralization that we have observed in *Recq14*^{-/-} ECM in this study.

Also over-represented in mutant ECM are 10 proteins found in stress granules, including the stress granule nucleator G3BP1 (FC 2.6), an endonuclease (Tourrière *et al.* 2003; Kedersha *et al.* 2016) and YB1 (FC 3.5), a multifunctional nucleic acid-binding

protein that activates G3BP1 translation under stress conditions (Somasekharan *et al.* 2015), two proteins necessary for stress granule genesis. The other 8 proteins (Rsl1d1, Rbm3, Hmga1, Khshp, Eif2s1, Nexn, Eif4b, Atp6v1g1) have been identified in stress granules in proteomic studies (Jain *et al.* 2016; Markmiller *et al.* 2018) but have not yet been assigned any particular role in their formation or function. This result is intriguing, since, to the best of my knowledge, nobody has yet demonstrated that stress granules could be secreted in the extracellular space, although YB1 itself has been shown to accumulate in stress granules before being secreted under oxidative stress conditions (Guarino *et al.* 2018).

Another very interesting result is the over-representation in the mutant matrix of lysyl oxidase Loxl4 (FC 1.9). We have determined that the organic part of the ECM is stiffer *Recql4*^{-/-} than control in control matrices. Loxl4 initiates the collagen cross-link formation (Trackman 2016). Its over-expression in the mutant ECM could result in greater number of cross-links and thereby stiffer matrix.

Finally, some other proteins over-represented in mutant ECM are worth mentioning: LTBP1 (Latent-transforming growth factor beta-binding protein, FC 2.1) and BSP (Bone Sialoprotein, FC 2.0).

LTBP1 controls the availability of TGF- β in the bone matrix (Dallas *et al.* 2000), a cytokine playing important role in bone remodeling coupling (Wu *et al.* 2016). However, the significance of LTBP1 overexpression in bone is not clear yet (Robertson *et al.* 2015).

Although BSP is considered to be a pro-mineralization molecule, since it promotes hydroxyapatite nucleation, as well as the differentiation and the activity of the osteoblasts and the osteoclasts (Bouleftour *et al.* 2016), its constitutive overexpression in the mouse led to osteopenic phenotype due to the uncoupling of

bone formation and resorption (Valverde *et al.* 2008). It is possible therefore, that the beneficial effect BSP has on bone metabolism is a matter of correct dose.

Table 5: Proteins under-represented in *Recql4*^{-/-} ECM. The proteins chosen for further analysis are highlighted in red, blue background indicates extracellular proteins.

UniProt accession	Gene name	Protein names	log ₂ FC mut vs ctr	FC mut vs ctr	p-value mut vs ctr
A0A0R4J227	Mark2	Serine/threonine-protein kinase MARK2	-5,16	0,03	8,52E-12
P00688	Amy2	Pancreatic alpha-amylase	-4,37	0,05	2,43E-10
Q3UMR5	Mcu	Calcium uniporter protein, mitochondrial	-4,05	0,06	5,98E-14
D3Z041	Acl1	Long-chain-fatty-acid-CoA ligase 1	-3,94	0,07	1,99E-09
A0A0U1RNJ1	Fasn	Fatty acid synthase	-3,72	0,08	1,48E-07
P55288	Cdh11	Cadherin-11	-3,69	0,08	1,32E-13
Q9CPP6	Ndufa5	NADH dehydrogenase [ubiquinone] 1 alpha subcomplex subunit 5	-3,65	0,08	3,41E-08
Q7TPZ8	Cpa1	Carboxypeptidase A1	-3,60	0,08	2,44E-12
Q6PE70	Itgb5	Integrin beta-5	-3,54	0,09	5,38E-11
Q9R1P1	Psmb3	Proteasome subunit beta type-3	-3,53	0,09	9,66E-12
Q6PE80	Axl	Tyrosine-protein kinase receptor UFO	-3,51	0,09	7,37E-11
Q9JLI2	Col5a3	Collagen alpha-3 (V) chain	-3,48	0,09	2,35E-14
A0A140LHQ8	Picalm	Phosphatidylinositol-binding clathrin assembly protein	-3,43	0,09	1,11E-12
P40240	Cd9	CD9 antigen	-3,32	0,10	4,65E-10
Q7TNC4-2	Luc7l2	Putative RNA-binding protein Luc7-like 2 isoform 2	-3,28	0,10	1,32E-09
Q99L13	Hibadh	3-hydroxyisobutyrate dehydrogenase, mitochondrial	-3,25	0,10	2,44E-07
P11404	Fabp3	Fatty acid-binding protein, heart	-3,16	0,11	9,68E-04
Q3TYS2	Cybc1	Uncharacterized protein C17orf62 homolog	-2,89	0,13	9,04E-10
Q61425	Hadh	Hydroxyacyl-coenzyme A dehydrogenase, mitochondrial	-2,79	0,14	4,94E-09
P62071	Rras2	Ras-related protein R-Ras2	-2,77	0,15	3,16E-09
A2A4N9	Dhx8	ATP-dependent RNA helicase DHX8	-2,66	0,16	1,73E-03
E9PYT3	Ati3	Atlantin-3	-2,63	0,16	4,75E-09
Q91WH7	Atp4a	Potassium-transporting ATPase alpha chain 1	-2,47	0,18	4,73E-03
D3Z6P0-2	Pdia2	Protein disulfide-isomerase A2 isoform 2	-2,41	0,19	2,93E-09
A0A1D5RLB4	Tecr	Very-long-chain enoyl-CoA reductase	-2,16	0,22	7,35E-08
Q8CAG6	Plek	Pleckstrin	-2,09	0,23	9,49E-06
P23953	Ces1c	Carboxylesterase 1C	-2,08	0,24	1,19E-06
Q9EQ20	Aldh6a1	Methylmalonate-semialdehyde dehydrogenase , mitochondrial	-2,05	0,24	4,88E-11
O88587-2	Comt	Catechol O-methyltransferase isoform 2	-1,96	0,26	3,47E-04
Q5RL79	Krtcap2	Keratinocyte-associated protein 2	-1,90	0,27	5,47E-07
Q62261	Sptbn1	Spectrin beta chain, non-erythrocytic 1	-1,88	0,27	6,70E-11
E9QAS4	Chd4	Chromodomain-helicase-DNA-binding protein 4	-1,86	0,28	2,63E-09
Q63918	Sdpr	Serum deprivation-response protein	-1,84	0,28	2,30E-08
Q8VHY0	Cspg4	Chondroitin sulfate proteoglycan 4	-1,81	0,28	1,22E-10
Q8CHT0	Aldh4a1	Delta-1-pyrroline-5-carboxylate dehydrogenase, mitochondrial	-1,69	0,31	3,66E-08
Q3U9N4	Grn	Granulins	-1,68	0,31	4,04E-05

Results: part 1-2 – Matrix characterization

UniProt accession	Gene name	Protein names	log ₂ FC mut vs ctr	FC mut vs ctr	p-value mut vs ctr
Q8BPB5	Efemp1	EGF-containing fibulin-like extracellular matrix protein 1	-1,68	0,31	4,97E-07
E9Q6Z0	Cul5	Cullin-5	-1,66	0,32	1,40E-07
Q02013	Aqp1	Aquaporin-1	-1,63	0,32	1,83E-07
B7ZNH7	Col14a1	Collagen alpha-1(XIV) chain	-1,63	0,32	4,72E-08
F6VF36	Srpr	Signal recognition particle receptor subunit alpha	-1,63	0,32	1,20E-04
Q9DCS3	Mecr	Trans-2-enoyl-CoA reductase, mitochondrial	-1,61	0,33	1,36E-07
E9Q7L8	Cped1	Cadherin-like and PC-esterase domain-containing 1	-1,61	0,33	9,86E-07
O88452	Stc2	Stanniocalcin-2	-1,54	0,34	4,63E-05
P34884	Mif	Macrophage migration inhibitory factor	-1,53	0,35	1,88E-03
A0A0A6YVZ1	Ssr2	Translocon-associated protein subunit beta	-1,52	0,35	1,81E-06
Q8C3X8	Lmf2	Lipase maturation factor 2	-1,46	0,36	1,01E-03
Q9D3D9	Atp5d	ATP synthase subunit delta, mitochondrial	-1,36	0,39	1,69E-04
O88271	Cfdp1	Craniofacial development protein 1	-1,34	0,40	2,21E-06
Q9R1Q9	Atp6ap1	V-type proton ATPase subunit S1	-1,32	0,40	3,86E-07
Q3UZ15	Ptn	Pleiotrophin	-1,28	0,41	4,13E-07
Q9CPU4	Mgst3	Microsomal glutathione S-transferase 3	-1,28	0,41	3,98E-08
A0A0N4SVB8	Arl8a	ADP-ribosylation factor-like protein 8A	-1,28	0,41	2,56E-04
P31428	Dpep1	Dipeptidase 1	-1,27	0,41	8,68E-07
Q8C7E4	Rnase4	Ribonuclease 4	-1,27	0,41	4,04E-06
P54823	Ddx6	Probable ATP-dependent RNA helicase DDX6	-1,26	0,42	4,54E-08
A2RT60	Htra4	Serine protease HTRA4	-1,26	0,42	4,25E-06
P50637	Tspo	Translocator protein	-1,24	0,42	4,88E-04
P29699	Ahsg	Alpha-2-HS-glycoprotein	-1,24	0,42	3,38E-04
E9QAS9	Fmr1	Fragile X mental retardation protein 1 homolog	-1,23	0,43	4,20E-05
A2AEC9	Stxbp3a	Syntaxin-binding protein 3	-1,22	0,43	2,64E-04
Q62095	Ddx3y	ATP-dependent RNA helicase DDX3Y	-1,22	0,43	2,82E-06
Q3TG45	Psm8	26S proteasome non-ATPase regulatory subunit 8	-1,21	0,43	6,12E-07
Q04447	Ckb	Creatine kinase B-type	-1,21	0,43	1,43E-04
A0A140LHR4	Serpinh1	Serpin H1	-1,19	0,44	7,00E-09
P62843	Rps15	40S ribosomal protein S15	-1,18	0,44	4,07E-07
P10925	Zfy1	Zinc finger Y-chromosomal protein 1	-1,18	0,44	5,22E-03
Q3THE2	Myl12b	Myosin regulatory light chain 12B	-1,15	0,45	1,02E-03
F6R8S6	Akt1s1	Proline-rich AKT1 substrate 1	-1,13	0,46	5,10E-04
Q3UNZ8	Cryz12	Quinone oxidoreductase-like protein 2	-1,13	0,46	1,29E-07
Q99JI4	Psm6	26S proteasome non-ATPase regulatory subunit 6	-1,13	0,46	1,84E-07
D3YYT1	Gly1	Putative oxidoreductase GLYR1	-1,11	0,46	2,97E-07
Q9JLZ6-2	Hic2	Hypermethylated in cancer 2 protein isoform 2	-1,10	0,47	1,44E-04
Q8BJS4-3	Sun2	SUN domain-containing protein 2 isoform 3	-1,10	0,47	1,19E-05
A0A0M3HEP8	Vkorc111	Vitamin K epoxide reductase complex subunit 1-like protein 1	-1,08	0,47	4,49E-06
P62196	Psmc5	26S protease regulatory subunit 8	-1,05	0,48	3,07E-07
P05132-2	Prkaca	cAMP-dependent protein kinase catalytic subunit alpha isoform 2	-1,04	0,48	1,07E-05
F6TQL3	Dnajc8	DnaJ homolog subfamily C member 8, NA	-1,04	0,49	1,36E-03

Results: part 1-2 – Matrix characterization

UniProt accession	Gene name	Protein names	log ₂ FC mut vs ctr	FC mut vs ctr	p-value mut vs ctr
G5E866	Sf3b1	Splicing factor 3B subunit 1	-1,03	0,49	1,69E-08
Q9Z1K5	Arih1	E3 ubiquitin-protein ligase ARIH1	-1,02	0,49	1,63E-06
P62331	Arf6	ADP-ribosylation factor 6	-1,01	0,50	3,45E-05
Q792Z1	Try10	MCG140784 (Trypsinogen 10)	-1,01	0,50	6,15E-03
Q80VB6	Dclk1	Serine/threonine-protein kinase DCLK1	-1,00	0,50	7,28E-06
P61961	Ufm1	Ubiquitin-fold modifier 1	-0,99	0,50	3,85E-06
O08532-3	Cacna2d1	Voltage-dependent calcium channel subunit alpha-2/delta-1 isoform 2	-0,99	0,50	1,16E-08
Q80T21	Adamts4	ADAMTS-like protein 4	-0,99	0,50	3,19E-07
Q3V117	Acy	ATP-citrate synthase	-0,99	0,50	3,36E-06
A0A0A6YVU8	Gm9774	Proteasomal ubiquitin receptor ADRM1	-0,99	0,50	7,34E-06
A0A0R4J2B2	Kctd12	BTB/POZ domain-containing protein KCTD12	-0,99	0,50	2,00E-05
Q9WVB4	Slit3	Slit homolog 3 protein	-0,98	0,51	2,60E-06
P11370	Fv4	Retrovirus-related Env polyprotein from Fv-4 locus	-0,98	0,51	1,87E-06
Q9CR61	Ndufb7	NADH dehydrogenase [ubiquinone] 1 beta subcomplex subunit 7	-0,98	0,51	4,15E-08
Q9EQP2	Ehd4	EH domain-containing protein 4	-0,97	0,51	8,37E-07
Q8R4V4	Cpz	Carboxypeptidase Z	-0,97	0,51	2,51E-05
A2AQE4	Cops2	COP9 signalosome complex subunit 2	-0,95	0,52	4,20E-06
Q6ZWQ7	Spcs3	Signal peptidase complex subunit 3	-0,94	0,52	2,26E-04
Q99J56	Der1	Derlin-1	-0,94	0,52	5,42E-04
P23780	Glb1	Beta-galactosidase	-0,94	0,52	1,39E-07
Q9D666-5	Sun1	SUN domain-containing protein 1 isoform 5	-0,94	0,52	5,39E-06
E9QMH7	Ikbip	Inhibitor of nuclear factor kappa-B kinase-interacting protein	-0,93	0,52	2,42E-07
A0A0U1RPW2	Tjp1	Tight junction protein ZO-1	-0,93	0,53	7,92E-04
E9PWW2	Tor1aip1	Torsin-1A-interacting protein 1	-0,92	0,53	2,41E-04
Q5SV64	Myh11	Myosin-11	-0,91	0,53	2,07E-06
E9PUX0	Mtdh	Protein LYRIC	-0,91	0,53	1,27E-05
Q8K2C9	Hacd3	Very-long-chain (3R)-3-hydroxyacyl-CoA dehydratase 3	-0,90	0,54	4,11E-05
I7HLV2	Rpl10	60S ribosomal protein L10	-0,90	0,54	1,08E-03
B2RQA5	Sost	Sclerostin	-0,90	0,54	1,84E-04
P14152	Mdh1	Malate dehydrogenase, cytoplasmic	-0,88	0,54	2,04E-04
E9Q6R3	Sec22b	Vesicle-trafficking protein SEC22b	-0,88	0,54	1,97E-03
Q01149	Col1a2	Collagen alpha-2(I) chain	-0,88	0,54	4,73E-06
Q9EST5	Anp32b	Acidic leucine-rich nuclear phosphoprotein 32 family member B	-0,88	0,54	2,46E-06
Q91V41	Rab14	Ras-related protein Rab-14	-0,88	0,54	6,82E-05
Q99KQ4	Nampt	Nicotinamide phosphoribosyltransferase	-0,87	0,55	3,67E-03
D3Z158	Qars	Glutamine--tRNA ligase	-0,86	0,55	6,45E-06
Q5DTZ0	Nynrin	Protein NYNRIN	-0,85	0,55	3,53E-03
Q8BWZ3-2	Naa25	N-alpha-acetyltransferase 25, NatB auxiliary subunit isoform 2	-0,85	0,55	3,23E-03
Q9ET01	Pygl	Glycogen phosphorylase, liver form	-0,85	0,56	8,21E-04
E9PYF4	Lmo7	LIM domain only 7	-0,84	0,56	6,32E-03
A2A7S7	Yars	Tyrosine--tRNA ligase	-0,84	0,56	3,47E-04
P10922	H1f0	Histone H1.0	-0,84	0,56	5,27E-03

UniProt accession	Gene name	Protein names	log ₂ FC mut vs ctr	FC mut vs ctr	p-value mut vs ctr
Z4YKV1	Gnas	Guanine nucleotide-binding protein G(s) subunit alpha isoforms short	-0,84	0,56	1,71E-05
Q8CGF7-2	Tcerg1	Transcription elongation regulator 1 isoform 2	-0,82	0,57	1,38E-04
Q8R059	Gale	UDP-glucose 4-epimerase	-0,82	0,57	1,04E-03
Q6ZWZ4	Rpl36	60S ribosomal protein L36	-0,81	0,57	7,82E-05

Although we have seen with Sirius Red assays that there was no difference in collagen amounts between *Recq14^{+/-}* and *Recq14^{-/-}* ECM, our proteomic results show that three collagen chains are under-represented in the mutant ECM: Collagen V α -3 (Col5a3, FC 0.09), Collagen XIV α -1 (Col14a1, FC 0.32) and Collagen I α -2 (Col1a2, FC 0.54). Collagen V is a fibrillar collagen expressed in the bone at low levels in association with Collagen I (Birk 2001). The major molecular isoform of Collagen V is a trimer of two α 1 and one α 2 chains (Mak *et al.* 2016). Mutations in these genes cause the Ehlers–Danlos syndrome, in which patients suffer from fragile, hyperextensible skin and hyper-mobile joints. However, the function of Collagen V α -3 chain is unclear. Collagen XIV is a FACIT (fibril-associated collagen with interrupted triple helices) expressed in the osteoprogenitors and the developing bone (Walchli *et al.* 1994; Clough *et al.* 2015) the role of which remains unclear in bone. Nevertheless, these collagens seem to be deficient in the mutant ECM. However, given our protein extraction method, the proteomic results regarding collagen must be considered with caution. Indeed, we have mainly examined soluble protein fraction. We cannot exclude that part of collagens remained in insoluble aggregates. Moreover, it is possible that under-representation of collagen in mutant ECM extract is due to the higher expression of lysyl oxidase LOXL4: if mutant collagen is more cross-linked, it would be less soluble and thus less extractable than in control conditions.

The lower abundance in mutant matrix of sclerostin (FC 0,54) and fetuin-A (FC 0.42), which are respectively inhibitors of bone formation (Li *et al.* 2005) and

hydroxyapatite apposition (Schinke *et al.* 1996), was not expected taking into account the decreased mineralization in these *Recq14*^{-/-} ECM. Nevertheless, studies show unexpected effects of these proteins on bone metabolism. Indeed, Ueland *et al.* have recently demonstrated that in postmenopausal women levels of sclerostin in the bone matrix positively correlated with bone mineral density (Ueland *et al.* 2019). Several other studies have shown that fetuin-A promotes collagen I matrix mineralization in cell-free conditions (Price *et al.* 2004; Hamlin and Price 2004) and protects osteoblasts from hydroxyapatite-induced apoptosis (Cai *et al.* 2015).

Next, using PANTHER (Mi *et al.* 2019), DAVID (Huang *et al.* 2009b), Gorilla (Eden *et al.* 2009) and IPA (version 0.1-0.7; QIAGEN) online analysis tools, we attempted to further refine the analysis in order to find out if any signaling pathways, molecular functions or biological process could be affected by differentially abundant proteins. No significant changes were found in any of these categories, with the exception of two GO “Molecular function” terms in the case of proteins overexpressed in the *Recq14*^{-/-} ECM (Figure Gb):

1) “Protein-containing complex binding” – 22 proteins in our data set amongst those over-represented in the *Recq14*^{-/-} ECM; 4.9-fold term enrichment, and

2) “Glycosaminoglycan binding” – 8 proteins in our data set, 5 of which are extracellular (shown on the blue background in the right panel of the Figure 3b); 10.6-fold term enrichment.

The former function seemed too general for a meaningful biological interpretation in our case, therefore we have decided to concentrate on the latter, and, in particular, on the structural ECM protein Decorin (DCN, FC 1.93), a small leucine-rich proteoglycan (SLRP). It has been shown to regulate collagen fibrillogenesis, in particular collagen fiber diameter (Corsi *et al.* 2002b; Douglas *et al.*

2006) and the density of collagen ECM network (Iwasaki *et al.* 2008). Moreover, DCN was suggested to act as a kind of molecular cross-linker, stiffening the matrix (Cribb and Scott 1995; Iwasaki *et al.* 2008), which would be in accordance with what we saw in *Recq14*^{-/-} matrices. Besides direct effects on ECM architecture, DCN also affects mineralization: in MC3T3 cells overexpressing DCN the timing and the level of mineralization is inversely correlated with the level of DCN synthesis (Mochida *et al.* 2003b) and the transplants of these cells in mouse fail to mineralize (Mochida *et al.* 2009b).

We selected three other candidate proteins for further investigations, based on the literature and their possible implication in either bone function or DNA metabolism. One of them are over-represented in the *Recq14*^{-/-} ECM: (1) Y-box-binding protein 1 (YB1, FC 3.52). The other two are under-represented in the *Recq14*^{-/-} ECM: (2) Slit homolog 3 protein (SLIT3, FC 0.51) and (3) Pleiotrophin (PTN, FC 0.41), both of which are chemotaxic molecules implicated in the osteoblast recruitment (Yang *et al.* 2003; Kim *et al.* 2018). The reasons for choosing these particular proteins are described below.

(1) YB1 is a nucleic acid-binding protein with pleiotropic functions in DNA and RNA metabolism (Alemasova and Lavrik 2017) and can be found both inside the cell (cytoplasm and nucleus) and in the extracellular space (Frye *et al.* 2009). It is the only differentially abundant protein in our data set that has been shown to physically interact with RECQL4 (Mo *et al.* 2016). YB1 is also known to suppress the transcription of genes coding for both chains of collagen I (Dhalla *et al.* 1998; Norman *et al.* 2001; Higashi *et al.* 2003) and to play a role in the prevention of premature senescence (Lu *et al.* 2005).

(2) SLIT3 is known as the axon-guiding molecule (Wu *et al.* 1999). However, a very recent study (Kim *et al.* 2018) has described an important role played by this protein in bone remodeling. Osteoclast-secreted SLIT3 was shown to be a coupling factor, stimulating osteoblast migration and proliferation while inhibiting osteoclast resorption. Its deficiency in the *Recq14*^{-/-} matrix could hypothetically lead to the bone phenotype found in our mice.

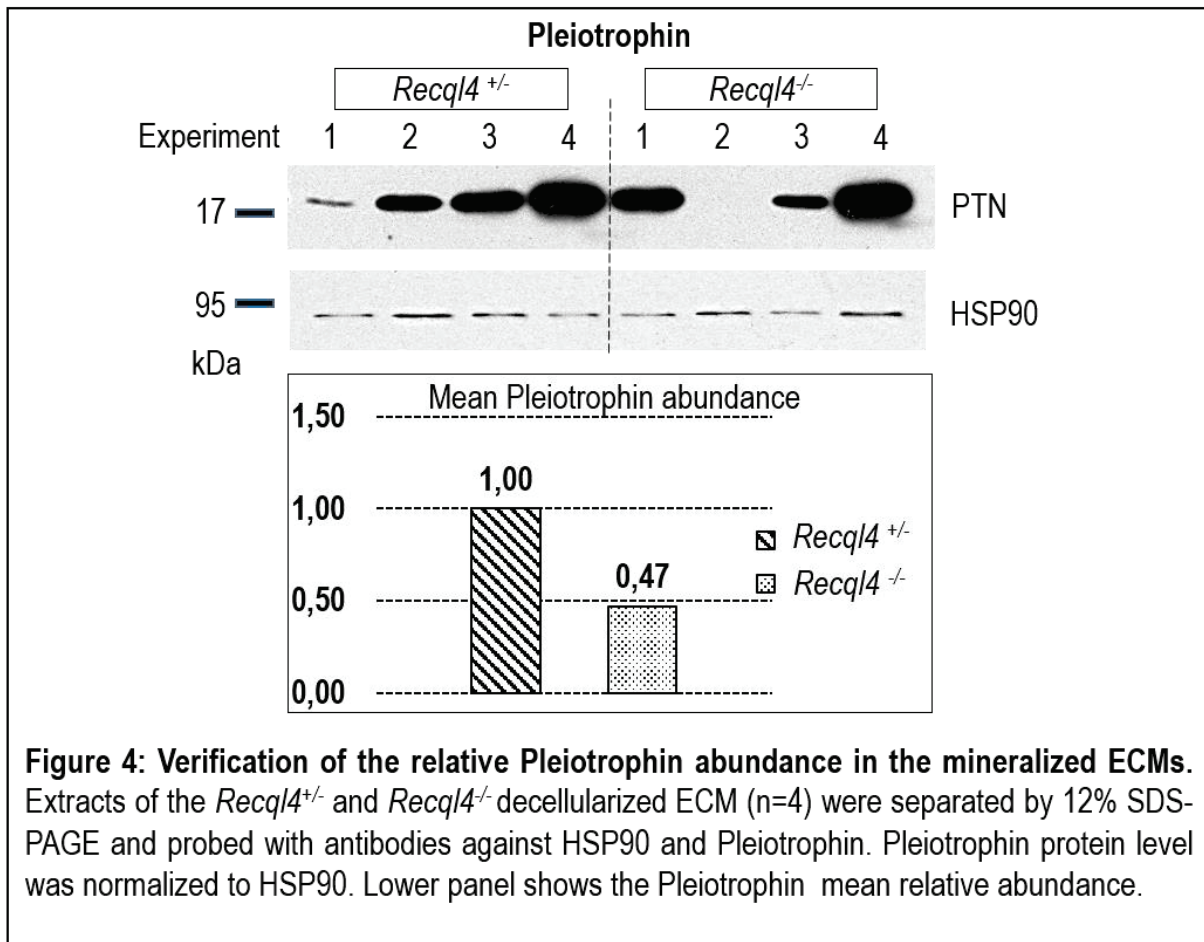
(3) PTN was also initially identified as an axon-guiding molecule (Li *et al.* 1990), although many other functions were ascribed to this protein subsequently. PTN induces chemotaxis, proliferation and differentiation *ex vivo* in human primary osteoblasts (Yang *et al.* 2003). Transgenic mice overexpressing human *PTN* gene have been shown to achieve a higher bone mass peak, which compensated for bone loss caused by estrogen deficiency (Masuda *et al.* 1997) and to display a 10% increase of bone mineral content (Tare *et al.* 2002). This effect was specific to female mice (Hashimoto-Gotoh *et al.* 2004). We can hypothesize that partial protection of female mice from accelerated bone loss that we see in our model (see submitted manuscript) could be due to the PTN action.

C. Validation of selected proteins by western blotting

The samples for Western Blot (WB) were prepared using the same protein extraction protocol as those used for proteomics. In order to limit the effect of the inter-individual variability, the matrices were synthesized by the osteoblasts pooled from 3 mice.

For WB performed on the ECM extracts, there is no “housekeeping” protein that is generally accepted as a loading control. Therefore, we selected our loading control, the HSP90, using mass spectrometry data, where it had an overall fold change close to 1 (1.06), was identified in all MS/MS runs and had the least intensity variation

between runs. Intracellularly, HSP90 is a highly abundant protein (1-3% of total intracellular proteins) functioning primarily as a molecular chaperon. Extracellularly, it may be found attached to the outer cell surface or as an unbound molecule (Cortes *et al.* 2018). HSP90 is a 90 kDa protein that migrated in our SDS-PAGE gels with an

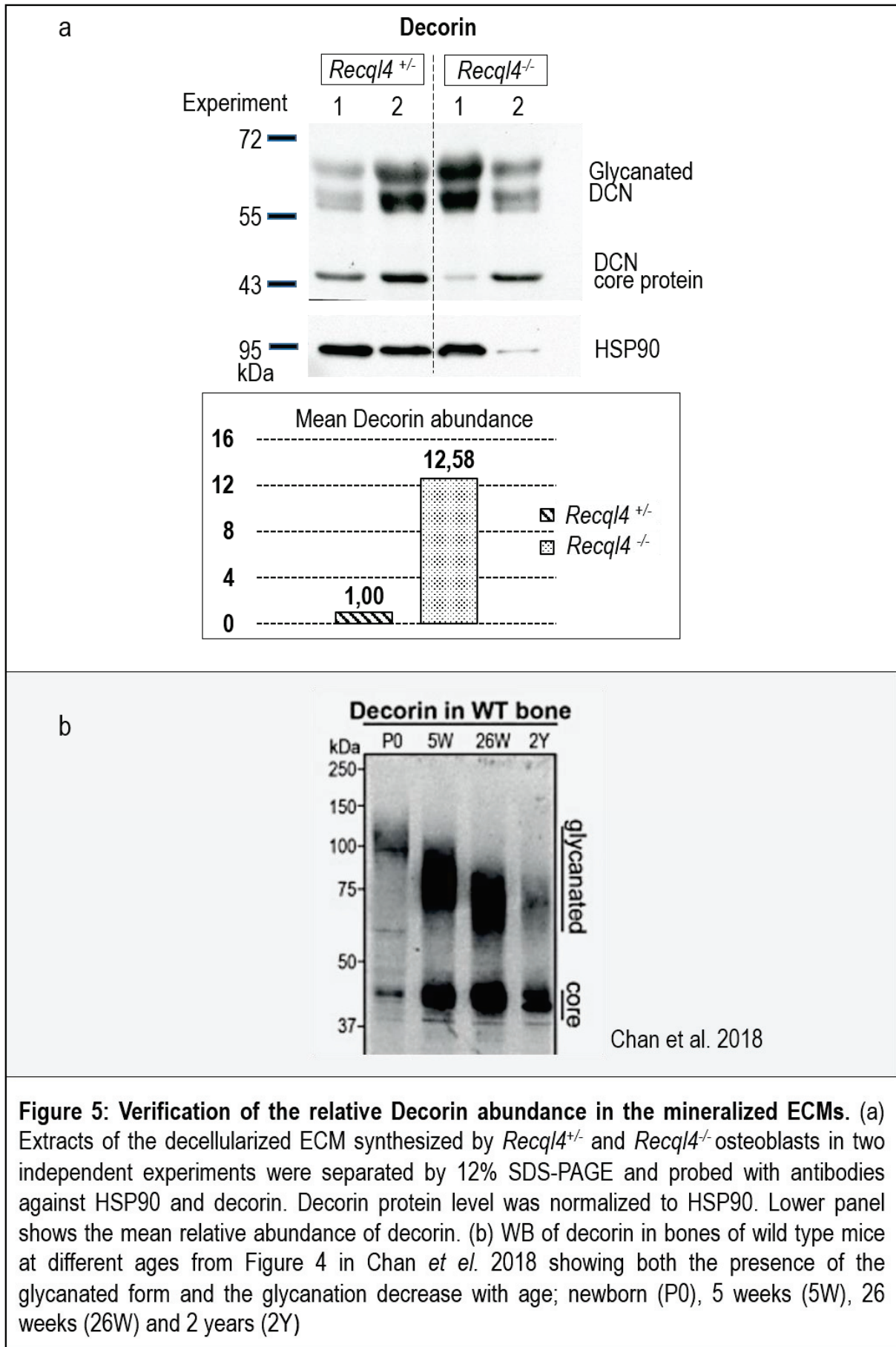


apparent weight of ~94 kDa and that we used as a loading control and for normalization.

Proteomics results indicated that the 23 kDa protein Pleiotrophin (PTN) is 2.44 less abundant in mutant matrix. We separated it on 14 % SDS-PAGE gel, where it migrated as a slightly smaller protein of ~18 kDa. It was highly abundant in our matrix extracts, so only 5 µg of proteins per sample were loaded in gels. Extracts from 4 independent experiments (Figure 4) were charged on the same gel. As seen in figure H, there is a great variability between experiments: relative normalized PTN levels in

Recq14^{+/-} ECM varied from 0.09 (experiment 1) to 7.72 (experiment 4); and in *Recq14*^{-/-} ECM, from baseline (experiment 2) to 2.93 (experiment 4). Although PTN levels turned out to be higher in the control than in the mutant ECM in the experiments 2, 3 and 4, in the experiment 1 it was not the case. However, on average (including experiment 1), there was 2,13 times as much PTN in *Recq14*^{+/-} ECM as in *Recq14*^{-/-} ECM, a figure close to what was expected from the proteomic analysis.

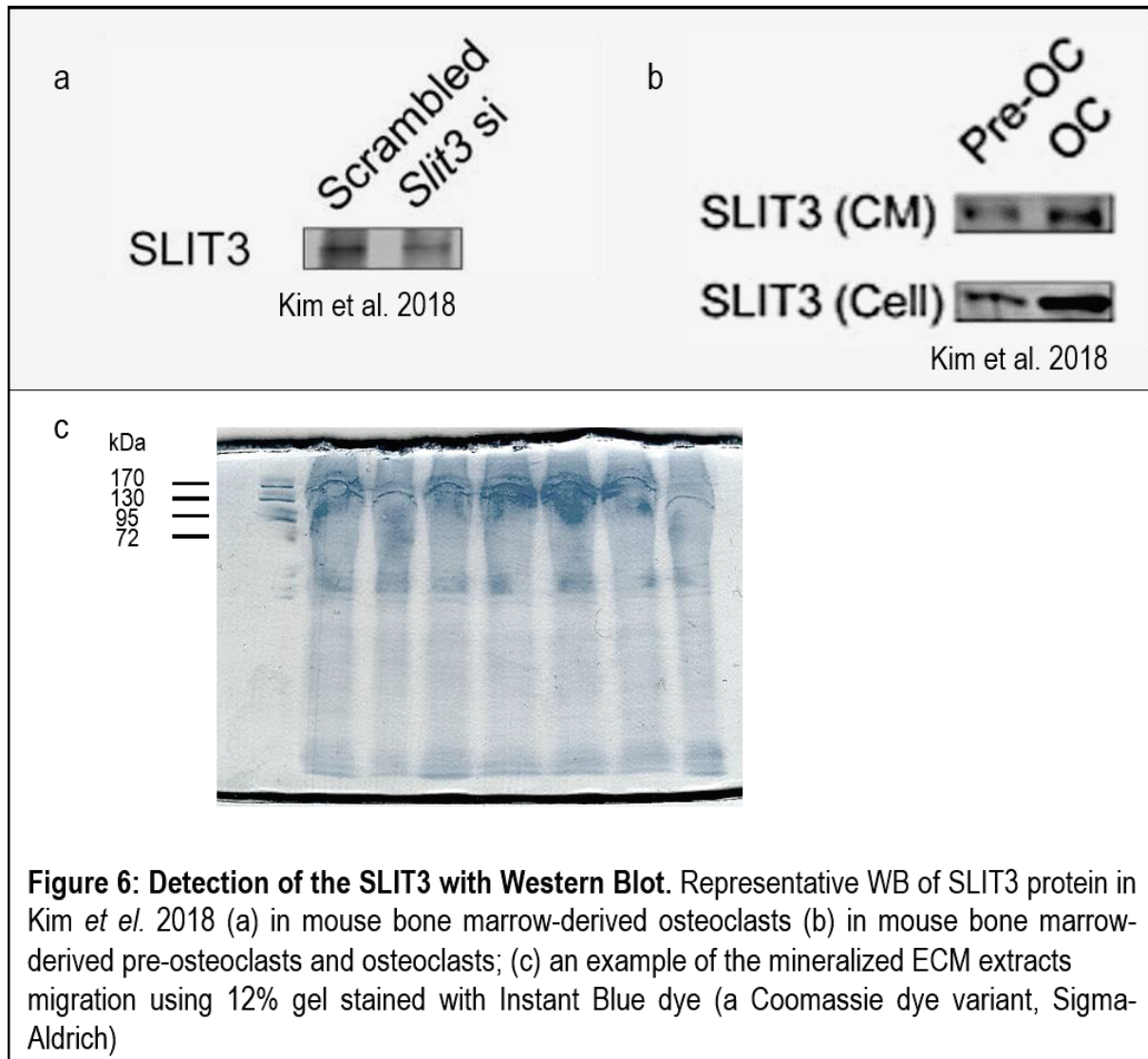
Decorin is present in the ECM in the glycanated form, *i.e.* bound to glycosaminoglycan chains, and/or as a core protein of ~40-45 kDa. Due to its high and variable glycanation, DCN detection and quantification in WB are challenging. In our case, we were unable to detect it with the first antibody that we have tried. It should be noted that the synthesis of mineralized matrices takes approximately 45-50 days and that the amount of proteins obtained in each case is about 100-150 µg per sample. Therefore, after optimization of WB protocol using new primary antibody, we were able to verify DCN ECM levels in only two independent experiments (Figure 5a). We have detected signals from both glycanated and core-protein forms of the DCN. For comparison, similar band pattern was observed in another study (Figure 1b), where the authors followed DCN expression in mouse bones at different ages (Chan *et al.* 2018). Figure 1b shows that with age the DCN glycanation decreases and its band shifts lower. For 26-week old mice, the band of glycanated DCN is found between ~60 and 80 kDa (Figure 5b, lane 26W). The ECMs in our experiments were synthesized by the osteoblasts derived from mice more than twice older (~60-weeks old). Therefore, it seems reasonable to assume that in our case the DCN glycanation would have decreased even more, moving its corresponding band still lower, to the position between 55 and 72 kDa that we see in Figure 1a. We have also noted that the levels



of DCN glycanation in the *Recq14*^{-/-} ECM varied between the experiment 1 and the experiment 2, while being negatively correlated with the levels of the core-protein: the high amount of glycanated protein and the low amount of the core-protein in the experiment 1 contrasts with the low amount of glycanated protein and higher amount of the core-protein in the experiment 2. In order to quantify total DCN levels in the ECM as accurately as possible, we have thereby decided to sum the intensities of the glycanated and the core protein bands. Proteomics indicated 1.93-fold DCN over-representation in the *Recq14*^{+/-} ECM. Our preliminary WB results confirm this conclusion: on average, PTN is 12.6 times more abundant in the control than in the mutant ECM. However, more experiments are necessary ascertain this statistically.

SLIT3 has a predicted molecular weight of 169 kDa. Due to this large size, we separated it on the 8% SDS-PAGE gels. We have used the same antibody as the authors of the study describing the discovery of SLIT3 as a coupling factor in bone remodeling (Kim *et al.* 2018). SLIT3 WB from Kim *et al.* are shown in the Figure 6a and 6b. In panel (a) the background is heavily stained and the bands are discontinuous in both panels, but they are detectable. In our case, there was no SLIT3 signal at all. As far as we know, antibody used for these blots is the best currently available for the mouse SLIT3. Detection of this protein in WB is problematic, because high MW proteins are notoriously difficult to transfer to the membrane (Bolt and Mahoney 1997). We have tried unsuccessfully several transfer conditions. This led us to ponder whether the problem originated from our extracts. As shown in Figure 6c, the proteins migrated poorly in the high MW region, most likely due either to the mineral that was still associated with them, or to the presence of molecules that were not completely solubilized or heavily modified with side chains (glycanation, glycosylation). Kim *et al.* have demonstrated that, among bone cells, SLIT3 expression was highest in the

osteoclasts (Kim *et al.* 2018). Thus we decided to perform SLIT3 WB on the osteoclast extracts obtained from differentiating mouse monocyte / macrophage RAW 264.7 cells. However, no signal was detected with osteoclast extracts either. Our results imply that a better antibody is necessary for the WB detection of SLIT3. Meanwhile, other approaches, such as immunohistochemistry and/or immunofluorescence, could be



used to confirm the lower abundance of SLIT3 in *Recq14*^{-/-} ECM.

Though the actual molecular weight of YB-1 is 35,9 kDa, it most often exhibits an electrophoretic mobility of ~50 kDa. Depending on the stimulus, YB1 can be found secreted (Frye *et al.* 2009) and/or in various subcellular localizations, such as cytoplasm, stress granules, p-bodies and nucleus (Alemasova and Lavrik 2017).

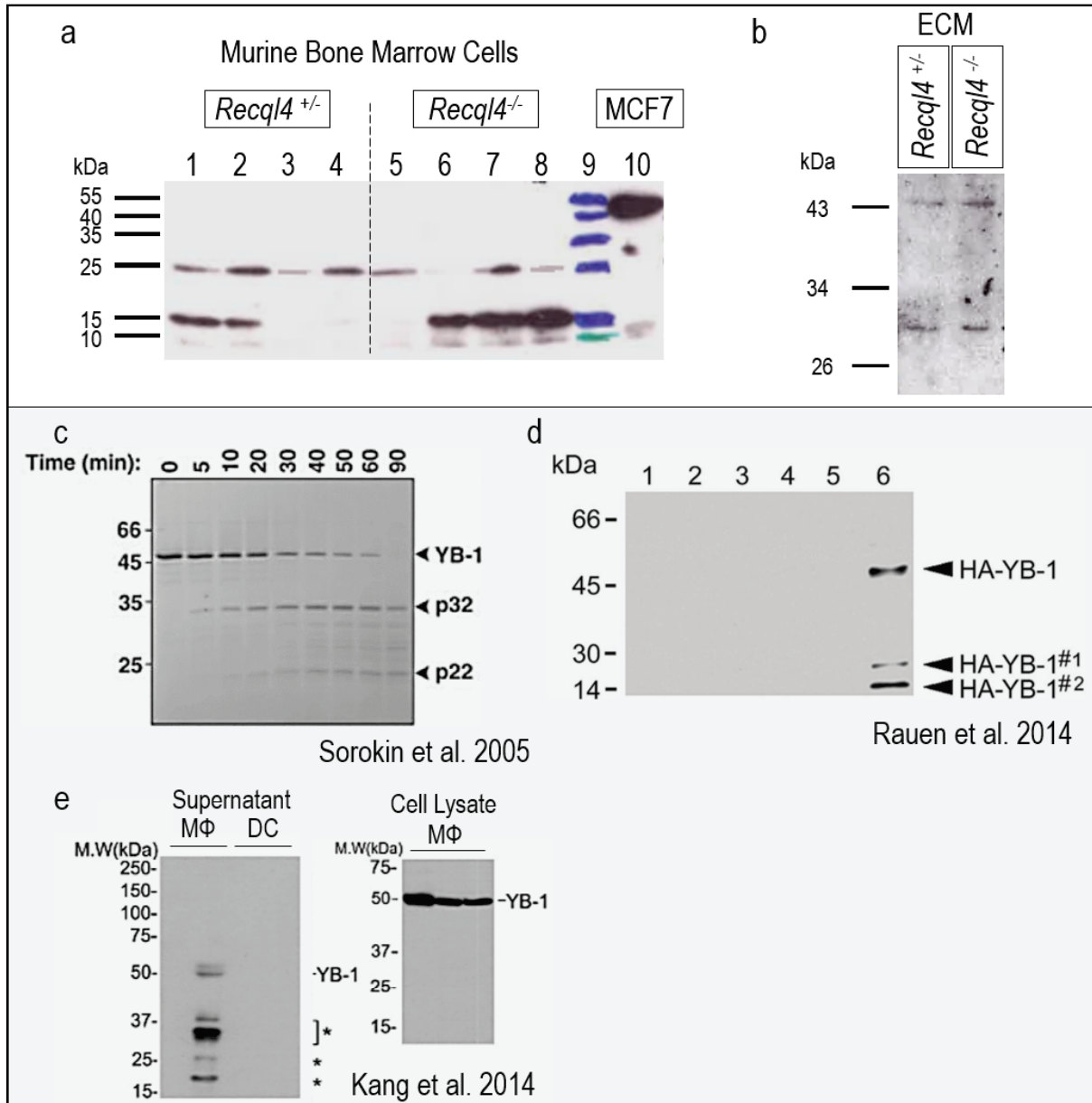


Figure 7: Detection of the YB1 with Western Blot. (a) WB using polyclonal antibody (pAb) against human YB1 (hYB1) C-term in *Recq14*^{+/-} and *Recq14*^{-/-} bone marrow (BM) cells. Lanes: [1 – 8] each lane corresponds to cells derived from different mice: [1 – 4] *Recq14*^{+/-} cells, [5 – 8] *Recq14*^{-/-} cells, [9] MW standard, [10] human breast cancer MCF7 cell line (positive control). Bands of 25 and 15 kDa were detected. (b) WB analysis of by *Recq14*^{+/-} and *Recq14*^{-/-} decellularized ECMs using anti-hYB1 N-term (c)-(e) Examples of YB1 WB from literature: (c) From Sorokin *et al.* 2005. Time course of *in vitro* YB-1 cleavage by the 20S proteasome. Rabbit YB1 was expressed in *E. coli* and purified. Bands for full length YB1 (~47 kDa) and two proteolytic fragments (22 and 32 kDa) were detected with pAb raised against full-length rabbit YB1. (d) From Rauen *et al.* 2014. WB using anti-HA tag Ab. Lane 6: microvesicles purified from the culture medium of rat mesangial cells expressing HA-YB1 and stimulated with PDGF. Full-length HA-YB-1 (50 kDa) and two fragments (~27 and 15 kDa) were detected. (e) From Kang *et al.* 2014. WB with anti-hYB1 C-term Ab in murine RAW 264.7 macrophages and murine BM-derived dendritic cells. Bands of low weight fragments were detected in the extracellular supernatant from macrophages but not dendrocytes, while whole-cell macrophage lysate contained only full length YB1.

Moreover, studies have shown that its secretion is cell-type specific (Kang *et al.* 2014). However, reports concerning YB1 expression levels and localization that are based on WB detection are often contradictory, because of different immunoreactivities of the antibodies (Ab) used in these studies (Woolley *et al.* 2011). The first Ab we tried was directed against YB1 carboxy-terminus. We did not obtain any signal with the ECM extracts (not shown), but were able to detect 2 bands with the bone marrow cell extracts (25 kDa and 15 kDa, Figure 7a), the size of which did not correspond to 50 kDa predicted for YB1. On the other hand, the band of 50 kDa was observed in the lane 10 charged with the positive control (human breast cancer MCF7 cell line) provided by Ab manufacturer. The WB of the decellularized *Recq14^{+/-}* and *Recq14^{-/-}* ECM using pAb against YB1 N-terminal epitope revealed bands of 44 kDa and 30 kDa (Figure 7b). Taken together, the results appeared puzzling: do the bands detected in our extracts correspond to YB1 or are they non-specific? We have no basis for comparison since, to the best of our knowledge, no YB1 WB has yet been performed on bone or bone cell extracts. Nonetheless, due to the YB1's emerging importance in cancerology, many studies have explored its electrophoretic behavior in other cell types or *in vitro* (Sorokin *et al.* 2005; Rauen *et al.* 2009; Kim *et al.* 2013a; Kang *et al.* 2014b; Pagano *et al.* 2016). First, Sorokin and his colleagues (Sorokin *et al.* 2005) demonstrated that YB1 is cleaved by 20S proteasome into two fragments, the N-terminal p32 and the C-terminal p22 (Figure 7c). As shown in Figure 7d, two fragments (~27 and ~15 kDa) and full-length (~47 kDa) YB1 were also found in the extracellular microvesicles secreted by rat mesangial cells expressing HA-YB1 (Rauen *et al.* 2009).

The elaborate pattern of YB1 cleavage and multimer formation is further illustrated by multiple bands in the left panel of the Figure 7e (Kang *et al.* 2014).

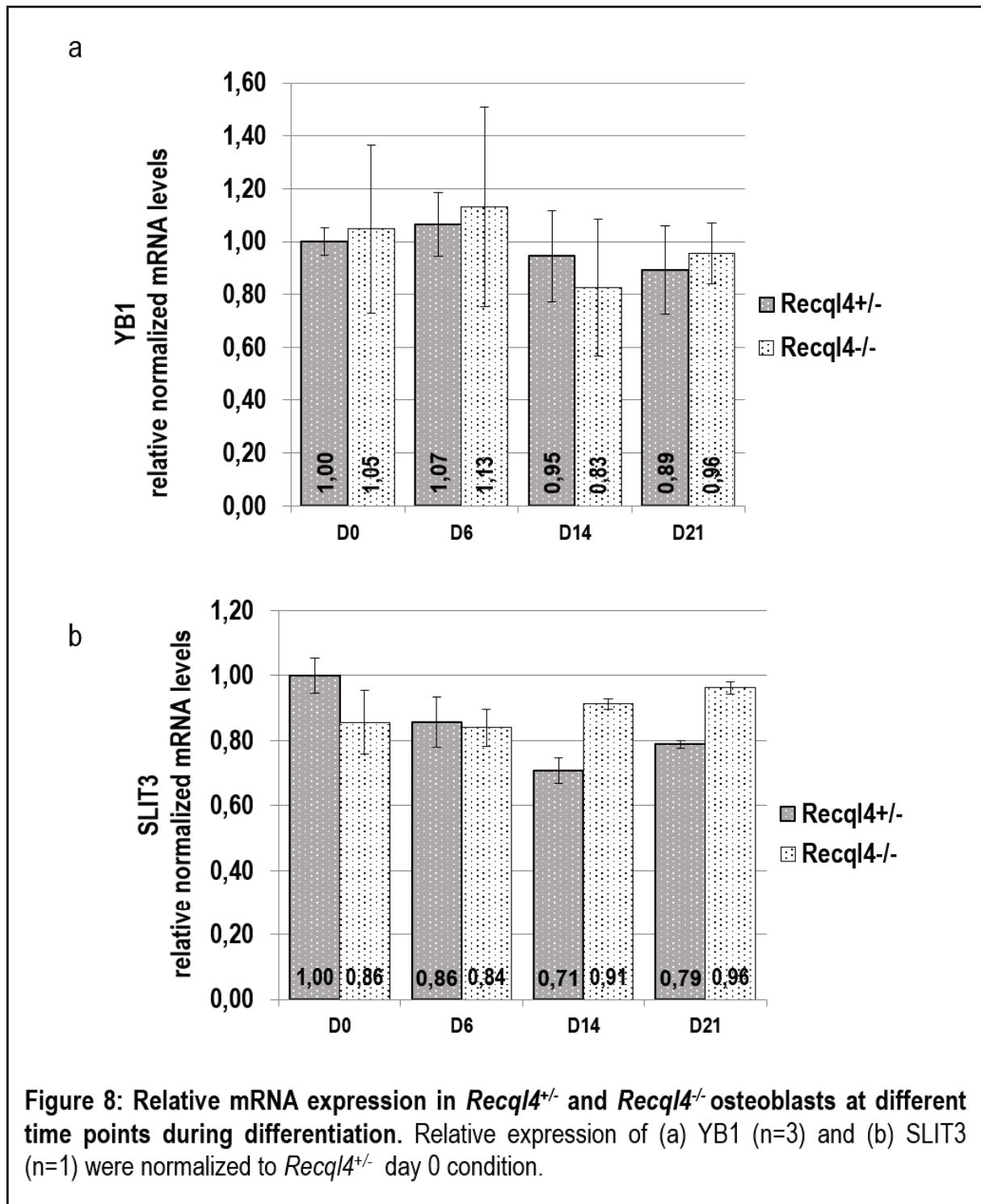
Figure 7e shows macrophage-specific difference between intracellular (right panel) and secreted (left panel) YB1 species in RAW 264.7 cells. In these cells, secreted YB1 is mostly present as fragments. It is thus likely that YB1 in the OB-secreted ECM could also exist in fragmented form. Interestingly, at least two YB1 fragments have been shown to be biologically active. Truncated N-terminal YB1 fragment accumulates in the nuclei of cells treated with DNA damaging drugs where it is capable of protecting cells against DNA damage-induced stress (Kim *et al.* 2013). The carboxy-terminal fragment, which also localized to the nucleus, acts dominant-negatively on full-length YB1-dependent gene transcription (van Roeyen *et al.* 2013). Moreover, overexpression of full-length YB1 in the human premalignant breast epithelial MCF10AT cells leads to the over-expression of the DCN (Evdokimova *et al.* 2009). Taking into account all these observations, it would be interesting to precisely identify, probably by mass spectrometric analysis, which YB1 fragments are present in our ECM extracts.

D. RT-qPCR

Complementary to the end-point protein expression analysis, we have conducted the time course examination of the *Ybx1* (coding for YB1 protein) and *Slit3* gene expression (Figure 8). The mRNAs were extracted from *Reqc14^{+/-}* and *Reqc14^{-/-}* osteoblasts on days 0, 6, 14 and 21 of mineralization.

Throughout the mineralization process, the *Ybx1* mRNA levels remained stable, both in *Reqc14^{+/-}* and in *Reqc14^{-/-}* osteoblasts (Figure 8a). No differences between control and mutant samples were revealed, although considerable standard error values caused by high variation in the expression levels between experiments could have hidden a low-level trend. According to recent study, such fluctuation in *Ybx1* gene expression could be due to the fact that it is regulated by circadian clock (Pagano *et*

al. 2016). Therefore, the small difference in the samples collection times could result in the big difference in gene expression. Nonetheless, the YB1 over-abundance in the



mutant ECM does not seem to originate at the transcriptional level.

The *Slit3* expression in *Recq14^{+/-}* osteoblasts during mineralization followed a slight decreasing trend (from 1 on day0 (D0), to 0.86 on D6, to 0.71 on D14), while it remained stable in *Recq14^{-/-}* osteoblasts (Figure 8b). If this is the case, higher accumulation of the SLIT3 in *Recq14^{+/-}* ECM is also independent from transcriptional control. However, these are very preliminary results, and have to be taken with extreme caution.

The interest for SLIT3 and YB1 in connection with bone is either very recent or nonexistent. This could be the first study to establish their gene expression pattern in mineralizing osteoblasts.

References

- Alemasova EE and Lavrik OI 2017 *Acta Naturae* **9** 4–16
- Ashburner M *et al.* 2000 *Nat. Genet.* **25** 25–9
- Balcerzak M, Malinowska A, Thouverey C, Sekrecka A, Dadlez M, Buchet R, and Pikula S 2008 *Proteomics* **8** 192–205
- Benjamini Y and Hochberg Y 1995 *J. R. Stat. Soc. Ser. B Methodol.* **57** 289–300
- Birk DE 2001 *Micron* **32** 223–37
- Bolt MW and Mahoney PA 1997 *Anal. Biochem.* **247** 185–92
- Bouleftour W *et al.* 2016 *Matrix Biol.* **52–54** 60–77
- Cai MMX, Smith ER, and Holt SG 2015 *BoneKEy Rep.* **4**
<https://doi.org/10.1038/bonekey.2015.39>
- Chan WL *et al.* 2018 *PLoS Genet.* **14** <https://doi.org/10.1371/journal.pgen.1007242>
- Clough BH *et al.* 2015 *J. Bone Miner. Res. Off. J. Am. Soc. Bone Miner. Res.* **30** 83–94
- Collins MJ *et al.* 2002 *Archaeometry* **44** 383–94
- Corsi A *et al.* 2002 *J. Bone Miner. Res.* **17** 1180–9
- Cortes S, Baker-Williams AJ, Mollapour M, and Bourboulia D 2018 *Methods Mol. Biol. Clifton NJ* **1709** 321–9
- Cox J, Hein MY, Luber CA, Paron I, Nagaraj N, and Mann M 2014 *Mol. Cell. Proteomics MCP* **13** 2513–26
- Cribb AM and Scott JE 1995 *J. Anat.* **187** 423–8
- Dallas SL, Keene DR, Bruder SP, Saharinen J, Sakai LY, Mundy GR, and Bonewald LF 2000 *J. Bone Miner. Res.* **15** 68–81
- Dhalla AK, Ririe SS, Swamynathan SK, Weber KT, and Guntaka RV 1998 *Biochem. J.* **336** 373–9
- Douglas T, Heinemann S, Bierbaum S, Scharnweber D, and Worch H 2006 *Biomacromolecules* **7** 2388–93
- Eden E, Navon R, Steinfeld I, Lipson D, and Yakhini Z 2009 *BMC Bioinformatics* **10** 48
- Eng JK, McCormack AL, and Yates JR 1994 *J. Am. Soc. Mass Spectrom.* **5** 976–89

- Evdokimova V, Tognon C, Ng T, Ruzanov P, Melnyk N, Fink D, Sorokin A, Ovchinnikov LP, Davicioni E, Triche TJ, and Sorensen PHB 2009 *Cancer Cell* **15** 402–415
- Frye BC *et al.* 2009 *EMBO Rep.* **10** 783–9
- Gianetto QG 2019 *imp4p: Imputation for Proteomics*
- Greene RF and Pace CN 1974 *J. Biol. Chem.* **249** 5388–93
- Guarino AM *et al.* 2018 *Genes* **9** <https://doi.org/10.3390/genes9100513>
- Hamlin NJ and Price PA 2004 *Calcif. Tissue Int.* **75** 231–42
- Hashimoto-Gotoh T, Ohnishi H, Tsujimura A, Tsunozuka H, Imai K, Masuda H, and Nakamura T 2004 *J. Bone Miner. Metab.* **22** 278–82
- Higashi K, Inagaki Y, Suzuki N, Mitsui S, Mauviel A, Kaneko H, and Nakatsuka I 2003 *J. Biol. Chem.* **278** 5156–62
- Huang DW, Sherman BT, and Lempicki RA 2009a *Nat. Protoc.* **4** 44–57
- Iwasaki S, Hosaka Y, Iwasaki T, Yamamoto K, Nagayasu A, Ueda H, Kokai Y, and Takehana K 2008 *Arch. Histol. Cytol.* **71** 37–44
- Jain S, Wheeler JR, Walters RW, Agrawal A, Barsic A, and Parker R 2016 *Cell* **164** 487–98
- Kang S, Lee TA, Ra EA, Lee E, Choi H jin, Lee S, and Park B 2014a *PLoS ONE* **9** <https://doi.org/10.1371/journal.pone.0112754>
- Kedersha N *et al.* 2016 *J. Cell Biol.* **212** 845–60
- Kim B-J *et al.* 2018 *J. Clin. Invest.* **128** 1429–41
- Kim ER, Selyutina AA, Buldakov IA, Evdokimova V, Ovchinnikov LP, and Sorokin AV 2013 *Cell Cycle* **12** 3791–803
- Li YS, Milner PG, Chauhan AK, Watson MA, Hoffman RM, Kodner CM, Milbrandt J, and Deuel TF 1990 *Science* **250** 1690–4
- Li X, Zhang Y, Kang H, Liu W, Liu P, Zhang J, Harris SE, and Wu D 2005 *J. Biol. Chem.* **280** 19883–7
- Lu ZH, Books JT, and Ley TJ 2005 *Mol. Cell. Biol.* **25** 4625–37
- Lukesh JC, Palte MJ, and Raines RT 2012 *J. Am. Chem. Soc.* **134** 4057–9
- Mak KM, Png CYM, and Lee DJ 2016 *Anat. Rec.* **299** 613–29
- Markmiller S *et al.* 2018 *Cell* **172** 590-604.e13
- Masuda H *et al.* 1997 *Biochem. Biophys. Res. Commun.* **238** 528–33

- Mi H, Muruganujan A, Ebert D, Huang X, and Thomas PD 2019 *Nucleic Acids Res.* **47** D419–26
- Mo D *et al.* 2016 *Cancer Res.* **76** 3057–66
- Mochida Y, Duarte WR, Tanzawa H, Paschalis EP, and Yamauchi M 2003 *Biochem. Biophys. Res. Commun.* **305** 6–9
- Mochida Y, Parisuthiman D, Pornprasertsuk-Damrongsri S, Atsawasuwan P, Sricholpech M, Boskey AL, and Yamauchi M 2009 *Matrix Biol. J. Int. Soc. Matrix Biol.* **28** 44–52
- Nettleton D, Hwang JTG, Caldo RA, and Wise RP 2006 *J. Agric. Biol. Environ. Stat.* **11** 337
- Norman JT, Lindahl GE, Shakib K, En-Nia A, Yilmaz E, and Mertens PR 2001 *J. Biol. Chem.* **276** 29880–90
- Orriss IR, Arnett TR, and Russell RGG 2016 *Curr. Opin. Pharmacol.* **28** 57–68
- Pagano C *et al.* 2016 *Oncotarget* **8** 6193–205
- Prewitz MC *et al.* 2013 *Nat. Methods* **10** 788–94
- Price PA, June HH, Hamlin NJ, and Williamson MK 2004 *J. Biol. Chem.* **279** 19169–80
- Rauen T *et al.* 2009 *J. Biol. Chem.* **284** 26928–40
- Ritchie ME, Phipson B, Wu D, Hu Y, Law CW, Shi W, and Smyth GK 2015 *Nucleic Acids Res.* **43** e47
- Robertson IB, Horiguchi M, Zilberberg L, Dabovic B, Hadjiolova K, and Rifkin DB 2015 *Matrix Biol. J. Int. Soc. Matrix Biol.* **47** 44–53
- Roeyen CR van *et al.* 2013 *Cell Commun. Signal.* **11** 63
- Schinke T, Amendt C, Trindl A, Pöschke O, Müller-Esterl W, and Jahnen-Dechent W 1996 *J. Biol. Chem.* **271** 20789–96
- Somasekharan SP *et al.* 2015 *J. Cell Biol.* **208** 913–29
- Sorokin AV *et al.* 2005 *EMBO J.* **24** 3602–12
- Sroga GE, Karim L, Colón W, and Vashishth D 2011 *Mol. Cell. Proteomics MCP* **10** <https://doi.org/10.1074/mcp.M110.006718>
- Stenn KS, Link R, Moellmann G, Madri J, and Kuklinska E 1989 *J. Invest. Dermatol.* **93** 287–90
- Stratton KG *et al.* 2019 *J. Proteome Res.* **18** 1418–25

- Swift J *et al.* 2013 *Science* **341** 1240104
- Tare RS, Oreffo ROC, Sato K, Rauvala H, Clarke NMP, and Roach HI 2002 *Biochem. Biophys. Res. Commun.* **298** 324–32
- Termine JD, Belcourt AB, Conn KM, and Kleinman HK 1981 *J. Biol. Chem.* **256** 10403–8
- The Gene Ontology Consortium 2019 *Nucleic Acids Res.* **47** D330–8
- The UniProt Consortium 2019 *Nucleic Acids Res.* **47** D506–15
- Tourrière H, Chebli K, Zekri L, Courselaud B, Blanchard JM, Bertrand E, and Tazi J 2003 *J. Cell Biol.* **160** 823–31
- Trackman PC 2016 *Matrix Biol. J. Int. Soc. Matrix Biol.* **52–54** 7–18
- Tyanova S, Temu T, and Cox J 2016 *Nat. Protoc.* **11** 2301–19
- Ueland T, Stilgren L, and Bollerslev J 2019 *Int. J. Mol. Sci.* **20** <https://doi.org/10.3390/ijms20122896>
- Valverde P, Zhang J, Fix A, Zhu J, Ma W, Tu Q, and Chen J 2008 *J. Bone Miner. Res. Off. J. Am. Soc. Bone Miner. Res.* **23** 1775–88
- Walchli C, Koch M, Chiquet M, Odermatt BF, and Trueb B 1994 *J. Cell Sci.* **107** 669–81
- Wendel M, Sommarin Y, and Heinegård D 1998 *J. Cell Biol.* **141** 839–47
- Werner HB *et al.* 2007 *J. Neurosci.* **27** 7717–30
- Wieczorek S *et al.* 2017 *Bioinformatics* **33** 135–6
- Woolley AG *et al.* 2011 *PLoS ONE* **6** <https://doi.org/10.1371/journal.pone.0020603>
- Wu M, Chen G, and Li Y-P 2016 *Bone Res.* **4** 16009
- Wu W, Wong K, Chen J, Jiang Z, Dupuis S, Wu JY, and Rao Y 1999 *Nature* **400** 331–6
- Xiao Z *et al.* 2007 *J. Cell. Physiol.* **210** 325–35
- Yang X, Tare RS, Partridge KA, Roach HI, Clarke NM, Howdle SM, Shakesheff KM, and Oreffo RO 2003 *J. Bone Miner. Res.* **18** 47–57

III. DISCUSSION

Rothmund-Thomson type II syndrome (RTS-II) patients, presenting mutations in the *RECQL4* gene, display, besides other symptoms, skeletal and skin abnormalities, accompanied by accelerated aging of both tissues. The specific injury of these two tissues raises the question of whether there is a particular link between the RECQL4 helicase and the extracellular matrix (ECM), which plays an important role in the biology of these two connective tissues.

To the best of my knowledge, no such connection has as yet been established. In addition, the known functions of RECQL4, such as its roles in DNA replication, DNA repair, telomere as well as mitochondrial genome maintenance⁵²¹, do not suggest an obvious link between this helicase and the extracellular matrix. The goal of this project was to investigate the role of RECQL4 in bone tissue biology and to determine if RECQL4 dysfunction could affect bone ECM.

Our first objective was to establish if RECQL4-deficient mice available in the laboratory could serve as the appropriate model for this project, *i.e.* if they recapitulate the skeletal phenotype observed in RTS-II patients. This model has been generated in Dr. G. Luo laboratory (Department of Genetics, Case Western Reserve University, Cleveland)⁵³⁰. The authors have reported chromosomal instability found in cells from the mutant mice. They also described skin abnormalities (hypo- or hyperpigmentation of the tail) and skeleton defects (such as inborn polydactyly and a range of palatal deformities) in these *Recql4*^{-/-} mice. While our RECQL4-deficient mice also developed tail skin pigmentation deficiency by the age of 6 months, they exhibited neither polydactyly nor palatal patterning defects. This might be due to differences in the genetic background between the mice studied in the two laboratories: 75% B6 / 25% 129S7 in G. Luo's lab and 95 % B6 in our case. On the other hand, detailed

examination of bone phenotype in our *Recq14*^{-/-} mice showed accelerated bone aging in both sexes, illustrated by premature bone loss and by deleterious alterations of trabecular architecture as evidenced by microCT examination of femurs and caudal vertebrae. Similar modifications have already been described for the normal bone aging in mice^{242,243} and humans⁵⁸⁵, and for the premature bone aging in the RTS-II patients^{508,509}. Therefore, this mouse model is relevant for the exploration of the mechanism underlying bone loss in RTS-II patients and also for the characterization of potential bone ECM modifications induced by RECQL4 dysfunction.

It is very difficult to define the term “aging”. The best approximation is the functional decline caused by the passage of time. In every tissue throughout the body its primary cause is thought to be the accumulation of cellular and molecular damage that eventually leads to tissue dysfunction⁵⁸⁶. In bone, this deterioration is manifested as osteoporosis. Many mechanisms of bone aging have been described including, genomic instability⁵⁸⁷.

Our understanding of the relationship between age-related bone loss and impaired DNA metabolism is based on a few mouse models that were generated to recapitulate human progeroid syndromes, generally associated with the loss-of-function mutations in genes implicated in genome maintenance^{587,588}, and on the examination of human patient’s cells (usually fibroblasts) *ex vivo*⁵⁸⁹. The best characterized of these syndromes are Hutchinson-Gilford progeria syndrome (HGPS) and Werner syndrome (WS). In HGPS the accumulation of the truncated form of Lamin A known as Progerin within the nuclear matrix leads to the disruption of nuclear shape and of chromatin organization⁵⁹⁰. WS is caused by the mutation in *WRN*, another RecQ family helicase involved in DNA repair and telomere maintenance.

Similar to RECQL4-deficient mice, murine models for HGPS and WS are characterized by low bone mass⁵.

One of the mechanisms proposed for the premature aging of various tissues in all three models – the HGPS^{591–593}, the WS^{594,595} and the RTS-II⁵⁴⁵ – is cellular senescence, a state of permanent cell cycle arrest, leading to the exhaustion of adult stem cell pool and decreased tissue regeneration potential. The primary driver for the senescence in the HGPS and the WS is thought to be telomere dysfunction^{594,596}, which is not the case for RTS-II, where senescence is due to the unresolved DNA damage at non-telomeric sites⁵⁴⁵.

Lu *et al.* have used for their study the same mouse model as us. They have observed in RECQL4-deficient mice a decreased number of blood cells, attributed to the higher number of senescent bone marrow cells, as revealed by SA-βGal (Senescence-Associated-beta-Galactosidase) staining, p21 expression and quantification of DNA damage foci⁵⁴⁵. It is therefore surprising that we did not see any sign of increased senescence in our *Recq14*^{-/-}-derived cells.

The absence of the reliable and accurate markers makes senescence detection difficult and uncertain. For example, transient DNA damage induces the expression of p21 leading to a reversible cell cycle pause that provides time for DNA repair⁵⁹⁷. Therefore, even simultaneous presence of the DNA damage and of high levels of p21 does not necessarily mean that the cell is senescent. Moreover, the most widespread senescence marker, the SA-βGal activity, is enriched in mature activated macrophages and osteoclasts^{598,599} potentially found among bone marrow cells. This enzymatic activity is also high when cells are maintained at confluence for prolonged periods⁶⁰⁰.

Although it cannot be formally ruled out that there are more senescent bone cell precursors in *Recql4*^{-/-} mice than in *Recql4*^{+/-} mice, several of our observations argue against it. Indeed, bone marrow cellularity was similar in the mutant and the control mice (submitted manuscript, Figure 5A). Moreover, the flow cytometry analysis of *Recql4*^{+/+}, *Recql4*^{+/-} and *Recql4*^{-/-} marrow cells (2 mice per genotype) did not reveal significant difference in numbers of any hematopoietic or mesenchymal cell types (not shown). CFU-assay results also led to the conclusion that the frequency of mesenchymal progenitors was comparable in *Recql4*^{+/-} and *Recql4*^{-/-} mice (submitted manuscript, Figure 6A). Pre-osteoblasts isolated from control or mutant mice exhibited similar proliferation rates (submitted manuscript, Figure 6B). And, although SA-βGal activity was generally high in our *ex vivo* osteoblast and bone marrow cell cultures (derived from 60-weeks old mice), it was equally high in *Recql4*^{+/-} and *Recql4*^{-/-} cells (not shown). Finally, according to the proteomic analysis of the mineralized matrices (appendix 2), we do not see any accumulation in the *Recql4*^{-/-} ECM of the secreted senescence markers, such as the plasminogen activator inhibitor type-1 (*Serpine1*, FC 0.96)^{601,602} and IGFBP3 (insulin-like growth factor binding protein-3, FC 0.77)^{603,604}.

The difference with the study from Bohr laboratory⁵⁴⁵ may well be the cell types that we examined (cells of the osteoblastic lineage in our case versus fibroblasts and cultured primary bone marrow cells for Lu *et al.*), since senescence phenotype can be heterogeneous and, depending on the stress, could be triggered in certain cell types but not others^{605,606}. Nevertheless, our investigations seem to rule out bone cell senescence as the cause of the premature skeletal aging in our model.

Our further research revealed that the differentiation and function of the osteoclasts was not activated by RECQL4 deficiency: neither by cell-autonomous mechanisms, nor via paracrine action of osteoblasts. And though the extracellular

matrices produced *ex-vivo* by the *Recq14*^{-/-} osteoblasts were less mineralized than those synthesized by *Recq14*^{+/-} osteoblasts, the difference did not reach statistical significance. However, the observed trend indicated a possible alteration of the *Recq14*^{-/-} osteoblast secretion, the hypothesis that got further support from the analysis of *Recq14*^{-/-} ECM.

Indeed, based on the AFM analysis, the organic part of the *Recq14*^{-/-} ECM is more rigid compared to the control ECM, despite equal amounts of collagen deposited by the osteoblasts of both genotypes. Several mechanisms could account for the matrix stiffening, one of them being the increased number of collagen crosslinks⁶⁰⁷. These can form via two mechanisms: either through enzymatic reaction mediated by lysyl oxidases (LOX) or through spontaneous glycation leading to AGE (Advanced Glycation End-products)³¹³. At the same time, proteomic analysis of mineralized ECM in our model shows an over-abundance of the LOX4 enzyme in mutant matrix, which could explain, at least partially, the increased rigidity of the *Recq14*^{-/-} ECM. The small leucine-rich repeat proteoglycan Decorin (DCN), also over-represented in the *Recq14*^{-/-} ECM, could be another stiffening factor, since it forms bridges between neighboring collagen fibrils and could serve as a molecular cross-linker^{608,609}.

The formation of AGE is mostly due to the presence of reducing sugars, such as glucose and fructose, and *in vivo* takes place over a period of weeks⁶¹⁰. However, oxidative stress can accelerate the AGE generation⁶¹¹. We have detected similar levels of the ROS in *Recq14*^{+/-} and *Recq14*^{-/-} osteoclastic precursors (Figure 5B, submitted manuscript), but have not verified it in osteoblasts. Therefore, and despite the fact that our osteoblast cultures were maintained in identical conditions (implying equal amount of sugars in the medium), we cannot exclude that there might be a difference in AGE accumulation according to genotype. This remains to be verified experimentally.

A recent study suggests that modifications leading to a stiffer bone matrix could promote bone resorption⁶¹². This is consistent with our observation of larger bone perimeter covered by osteoclasts in RECQL4-deficient mice. Thereby altered rigidity of the ECM could be one of the mechanisms leading to the premature bone loss in our model.

Another alteration of the *Recql4*^{-/-} matrix revealed by proteomic analysis is the lack of two osteoblast chemoattractant molecules: pleiotrophin⁶¹³ and SLIT3²⁶. This deficiency could result in diminished osteoblast recruitment to the remodeling sites, effect that would accumulate with that of increased resorption due to the rigidity of the matrix.

Taken together, our results suggest that RECQL4 dysfunction is associated with bone ECM alterations, even if underlying mechanisms remain to be clarified. One tantalizing possibility could be the role played by the multifunctional nucleic acid-binding protein YB1, over-abundant in mutant matrix (Appendix 2). YB1 participates in DNA repair, pre-mRNA transcription and splicing, mRNA packaging, and regulation of mRNA stability and translation⁶¹⁴. The study of Mo *et al.* demonstrated that physical interaction of RECQL4 and YB1 promotes phosphorylation and nuclear translocation of the latter⁶¹⁵. Thereby the absence of functional RECQL4 could lead to the cytoplasmic accumulation of the YB1. There, YB1 may affect cell in various ways. On the one hand, it can inhibit translation of multiple mRNAs⁶¹⁶, possibly including those encoding proteins lacking in the *Recql4*^{-/-} matrix. On the other hand, in the cytoplasm, YB1 is susceptible to the proteolytic cleavage associated with the stress response to DNA damage⁶¹⁷ which could be a common occurrence in the RECQL4-deficient cells. Resulting proteolytic YB1 fragments can then reach the extracellular space^{618,619} or the nucleus, where they display biological activity distinct

from that of the full-length protein^{620,621}, thus adding possibilities for modifying gene expression. For example, over-expression of the N-terminal YB1 fragment in the murine NIH3T3 cells has been shown to down-regulate the expression of decorin⁶²², while the over-expression of the full-length YB1 in the human premalignant breast epithelial MCF10AT cells enhances decorin's transcription and translation⁶²³. Full-length YB1 can also be secreted^{624,625}, although its extracellular role is controversial, either mitogenic⁶²⁶ or anti-proliferative⁶²⁴, and possibly cell type specific⁶¹⁸. The hypotheses involving the role of this protein in RECQL4-deficiency induced pathogenesis are numerous and have to be investigated in orderly fashion, starting probably with the precise identification of the extracellular YB1 found over-represented in the *Recq14*^{-/-} matrix, followed by the analysis of YB1 intra- and extra-cellular distribution, before finally conducting functional studies of the YB1 effect on the bone cells in our model.

In this study we have characterized the bone phenotype in mice with bi-allelic constitutive deletion of the *Recq14* helicase domain. This mouse model, which shows accelerated bone loss reminiscent of age-related osteopenia, could be useful both for studying how altered DNA metabolism affects bone biology and for exploring new mechanisms governing normal bone aging. We have also demonstrated a senescence-independent modification of the *Recq14*^{-/-} extracellular matrix and identified several mechanisms that could underlie accelerated bone loss induced by RECQL4 deficiency. I believe that my project opened up promising new avenues for research on the interaction between the ECM and bone cells.

RESULTS PART 2

THE EFFECT OF NATURAL URANIUM ON THE OSTEOCLASTS.

I.	Publication	
	“Natural uranium impairs the differentiation and the resorbing function of osteoclasts”.....	181 - 193
II.	Manuscript in preparation	
	“The effect of uranium-modified extracellular matrix on osteoclasts”.....	194 – 225
III.	Discussion.....	226 - 233

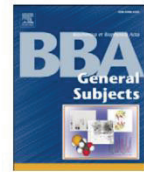
I. PUBLICATION

Biochimica et Biophysica Acta 1861 (2017) 715–726



Contents lists available at ScienceDirect

Biochimica et Biophysica Acta

journal homepage: www.elsevier.com/locate/bbagen

Natural uranium impairs the differentiation and the resorbing function of osteoclasts



Tatiana Gritsaenko^a, Valérie Pierrefite-Carle^a, Thomas Lorivel^b, Véronique Breuil^{a,c},
Georges F. Carle^a, Sabine Santucci-Darmanin^{a,*}

^a UMR E-4320 TIRO-MATOs CEA/DRF/BIAM, Université Nice Sophia-Antipolis, Faculté de Médecine Nice, 28 avenue de Valombrose, 06107, Nice, France

^b Institut de Pharmacologie Moléculaire et Cellulaire, UMR7275, CNRS, Université Nice Sophia-Antipolis, 660 route des Lucioles, 06560, Valbonne, France

^c Service de Rhumatologie, CHU de Nice, Nice, France

ARTICLE INFO

Article history:

Received 23 August 2016

Received in revised form 13 December 2016

Accepted 5 January 2017

Available online 9 January 2017

Keywords:

Uranium

Osteoclast

Osteoclastogenesis

Resorption

SQSTM1/p62

ABSTRACT

Background: Uranium is a naturally occurring radionuclide ubiquitously present in the environment. The skeleton is the main site of uranium long-term accumulation. While it has been shown that natural uranium is able to perturb bone metabolism through its chemical toxicity, its impact on bone resorption by osteoclasts has been poorly explored. Here, we examined for the first time *in vitro* effects of natural uranium on osteoclasts.

Methods: The effects of uranium on the RAW 264.7 monocyte/macrophage mouse cell line and primary murine osteoclastic cells were characterized by biochemical, molecular and functional analyses.

Results: We observed a cytotoxicity effect of uranium on osteoclast precursors. Uranium concentrations in the μM range are able to inhibit osteoclast formation, mature osteoclast survival and mineral resorption but don't affect the expression of the osteoclast gene markers *Nfatc1*, *Dc-stamp*, *Ctsk*, *Acp5*, *Atp6v0a3* or *Atp6v0d2* in RAW 274.7 cells. Instead, we observed that uranium induces a dose-dependent accumulation of SQSTM1/p62 during osteoclastogenesis.

Conclusions: We show here that uranium impairs osteoclast formation and function *in vitro*. The decrease in available precursor cells, as well as the reduced viability of mature osteoclasts appears to account for these effects of uranium. The SQSTM1/p62 level increase observed in response to uranium exposure is of particular interest since this protein is a known regulator of osteoclast formation. A tempting hypothesis discussed herein is that SQSTM1/p62 dysregulation contributes to uranium effects on osteoclastogenesis.

General significance: We describe cellular and molecular effects of uranium that potentially affect bone homeostasis.

© 2017 Elsevier B.V. All rights reserved.

1. Introduction

Uranium (U) is a radioactive heavy metal naturally present in soils, air, water and therefore in animal and human diet. Its extensive use in civil and military activities has led to an increased risk of exposure to U, not only for workers engaged in milling and mining, but also for populations. Naturally occurring U is composed of 99.27% ²³⁸U, 0.72% ²³⁵U and 0.006% ²³⁴U and is found, in most environmental systems, in its oxocationic form {U(VI)O₂²⁺} (called uranyl form and referred to as U(VI) below). Due to the very low specific activity of its main component ²³⁸U, radiological toxicity of natural U(VI) is minimal while its chemical toxicity is well established. Individuals can be exposed to U(VI) by ingestion, inhalation and dermal contact. In all cases, most of U(VI) entering the body is eliminated in feces and only a small part reaches the bloodstream. 80 to 90% of the uranium present in the blood is filtered through the kidneys and

cleared within a few days in urine [58]. The remainder is mostly deposited in bones and kidneys, as assessed by animal studies [4,43] and follow-up of human exposure [23,24,29,53].

In bones, U(VI) accumulates mainly near vascularized areas and sites of active calcification [3,6,49]. With a half-life retention of 70 to 200 days the removal of uranium stored in the bone is slow [3]. Thus a fraction of the absorbed uranium remains trapped in bones for several decades and the skeleton is considered as the major site of long-term storage of U(VI) [4,33,56]. Therefore, several animal and human studies have explored the effect of U(VI) on bone metabolism. Acute as well as chronic exposure to U(VI) have been shown to inhibit bone formation in rats [7, 10, 16, 17, 55, 57]. Consistently, *in vivo* and *in vitro* studies have demonstrated that both the number and the activity of osteoblasts, the cells responsible for bone formation and mineralization, were altered by U(VI) [7, 10, 38, 54]. More recently, our team has shown that U(VI) perturbs osteoblastic functions by reducing mineralization capacity. In addition, our results suggest that U(VI) exerts its toxicity in osteoblasts in part through the inhibition of autophagy, a major cellular catabolic process [46].

* Corresponding author at: UMR E-4320 TIRO-MATOs CEA/DRF/BIAM, Faculté de Médecine, Avenue de Valombrose, 06107 Nice cedex 2, France.
E-mail address: santucci@unice.fr (S. Santucci-Darmanin).

While a number of studies have focused on the effect of U(VI) on bone formation and osteoblasts [2], the impact of U(VI) on bone resorption has been poorly explored. Ubios et al. have observed an increase in bone resorption of the alveolar bone after intraperitoneal injection of uranyl nitrate in Wistar rats [55]. Analysis of histomorphometric parameters of mouse metaphyseal bone, after oral administration of a lethal dose of uranyl nitrate, has also revealed an extension of resorption surfaces compared to untreated animals [7]. These results are not confirmed by those of Fukuda et al. [15]. Indeed, after an intramuscular injection of depleted uranium to rats, the authors have failed to detect any significant modification in bone resorption of proximal tibial metaphyses [15]. Besides animal studies, several epidemiological investigations have addressed the question of the health effects of naturally occurring uranium in drinking water [59]. Among them, the study from Kurttio et al. [30] provided some evidence of a positive association (only in males) between uranium exposure and serum levels of carboxy-terminal telopeptide, an indicator of bone resorption. The aforementioned *in vivo* studies have led to the proposal that U(VI) could promote bone resorption. Nonetheless, as far as we know, the cellular and molecular mechanisms underlying this possible effect of uranium have never been explored. Bone resorption is performed by large multinuclear cells, called osteoclasts. These cells result from the fusion of precursor cells of hemopoietic origin and are unique in their ability to solubilize both the mineral and organic components of the bone matrix [20].

In the present study, we examined for the first time the effect of natural uranium on osteoclast differentiation and function. Moreover, we sought to identify molecular signaling pathways disrupted by exposure of osteoclastic cells to uranium.

2. Materials and methods

2.1. Uranium exposure

Uranium solutions were prepared extemporaneously in conditions allowing the control of uranium speciation in exposure cell culture media [39]. First, an uranyl acetate stock solution ($[UO_2^{2+}] = 100$ mM, pH 4) was diluted to 10 mM in a cold sodium bicarbonate aqueous solution ($[HCO_3^-] = 100$ mM, Sigma-Aldrich, #S8761), thus bringing the pH to 7.0. This intermediate solution was equilibrated for 3 h at room temperature. Next, appropriate amounts of the 10 mM uranyl solution were diluted drop by drop to desired working concentration in the following basic culture medium: alpha modified Minimum Essential Medium (α MEM, Lonza, #BE12-169F) with 2 mM L-Glutamine (Sigma-Aldrich, #G7513) and supplemented or not with 5% HyClone fetal bovine serum (Thermo Scientific, #SH30071.03). A control medium was prepared simultaneously by adding the amount of bicarbonate used in the most concentrated U(VI)-treated condition, to the basic medium. Resulting control and uranium-containing media were then incubated for 3 h at room temperature before being added to cells.

2.2. Care of animals

The mice were housed and bred in the Faculty of Medicine animal facility, University of Nice, France. The procedures for the care and sacrifice

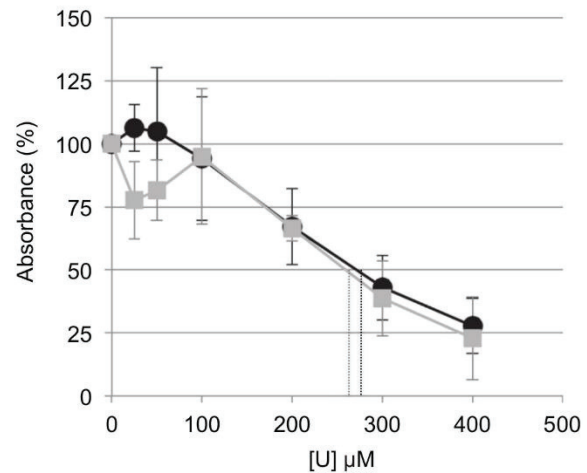


Fig. 1. Uranium (VI) cytotoxicity in the RAW 264.7 cell model. RAW 264.7 cells were exposed for 24 h to the indicated concentrations of U(VI) in culture medium containing (black circle) or not (grey square) 5% of fetal bovine serum. The colorimetric MTT assay was used to evaluate cytotoxicity. Relative absorbance values presented are the means \pm standard deviation of 5 independent experiments each performed in triplicate. Mean absorbance in the control condition (without U) is set as 100%.

of the animals were in accordance with the EU Directive 2010/63/EU for animal experiments and approved by the local experimentation committee. For bone marrow culture, 3 month-old C57BL/6 mice were killed by cervical dislocation. Femur and tibia were then dissected out and processed in sterile conditions as described below.

2.3. Cell culture

The mouse monocyte/macrophage cell line RAW 264.7 was purchased from American Type Culture Collection (#TIB-71) and cultured in Dulbecco's modified Eagle medium (DMEM, Lonza, #BE12-604F/12) supplemented with 5% HyClone serum and antibiotics (100 IU/ml penicillin and 100 μ g/ml streptomycin, Sigma-Aldrich, #P4333). Cells were grown in 75 cm² flasks and passed by mechanical scrapping. Only cells from passages 5 to 9 were used in our experiments. Where indicated, cells were incubated for 2 h with 100 nM of Bafilomycin-A1 (Sigma-Aldrich, #B1793).

Bone marrow cells were flushed-out from cleaned long bones with Dulbecco's phosphate buffered saline modified (Sigma-Aldrich, #D8537) dispensed by a 2.5 ml syringe with a 26-gauge needle. After the red blood cells were removed with ACK buffer (0.01 mM EDTA, 0.011 M KHCO₃, and 0.155 M NH₄Cl, pH 7.3), the bone marrow cells were suspended in alpha-MEM containing 10% HyClone fetal bovine serum complemented with 2 mM L-Glutamine and cultured for 24 h in the presence of 10 ng/ml M-CSF (PeproTech, #315-02). The nonadherent cells were collected and used as bone marrow-derived macrophages (BMM) for osteoclast differentiation experiments.

Table 1
Primer sequences.

Gene	Accession number	Forward primer	Reverse primer
<i>Rplp0</i>	NM_007475.5	5'-TCCAGGCTTTGGGCATCA-3'	5'-CTTATCAGCTGCAGATCACTCAGA-3'
<i>Nfatc1</i>	NM_016791.4	5'-TGAGGCTGGTCTCCGAGTT-3''	5'-CGTGGGAACACTCGATAGG-3''
<i>Acp5</i>	NM_007388.3	5'-TGCCTACCTGTGGACATGA-3''	5'-CACATAGCCACACCGTTCTC-3''
<i>Dc-stamp</i>	NM_029422.4	5'-AAGCGGAACCTAGACACAGGG-3'	5'-AAGCGGAACCTAGACACAGGG-3'
<i>Ctsk</i>	NM_007802.4	5'-CAGCAGAGGTGTACTATG-3''	5'-GCGTTGTCTTATCCGAGC-3''
<i>ATP6v0d2</i>	NM_175406.3	5'-CCTTTGTTGACGCTGTCCG-3'	5'-ATTGCCTGTTGAATGCCAGC-3'
<i>ATP6v0a3</i>	NM_001167784.1	5'-GGACCATATCCCTTT GGCAIT-3'	5'-AAAGCTCAGGTGGTTCGTGG-3'

2.4. Cytotoxicity assays

Uranium cytotoxicity on RAW 264.7 cells was determined by using the MTT (methylthiazol tetrazolium) colorimetric assay that assesses cell metabolic activity and therefore cell viability. 24 h after seeding in 24-well plates at 5000 cells/cm², RAW 264.7 cells were treated with control or uranium-containing media for further 24 h. After exposure, cells were washed in PBS and incubated in the dark at 37 °C with 400 µl/well of MTT solution. This working solution was prepared by a ten-fold dilution of the MTT stock solution (5 mg/ml, Sigma-Aldrich, #M5655) in Eagle's Minimum Essential Medium without Phenol Red (EMEM, Lonza, #12-668E) enriched with 5% HyClone serum. After 2.5 h, intracellular formazan crystals were dissolved in 220 µl of DMSO (Sigma-Aldrich, #D5879) for 10 min and absorbance was read at 570 nm (formazan specific) and 690 nm (background) using a

microplate reader (SPECTROstar Nano, BMG Labtech). Background absorbance (690 nm) and 570 nm absorbance from empty wells (without cells) were subtracted to obtain corrected absorbance values for each experimental condition. After correction, absorbance values were normalized by setting the control condition ([U] = 0 µM) to 100% viability. Cytotoxicity index 50 (CI50), defined as the U(VI) concentration leading to 50% cell death after 24 h exposure was then determined using a dose-response curve showing normalized values averaged over 5 independent experiments performed in triplicate.

2.5. Osteoclast generation and TRAP staining

RAW 264.7 cells were seeded in 24-well plates at a density of 5000 cells/cm². Six hours after seeding, medium was changed to uranium containing media prepared as described above and supplemented

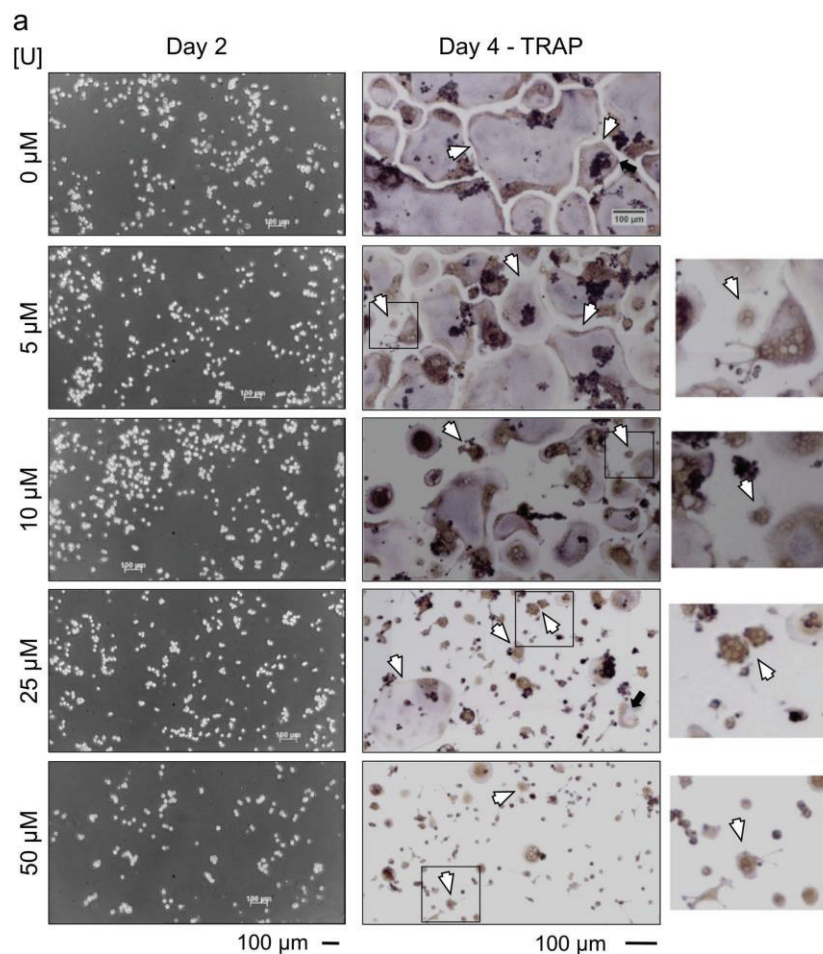


Fig. 2. RAW 264.7 osteoclastogenesis in the presence of U(VI). (a) RAW 264.7 cells cultured in the presence of the indicated concentrations of U(VI) were treated with RANKL to induce differentiation. Representative photomicrographs of cells at various times after initial addition of RANKL are shown. At day 2, cells were still mononucleated and their number decreased with increasing concentration of U(VI). At day 4, multinucleated osteoclasts positive for tartrate-resistant acid phosphatase (TRAP) activity are present in all conditions (examples are indicated with arrows), however their size decreased with increasing concentration of U(VI). Scale bar: 100 µm. Examples of small osteoclasts (boxed areas) are shown at a higher magnification. (b) The number of TRAP-positive osteoclasts (>3 nuclei) per well following 4 days of culture after RANKL-induction was determined. Data represent the respective minima, first quartile, median, third quartile and maxima of cells number obtained from 3 independent experiments each performed in triplicate. Kruskal-Wallis test: $X^2 = 33.73$, $p < 0.001$. Comparisons to control conditions: ** $p < 0.01$, *** $p < 0.001$. (c) The size of TRAP-positive osteoclasts was evaluated. Data shown were obtained from measurements of $n > 400$ cells for each condition in 3 independent experiments. Kruskal-Wallis test: $X^2 = 1105.67$, $p < 0.001$. Comparisons to control conditions: *** $p < 0.001$. (d) The colorimetric MTT assay was used to evaluate cytotoxicity of U(VI) at day 1 (white boxes) and day 2 (grey boxes) after RANKL induction of RAW 264.7 cells. Absorbance values presented were obtained from 3 independent experiments each performed in triplicate. Kruskal-Wallis test day 1: $X^2 = 5.63$, $p > 0.05$. Kruskal-Wallis test day 2: $X^2 = 35.17$, $p < 0.001$. Comparisons to control conditions: *** $p < 0.001$.

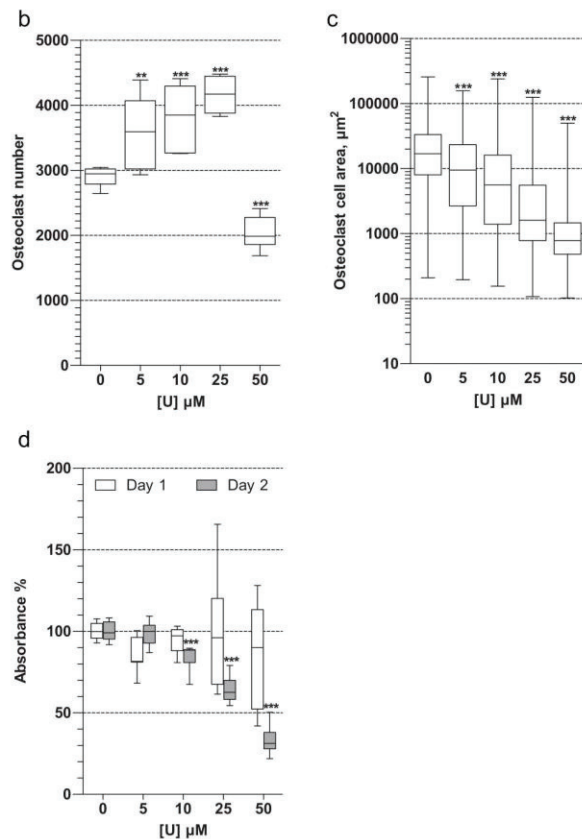


Fig. 2 (continued).

with 50 ng/ml of GST-RANKL [5] for differentiation into osteoclasts. On day 2 media were changed and on day 4 cells were fixed for 2 min at room temperature with 3% formaldehyde and 66% acetone in 7 mM citrate solution. After two washes in water, fixed cells were subjected to Tartrate-resistant acid phosphatase (TRAP) staining using Leukocyte acid phosphatase kit as described by the manufacturer (Sigma-Aldrich, #387A-1KT). Mosaic images of each well were obtained using Axio Observer Z1 motorized inverted microscope and Zen imaging software (Zeiss). Resulting images were analyzed with ImageJ software (National Institute of Health, USA) to determine osteoclast count and size in the various experimental conditions. Multinucleated (≥ 3 nuclei) TRAP-positive cells were considered as differentiated osteoclasts. Each experimental condition ([U] = 0, 5, 10, 25 or 50 μM) was tested in 3 independent experiments with three replicates per experiment.

BMM were seeded in 24-well plates at a density of 5×10^4 cells/cm². Six hours after seeding, uranium containing media supplemented with 50 ng/ml of GST-RANKL and 25 ng/ml of M-CSF were added. On day 3, media were changed and on day 5 cells were subjected to TRAP staining, as described above. Each U concentration was tested on cells isolated from different mice ($n = 4$) with two to three replicates per condition.

2.6. Pit resorption assay

RAW 264.7 cells were cultivated in differentiation conditions in 24-well Osteo assay plates that provide a synthetic inorganic bone mimetic surface (Corning Life Science, #3987). After 4 or 5 days, resulting osteoclasts were removed from the bone mimetic surface by incubation with 10% bleach for 5 min at room temperature. After two washes in water, plates were incubated 2 min with an Alizarin Red S sodium salt 1%

solution (Alfa Aesar, #42746), which stains calcium salts, and washed again in water. In order to evaluate the percentage of resorbed area, images of each well were analyzed with ImageJ software. Two to four wells per condition were analyzed in 4 independent experiments. The resorbed surface fraction was then measured using the “limit to threshold” algorithm.

Bone marrow-derived macrophages were seeded in 24-well Osteo assay plates and cultivated in differentiation conditions for 5 days. The percentage of resorbed area, was evaluated, as described for differentiated RAW 264.7 cells, from cells isolated from 4 different mice with two replicates per condition.

2.7. Real-time PCR experiments

Total RNA samples were prepared using TRIzol reagent (Life Technologies, #15596-018) following manufacturer's instructions. Reverse transcription (RT) was performed using SuperScript II reverse transcriptase (Invitrogen, #18064-022), 1 μg of RNA and random hexamer primers (Invitrogen, #48190-011). Triplicates of each 10-fold diluted cDNAs were subjected to real-time PCR analysis in an ABI PRISM 7000 system (Applied Biosystems). Reactions were performed in a 20 μl final volume using 5 μl of diluted cDNAs and MESA GREEN qPCR Mastermix Plus (Eurogentec, #RT-SY2X-03 + WOULR). Amplification conditions were: 95 °C, 2 min followed by (95 °C, 15 s, 60 °C, 1 min) cycled 40 times. Nucleotide sequences of PCR primers are shown in Table 1. Cycle thresholds (Ct) were obtained graphically (ABI PRISM 7000 Sequence Detection System version 1.2.3). ΔCt values were then calculated by subtracting the Ct value of the endogenous reference gene Rplp0 (Acidic Ribosomal Phosphoprotein P0). Relative expression was calculated as $2^{-\Delta\Delta\text{Ct}}$, $\Delta\Delta\text{Ct}$ being the difference between ΔCt of a target gene at any given point and ΔCt of the same gene at day 0. Values presented are means \pm standard deviations from 3 experiments

2.8. Cell lysis and Western blot analysis

Cells were washed with phosphate-buffered saline (PBS), scraped in ice-cold PBS with a rubber policeman and centrifuged at 500 g for 5 min. The cell pellets were resuspended directly in 10 volumes of: 60 mM Tris-HCl, pH 6.8; 2% Sodium Dodecyl Sulfate; 100 mM DL-Dithiothreitol with complete EDTA-free Protease inhibitors cocktail (Roche Diagnostics, #11836170001). The resulting lysates were homogenized by sonication using a Bioruptor (Next Gen, Diagenode) for 20 cycles: 15 s ON/30 s OFF.

Protein samples were denatured at 95 °C for 4 min in Laemmli sample buffer, separated on a SDS-polyacrylamide gel and electrotransferred to polyvinylidene difluoride membranes (Millipore, #IPV00010). Blots were blocked for 1 h with Tris-buffered saline (TBS) supplemented with 5% nonfat milk and incubated overnight at 4 °C with the primary antibodies diluted in Tris-buffered saline supplemented with 0.05% Tween 20 (TBS-T). Filters were then washed in TBS-T, incubated for 45 min at room temperature with appropriate secondary antibodies conjugated to horseradish peroxidase and washed again prior to detection of signal with ECL plus chemiluminescent detection kit (GE Healthcare, #RPN2232). Primary antibodies used in this study were mouse monoclonal anti-LC3 (MBL, #M186-3), mouse monoclonal anti- β -actin (Sigma-Aldrich, clone AC-15) and rabbit polyclonal anti-p62/SQSTM1 (Sigma-Aldrich, #A1978) antibodies.

2.9. Statistical analysis

Statistical analyses were performed with R (R Development Core Team). Due to the size of the samples and violations of parametric assumptions, we used a non-parametric approach. Data were submitted to Kruskal-Wallis test (Monte-Carlo method) followed by pairwise comparisons using Mann-Whitney test with FDR (False Discovery Rate) correction. Null hypotheses were rejected at the 0.05 level.

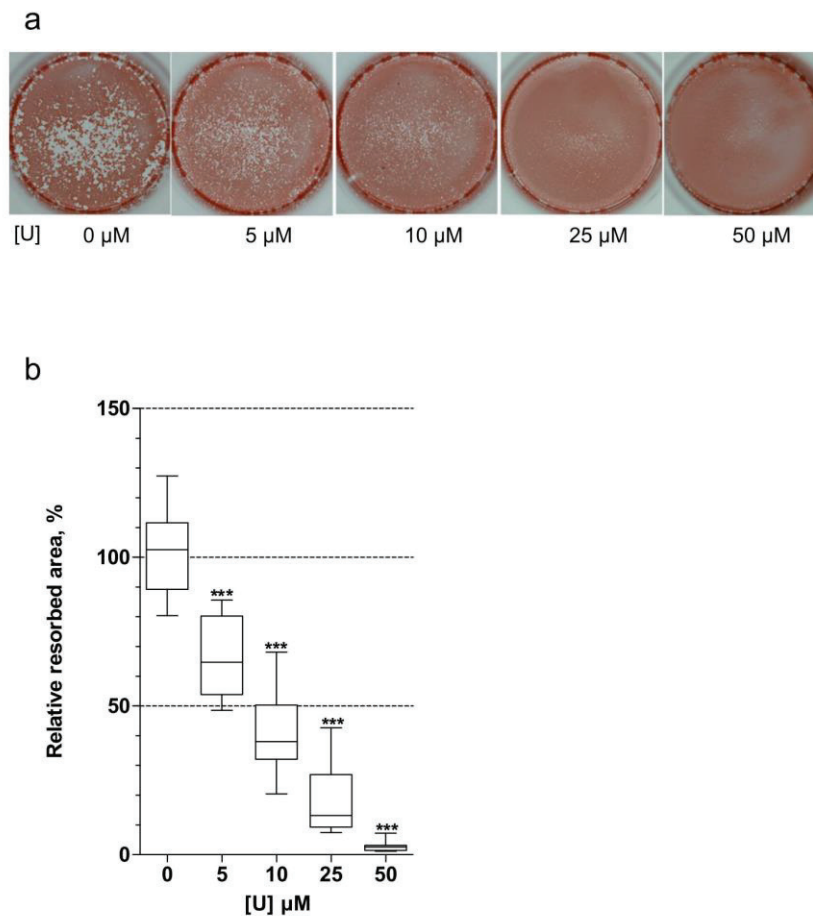


Fig. 3. Impact of U(VI) on RAW 264.7 osteoclastic resorption. Resorptive activity of osteoclasts was determined by culturing differentiating RAW 264.7 cells for 4 days on a synthetic inorganic bone mimetic surface. After 4 days, osteoclasts were removed and non-resorbed area were stained with Alizarin Red S. (a) Representative micrographs of resorbed synthetic matrix stained with Alizarin Red S. (b) Box plot representation of the relative quantification of resorbed area from 4 independent experiments with median resorbed area in control condition as 100%. Kruskal-Wallis test: $\chi^2 = 58.32$, $p < 0.001$. Comparisons to control conditions: *** $p < 0.001$.

3. Results

3.1. Effect of U(VI) on RAW 264.7 osteoclast precursors viability

RAW 264.7 are murine macrophage cells that differentiate into osteoclastic cells when cultured in the presence of RANKL for 4 or 5 days. Cytotoxicity of U(VI) was analyzed in undifferentiated RAW 264.7 cells after 24 h exposure to U(VI). Previous studies have highlighted the influence of cell culture medium composition on U(VI) speciation and cytotoxicity [8,38–41]. In particular, U(VI) forms various complexes with carbonate and proteins present in the serum [12] that could modify its cellular toxicity. For this reason, we analyzed U(VI) cytotoxicity with or without addition of 5% fetal bovine serum to the exposure medium. The viability of RAW 264.7 cells in both media was assessed by measuring cellular metabolism using a colorimetric MTT assay (Fig. 1). Dose-response curves as a function of U(VI) concentrations were drawn and used to determine a cytotoxic index (CI50) corresponding to the concentration needed to kill 50% of cells. The presence of serum in the exposure medium had no significant effect on CI50 values (285 μM in the presence of serum vs. 273 μM in the absence of serum). Thereafter, all the experiments were conducted with RAW 264.7 cells cultured in the presence of serum.

3.2. Effect of U(VI) on RAW 264.7 osteoclastic differentiation and function

The next step was to determine whether U(VI) may affect osteoclastic differentiation. For this purpose, RAW 264.7 cells were maintained in differentiation conditions for 4 days and exposed all this time to various U(VI) concentrations (5, 10, 25 and 50 μM). As expected, in control conditions (Fig. 2a, [U]: 0 μM), RAW 264.7 cells, stimulated by RANKL for 4 days, form osteoclasts defined as cells having >3 nuclei and positive for tartrate-resistant acid phosphatase (TRAP) activity staining. In the presence of U(VI), we observed a dose-dependent alteration in osteoclastic formation (Fig. 2a). When U(VI) was added at concentrations ranging from 5 to 25 μM , the number of TRAP-positive cells having 3 or more nuclei was increased compared to untreated conditions (Fig. 2a and b) but their sizes were markedly reduced and this reduction was dose-dependent (Fig. 2a and Supplementary Fig. 1). The accumulation of smaller but more numerous osteoclasts suggests that the number of cell fusion events was reduced when osteoclastogenesis occurred in the presence of 5 to 25 μM of U(VI). Exposure to 50 μM U(VI), which led to a reduction of the precursor number visible in Fig. 2a (Day 2 picture) resulted in a decrease of both the number and the size of multinucleated TRAP-positive cells (Fig. 2b and c). In order to determine whether these effects of U(VI) were caused by a decline of the

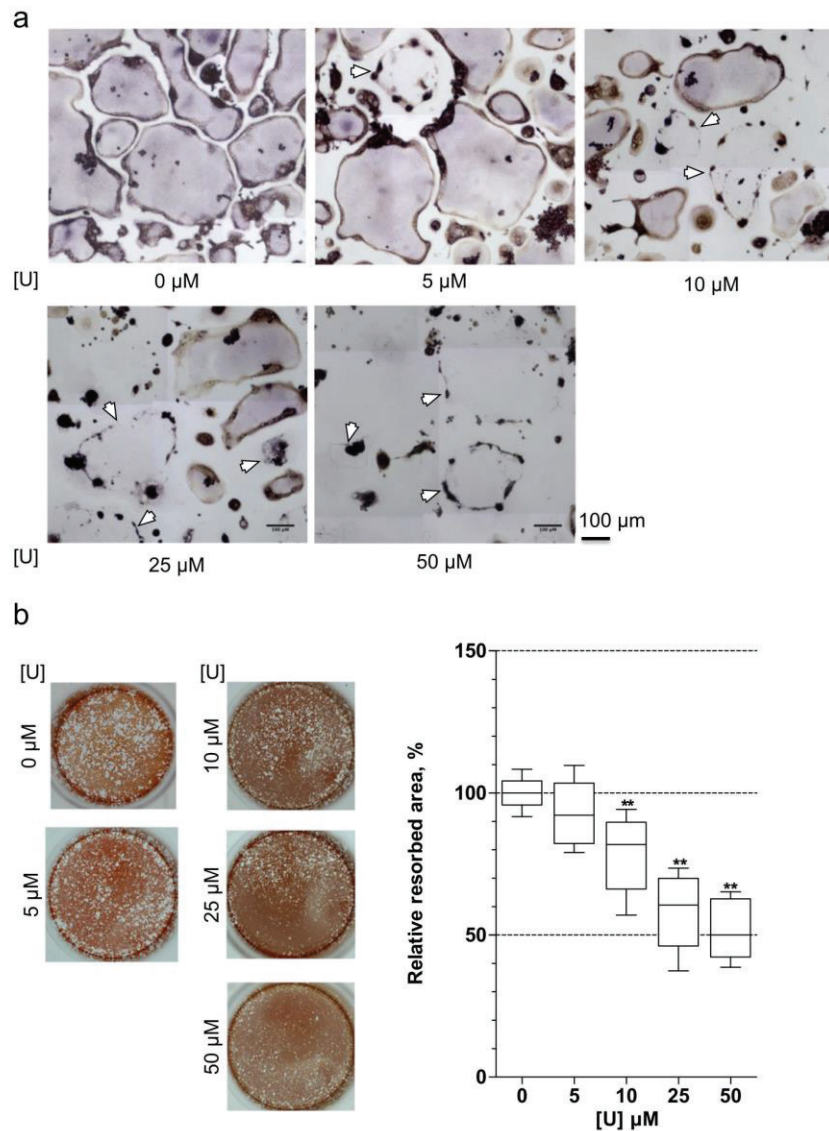


Fig. 4. Effect of U(VI) exposure on RAW 264.7 mature osteoclasts. RAW 264.7 cells were cultured in the presence of RANKL for 4 days and treated for an additional day with the indicated concentrations of U(VI). (a) Light microscopy illustrating the dose-dependent effect of U(VI) on mature osteoclasts. Examples of dead osteoclasts are indicated by arrows. (b) Quantification of resorbed area based on 4 independent experiments. Kruskal-Wallis test: $X^2 = 29.73$ $p < 0.001$. Comparisons to control conditions (arbitrarily set a 100%): ** $p < 0.01$.

number of living mononucleated precursors, we tested the viability of RAW 264.7 after 1 or 2 days of culture in the presence of RANKL and increasing concentrations of U(VI) (Fig. 2d). The viability of differentiating RAW 264.7 cells was not affected after 24 h of exposure to U(VI) concentrations up to 50 μM, while after 48 h a cytotoxic effect was observed at a dose of 10 μM [U] and above. This observation suggests that U(VI) impact on osteoclast number and size might be due in part to its effect on viability of mononuclear pre-osteoclasts, considering that the precursors density is critical for osteoclast formation [44].

Nevertheless, it is noteworthy that, when used at 5 μM, U(VI) induced both an increase of the osteoclast number (Fig. 2b) and a decrease of osteoclast size (Fig. 2c), without affecting pre-osteoclast viability (Fig. 2d). These findings suggest that U(VI) may attenuate cell fusion events, independently of its cytotoxic effect on osteoclast precursors.

We then investigated whether U(VI) is able to alter osteoclast resorptive activity. Fig. 3a shows photomicrographs of synthetic hydroxyapatite mineral surfaces where resorption has occurred in the presence of increasing concentration of U(VI). The quantified resorption areas from these experiments were determined (Fig. 3b) and these analyses indicated that U(VI) inhibits osteoclastic resorption in a dose-dependent manner.

In order to study osteoclast resorption independently of osteoclast formation, RAW 264.7 cells were treated with U(VI) for 24 h once mature osteoclasts was formed.

We first observed that U(VI) affects survival of mature osteoclasts (Fig. 4a). The median size of osteoclasts was dose-dependently reduced (Supplementary Fig. 2), reflecting the fact that the largest osteoclasts appeared to be the most sensitive to U(VI) exposure (Fig. 4a). Bone

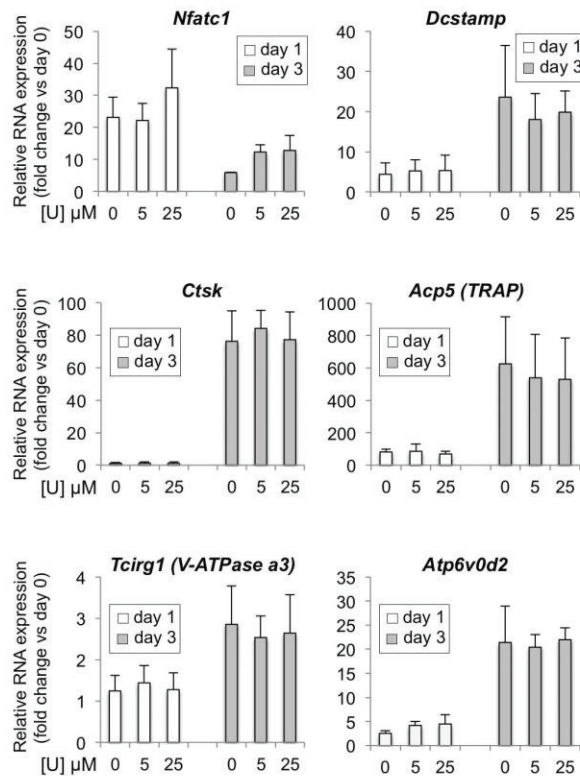


Fig. 5. Expression of osteoclast marker genes in the presence of U(VI). mRNAs from RAW 264.7 cultured in the presence of 0, 5 or 25 μM of U(VI) were prepared at day 1 and 3 after initial addition of RANKL. Quantitative analyses of transcripts were performed by real-time polymerase chain reaction (RT-PCR) using primers specific for *Nfatc1*, *Dcstamp*, *Ctsk*, *Acp5*, *Atp6v0a3* and *Atp6v0d2*. Results are reported as fold change in gene expression relative to day 0 after normalization against Rplp0. Data are presented as mean ± standard deviation; *n* = 3.

resorption was also attenuated (Fig. 4b) most probably as a result of accelerated cell death of the larger and thereby the most active mature osteoclasts [19,32].

3.3. Effect of U(VI) on the expression of osteoclast marker genes in RAW 264.7 cells

Altogether, our findings suggest that U(VI) impairs osteoclast formation and function through its cytotoxic effect on both mononucleated precursors and multinucleated mature cells. Nevertheless, as seen above, cell death does not account for all the observed effects. This prompted us to investigate U(VI) impact on molecular events involved in osteoclast differentiation and function. We thus analyzed U(VI) impact on the expression of osteoclast marker genes in RAW 264.7 cells at different stages of RANKL-induced differentiation (Fig. 5). NFATc1 is a member of the NFAT family of transcription factors and is a master regulator of the genetic program required for osteoclast differentiation and resorptive activity [25]. As expected, *Nfatc1* mRNA expression was induced at an early stage of differentiation (day 1) in control conditions ([U] 0 μM). Moreover, we found that the expression profile of this transcription factor was not affected in the presence of 5 or 25 μM uranium. We next tested the effect of U(VI) on the expression of late differentiation marker genes and we focused on genes known to be involved in cell fusion and/or resorptive activity. *Acp5* encodes a tartrate-resistant acid phosphatase (TRAP) which is highly expressed in mature osteoclasts and extensively used as marker for osteoclast differentiation.

Experimental evidences support a role for TRAP in attachment and migration of osteoclasts as well as in matrix degradation [1,13]. DC-STAMP (dendritic cell-specific transmembrane protein) is a trans-membrane protein [18] indispensable for cell fusion of osteoclasts [61]. Cathepsin K (CTSK) is a protease secreted into the extracellular compartment at the attachment site between osteoclasts and the bone surface and is a key enzyme for the degradation of the organic fraction of bone matrix [9,21]. Finally, *Atp6v0a3* and *Atp6v0d2* encodes two essential subunits (a3 and d2) of the vacuolar type H⁺-ATPase which is an ATP-driven proton pump responsible for the extracellular acidification and degradation of inorganic minerals of bone matrix [36]. In addition to being involved in the acidification of bone resorption lacunae [60], d2 is a regulator of cell fusion in osteoclast differentiation as supported by the analysis of osteoclasts from *d2* gene-deficient mice [31]. As shown in Fig. 5, the expression of all these genes was induced in a late stage of differentiation (day 3) and for all of them, levels of induction observed in the presence of 5 or 25 μM U(VI) were similar to those obtained in control conditions. Together, these results suggest that defects in osteoclast formation and function observed in the presence of U(VI) do not result from impaired induction of the key osteoclastic genes tested in our experiments.

3.4. Effect of U(VI) on the SQSTM1/p62 protein level in RAW 264.7 cells

We went on to determine the mechanisms potentially impacted by U(VI) during osteoclastogenesis by examining the level of the SQSTM1/p62 protein in differentiating RAW 264.7. SQSTM1/p62 is an important modulator of osteoclastogenesis pathway [37].

As shown in (Fig. 6a), exposure to U(VI) during osteoclast differentiation led to a dose-dependent increase of SQSTM1/p62 protein levels. Since SQSTM1/p62 is a substrate of autophagy [45], its accumulation may be caused by autophagy dysfunction. In order to examine this possibility, we monitored autophagy by western blotting quantification of the LC3-II protein, a specific marker of autophagic activity [27] (Fig. 6a). The basal level of LC3-II in differentiating RAW 264.7 cells remained unchanged in the presence of U(VI), suggesting that autophagy was not affected by U(VI) in these cells at this time point. In order to confirm these results, we analyzed both LC3-II and SQSTM1/p62 in cells treated or not by the Bafilomycin-A1 (Fig. 6b). Bafilomycin-A1 is a lysosomal proton pump inhibitor, commonly used to block a late step of the autophagic process and to impair autophagic degradation [27]. When the autophagy is functional, treatment by Bafilomycin-A1 leads to increased levels of LC3-II and autophagic substrates. As depicted in Fig. 6b, the treatment with Bafilomycin-A1 induced the accumulation of LC3-II to similar levels whether the differentiation took place in the absence or in the presence of U(VI). Bafilomycin-A1 also induced an increase of SQSTM1/p62 protein levels in cells exposed or not to U(VI) (Fig. 6b). These observations confirmed that U(VI) does not impair autophagy in RAW 264.7.

3.5. Effect of U(VI) on mouse primary osteoclastic cells

In order to explore the effects of U(VI) in a more physiological system, we investigated the consequences of U(VI) exposure on mouse primary osteoclastic cells. Bone marrow-derived macrophages (BMM) isolated from four C57BL/6 mice were maintained in differentiation condition for 5 days on either plastic or hydroxyapatite surfaces, in the presence of the indicated U(VI) concentration (Fig. 7). Both the number (Fig. 7a) and the size of TRAP-positive multinucleated primary osteoclasts (Fig. 7b) were found dose-dependently affected by exposure to U(VI). Resorption was also strongly impaired (Fig. 7c). In particular, concentration as low as 2.5 μM U(VI) resulted in a >2-fold decrease of the resorbed area (Fig. 7c). These results were in agreement with those obtained with the RAW 264.7 cell line.

We next assessed whether SQSTM1/p62 protein level increases in response to U(VI).

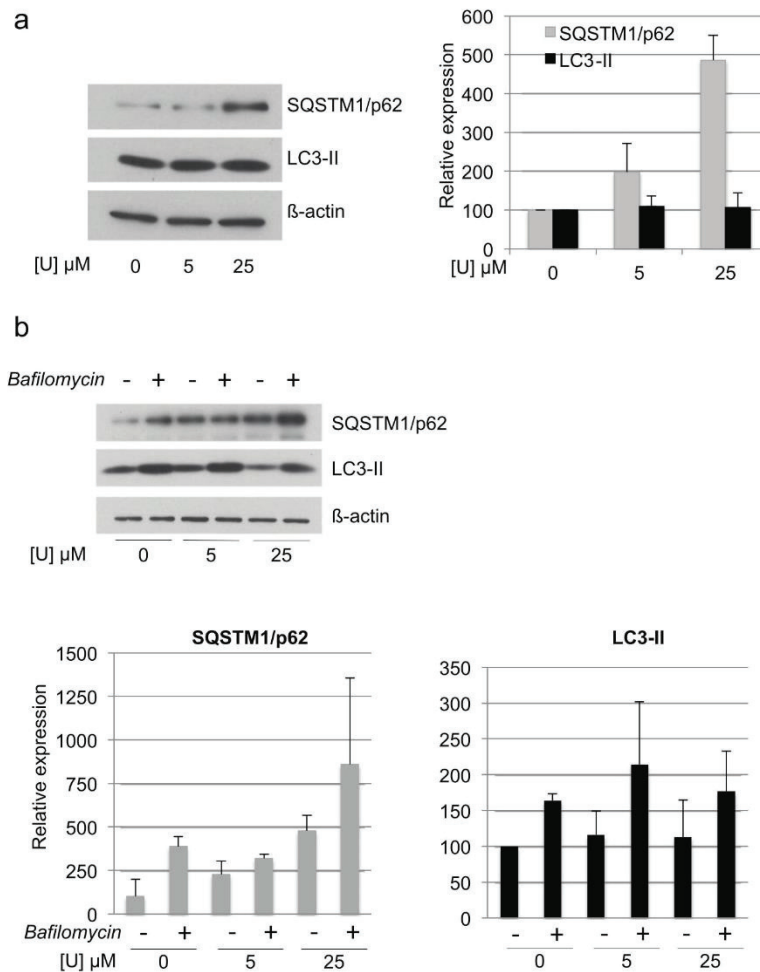


Fig. 6. SQSTM1/p62 protein level and autophagy analysis. (a) Western blot analysis of SQSTM1/p62 and LC3-II proteins in RAW 264.7, cultured in the presence of 0, 5 or 25 μM of U(VI) and of RANKL for 3 days. β -actin was used as a loading control. Graphs showing quantified data normalized to β -actin and expressed as mean \pm standard deviation are presented, $n = 3$. (b) RAW 264.7 cells cultured in the same conditions as in (a) were treated or not with bafilomycin-A1 (100 nM) for 2 h before protein extraction. A representative western blot and graphs showing the relative quantification of SQSTM1/p62 and LC3-II protein levels are presented, $n = 3$.

during primary osteoclast differentiation. As shown in (Fig. 7d), a dose-dependent accumulation of SQSTM1/p62 protein was detected in the presence of U(VI) while the level of LC3-II remained unchanged. Moreover, upon Bafilomycin-A1 treatment, LC3-II accumulated in primary osteoclasts to similar levels whether the differentiation took place in the absence or in the presence of U(VI) (Supplementary Fig. 3). These results suggested that U(VI) treatment during osteoclastogenesis promotes SQSTM1/p62 accumulation through mechanisms independent of autophagy.

4. Discussion

To the best of our knowledge, this study is the first to investigate the effect of natural uranium on resorbing bone cells. Our results showed that *in vitro* exposure to this radionuclide induces significant effects on osteoclastic cells. First, we observed a dose- and time-dependent uranium cytotoxicity response of RAW 264.7 pre-osteoclast cell line. It has been shown that uranium cytotoxicity is influenced by its speciation which itself is dependent on the composition of the cell culture medium [8,38–41]. In particular, complexation of inorganic and organic serum components with U(VI) is known to impact its speciation [12]. Here,

we observed that the presence of 5% fetal bovine serum in the exposure medium does not affect significantly U(VI) toxicity in RAW 264.7 cells. This observation does not imply that the presence of serum has no effect on U(VI) speciation, but rather that if there is a modification of the speciation, it does not affect U(VI) cytotoxicity in our conditions. This allowed us to investigate the effect of exposure to low U(VI) concentrations throughout the entire osteoclast differentiation process, which requires the presence of serum in the culture medium.

Analysis of osteoclastogenesis, by using either the RAW 264.7 model cell line or mouse primary bone marrow-derived macrophages, revealed that U(VI) impairs osteoclast formation in a dose-dependent manner. Likewise, we observed a dose-related effect of U(VI) on mineral resorption. Viewed together, our findings suggest that several mechanisms could contribute to the deleterious effects of U(VI) on osteoclast formation and function. First, experiments conducted with RAW 264.7 cells shown that after 48 h of exposure to U(VI) (from 10 to 50 μM), the number of mononucleated osteoclast precursors was significantly and dose-dependently reduced. Recently, Motiur Rahman and colleagues have clearly demonstrated that the density of pre-osteoclast at day 2 of differentiation is a critical determinant for osteoclast formation and function [44]. They have proposed that cell density governs the

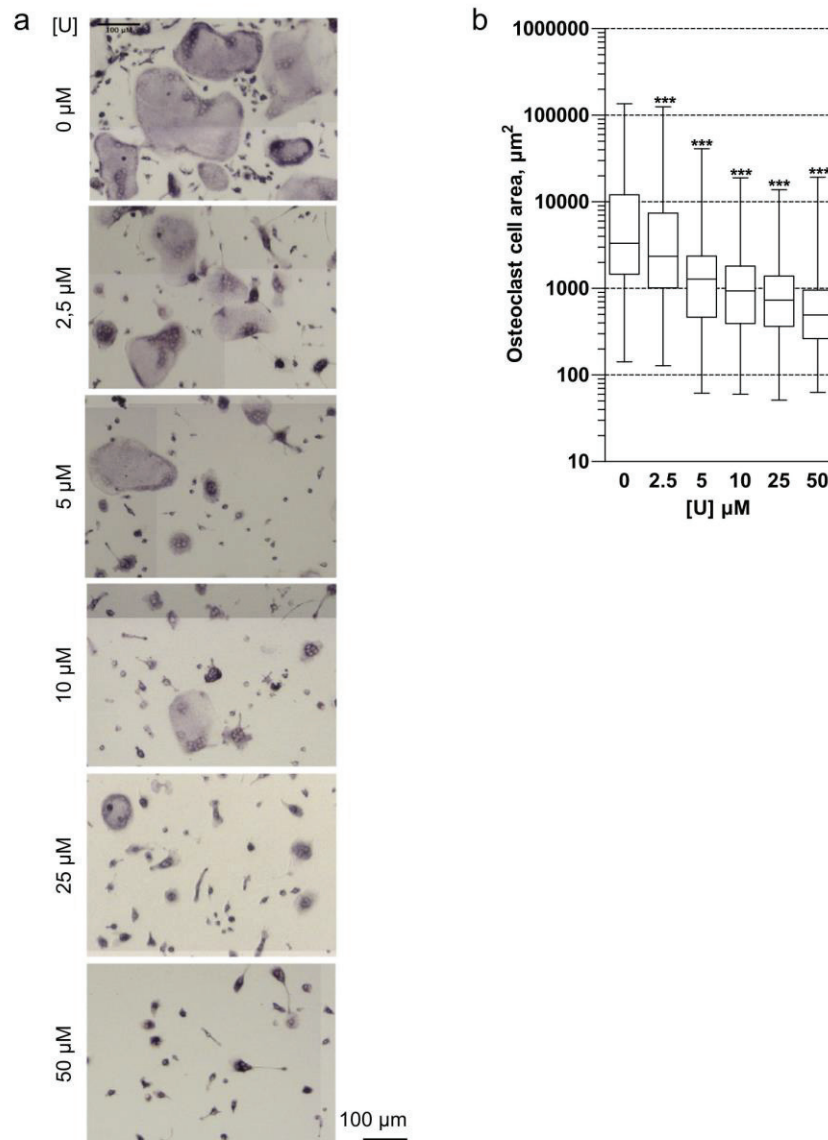


Fig. 7. Impact of U(VI) on mouse primary bone marrow-derived macrophage osteoclastogenesis. BMM from 4 mice were cultured independently, in the presence of RANKL and M-CSF to induce differentiation, and with the indicated concentrations of U(VI). (a) Micrographs of osteoclasts obtained after 5 days of culture are shown. Multinucleated and TRAP positive osteoclasts were present in all conditions but their size decreased with increasing concentration of U(VI). (b) The size of osteoclasts was evaluated from triplicates of BMM cultures derived from 4 mice. Kruskal-Wallis test: $X^2 = 790.57$, $p < 0.001$. Comparisons to control conditions: *** $p < 0.001$. (c) Differentiating BMM were cultured on an inorganic bone mimetic surface for 5 days. The resulting resorbed matrices were stained with Alizarin Red S and the relative quantification of resorbed area was performed. Kruskal-Wallis test: $X^2 = 45.026$, $p < 0.001$. Comparisons to control conditions: *** $p < 0.001$. (d) Western blot analysis of SQSTM1/p62 and LC3-II proteins, in mouse BMM after 3 days of culture with RANKL and M-CSF and in the presence of the indicated concentrations of U(VI). β -actin was used as a loading control. Graphs show quantified data normalized to β -actin and expressed as mean \pm standard deviation, $n = 4$.

opportunity for mononuclear pre-osteoclasts to come into contact with one another and/or to be incorporated into multinuclear osteoclasts. Thus, our results suggest that the impact of U(VI) on osteoclast formation is mediated in part by its cytotoxic effect on mononuclear pre-osteoclasts. Second, we observed that 5 μ M of U(VI) was sufficient to attenuate cell fusion although it had no effect on RAW 264.7 pre-osteoclastic cell viability. This observation supports that, besides its cytotoxic effect, U(VI) could impair mechanisms important for osteoclast cell fusion. These could be mechanisms involved either in the fusing process itself or in cellular migration, which is a prerequisite of cell-cell contact

and pre-osteoclast fusion [14,34]. Third, by applying treatment to mature RAW 264.7 osteoclasts, we showed that fully differentiated osteoclasts were sensitive to U(VI). Large mature osteoclasts are known to be highly resorptive but also short-lived cells [22], our findings imply that U(VI) can cause an accelerated cell death of these active cells. Finally, based on these findings, and because resorption activity is known to correlate with the size of osteoclasts [19,32], it is likely that U(VI) inhibits indirectly resorption by hampering both the formation and the survival of large osteoclasts, yet we cannot exclude the possibility that U(VI) has also a direct effect on resorption activity.

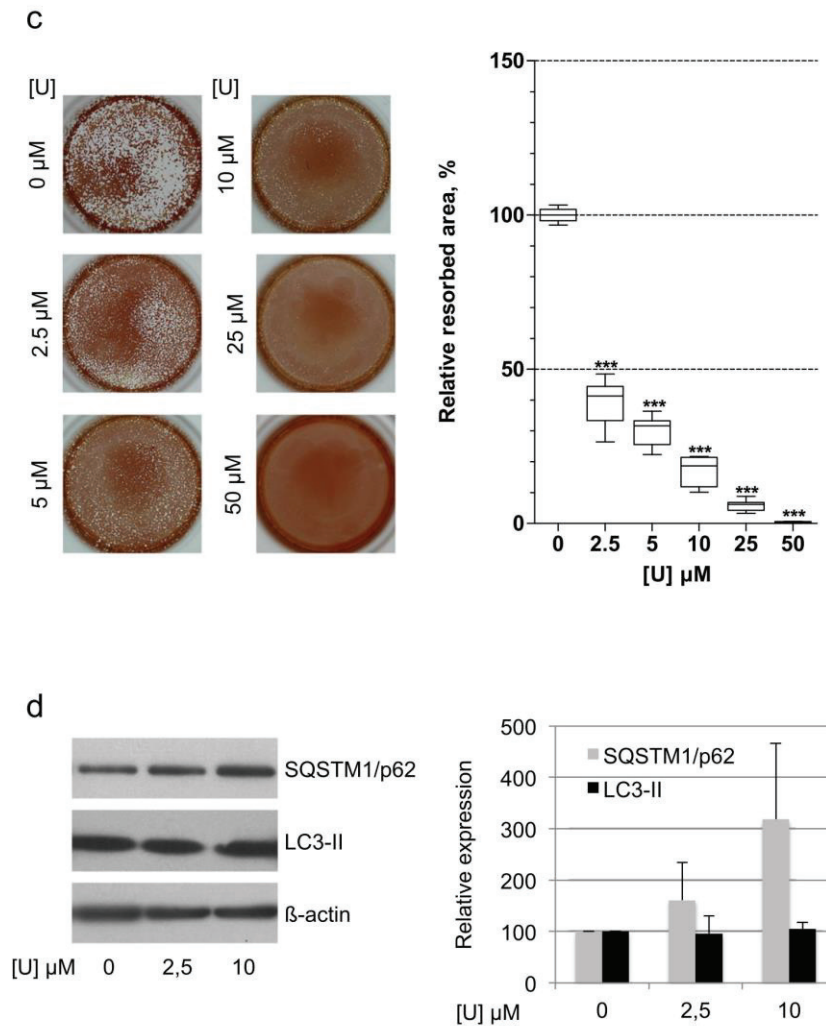


Fig. 7 (continued).

Signaling by RANKL has been extensively characterized [26]. RANKL induces the expression of the transcription factor NFATc1, through the activation of NF κ B and c-Fos. Moreover, RANKL elicits Ca²⁺ oscillations which contributes to a sustained activation of NFATc1 via a calcineurin-dependent mechanism [26]. In turn, NFATc1 activates several genes that are essential for osteoclast formation and function [25]. We found that U(VI) does not affect mRNA levels of the master transcription factor NFATc1, suggesting that upstream NF κ B, c-Fos and Ca²⁺ oscillations/calcineurin-related pathways remain unchanged in the presence of low concentrations of uranium. The same observation was made for genes expressed downstream of *Nfatc1* and involved either in cell-cell fusion (*Dc-stamp*, *ATP6v0d2*) or in resorption of bone mineral matrix (*Ctsk*, *ATP6v0a3*, *Acp5*). These findings imply that the effect of U(VI) on cell fusion (discussed above) was not caused by an inhibition of the expression of *Dc-stamp* or *ATP6v0d2* gene. We do not exclude the possibility that U(VI) impacts the abundance of the corresponding proteins. However, it is important to stress that several other factors are critical for osteoclast fusion ([42] and introduction therein; [14,34]). Although the expression of many other osteoclastogenesis-related genes remains to be analyzed, our results indicate that, at least at low doses, U(VI) has

no impact on the expression of the master regulator of osteoclast differentiation, *Nfatc1*, and several of its downstream targets.

On the other hand, we demonstrated that the SQSTM1/p62 protein accumulates in differentiating RAW 264.7 cells and mouse BMM, in response to U(VI) exposure. *Sqstm1/p62* gene mutations are involved in Paget's disease of bone (PDB), a skeletal disorder characterized by hyper-resorptive osteoclasts [48]. Thanks to its multiple protein-protein interaction domains, *Sqstm1/p62* acts as a scaffold for the formation of multiprotein complexes involved in diverse signaling pathways. In response to RANKL, *Sqstm1/p62* links TRAF6 to downstream effectors and thereby positively regulates NF κ B signaling and osteoclastogenesis [11]. Intriguingly, both overexpression [47,62] and knockdown of *Sqstm1/p62* [35] in RAW 264.7 cells, have been shown to inhibit osteoclast formation, while the expression of mutant forms of the protein in these same cells results in intensified osteoclast differentiation and resorption [47,62]. These results have contributed to the proposal that in addition to its positive role in NF κ B signaling, SQSTM1/p62 may be involved in a negative feedback mechanism after sustained NF κ B activation (reviewed in [48]). Collectively, these studies highlight the fact that dysregulation of SQSTM1/p62 expression may affect

osteoclastogenesis [37]. Therefore, it is tempting to speculate that accumulation of the SQSTM1/p62 protein may contribute to the effect of U(VI) on osteoclastogenesis. Beside its role in NfκB-dependent pathway, SQSTM1/p62 is involved in oxidative stress signaling pathway [28,50,51,62], which is also playing a crucial role in osteoclast differentiation through the regulation of NFATc1 [26]. Since U(VI) did not alter *Nfatc1* expression during the differentiation of RAW 264.7 cells, we propose that in response to U(VI) exposure SQSTM1/p62 could affect osteoclast formation through mechanisms independent of NfκB- or oxidative stress-related signalings.

SQSTM1/p62 is a ubiquitin binding protein and as such regulates ubiquitinated proteins turnover by directing them either to the proteasome or to the autophagic machinery [45,52]. Thus, one possibility is that SQSTM1/p62 accumulation induced by U(VI) promotes the degradation and thus alters the level of target proteins that are involved in osteoclast formation.

In vivo, the very few studies which assessed U(VI) effects on bone resorption, used several rodent models, various uranium doses and administration routes [7,15,55] which limited the identification of the molecular and cellular mechanisms potentially affected by U(VI). Here, using an *in vitro* approach, we provide evidence that U(VI) affects osteoclast resorption by impairing both osteoclast formation and survival. Although decreased viability of pre-osteoclasts and mature osteoclasts may account for a large part of the observed effects, our data also suggest that pre-osteoclast fusion might be hampered by U(VI) treatment. We also demonstrate that osteoclasts accumulate SQSTM1/p62 in response to U(VI) exposure. Further studies are now required to fully decipher the mechanisms acting in response to U(VI) during osteoclastogenesis, especially those leading to the accumulation of SQSTM1/p62 as well as those resulting from this accumulation. Interestingly, an induction of the SQSTM1/p62 gene expression has also been described in the renal tissue of mice acutely exposed to uranyl nitrate [63], raising the possibility that SQSTM1/p62 could be a hallmark of the cellular response to uranium chemical toxicity.

Supplementary data to this article can be found online at <http://dx.doi.org/10.1016/j.bbagen.2017.01.008>.

Compliance with ethical standards

The authors declare they have no competing financial interests.

Transparency Document

The Transparency document associated with this article can be found, in the online version.

Acknowledgments

The authors would like to thank Chantal Cros for helpful technical assistance, the Pasteur animal facility for animal care and housing and the IRCAN's Molecular and Cellular Core Imaging (PICMI) Facility. We are grateful to Drs Gaëlle Creff, Christophe Den Auwer and Claude Vidaud for helpful discussions and the procedure for preparing stable solutions of uranium salts.

This research was funded by grants of the “Commissariat à l’Energie Atomique et aux Energies Alternatives” (URANOs—Programme Transversal de Toxicologie du CEA and CPRR CEA-AREVA), the University of Nice Sophia-Antipolis and the CNRS.

References

- N.Z. Angel, N. Walsh, M.R. Forwood, M.C. Ostrowski, A.I. Cassady, D.A. Hume, Transgenic mice overexpressing tartrate-resistant acid phosphatase exhibit an increased rate of bone turnover, *J. Bone Miner. Res.* 15 (2000) 103–110.
- X. Arzuaga, M. Gehlhaus, J. Strong, Modes of action associated with uranium induced adverse effects in bone function and development, *Toxicol. Lett.* 236 (2015) 123–130.
- ATSDR, Toxicological Profile for Uranium. U. S. Department of Health and Human Services, Agency for Toxic Substances and Diseases Registry (ATSDR), Atlanta, GA, 2013.
- J.E. Ballou, R.A. Gies, A.C. Case, D.L. Haggard, R.L. Buschbom, J.L. Ryan, Deposition and early disposition of inhaled $^{233}\text{UO}_2(\text{NO}_3)_2$ and $^{232}\text{UO}_2(\text{NO}_3)_2$ in the rat, *Health Phys.* 51 (1986) 755–771.
- G.E. Beranger, D. Momier, J.-M. Guignon, M. Samson, G.F. Carle, J.-C. Scimeca, Differential binding of poly(ADP-Ribose) polymerase-1 and JunD/Fra2 accounts for RANKL-induced *Tcrg1* gene expression during osteoclastogenesis, *J. Bone Miner. Res.* 22 (2007) 975–983.
- D. Bourgeois, B. Burt-Pichat, X. Le Goff, J. Garrevoet, P. Tack, G. Falkenberg, L. Van Hoorebeke, L. Vincze, M.A. Denecke, D. Meyer, et al., Micro-distribution of uranium in bone after contamination: new insight into its mechanism of accumulation into bone tissue, *Anal. Bioanal. Chem.* 407 (2015) 6619–6625.
- C.B. Bozal, A.B. Martinez, R.L. Cabrini, A.M. Ubios, Effect of ethane-1-hydroxy-1,1-bisphosphonate (EHBP) on endochondral ossification lesions induced by a lethal oral dose of uranyl nitrate, *Arch. Toxicol.* 79 (2005) 475–481.
- M. Carrière, L. Avoscan, R. Collins, F. Carrot, H. Khodja, E. Ansoberlo, B. Gouget, Influence of uranium speciation on normal rat kidney (NRK-52E) proximal cell cytotoxicity, *Chem. Res. Toxicol.* 17 (2004) 446–452.
- J.M. Delaissé, M.T. Engsig, V. Everts, M. del Carmen Ovejero, M. Ferreras, L. Lund, T.H. Vu, Z. Werb, B. Winding, A. Lochter, et al., Proteinases in bone resorption: obvious and less obvious roles, *Clin. Chim. Acta* 291 (2000) 223–234.
- P.L. Díaz-Sylvester, R. López, A.M. Ubios, R.L. Cabrini, Exposure to subcutaneously implanted uranium dioxide impairs bone formation, *Arch. Environ. Health* 57 (2002) 320–325.
- A. Durán, M. Serrano, M. Leitges, J.M. Flores, S. Picard, J.P. Brown, J. Moscat, M.T. Diaz-Meco, The atypical PKC-interacting protein p62 is an important mediator of RANK-activated osteoclastogenesis, *Dev. Cell* 6 (2004) 303–309.
- P.W. Durbin, Actinides in animals and man, in: L.R. Morss, N.M. Edelstein, J. Fuger (Eds.), *The Chemistry of the Actinide and Transactinide Elements V. 3*, Springer, Dordrecht, The Netherlands 2006, pp. 3339–3440.
- B. Ek-Rylander, M. Flores, M. Wendel, D. Heinegård, G. Andersson, Dephosphorylation of osteopontin and bone sialoprotein by osteoclastic tartrate-resistant acid phosphatase. Modulation of osteoclast adhesion *in vitro*, *J. Biol. Chem.* 269 (1994) 14853–14856.
- C. Fiorino, R.E. Harrison, E-cadherin is important for cell differentiation during osteoclastogenesis, *Bone* 86 (2016) 106–118.
- S. Fukuda, M. Ikeda, M. Chiba, K. Kaneko, Clinical diagnostic indicators of renal and bone damage in rats intramuscularly injected with depleted uranium, *Radiat. Prot. Dosim.* 118 (2006) 307–314.
- M.B. Guglielmotti, A.M. Ubios, B.M. de Rey, R.L. Cabrini, Effects of acute intoxication with uranyl nitrate on bone formation, *Experientia* 40 (1984) 474–476.
- M.B. Guglielmotti, A.M. Ubios, R.L. Cabrini, Alveolar wound healing alteration under uranyl nitrate intoxication, *J. Oral Pathol.* 14 (1985) 565–572.
- F.C. Hartgers, J.L. Vissers, M.W. Looman, C. van Zoelen, C. Huffine, C.G. Figdor, G.J. Adema, DC-STAMP, a novel multimembrane-spanning molecule preferentially expressed by dendritic cells, *Eur. J. Immunol.* 30 (2000) 3585–3590.
- Y. Hu, B. Ek-Rylander, E. Karlström, M. Wendel, G. Andersson, Osteoclast size heterogeneity in rat long bones is associated with differences in adhesive ligand specificity, *Exp. Cell Res.* 314 (2008) 638–650.
- K. Ikeda, S. Takeshita, The role of osteoclast differentiation and function in skeletal homeostasis, *J. Biochem.* 159 (2016) 1–8.
- T. Inui, O. Ishibashi, T. Inaoka, Y. Origane, M. Kumegawa, T. Kokubo, T. Yamamura, Cathepsin K antisense oligodeoxynucleotide inhibits osteoclastic bone resorption, *J. Biol. Chem.* 272 (1997) 8109–8112.
- M. Ishii, Y. Saeki, Osteoclast cell fusion: mechanisms and molecules, *Mod. Rheumatol.* 8 (2008) 220–227.
- R.L. Kathren, R.H. Moore, Acute accidental inhalation of U: a 38-year follow-up, *Health Phys.* 51 (1986) 609–619.
- R.L. Kathren, J.F. McInroy, R.H. Moore, S.E. Dietert, Uranium in the tissues of an occupationally exposed individual, *Health Phys.* 57 (1989) 17–21.
- J.H. Kim, N. Kim, Regulation of NFATc1 in osteoclast differentiation, *J. Bone Miner. Res.* 21 (2014) 233–241.
- J.H. Kim, N. Kim, Signaling pathways in osteoclast differentiation, *Chonnam Med. J.* 52 (2016) 12–17.
- D.J. Klionsky, F.C. Abdalla, H. Abeliovich, R.T. Abraham, A. Acevedo-Arozena, K. Adeli, L. Agholme, M. Agnello, P. Agostinis, J.A. Aguirre-Ghisso, et al., Guidelines for the use and interpretation of assays for monitoring autophagy, *Autophagy* 8 (2012) 445–544.
- M. Komatsu, H. Kurokawa, S. Waguri, K. Taguchi, A. Kobayashi, Y. Ichimura, Y.-S. Sou, I. Ueno, A. Sakamoto, K.I. Tong, et al., The selective autophagy substrate p62 activates the stress responsive transcription factor Nrf2 through inactivation of Keap1, *Nat. Cell Biol.* 12 (2010) 213–223.
- P. Kurttio, A. Auvinen, L. Salonen, H. Saha, J. Pekkanen, I. Mäkeläinen, S.B. Väisänen, I.M. Penttilä, H. Komulainen, Renal effects of uranium in drinking water, *Environ. Health Perspect.* 110 (2002) 337–342.
- P. Kurttio, H. Komulainen, A. Leino, L. Salonen, A. Auvinen, H. Saha, Bone as a possible target of chemical toxicity of natural uranium in drinking water, *Environ. Health Perspect.* 113 (2005) 68–72.
- S.-H. Lee, J. Rho, D. Jeong, J.-Y. Sul, T. Kim, N. Kim, J.-S. Kang, T. Miyamoto, T. Suda, S.-K. Lee, et al., v-ATPase V0 subunit d2-deficient mice exhibit impaired osteoclast fusion and increased bone formation, *Nat. Med.* 12 (2006) 1403–1409.
- R.L. Lees, V.K. Sabharwal, J.N. Heersche, Resorptive state and cell size influence intracellular pH regulation in rabbit osteoclasts cultured on collagen-hydroxyapatite films, *Bone* 28 (2001) 187–194.

- [33] R.W. Leggett, Basis for the ICRP's age-specific biokinetic model for uranium, *Health Phys.* 67 (1994) 589–610.
- [34] R. Leung, Y. Wang, K. Cuddy, C. Sun, J. Magalhaes, M. Grynps, M. Glogauer, Filamin A regulates monocyte migration through Rho small GTPases during osteoclastogenesis, *J. Bone Miner. Res.* 25 (2010) 1077–1091.
- [35] R.F. Li, G. Chen, J.-G. Ren, W. Zhang, Z.-X. Wu, B. Liu, Y. Zhao, Y.-F. Zhao, The adaptor protein p62 is involved in RANKL-induced autophagy and osteoclastogenesis, *J. Histochem. Cytochem.* 62 (2014) 879–888.
- [36] N. Matsumoto, S. Daido, G.-H. Sun-Wada, Y. Wada, M. Futai, M. Nakanishi-Matsui, Diversity of proton pumps in osteoclasts: V-ATPase with a3 and d2 isoforms is a major form in osteoclasts, *Biochim. Biophys. Acta* 1837 (2014) 744–749.
- [37] S. McManus, S. Roux, The adaptor protein p62/SQSTM1 in osteoclast signaling pathways, *J. Mol. Signal.* 7 (2012) 1.
- [38] S. Milgram, M. Carrière, L. Malaval, B. Gouget, Cellular accumulation and distribution of uranium and lead in osteoblastic cells as a function of their speciation, *Toxicology* 252 (2008) 26–32.
- [39] S. Milgram, M. Carrière, C. Thiebault, L. Malaval, B. Gouget, Cytotoxic and phenotypic effects of uranium and lead on osteoblastic cells are highly dependent on metal speciation, *Toxicology* 250 (2008) 62–69.
- [40] H. Mirto, M.P. Barrouillet, M.H. Hengé-Napoli, E. Ansoberlo, M. Fournier, J. Cambar, Influence of uranium(VI) speciation for the evaluation of in vitro uranium cytotoxicity on LLC-PK1 cells, *Hum. Exp. Toxicol.* 18 (1999) 180–187.
- [41] H. Mirto, M.H. Hengé-Napoli, R. Gibert, E. Ansoberlo, M. Fournier, J. Cambar, Intracellular behaviour of uranium(VI) on renal epithelial cell in culture (LLC-PK1): influence of uranium speciation, *Toxicol. Lett.* 104 (1999) 249–256.
- [42] A.M. Moller, J.M. Delaissé, K. Soe, Osteoclast fusion: time-lapse reveals involvement of CD47 and Syncytin-1 at different stages of nuclearity, *J. Cell. Physiol.* (2016)<http://dx.doi.org/10.1002/jcp.25633>.
- [43] P. Morrow, R. Gelein, H. Beiter, J. Scott, J. Picano, C. Yuile, Inhalation and intravenous studies of UF₆/UO₂F₂ in dogs, *Health Phys.* 43 (1982) 859–873.
- [44] M. Motiur Rahman, S. Takeshita, K. Matsuoka, K. Kaneko, Y. Naoe, A. Sakaue-Sawano, A. Miyawaki, K. Ikeda, Proliferation-coupled osteoclast differentiation by RANKL: cell density as a determinant of osteoclast formation, *Bone* 81 (2015) 392–399.
- [45] S. Pankiv, T.H. Clausen, T. Lamark, A. Brech, J.-A. Bruun, H. Outzen, A. Øvervatn, G. Bjørkøy, T. Johansen, p62/SQSTM1 binds directly to Atg8/LC3 to facilitate degradation of ubiquitinated protein aggregates by autophagy, *J. Biol. Chem.* 282 (2007) 24131–24145.
- [46] V. Pierrefite-Carle, S. Santucci-Darmanin, V. Breuil, T. Gritsaenko, C. Vidaud, G. Creff, P.L. Solari, S. Pagnotta, R. Al-Sahlane, C. Den Auwer, G.F. Carle, Effect of natural uranium on osteoblastic cells: impairment of the autophagic process as an underlying mechanism of uranium toxicity, *Arch. Toxicol.* (2016)<http://dx.doi.org/10.1007/s00204-016-1833-5>.
- [47] S.L. Rea, J.P. Walsh, L. Ward, K. Yip, B.K. Ward, G.N. Kent, J.H. Steer, J. Xu, T. Ratajczak, A novel mutation (K378X) in the sequestosome 1 gene associated with increased NF- κ B signaling and Paget's disease of bone with a severe phenotype, *J. Bone Miner. Res.* 21 (2006) 1136–1145.
- [48] S.L. Rea, J.P. Walsh, R. Layfield, T. Ratajczak, J. Xu, New insights into the role of sequestosome 1/p62 mutant proteins in the pathogenesis of Paget's disease of bone, *Endocr. Rev.* 34 (2013) 501–524.
- [49] G. Rodrigues, J.D.T. Arruda-Neto, R.M.R. Pereira, S.R. Kleeb, L.P. Geraldo, M.C. Primi, L. Takayama, T.E. Rodrigues, G.T. Cavalcante, G.C. Genofre, et al., Uranium deposition in bones of Wistar rats associated with skeleton development, *Appl. Radiat. Isot.* 82 (2013) 105–110.
- [50] L. Sanz, P. Sanchez, M.J. Lallena, M.T. Diaz-Meco, J. Moscat, The interaction of p62 with RIP links the atypical PKCs to NF- κ B activation, *EMBO J.* 18 (1999) 3044–3053.
- [51] L. Sanz, M.T. Diaz-Meco, H. Nakano, J. Moscat, The atypical PKC-interacting protein p62 channels NF- κ B activation by the IL-1-TRAF6 pathway, *EMBO J.* 19 (2000) 1576–1586.
- [52] M.L. Seibenhener, J.R. Babu, T. Geetha, H.C. Wong, N.R. Krishna, M.W. Wooten, Sequestosome 1/p62 is a polyubiquitin chain binding protein involved in ubiquitin proteasome degradation, *Mol. Cell. Biol.* 24 (2004) 8055–8068.
- [53] N.P. Singh, D.B. Bennett, M.E. Wrenn, Macro-distribution of naturally occurring alpha-emitting isotopes of U in the human skeleton, *Health Phys.* 52 (1987) 769–773.
- [54] D.R. Tasat, N.S. Orona, P.M. Mandalunis, R.L. Cabrini, A.M. Ubios, Ultrastructural and metabolic changes in osteoblasts exposed to uranyl nitrate, *Arch. Toxicol.* 81 (2007) 319–326.
- [55] A.M. Ubios, M.B. Guglielmotti, T. Steimetz, R.L. Cabrini, Uranium inhibits bone formation in physiologic alveolar bone modeling and remodeling, *Environ. Res.* 54 (1991) 17–23.
- [56] C. Vidaud, D. Bourgeois, D. Meyer, Bone as target organ for metals: the case of f-elements, *Chem. Res. Toxicol.* 25 (2012) 1161–1175.
- [57] N.M. Wade-Gueye, O. Delissen, P. Gourmelon, J. Aigueperse, I. Dublineau, M. Souidi, Chronic exposure to natural uranium via drinking water affects bone in growing rats, *Biochim. Biophys. Acta* 1820 (2012) 1121–1127.
- [58] WHO, Depleted Uranium, Sources, Exposure and Health Effects, Department of Protection of the Human Environment, (WHO/SDE/PHE/01.1), World Health Organization (WHO), Geneva, 2001.
- [59] WHO, Uranium in Drinking Water, Background document for development of WHO Guidelines for Drinking-water Quality, (WHO/SDE/WSH/03.04/118), World Health Organization (WHO), 2004.
- [60] H. Wu, G. Xu, Y.-P. Li, Atp6v0d2 is an essential component of the osteoclast-specific proton pump that mediates extracellular acidification in bone resorption, *J. Bone Miner. Res.* 24 (2009) 871–885.
- [61] M. Yagi, T. Miyamoto, Y. Sawatani, K. Iwamoto, N. Hosogane, N. Fujita, K. Morita, K. Ninomiya, T. Suzuki, K. Miyamoto, et al., DC-STAMP is essential for cell-cell fusion in osteoclasts and foreign body giant cells, *J. Exp. Med.* 202 (2005) 345–351.
- [62] K.H.M. Yip, H. Feng, N.J. Pavlos, M.H. Zheng, J. Xu, p62 ubiquitin binding-associated domain mediated the receptor activator of nuclear factor- κ B ligand-induced osteoclast formation: a new insight into the pathogenesis of Paget's disease of bone, *Am. J. Pathol.* 169 (2006) 503–514.
- [63] M. Taulan, F. Paquet, A. Argiles, J. Demaille, M.-C. Romey, Comprehensive analysis of the renal transcriptional response to acute uranyl nitrate exposure, *BMC Genomics* 7 (2006) 2.

II. MANUSCRIPT IN PREPARATION “THE EFFECT OF URANIUM-MODIFIED EXTRACELLULAR MATRIX ON OSTEOCLASTS”

1. Summary

Uranium (U) is a naturally occurring radioactive element. Due to its low specific radioactive activity, the major hazard to human health results from the high chemical toxicity of uranium. Bone is the primary site of the long-term uranium retention in the body. However, to this date, the specific effects of this metal on bone cells and the bone matrix have not been fully explored. In our previous study, we reported for the first time that exposure to uranium in solution induces inhibition of osteoclastic differentiation and function *in vitro*. This effect was observed using either a cell line (RAW 264.7) or primary cells (bone marrow-derived macrophages) as osteoclast precursors and for uranium concentrations ranging from 2.5 μM (primary cells) or 5 μM (RAW 264.7) to 50 μM . The decrease in available precursor cells, as well as the reduced viability of mature osteoclasts appears to account for these effects of uranium. Moreover, we observed that SQSTM1/p62, a known regulator of osteoclast formation, accumulates in response to uranium exposure, suggesting that SQSTM1/p62 dysregulation could contribute to uranium effects on osteoclastogenesis.

In the following study, we continued our analysis of the consequences of uranium exposure on osteoclast behavior by examining, this time, the effect of uranium when it is bound to the bone matrix. To this end, two bone matrix models containing uranium have been developed: (1) synthetic inorganic resorbable substrates containing various amounts of adsorbed uranium, (2) “biological” matrices synthesized by an osteoblastic cell line cultured in the presence of different concentrations of uranium. The resulting matrices were first characterized using different approaches (ICP/MS, EXAF, SEM/EDX, TEM), then used as culture support for osteoclasts. Uranium quantification in both types of matrices as well as in culture supernatants during and after osteoclastic differentiation demonstrates, for the first time, that uranium incorporated into a mineralized matrix can be remobilized by osteoclastic resorption. In addition, our data suggest that remobilized uranium in solution in the culture medium has opposite effects on osteoclastic function depending on its concentration. While it inhibits resorption at concentrations above 5 μM , this process is stimulated at uranium concentrations of 0.25 and 0.5 μM . The underlying molecular mechanisms are under investigation.

While the analysis of osteoclast behavior on both bone matrix models needs to be further consolidated, we already believe that these tools will be very useful for future work on the effect of uranium on bone cells, particularly in osteoblast/osteoclast co-culture experiments.

2. Introduction

Uranium is a naturally occurring radioactive heavy metal found in almost all rocks and soils. In most environmental systems, U is found in the oxidation state +VI as the uranyl ion UO_2^{2+} [referred as U(VI) hereafter]. It is widely used in various civil and military projects, which raises a problem of environmental pollution. As the specific radioactive activity of natural uranium is low, its toxicity is mainly due to chemical damage to target organs in the event of exposure (ATSDR, 2013). Regardless of the route of entry, uranium absorption is low and once uranium has reached the bloodstream it interacts with carbonate and proteins until it accumulates in its target organs, mainly the skeleton and the kidneys. In the skeleton, U(VI) can accumulate in a dose- and time- dependent manner (Arruda-Neto *et al.*, 2004; Larivière *et al.*, 2013) and can be retained for several years (ATSDR, 2013; Leggett, 1994).

The affinity of uranium for phosphate, one of the two main constituents of bone mineral, has been proposed to explain this behavior (Neuman and Neuman, 1949). Since then, several studies have been conducted to examine the distribution of uranium in bone samples and have shown that uranium is rapidly fixed onto bone surfaces, preferentially on those undergoing active calcification (Bourgeois *et al.*, 2015; Priest *et al.*, 1982; Rodrigues *et al.*, 2013) and become buried with time by the apposition of new bone (Ellender *et al.*, 1995; Priest *et al.*, 1982). However, to date, no mechanism explaining the biomineralization of uranium is formally accepted. This is probably related to the complexity of the bone matrix and the different types of chemical interactions that can occur between uranyl cations and the different mineral and organic components of the bone matrix (Vidaud *et al.*, 2012). Among the mechanisms proposed in describing uranyl complexation to bone matrix, non-specific surface sorption of uranium onto apatite has been well documented (Arey *et al.*, 1999; Fuller

et al., 2002, 2003; Simon *et al.*, 2008). Co-precipitation of uranium with calcium and phosphate in the form of phosphate minerals such as autunite $[\text{Ca}(\text{UO}_2)_2(\text{PO}_4)_2 \cdot n\text{H}_2\text{O}]$ was also considered (Mehta *et al.*, 2016; Ohnuki *et al.*, 2004). The complexation of uranium to the organic part of the bone matrix was as well investigated. This organic matrix is composed of collagen fibrils (90%) and non-collagenous proteins (10%) that are secreted by bone cells or that originate from serum and become entrapped in the bone matrix (Boskey and Robey, 2013). Most non-collagenous proteins are involved in mineralization (Gorski, 2011). This is the case with Fetuin A and osteopontin, which are regulators of bone matrix mineralization and important systemic inhibitors of ectopic calcifications (Brylka and Jahnen-Dechent, 2013; Icer and Gezmen-Karadag, 2018; Triffitt *et al.*, 1976). These two proteins bind to calcium phosphate and have recently been shown to also have a high affinity for uranium which raises the possibility that uranium may be, at least in part, deposited in the bone via its binding to certain non-collagenous proteins (Basset *et al.*, 2013; Qi *et al.*, 2014).

The impact of U(VI) on bone metabolism has been studied *in vivo* in several studies agreeing that acute or chronic exposure to U(VI) can lead to inhibition of bone formation (Bozal *et al.*, 2005; Díaz Sylvester *et al.*, 2002; Guglielmotti *et al.*, 1985; Guglielmotti *et al.*, 1984; Ubios *et al.*, 1991; Wade-Gueye *et al.*, 2012). In accordance with this observation, *in vitro* investigations have shown that U(VI) affects the viability and the function of osteoblasts, the cells responsible for bone construction, in particular by reducing their mineralization capacity (Milgram *et al.*, 2008a; Pierrefite-Carle *et al.*, 2016; Tasat *et al.*, 2007). More recently, we have also reported an effect of U(VI) on the function of osteocytes which are cells embedded in the bone matrix that are considered as the main regulators of bone remodeling (Hurault *et al.*, 2019). Interestingly, our results suggest that in both osteoblasts and osteocytes, U(VI) exerts

its toxicity in part through its inhibition effect on autophagy, a major catabolic process (Hurault *et al.*, 2019; Pierrefite-Carle *et al.*, 2016). The third type of bone cells crucial for bone remodeling are osteoclasts, which are responsible for bone resorption. They are large multinucleated cells resulting from the fusion of hematopoietic precursor cells and are unique in their ability to solubilize both the mineral and organic components of the bone matrix. Autoradiographic and radiological analyses of rat bones that had undergone uranium injection led to the proposal that resorption contribute to the distribution of uranium in the skeleton as uranium could be resorbed from the bone surface, returned to the bloodstream and partially re-deposited in bone (Priest *et al.*, 1982). Conversely, few studies have examined the effect of U(VI) on bone resorption *in vivo*, using different rodent models, various uranium doses and administration routes, making it difficult to interpret the impact of uranium on bone resorption (Bozal *et al.*, 2005; Fukuda *et al.*, 2006; Ubios *et al.*, 1991). Nevertheless, these *in vivo* investigations have led to the proposal that uranium could promote resorption. At the cellular level, we have recently demonstrated that 5 μM of U(VI), in solution in the culture medium, is sufficient to strongly inhibit osteoclastic resorption due to an impairment of osteoclast formation and survival (Gritsaenko *et al.*, 2017). The mechanism underlying the apparent discrepancy between the *in vivo* and *in vitro* effect of U(VI) on resorption may be related to the complexity of the interactions involving uranium, organic and mineral matrix components and bone cells. To better understand these interactions, we decided to examine the effect of U (VI) embedded in the matrices, on the behavior and function of osteoclasts. To do this, we used a synthetic hydroxyapatite matrix as well as a "biological" matrix synthesized by a tumor osteoblast cell line *in vitro*. These two supports were compared and also used to determine if

osteoclasts are able to remobilize the uranium trapped in the matrix via resorption, which has never been formally demonstrated.

3. Materials and methods

A. Uranium exposure

Uranium solutions were prepared extemporaneously in conditions allowing the control of uranium speciation in exposure cell culture media, as previously described (Gritsaenko *et al.*, 2017, 2018).

B. Cell culture

The SAOS-2 cell line and the mouse monocyte/macrophage cell line RAW 264.7 were purchased from American Type Culture Collection. SAOS-2 cells were cultured as described by Lutter *et al.* (2010) with some modifications (Lutter *et al.*, 2010). Briefly, SAOS-2 cells were maintained in McCoy's 5A medium without phenol red (HyClone, Thermo Fisher Scientific) supplemented with 15% heat-inactivated fetal bovine serum (Biowest) and antibiotics (100 IU/mL penicillin, 100 µg/mL streptomycin, Sigma-Aldrich). RAW 264.7 cells were maintained in Dulbecco's modified Eagle medium (DMEM, Lonza) supplemented with 5% HyClone serum (HyClone, Thermo Fisher Scientific) and antibiotics (100 IU/ml penicillin and 100 µg/ml streptomycin, Sigma-Aldrich). Cells were grown in 75 cm² flasks and passed by mechanical scrapping.

C. Biomimetic matrices

24-well Osteo assay plates that provide a synthetic inorganic bone mimetic surface (Corning Life Science, #3987) were incubated at 37°C with α MEM medium (1ml/well) containing the indicated concentration of U(VI). After 48 hours, the medium was discarded and the plates were used directly either for U(VI) quantification or for osteoclastic differentiation and resorption assays.

For matrix production, 20,000 SAOS-2 cells/well/ml of complete McCoy's 5A medium were seeded in 24-well culture plates. When the confluence reached 90%, growth medium was replaced by differentiation medium (α -MEM, 10% heat-inactivated FBS, 300 μ M ascorbic acid, 10 mM β -glycerol phosphate) containing either 0, 0.5, 1 or 2 μ M U(VI). Culture medium without or with U(VI) was changed on days 3, 5 and 7 of culture. On day 10, the resulting matrices were decellularized with 20 mM NH₄OH for 10 min. at room temperature, then treated with DNase I (1 mg/ml in α -MEM) for 15 min. at 37°C, rinsed in α -MEM medium and immediately used either for U(VI) quantification or for osteoclastic differentiation and resorption assays.

D. Osteoclast generation, TRAP staining and pit resorption assays

Osteoclastic differentiation and resorption were analyzed as described before (Gritsaenko *et al.*, 2017, 2018) except that RAW 264.7 pre-osteoclastic cells were seeded at a density of 5000 cells/cm² on synthetic apatite matrices (osteo assay plates) and a density of 20,000 cells/cm² on matrices produced by SAOS-2 cells.

E. Scanning electron microscopy

For scanning electron microscopy (SEM) and energy-dispersive X-ray spectroscopy (EDX), cellularized samples were fixed in a 1.6 % glutaraldehyde solution in 0.1 M sodium phosphate buffer (pH 7.4) at room temperature for 1 hour and then stored at 4°C. After three rinsing in distilled water, samples were dehydrated in a series of ethanol baths (70%, 96 %, 100% three times, 15 min each). After a final bath in hexamethyldisilazane (HMDS, 5 minutes), samples were left to dry overnight. Decellularized samples were left to dry without fixation. Samples were then mounted on SEM stubs with carbon tape and silver paint. For SEM imaging, samples were coated with platinum (3 nm) prior to observations with a Jeol JSM-6700F SEM at an

accelerating voltage of 3 kV. For EDX analyses, samples were carbon coated and analyses were carried with a Tescan Vega3 XMU scanning electron microscope (TESCAN FRANCE, Fuveau, France) equipped with an Oxford X-MaxN 50 EDX detector (Oxford Instruments, Abingdon, U.K.) with a 20kV accelerating voltage. EDX data were processed with the Aztec software (version 3.1, Oxford Instruments).

F. Transmission Electron Microscopy

Samples were fixed with 1.6% Glutaraldehyde in 0.1 M phosphate solution immediately after medium removal. Cells were rinsed with 0.1 M cacodylate buffer and post-fixed for 1 h in the same buffer containing 1% osmium tetroxide. After rinsing with distilled water and progressive dehydration with increasing ethanol concentration solutions, cells were embedded in epoxy resin. Ultrathin sections (70 nm) were realized and put on Formvar-coated copper grids. Grids were stained with uranyl acetate and lead citrate before examination of sections with a Jeol JEM 1400 transmission electron microscope equipped with a SIS MORADA camera.

G. ICP/MS analysis

Culture supernatants were acidified with nitric acid (HNO_3) and stored at -20°C until ICP/MS analysis. Synthetic and biological matrices were dried at room temperature and rinsed 3 times using 65% concentrated HNO_3 (3 x 1 ml). Each solution was evaporated to dryness on a hotplate after being heated to 120°C during 3-4 h and re-dissolved into a HNO_3 solution at pH 1.

After appropriate dilution in HNO_3 1%, samples were injected via a peristaltic pump equipped with Tygon tubing at 400 $\mu\text{L}/\text{min}$ flow rate and nebulized by means of a microconcentric nebulizer. Quantification was performed by inductively coupled plasma mass spectrometry (ICP-MS; 7700, Agilent Technologies; Santa Clara, CA,

USA) at $m/z = 238$. ICP conditions were the following: nebulization gas flow rate: 1 L min^{-1} , dilution gas flow rate: 0.1 L/min, plasma gas flow rate: 15 L/min, auxiliary gas flow rate: 1 L/min. Plasma power was set to 1550 W. Other parameters were adjusted to both maximize the analyte signal and minimize oxide and doubly charged ions formation. The standard curve (0.4 to 40 nmol/L of U) was prepared from the PlasmaCAL standard (U 1000 $\mu\text{g}/\text{mL}$, SCPscience; Courtaboeuf, France). The detection limit calculated by the MassHunter software was 0.01 nmol/L. Each sample was measured in triplicate. Between analyses, the system was rinsed for 30 s with HNO_3 1% and 30 s with ultrapure water and a blank (HNO_3 1%) was injected to control the absence of any memory effect.

H. Extended X-Ray Absorption Fine Structure Analysis

EXAFS experiments at U LIII-edge were performed on the MARS beam line at the SOLEIL synchrotron facility (2.75 GeV; 400 mA), which is the French bending magnet beam line dedicated to the study of radioactive materials (Sitaud *et al.*, 2012). All the measurements were recorded in fluorescence mode using a 13-element high purity germanium solid-state detector. Data were processed with the Athena code (Ravel and Newville, 2005). The extracted EXAFS signal was fitted in R space, using theoretical models, by use of the Artemis code (Ravel and Newville, 2005). In all the fits, only one global amplitude factor and one energy threshold factor were considered for all the scattering contributions. Hanning windows with k^2 [2.8; 11.5 \AA^{-1}] and fitting range with R [1.0; 5.0 \AA] were selected. Phases and amplitudes were calculated with Feff9 code (Rehr *et al.*, 2010) using the crystal structure of uranyl phosphate $\text{Ca}[(\text{UO}_2)(\text{PO}_4)]_2(\text{H}_2\text{O})_{11}$ (Locock and Burns, 2003). The first two single scattering paths correspond to the 2 axial oxygen atoms O_{ax} and to the equatorial oxygen atoms O_{eq} . Additional single scattering path corresponding to phosphorous (U...P) was also added

to account for the third coordination shell. Several multiple scattering paths were also needed: triple and quadruple paths involving axial (U...O_{ax}...U...O_{ax}), and equatorial oxygens (U...P...O_{eq}), (U...O_{eq}...U...O_{eq}) and (U...O_{distal}...O_{eq}). During the fit procedure, the total coordination number (N) of the oxygen atoms was fixed to 2 (axial) + 5 (equatorial) as the usual coordination mode for uranyl. Only one global amplitude factor S_0^2 and one energy threshold factor e_0 were used for all paths. The r-factor (in %) and quality factor χ^2/n of the fit are both provided as an indication of fit quality in the R space.

I. Statistical analysis

Statistical analyses were performed with Prism 7.00 (GraphPad Software). Due to the size of the samples we used non-parametric approaches. Data were submitted to Kruskal-Wallis or two-way analysis of variance (ANOVA), as indicated, with the two-stage step-up method of Benjamini, Krieger and Yekutieli to control the false discovery rate.

4. Results

The synthetic apatite matrix model

Since our objective was to determine the consequences of the presence of uranium in a mineralized extracellular matrix on the behavior of osteoclasts, obtaining mineralized matrices containing uranium was a prerequisite. The first model we used was a commercially available synthetic surface made of an inorganic crystalline calcium phosphate (COAS for Corning Osteo-Assay Surface) (Faruqi *et al.*, 2011) that is usually used to assess osteoclast and osteoblast activity *in vitro* (Abdelmagid *et al.*, 2015; Gigliotti *et al.*, 2016; Gritsaenko *et al.*, 2017). 24-well COAS plates were incubated for 48 hours with alpha-MEM medium containing concentrations of uranyl acetate ranging from 0 to 100 μM . The medium was then removed and the amount of U(VI) retained on the synthetic surface was measured by ICP/MS. Fig 1A shows that U(VI) in culture medium was successfully retained on the calcium phosphate layer and that the amount of adsorbed uranium increased with the initial concentration of U(VI) in the culture medium. However, the fraction of uranium retained decreased with increasing U(VI) concentrations.

To define the speciation of uranium in the inorganic calcium phosphate coating, the EXAFS spectrum of these synthetic matrices exposed to a solution of 100 μM U(VI) for 48 h was recorded at the U LIII edge and compared with the EXAFS spectrum of a pure autunite sample $[\text{Ca}(\text{UO}_2)_2(\text{PO}_4)_2(\text{H}_2\text{O})_{11}]$. Autunite is the most stable form among uranyl phosphates and it is also very similar to the uranyl phosphate phase identified into osteoblastic and osteocytic cells exposed to uranium (Hurault *et al.*, 2019; Pierrefite-Carle *et al.*, 2016). The EXAFS experimental spectrum and corresponding Fourier transform are shown in Fig. 1B and the best parameters of the fit are presented in Table S1. In short, in the synthetic matrix metal coordination sphere consists of 2

O_{ax} at 1.83 Å, 5 O_{eq} at 2.39 Å and 1.6 P at 3.64 Å and in the case of autunite powder the distances are 1.80 Å for the O_{ax} , 2.32 Å for the O_{eq} and 3.61 Å for the phosphorus atoms. These data indicate that the phase on synthetic apatite matrix contaminated with U(VI) is a uranyl phosphate phase in which the U local structure resembles that in the autunite phase. However, U- O_{eq} distances are slightly greater in the synthetic matrix sample than in autunite crystalline powder which suggests a weak interaction of uranium with apatite.

Osteoclast behavior on synthetic U(VI)-containing matrices

The next step was to determine whether the presence of U(VI) in matrices can affect osteoclastic differentiation. For this purpose, we prepared several sets of synthetic matrices exposed to increasing concentrations of U(VI) (0, 5, 10, 25, 50 and 100 μ M). After U(VI) quantification in these sets of matrices we have chosen those containing amounts of U(VI) ranging from approximately 0.16 to 1 μ g. We made this choice to have U amounts in these synthetic matrices comparable to those found in the biological matrices we had prepared in parallel (see Fig. 5D). RAW 264.7 cells were seeded on synthetic matrices containing between 0 and 1 μ g U(VI) as indicated in Fig. 2B. After 4 days of culture in differentiation condition (i.e. in the presence of RANKL), the formation of osteoclasts was evaluated. As expected, in control condition (Fig. 2A, [U(VI)] = 0 μ M), RAW 264.7 cells formed osteoclasts, defined as cells having more than 3 nuclei and positive for tartrate-resistant acid phosphatase (TRAP) activity staining. In the presence of 1 μ g U(VI) in the matrix (Fig. 2A, [U(VI)] = 100 μ M), no obvious difference was observed compared to the control condition. However, it should be noted that to date, precise quantifications of the number and size of osteoclasts obtained under the various conditions have yet to be made to confirm this first impression. We then analyzed the impact of U(VI) on osteoclast resorption activity. Fig.

2B shows the quantification of resorbed synthetic matrix surfaces as a function of the amount of U(VI) in these matrices. Surprisingly, we observed a significant stimulation of resorption compared to the control condition in the case of matrices previously exposed to 5 or 10 μM U(VI) and containing on average 0.16 and 0.24 μg U(VI), respectively. For higher amounts of U(VI) in matrices (0.45, 0.75 and 1 μg) no significant effect were detected when compared to the condition without U(VI).

U(VI) release from synthetic matrices

We then evaluated the distribution of U(VI) between the culture medium and matrices during the 4 days of cell culture according to the protocol presented in Fig. 3A. Since one of our objectives was to determine whether part of U(VI) could be remobilized in the culture medium via osteoclastic resorption, the cultures were made in the absence of RANKL, therefore in the absence of resorbing cells or in the presence of RANKL, therefore in the presence of resorbing osteoclasts. It is important to note that the majority of the resorption occurs between culture days 3 and 4, *i.e.* after the change of culture medium that occurs at the beginning of day 3.

The histogram presented in Fig. 3B shows the U(VI) found in the culture medium at D3 and D4 as a percentage of the U(VI) present in the initial matrices. After 3 days of culture (D3 supernatants), a large part of U(VI), 49 to 70% depending on the conditions, was found released into the culture medium whether or not RANKL was present, which indicated that U(VI) adsorbed on synthetic apatite was massively and passively released into the medium during this culture period. Over the next 24 hours (D4 supernatants) 6 to 7.5% of U(VI) were measured in the culture medium under conditions without RANKL while this percentage was higher (9 to 13%) under all conditions tested in the presence of RANKL. The statistical analysis of the quantities of U(VI) present in D3 and D4 supernatants (box-and-whisker plots, Fig. 3C) further

highlighted the significance of the difference observed at D4 as a function of the presence of RANKL in the culture medium, whereas the presence of this cytokine did not impact the quantity of U(VI) found at D3. All these observations strongly suggested that part of the U(VI) adsorbed on synthetic apatite matrices was remobilized by osteoclastic resorption, which occurs only in the presence of RANKL and only after 3 days in our culture conditions. This was confirmed by the quantification of U(VI) in the final matrices which showed that all those maintained in culture in the presence of RANKL tend to contain less U(VI) than the others (Fig. 3D). This trend observed under all tested conditions became significant for matrices containing the most U(VI) (0.75 and 1 μg).

Effect of low U(VI) concentration in the culture medium on osteoclastic resorption

We observed that osteoclastic resorption was stimulated when the synthetic matrices contained between 0.16 and 0.24 μg U(VI) (Fig.2B). We also knew from the assays presented in Fig. 3B that when these matrices were maintained in culture, the U(VI) concentration in the culture medium could reach 0.35 and 0.57 μM , respectively, at D3 (Table S2), due to passive remobilization of the adsorbed U. We therefore wondered if the resorption stimulation we were observing could be due to U(VI) in solution. RAW 264.7 cells were seeded on synthetic matrices in the presence of RANKL and increasing concentrations of U(VI) from 0 to 5 μM , 5 μM being a concentration for which we had already reported resorption inhibition and analyzed resorption (Gritsaenko *et al.*, 2017). In doing so, we observed that U(VI) concentrations of 0.25 and 0.5 μM could stimulate resorption, that 1 and 3 μM U(VI) had no effect and that, as expected, 5 μM U(VI) caused significant resorption inhibition (Fig.4). These results suggested that the stimulation of resorption observed by using matrices

containing 0.16 and 0.24 μg U(VI) may actually be due to U(VI) in solution. These results could also explain why matrices containing 0.45, 0.75 and 1 μg U(VI) did not have a significant impact on resorption (Fig. 2B). Indeed, the use of these matrices resulted in the presence of 1, 1.8 and 3 μM U(VI) in D3 supernatants (Table S2), concentrations which, according to the work presented in Fig. 4, did not appear to have an impact on resorption. Taken together, the work carried out with synthetic matrices shows for the first time that osteoclasts are able to resorb adsorbed U(VI) on an apatite layer and that low concentrations of remobilized U(VI) in solution are able to stimulate osteoclast activity.

The biological SAOS-2 matrix model

In order to be closer to the physiological conditions, a second model has been developed which consists of culturing an osteoblastic cell line (SAOS-2) in the presence of low U(VI) concentrations and under conditions that allow the production of a bone mineralized extracellular matrix. By doing so, we have obtained extracellular matrices that we have characterized by several microscopy techniques. SEM analyses (Fig. 5A) showed that SAOS-2 synthesize a thin matrix on which globular structures are distributed. This architecture and, in particular, the frequency, size and shape of these globular structures did not seem to be affected by the presence of U(VI) (0.5 to 2 μM) during the synthesis phase, as illustrated by the representative images shown in Fig. 5A. Energy dispersive X-ray (EDX) analysis was used to identify the elemental composition of the globular structures (Fig. 5B) and showed, as expected, the presence and co-location of calcium (Ca) and phosphorus (P) in these structures, indicating that these « globules » actually correspond to the CA/P deposits produced by SAOS-2 cells. However, this technique was unable to detect U(VI) in these mineralization foci (Fig. 5B, right panel) or in the non-mineralized part of the SAOS-2

matrix. The transmission electron microscopy analysis showed the presence under both conditions of collagen fibrils recognizable by their band configuration (Fig. 5C). Taken together, these observations showed that, under our experimental conditions, SAOS-2s were capable of synthesizing an organic and mineralized extracellular matrix and that this process did not appear to be affected by the presence of 2 μM U(VI) in the culture medium.

U(VI) could not be detected by EDX in SAOS-2 matrices. To overcome a possible sensitivity problem and also because we wanted to compare the amount of U(VI) present in the synthetic and biological matrices using the same technique, we measured the U(VI) incorporated in the SAOS-2 matrices by ICP/MS (Fig. 5D). These assays showed that up to 1 μg U(VI) can be incorporated into a matrix synthesized by SAOS-2s in a well of a 24-well plate. This incorporation was highly reproducible and increased linearly with the amount of U(VI) present in the culture medium during matrix synthesis. The EXAFS analyses of biological matrix synthesized in the presence of 2 μM U(VI) was also performed and the resulting EXAFS spectrum (Fig. 5E) indicates the presence of a uranyl phosphate phase very similar to that of autunite. Moreover, the bond distances are closer to those of the autunite phase when compared to those found in the case of synthetic matrix samples (Table S2). This observation suggests that U(VI) is more tightly bound to the biological matrix than to the synthetic matrix.

Osteoclast behavior on biological U(VI)-containing matrices

Biological matrices prepared from SAOS-2 cell culture were decellularized and used to analyze osteoclast differentiation and resorption, as a function of the amount of U(VI) incorporated. We did not notice any obvious effect of U(VI) on either the number or size of osteoclasts (Fig. 6A). Nevertheless, here again, quantitative analyses remain to be done to confirm this observation. When we analyzed the function

of osteoclasts, we found a low resorption rate (Fig. 6B) compared to that obtained on synthetic matrices (Fig. 2B) and a high inter and intra-experimental variability that we do not explain at this time, even if we consider the possibility that it is related to the treatments carried out for decellularization. In any case, all the experiments carried out did not reveal any effect of the U(VI) incorporated in the matrices on resorption efficiency.

U(VI) release from biological matrices

We then evaluated the distribution of U(VI) between the culture medium and matrices according to the protocol presented in Fig. 3A, with one difference, which is that the culture lasted 5 days and not 4 and that, therefore, U(VI) was measured in culture supernatants from days 3 (D3) and 5 (D5) instead of days 3 and 4. The bar graph in Fig. 7A shows U(VI) found in D3 and D5 supernatants as a percent of the U(VI) measured in the initial matrices. We first noticed that the percentage of U(VI) remobilized in the culture medium, under all tested conditions (D3, D5 \pm RANKL), was at least 10 times lower than that obtained with synthetic matrices. Moreover, contrary to what was found with synthetic apatite matrices, the % U(VI) released differs only slightly between D3 and D5. These observations highlight the difference between our two matrix models and agree with the EXAFS data, since they suggest that the association of U(VI) with the matrix is much weaker in synthetic matrices than in SAOS-2 biomineralized matrices. Nevertheless, as in the case of synthetic matrices, the presence of RANKL appeared to be associated with an increase in U(VI) release (Fig. 7A). This was confirmed by statistical analysis of the quantities of U(VI) present in D5 supernatants (Fig. 7B). In the presence of RANKL, D3 supernatants tended also to contain more U(VI) compared to control samples, though without reaching significance (data not shown). Likewise, the amount of U(VI) present in the final SAOS-

2 matrices did not show statistically significant differences as a function of the absence or presence of RANKL in the culture medium (Fig. 7C). However, as can be seen in the box plot, the matrices with the lowest U(VI) initial content (0.28 and 0.5 μg U(VI)/well) tend to contain less U(VI) after 5 days of culture in the presence of RANKL. It should be noted that the low significance of these results is probably correlated with the low resorption efficiency obtained with SAOS-2 matrices. Although our data must be consolidated, they suggest that part of the U(VI) incorporated in mineralized extracellular biological matrices could be released into the culture medium via osteoclastic resorption.

TEM analysis of osteoclasts that have resorbed U(VI)-containing biological matrix

Using transmission electron microscopy, we then analyzed osteoclasts that have resorbed biological matrices containing either 0 or 1 μg U(VI). In 100% of osteoclasts formed on matrices with U(VI) that we have examined, we noticed one (Fig. 8A) or several large vesicles (Fig. 8B) containing isolated needle-like structures. No equivalent observations were made when we examined osteoclasts formed on matrices without U(VI). In addition, vesicles with the same content have not been observed on osteoclasts formed on synthetic matrices containing or not U(VI). These observations suggest that vesicles with such content are specific to osteoclasts that have resorbed mineralized organic matrices containing U(VI). However, the presence of U(VI) in these organelles remains to be verified. In addition, although these structures have some characteristics reminiscent of autophagic vesicles (Fig. 8C) - which are large double-membrane vesicles enclosing cytoplasmic components targeted for degradation -, their precise nature remains to be determined.

5. Figures

Figure 1

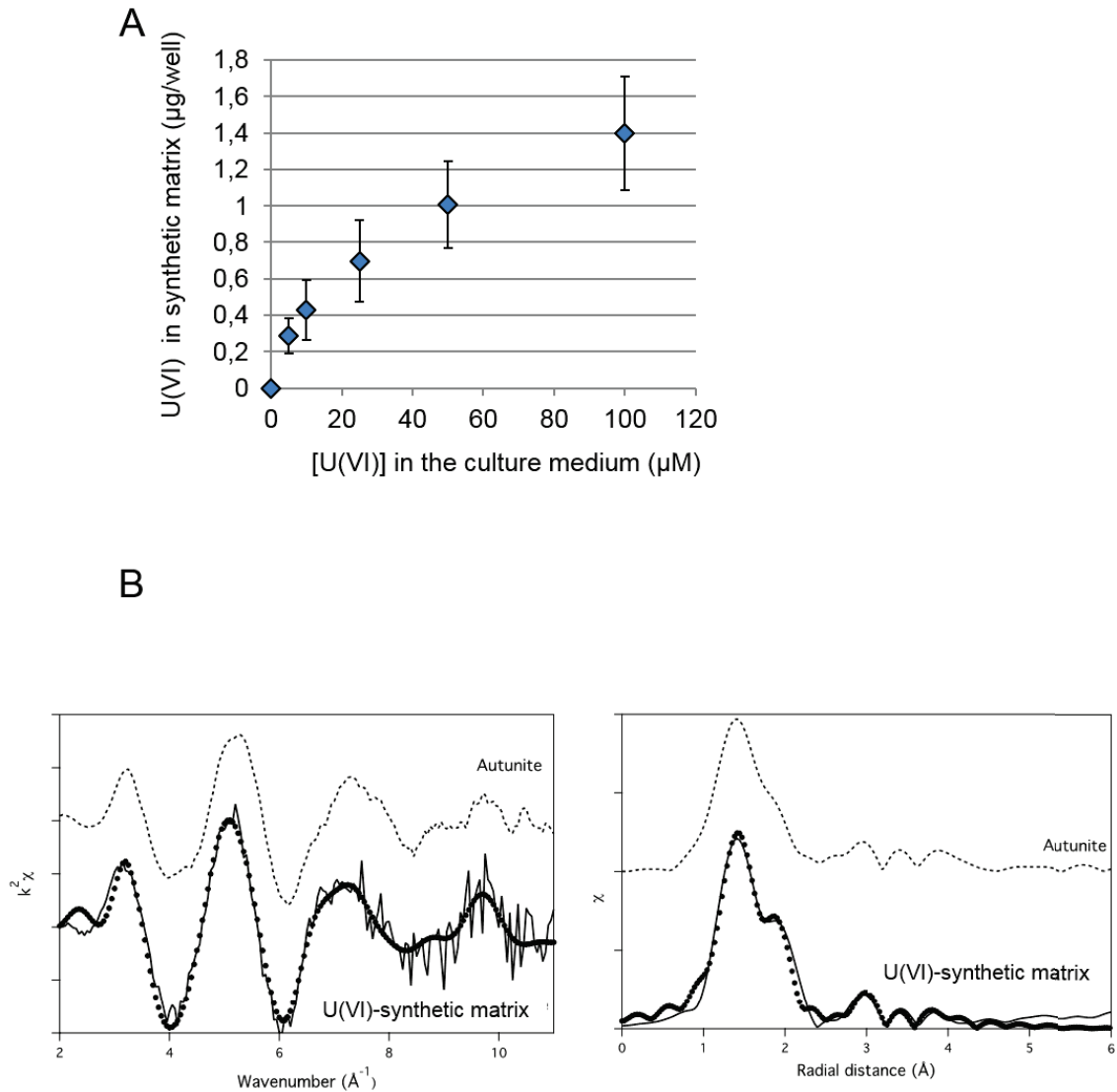
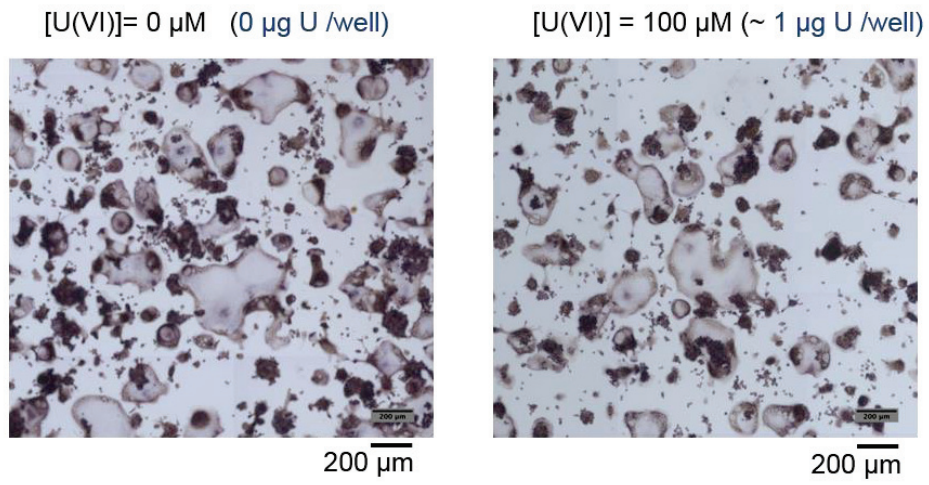


Fig. 1: U(VI) in synthetic apatite matrix. (A) 24-well COAS plates were incubated for 48 hours with alpha-MEM medium (1 ml / well) containing the indicated concentrations of uranyl acetate. U(VI) retained on matrix was quantified by using ICP/MS. Data represent the mean \pm SD obtained of 5 independent experiments each performed in duplicate or triplicate. (B) (left panel) Experimental (straight line) and adjusted (dots) EXAFS spectra at the U LIII edge of U(VI)-synthetic matrix. The experimental EXAFS spectrum of autunite model is also shown for comparison; (right panel) corresponding Fourier transforms.

Figure 2

A



B

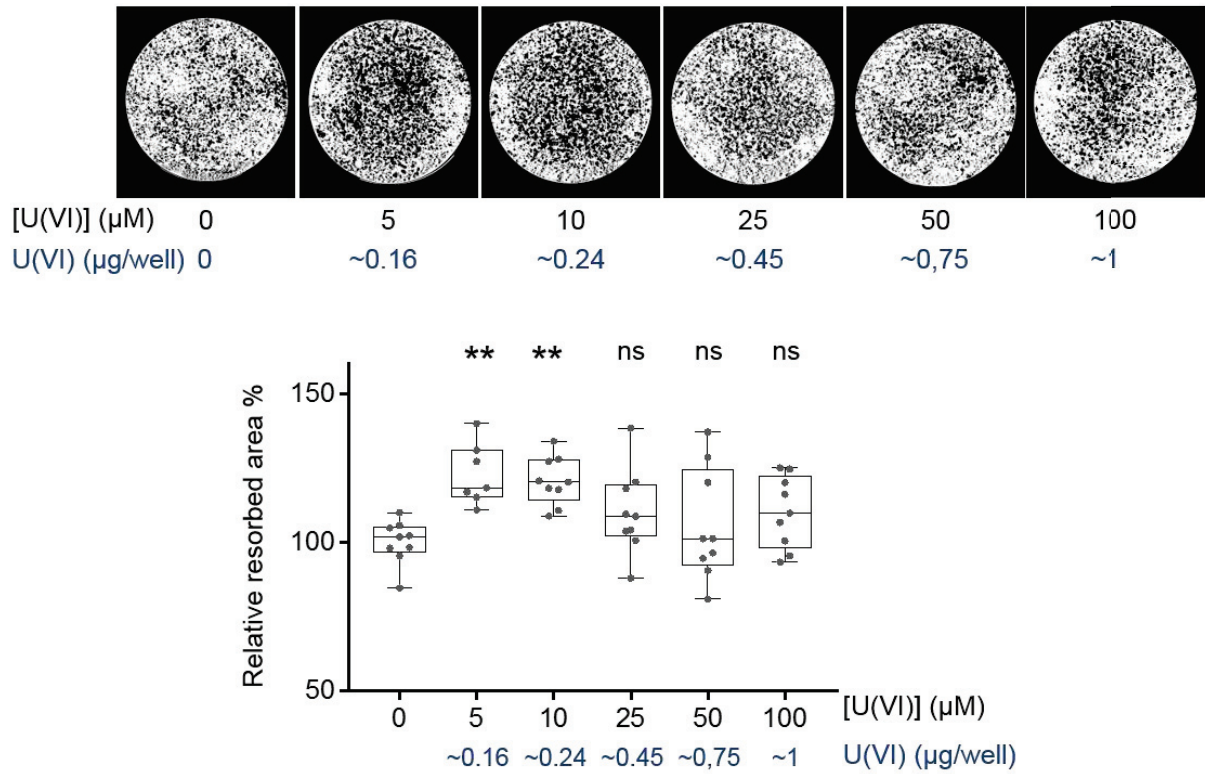


Fig. 2: Osteoclasts behavior on synthetic matrices containing U(VI). RAW 264.7 cells were cultured with RANKL onto synthetic apatite matrix, prepared in the presence of the indicated concentration (μM) of U(VI) and containing, on average, the indicated amount (μg / well) of U(VI). (A) Representative micrographs of TRAP-positive osteoclasts (> 3 nuclei) obtained after 4 days of culture on synthetic matrix in the absence or presence of U(VI). (B) Resorptive activity of osteoclasts was determined. After 4 days, osteoclasts were removed and non-resorbed area were evaluated using ImageJ processing of images from each well. Representative processed images of resorbed synthetic matrix are shown (resorbed area is in black). A box plot representation shows minima, first quartile, median, third quartile and maxima of the relative quantification of resorbed area from 4 independent experiments with median resorbed area in control condition as 100%. P values were calculated using the Kruskal-Wallis test corrected for multiple comparisons by controlling the false discovery rate with the Benjamini, Krieger, and Yekutieli test. ** $p < 0.01$, ns: non significant.

Figure 3

A

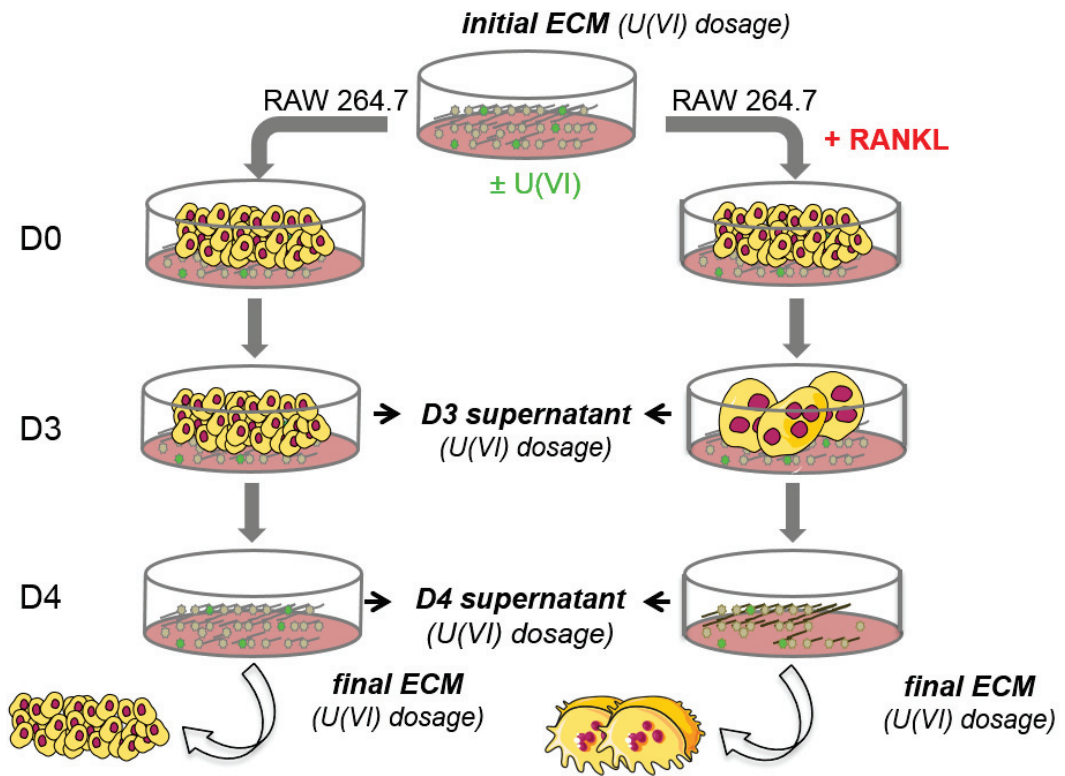


Figure 3 (suite)

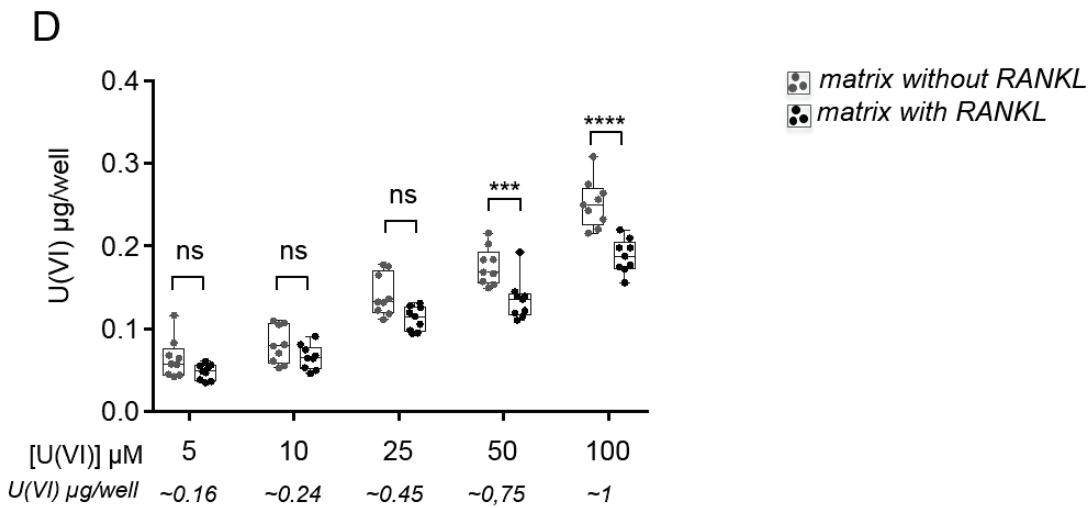
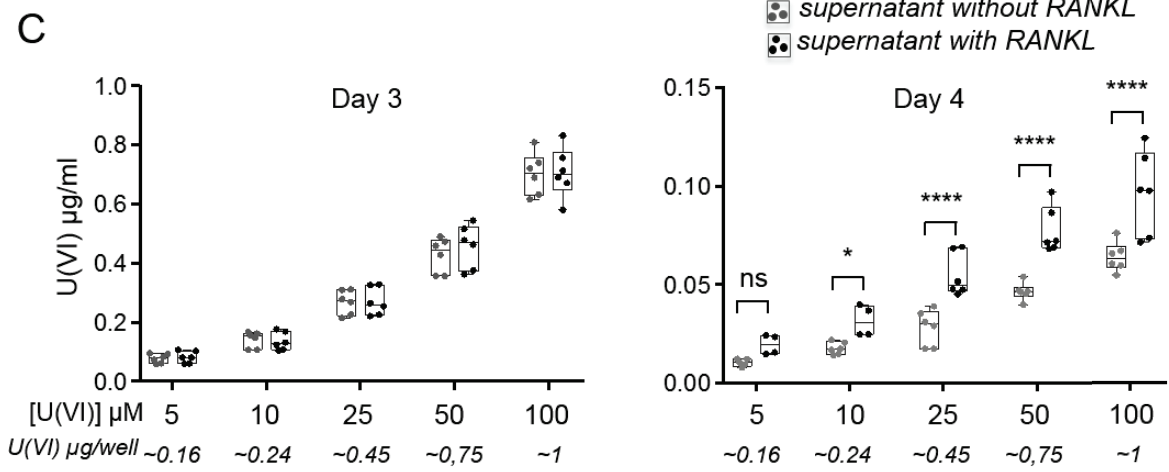
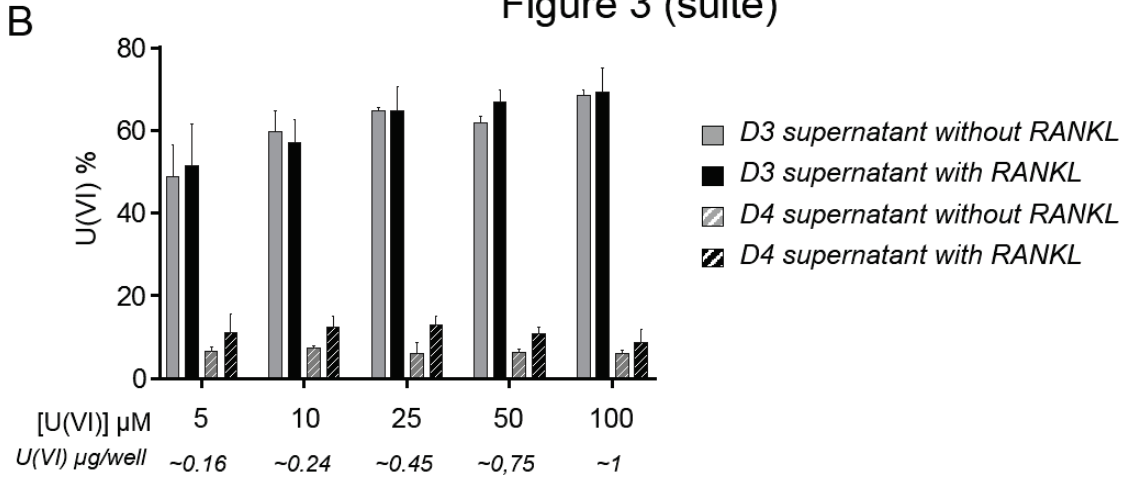


Fig. 3: U(VI) release from synthetic matrices. (A) Schematic illustration of the protocol. Series of synthetic containing different amounts of U(VI) were prepared. A part of them were used for initial U quantification (initial ECM) and another part was seeded on day 0 (D0) with RAW 264.7 cells in the absence or presence of RANKL. On day 3 (D3), culture supernatants (supernatant D3) were harvested and the cells were refed with fresh medium. On day 4, the culture medium was again collected (D4 supernatants), the matrices were de-cellularized and subjected to U quantification (final ECM). (B) A bar graph shows the release of U(VI) in culture D3 and D4 supernatants as the percent of U(VI) contained in initial matrices (C) Box plot representations show the quantification of U(VI) in D3 and D4 supernatants of synthetic matrix cultures, according to the presence of RANKL. Data are from 3 independent experiments. (C) Box plot representation of the quantification of U(VI) remaining in synthetic matrices at the end of the culture and after decellularization. Data are from 3 independent experiments. P values were determined using two-way analysis of variance (ANOVA) with two-stage step-up method of Benjamini, Krieger, and Yekutieli to control the false discovery rate. *p <0.05; ***p <0.001; ****p <0.0001 ns, not significant.

Figure 4

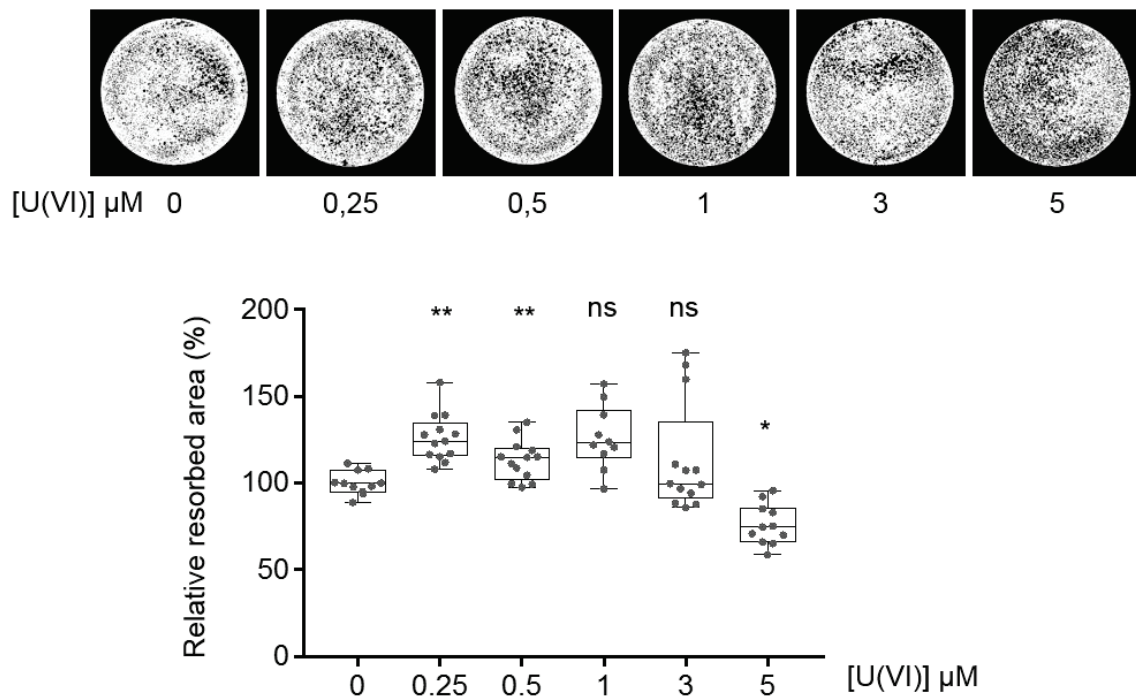


Fig. 4: Effect of low U(VI) concentrations in culture medium onto resorptive activity. RAW 264.7 cells cultured in the presence of the indicated concentrations of U(VI) were treated with RANKL to induce differentiation. After 4 days, osteoclasts were removed and resorption evaluated. Representative images of resorbed synthetic matrix and a box plot representation of the relative quantification of resorbed area from 4 independent experiments are shown. P values were calculated using the Kruskal-Wallis test corrected for multiple comparisons by controlling the false discovery rate with the Benjamini, Krieger, and Yekutieli test. ** $p < 0.01$, * $p < 0,05$; ns: non significant.

Figure 5

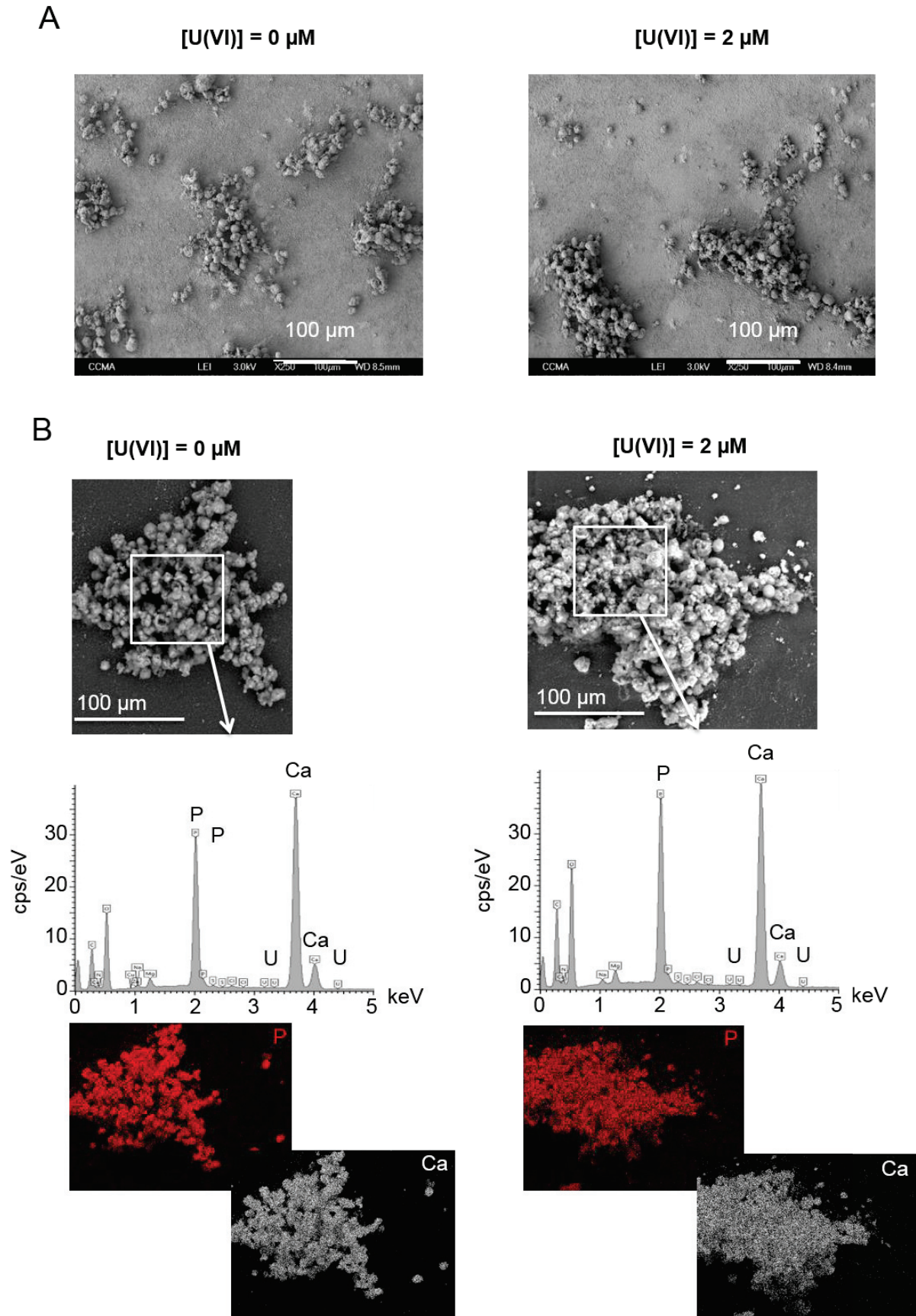


Figure 5 (suite)

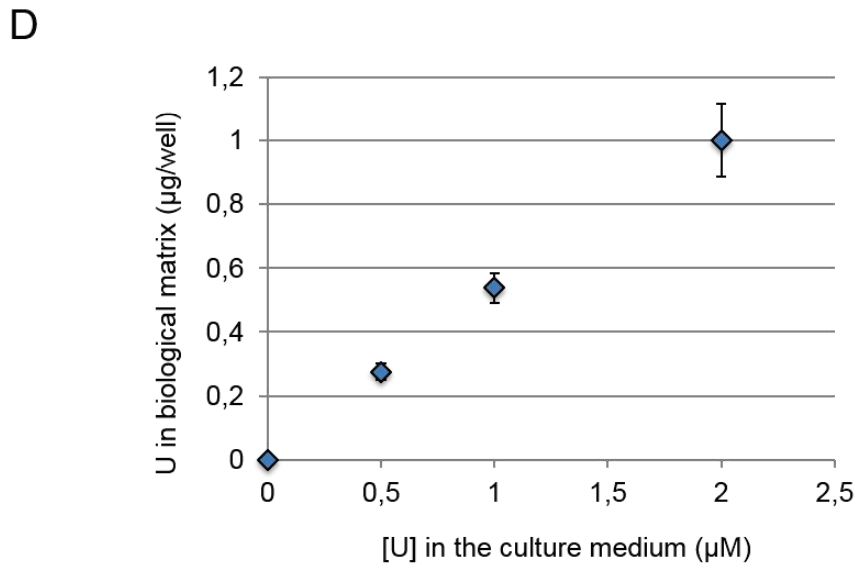
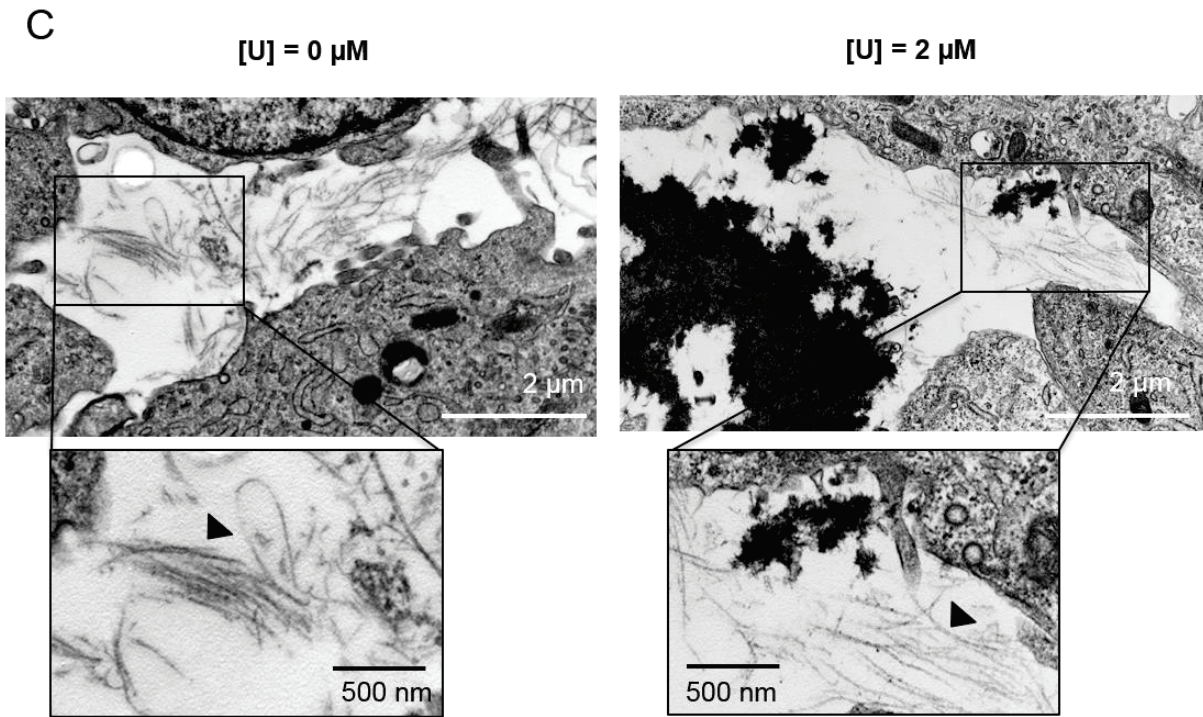


Figure 5 (suite)

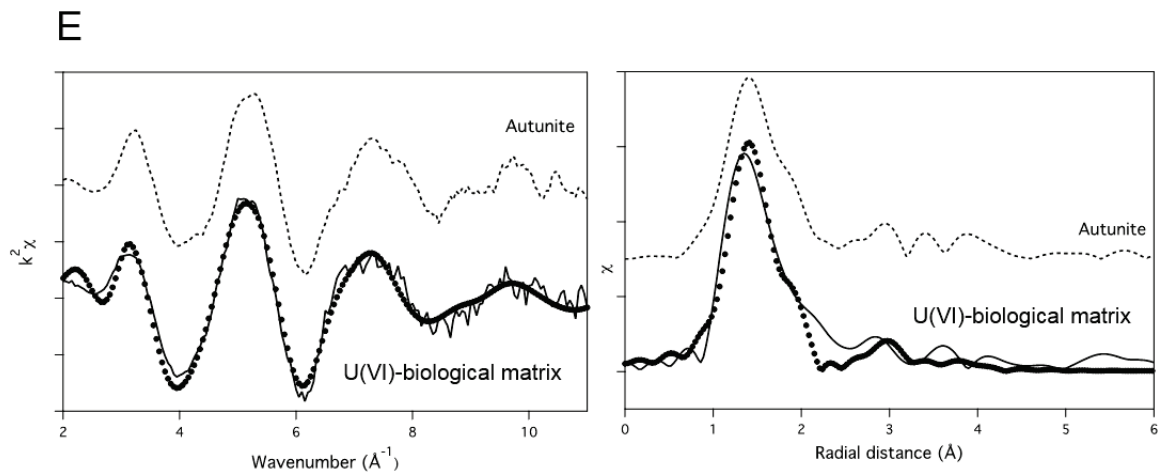
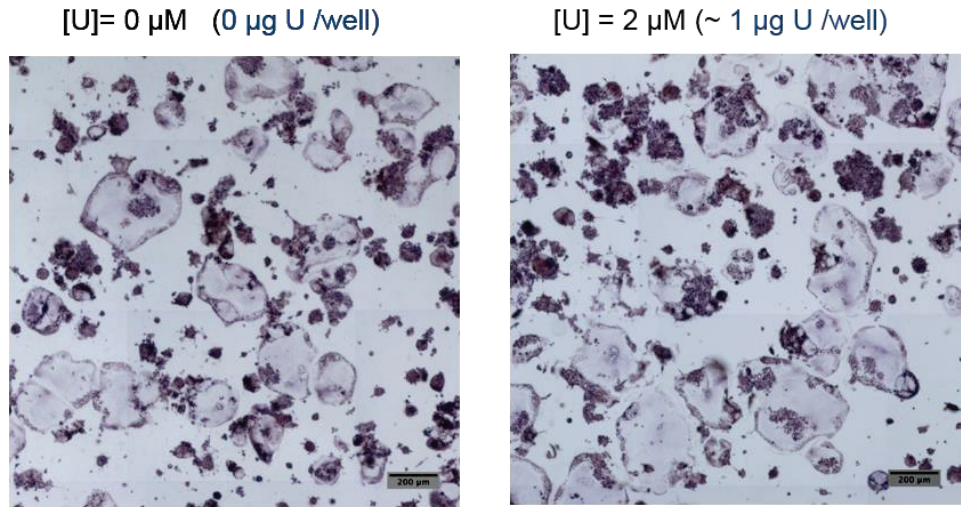


Fig. 5: U(VI) in biological SAOS-2 matrix. (A) Representative scanning electron micrographs of decellularized SAOS-2 matrix synthesized in the absence (left panel) or in the presence (right panel) of U(VI) in the culture medium. (B) Higher magnification of globular-shaped structures found in SAOS-2 matrix in the absence of presence of U(VI). X-ray microanalyses indicating calcium and phosphate composition of these structures are shown. (C) Transmission electronic images showing, in both conditions (0 and 2 μM [U(VI)]), collagen fibrils (black arrow heads) with their characteristic banding pattern. (D) SAOS-2 matrices produced in the presence of indicated concentrations of U(VI) (0, 0.5, 1 and 2 μM) were decellularized after a 10-day culture period and U(VI) incorporated therein was quantified using ICP/MS. Data represent the mean \pm SD of 4 independent experiments, each performed in duplicate or triplicate. (E) (left panel) Experimental (straight line) and adjusted (dots) EXAFS spectra at the U LIII edge of U(VI)-biological matrix shown with the experimental EXAFS spectrum of autunite model; (right panel) corresponding Fourier transforms.

Figure 6

A



B

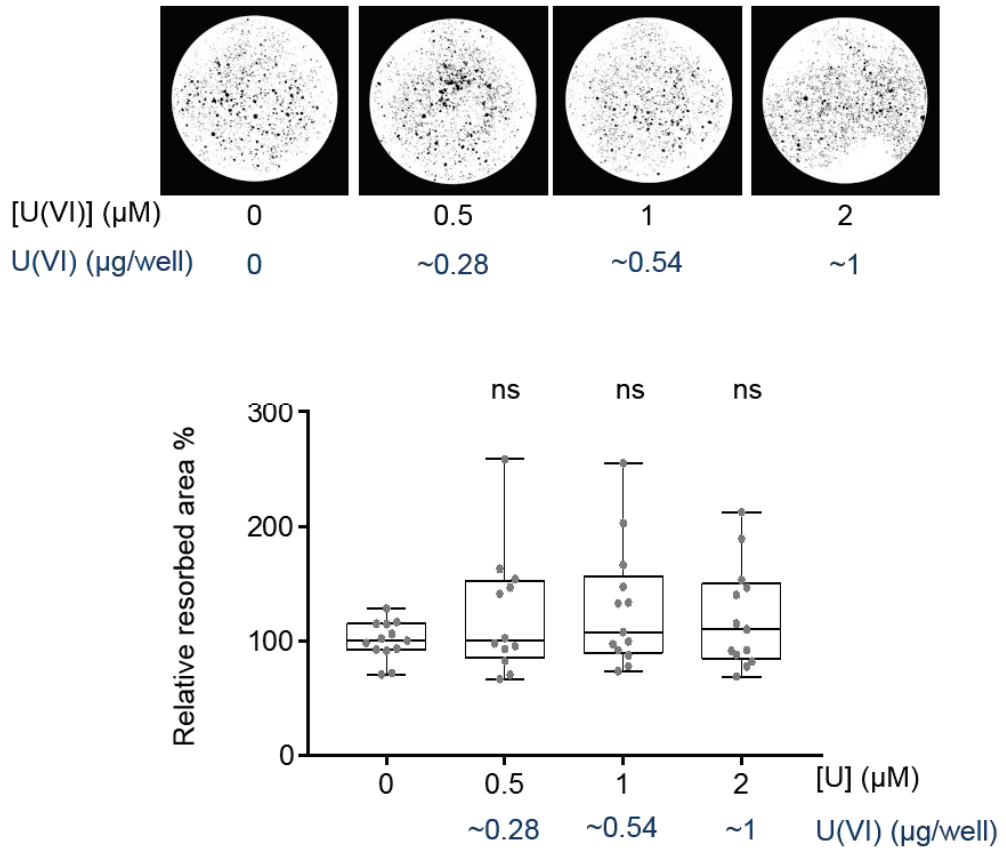


Fig. 6: Osteoclasts behavior on SAOS-2 matrices containing U(VI).

RAW 264.7 cells were cultured with RANKL onto decellularized SAOS-3 extracellular matrix, prepared in the presence of the indicated concentration (μM) of U(VI) and containing, on average, the indicated amount ($\mu\text{g}/\text{well}$) of U(VI). (A) Representative micrographs of TRAP-positive osteoclasts (> 3 nuclei) obtained after 5 days of culture in the absence or presence of U(VI). (D) Representative processed images of resorbed biological SAOS-2 matrix are shown (resorbed area is in black). A box plot representation shows the relative quantification of resorbed area from 5 independent experiments with median resorbed area in control condition as 100%. P values were calculated using the Kruskal-Wallis test corrected for multiple comparisons by controlling the false discovery rate with the Benjamini, Krieger, and Yekutieli test. ** $p < 0.01$, ns: non significant.

Figure 7

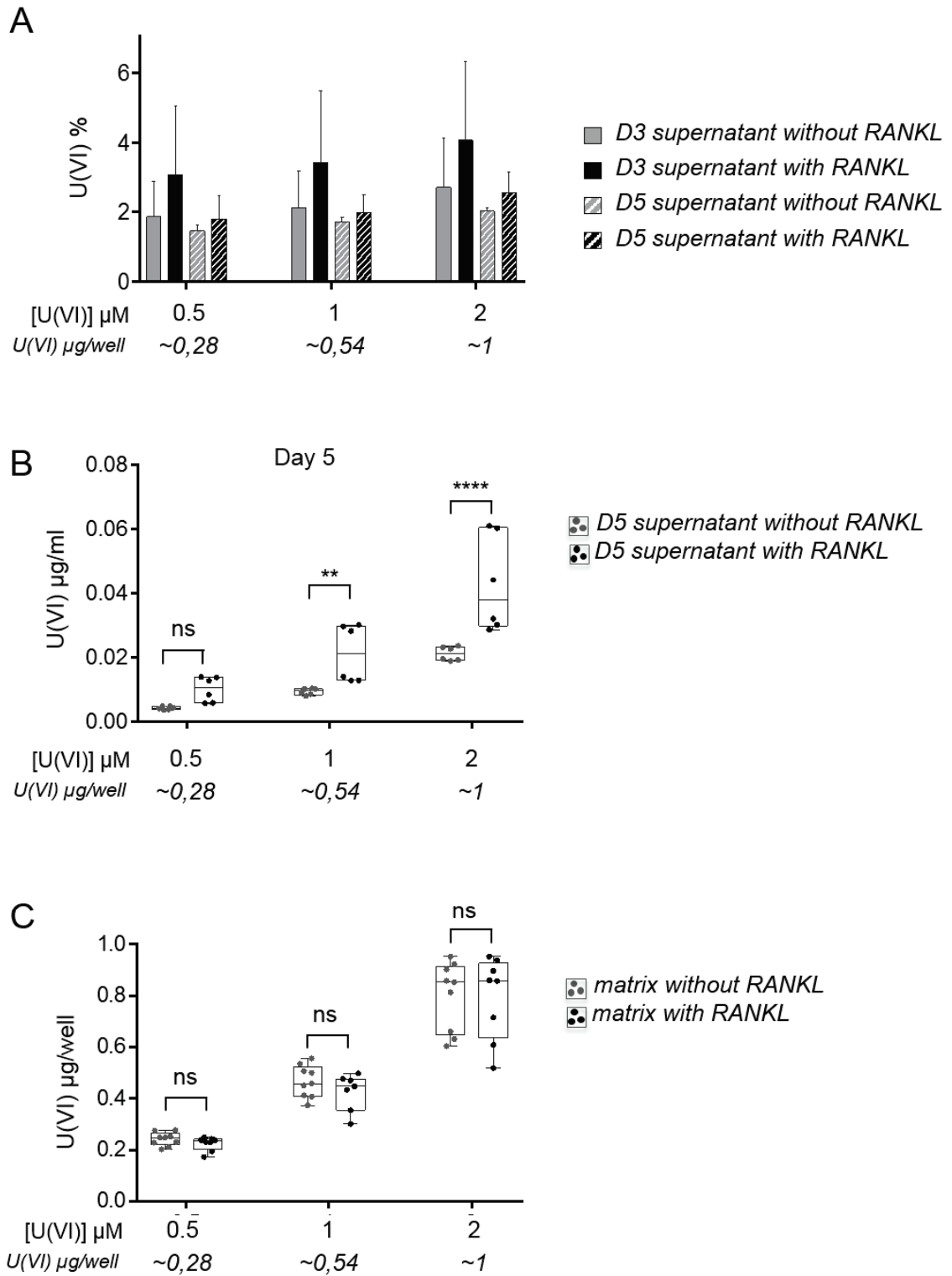


Fig. 7: U(VI) release from SAOS-2 extracellular matrices. Decellularized SAOS-2 matrices containing different amounts of U(VI) were prepared. They were used for initial U quantification or was seeded with RAW 264.7 cells in the absence or presence of RANKL. On day 3 (D3), culture supernatants (supernatant D3) were harvested and the cells were reseeded with fresh medium. On day 5 the culture medium was again collected (D5 supernatants), the matrices were de-cellularized and subjected to U quantification (final ECM). (A) A bar graph shows the release of U(VI) in D3 and D5 supernatants as the percent of U(VI) contained in initial matrices. (B) The box plot shows U(VI) quantification in D5 supernatants of SAOS-2 matrix cultures, according to the presence of RANKL. Data are from 2 independent experiments. (C) The box plot presents the quantification of U(VI) remaining in SAOS-2 matrices at the end of the culture and after de-cellularization. Data are from 3 independent experiments. P values were determined using two-way analysis of variance (ANOVA) with two-stage step-up method of Benjamini, Krieger, and Yekutieli to control the false discovery rate. **p <0.01; ***p <0.001 ns, not significant.

Figure 8

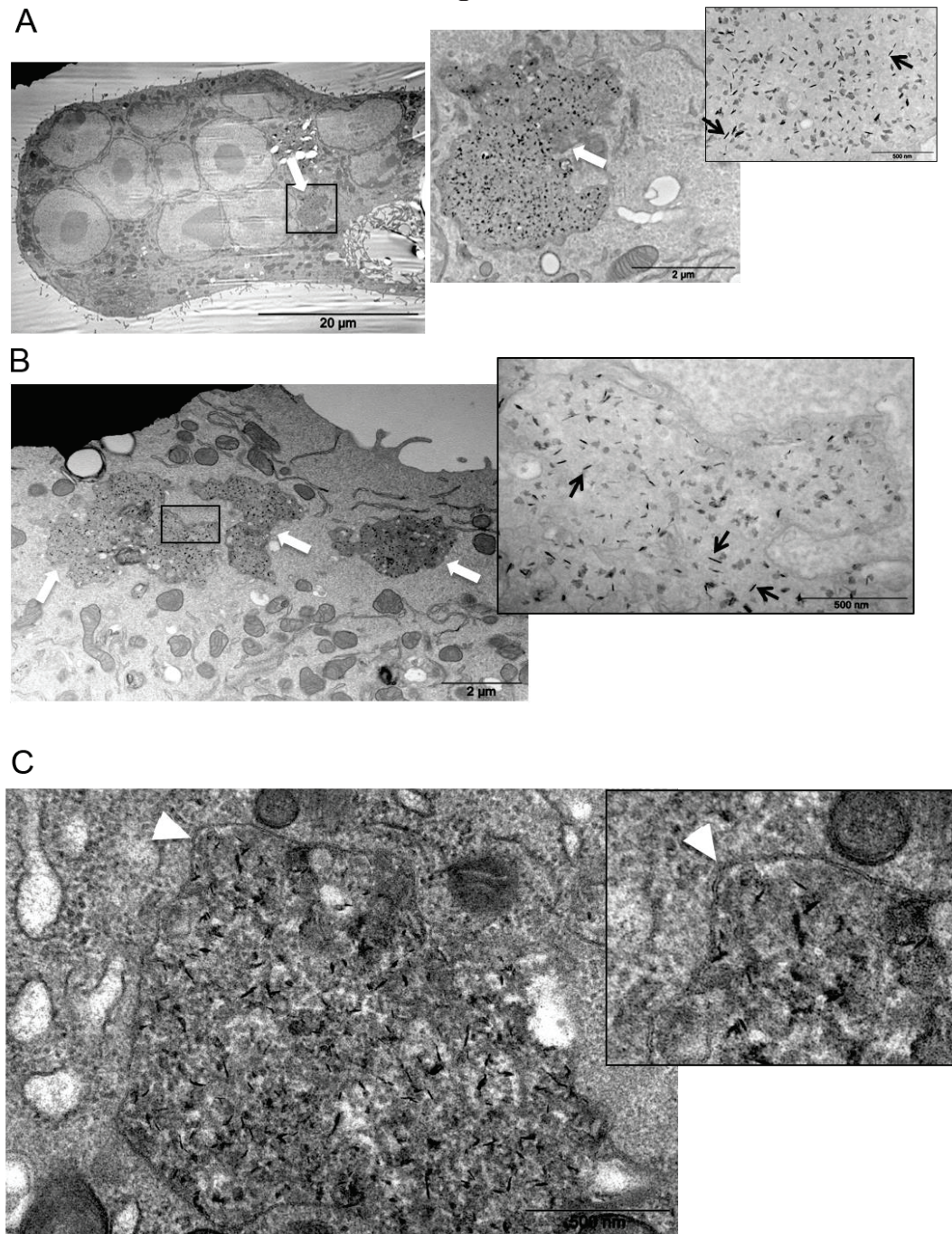


Fig. 8: Transmission electron microscopy of osteoclasts on a U-containing SAOS-2 matrix. Representative images of osteoclast with one (A) or several (B) vesicles (white arrows) containing needle-like structures (black arrows) are shown (C) Higher magnification showing the double membrane structure (white arrow head) of a vesicle containing needle-like structure, which is reminiscent of the double-membrane delimiting autophagic vesicles.

6. Supplementary data

samples	path and distance (Å)	σ^2 (Å ²)	ΔE_0 (eV); Amp
U(VI)- synthetic matrix (2.97; 2.45) ^a	2 O _{ax} at 1.83(4) 5 O _{eq} at 2.39(3) 1.6 (1) P at 3.64(1)	0.0032 0.011 0.0001	1.21; 2.28
U(VI)- Saos-2 matrix (3.10; 18.72) ^a	2 O _{ax} at 1.81(3) 5 O _{eq} at 2.32(x) 1.6 (1) P at 3.59(0)	0.0068 0.0163 0.0099	1.51; -2.44
U(VI)- Autunite (2.49; 45.29) ^a	2 O _{ax} at 1.80(x) 4 O _{eq} at 2.32(x) 4 P at 3.61(x)	0.0042 0.0110 0.0081	1.10; 0.94

^aRefers to (*r* %; χ^2/n) where *r* is the R factor of the fit in % and χ^2/n is the reduced quality factor of the fit.

Table S1 Best fit metrical parameters for the EXAFS spectra. σ^2 is the Debye Waller factor and N is the degeneracy of the path. Amp and ΔE_0 are the global amplitude factor and energy threshold of the fit. Numbers in italics have been fixed or linked, errors are given in brackets.

[U(VI)] in culture supernatant (μM)

[U(VI)] in exposure medium (μM)	Average amount of U(VI) in initial matrix (μg)	Day 3		Day 4	
		without RANKL	with RANKL	without RANKL	with RANKL
5	0,16	0,32	0,34	0,04	0,05
10	0,24	0,59	0,57	0,06	0,09
25	0,45	1,13	1,13	0,13	0,23
50	0,75	1,80	1,92	0,18	0,33
100	1	2,95	2,97	0,26	0,41

Table S2 Uranium concentrations in culture supernatants of synthetic matrices at days 3 and 4 were calculated based on ICP/MS quantification.

7. Discussion

Since U(VI) accumulates in the skeleton where it can be stored for a long time (Brugge and Buchner, 2011), several studies have focused on the effect of U(VI) on bone cells (Arzuaga *et al.*, 2015). Those were carried out *in vitro*, mainly by exposing cells to uranium in solution in the culture medium. Although this work has led to a better understanding of the mechanisms related to uranium cytotoxicity, the conditions used did not reproduce the *in vivo* situation in which uranium is embedded in the bone matrix. Supporting this point of view, a recent study showed a different effect of U(VI) on osteoblasts depending on whether it is integrated into an apatite matrix or in solution in the culture medium (Chatelain *et al.*, 2015). These findings have led us to develop bone biomimetic matrices contaminated with U(VI), a medium-term objective being to test the effect of this metal immobilized in the matrix on osteoclasts and osteoblasts, in co-culture, in order to better understand its impact on the bone remodeling cycle *in vivo*. As bone remodeling cycle begins with a resorption phase, we decided to start by studying osteoclasts. The assessment of these cell behavior in the presence of U(VI) was all the more interesting because we wanted to understand not only the effect of U(VI) on resorption but also the consequences of resorption on the distribution of U(VI). Indeed, autoradiographic and radiological analyses of rat bones that had undergone uranium injection led to the proposal that resorption contributes to the distribution of uranium in the skeleton as uranium could be resorbed from the bone surface, returned to the bloodstream and partially re-deposited in bone (Priest *et al.*, 1982). However, to the best of our knowledge, it has never been demonstrated at the cellular level that osteoclasts are able to remobilize U(VI) once it is incorporated into the bone matrix. As biomimetic matrix, we first used apatite supports containing controlled amounts of uranium and synthesized in Dr. Meyer's team (ICSM, UMR 5257, Bagnols-Sur-Cèze),

according to a published process (Chatelain *et al.*, 2015). While these mineral substrates allow the growth of osteoblastic cells (Chatelain *et al.*, 2015), we have observed a decreased viability of pre-osteoclasts on these same supports, which has hampered effective osteoclastic differentiation and resorption. The causes for this toxicity, which was observed regardless of the presence of uranium, remain to be determined. In order to find an alternative substrate, α MEM serum-free culture medium containing increasing concentrations of U(VI) was added to commercial culture plates coated with a synthetic inorganic crystalline calcium phosphate surface (COAS plates). This attempt was based on the following facts: (1) As is shown by the thermodynamic modeling of uranium speciation (Carrière *et al.*, 2004; Milgram *et al.*, 2008a, 2008b; Pierrefite-Carle *et al.*, 2016) and EXAFS analyzes (Pierrefite-Carle *et al.*, 2016), uranium is mainly in the form of soluble U(VI) carbonate complexes in MEM serum-free culture medium, and these are also among predominant species in body fluids (Ansoborlo *et al.*, 2006). (2) Apatite has a high affinity to uranium (Bourgeois *et al.*, 2015; Fuller *et al.*, 2003; Thakur *et al.*, 2009). (3) We and others routinely use COAS plates that allow an easy and reproducible evaluation of osteoclastic resorption (Gritsaenko *et al.*, 2017, 2018; Ochotny *et al.*, 2013; Zhao *et al.*, 2020). By doing so, we obtained biomimetic matrices containing 0.16 to 1.7 μg U(VI) as determined by ICP/MS. EXAFS analyses further showed that the main speciation of uranium in these bone-like surfaces is a uranyl phosphate phase in which the U local structure resembles that of the autunite phase. However, it should be noted that the interatomic distance U-O_{eq} is slightly greater in the matrix-U(VI) sample than in the autunite. This could be explained by a weak interaction between the metal and the matrix, which could be the case if U(VI) is simply adsorbed on the apatite surface. In good agreement with this assumption, we found that up to 70% of U(VI) incorporated in the matrices

could be passively released into the medium after three days of culture. The process of immobilization of U(VI) on apatite has been intensively studied (Bostick *et al.*, 1999; Fuller *et al.*, 2002, 2003; Thakur *et al.*, 2009). However, the mechanisms involved are not completely understood, perhaps because they are dependent on many parameters such as U(VI) speciation, concentration, pH, temperature, apatite composition, etc... (Mehta *et al.*, 2016; Thakur *et al.*, 2009). In our case, mechanisms of U(VI) uptake, likewise those governing the exchanges between the solid and liquid phase in our culture condition remain to be clarified. Nevertheless, these synthetic matrices seemed relevant to continue our work, as they contain U(VI) in a form previously detected inside osteoblasts and osteocytes (Hurault *et al.*, 2019; Pierrefite-Carle *et al.*, 2016) and in sufficient quantity to be quantified (using ICP/MS) both in the matrix and in culture supernatants throughout the experimental procedure.

In order to imitate bone matrix even better and because interaction between U(VI) and the organic part of the bone matrix might be of importance for uranium deposition (Basset *et al.*, 2013; Huynh *et al.*, 2016; Qi *et al.*, 2014), we have also undertaken to use biological matrices synthesized *in vitro* by an osteoblastic cell line grown in the presence of increasing concentrations of U(VI). We used the human osteosarcoma SAOS-2 cell line, known to synthesize an extracellular matrix suitable for resorption assays (Lutter *et al.*, 2010). The maximum concentration of U(VI) used was 2 μM in chronic exposure (10 days) because beyond this, the viability and the function of the SAOS-2 cells was too impaired to produce an extracellular matrix. In our experimental conditions, SAOS-2 cells produced a matrix with the expected mineral and organic phase, and incorporating a maximum of 1 μg of U(VI). As with synthetic matrices, EXAFS results suggest that U(VI) is mainly in the form of uranyl phosphate in these biological substrates. But this time, the U-O_{eq} distances are similar to those of autunite

crystalline powder. In addition, we found that no more than of 2 to 4% of U(VI) contained in the initial matrix is passively released after 3 days of culture, compared to 70% in the case of synthetic apatite surfaces. Together these data suggest a stronger interaction of U(VI) with biological matrices, which is not surprising given that U(VI) is probably biomineralized and incorporated into the biological matrix while it is simply deposited on the surface of the synthetic apatite. Although EXAFS data suggest that U(VI) is mainly present as a mineral autunite-like phase in SAOS-2-synthesized matrices, it cannot be excluded that part of U(VI) is complexed with matrix proteins. Osteopontin (OPN) is a non-collagenous protein produced by osteoblasts and belonging to the SIBLING protein family. OPN binds U(VI) with nanomolar affinity and shares with other non-collagenous SIBLING proteins features favorable to the binding of U(VI), which suggests that other non-collagenous proteins could be potential targets for uranyl cations (Qi *et al.*, 2014). This possibility underlines the interest of looking for potential interactions of U(VI) with organic components of SAOS-2 biological matrices. Unfortunately, likely due to the detection limit, element mapping using SEM/EDX did not allow us to detect U(VI) and therefore to examine the distribution of U(VI) between the mineral and organic phases of SAOS-2 matrices. Therefore, other techniques should be tried, for example scanning transmission X-ray microscopy (STXM), to detect U(VI) in our samples.

The next step was to examine osteoclastic differentiation and resorption on both types of matrices according to their initial uranium content. We will not discuss here the data on osteoclast differentiation because analyses (cell counting, cell size comparison, RT-PCR assessment of osteoclastic markers) are still in progress. On the other hand, resorption has been quantified and the results obtained show that resorption was more effective on synthetic matrices (up to 47 % of the well surface) than on biological

matrices (up to 13 % of the well surface), regardless of the presence of uranium. This could be explained by the fact that synthetic matrices are made of a very thin layer of highly homogeneous apatite while biological matrices are made of a thicker heterogeneous matrix with an organic and mineral phase. In addition, we believe that the SAOS-2 decellularization process we have used leaves too much cellular debris on the matrices, that could subsequently interfere with osteoclastic function. This is a step in our protocol that must be improved.

We also found that resorption was significantly increased in the case of synthetic matrices containing the lowest amount of U(VI) (0.16 and 0.24 μg). This last result was unexpected because in our previous study we had observed an inhibition of resorption in the presence of U(VI) in solution (from 5 μM of U(VI) in the case of RAW 264.7 and 2.5 μM for primary osteoclasts). Moreover, this stimulation was not found in the case of matrices derived from SAOS-2 cells, whereas the amounts of immobilized U(VI) were quite comparable in the two types of substrates. The concentrations of U(VI) in the various culture supernatants, determined by ICP/MS, led us to hypothesize that the differences observed between biological and synthetic matrices could originate from U(VI) in solution rather than from immobilized U(VI). On the basis of U(VI) quantifications done on the 3rd day of cultivation, it can be estimated that the passive release of U(VI) is on average nearly 20 times lower for biological matrices than for synthetic ones. Therefore, one can assume that the first steps of osteoclastogenesis occurred in the presence of very different U(VI) concentrations depending on the matrix used. We therefore evaluated the effect of U(VI) in solution, using concentrations close to those found in the culture supernatants of synthetic matrices on day 3 (Table S2). In doing so, we observed that the lowest concentrations of U(VI) (0.25 and 0.5 μM) induce a significant stimulation of resorption (of synthetic apatite) while at 5 μM , U(VI)

inhibits resorption, as previously demonstrated (Gritsaenko *et al.*, 2017). Taken together, these data suggest that the stimulation of resorption observed for synthetic matrices containing approximately 0.16 and 0.24 μg U(VI) may be due to the passive release of U(VI) into the culture medium. More importantly, these findings suggest for the first time that U(VI) has opposite effects on osteoclast behavior as a function of its concentration: 5 μM U(VI) inhibits resorption whereas 0.25 μM promotes it, in our *in vitro* conditions. These data should be compared with some *in vivo* studies that suggest an increase of resorption after exposure to U(VI) (Bozal *et al.*, 2005; Fukuda *et al.*, 2006; Kurttio *et al.*, 2005; Ubios *et al.*, 1991). It is possible that by decreasing the concentration of U(VI) in our experiments, we may approach the conditions *in vivo*. However, the comparison is complicated. Indeed, on the one hand, to reach 0.25 μM U(VI), or 59.5 $\mu\text{g/L}$ in human serum, the ingestion of 15 mg U(VI) would be necessary (2% intestinal absorption, 5L of blood) (Leggett and Harrison, 1995; Yue *et al.*, 2018), suggesting that U(VI) concentrations in our experimental conditions remain very high compared to *in vivo* conditions. On the other hand, since uranium is not homogeneously distributed in bone and is concentrated mainly in remodeling areas (Bourgeois *et al.*, 2015; Ellender *et al.*, 1995; Priest *et al.*, 1982), high local concentrations of U(VI) in bone remodeling units can be assumed. In conclusion, the use of the lowest possible U(VI) concentrations is certainly the best way to get closer to *in vivo* conditions, but it is possible that we are not so far from them. Our results also raise the question of molecular mechanisms related to the opposite effects of U (VI) on osteoclastic function. Ongoing comparison of osteoclastogenesis according to the type of matrix and the amount of U (VI) incorporated should help to clarify this point. By comparing the amount of U(VI) in supernatants and matrices resulting from cultures made without or with RANKL, we have shown that a small proportion of U(VI) is only

released from matrices in the presence of resorbing cells. This was observed for both synthetic and biological matrices. The results are significantly more robust in the case of synthetic apatite, certainly due to the low level of resorption obtained with SAOS-2 substrates. Thus, we provide here evidence in favor of the remobilization of U(VI) via osteoclastic resorption. During resorption, osteoclasts bind to the bone surface forming a resorption lacuna, isolated from the rest of the extracellular environment into which they secrete protons, chloride anions and proteases resulting in the degradation of the bone matrix (Feng and Teitelbaum, 2013; Väänänen *et al.*, 2000). Degradation products are internalized at the ruffled border, packaged into transcytosis vesicles and transported to a restricted area of the basolateral plasma membrane (called the functional secretory domain) where they are secreted (Ng *et al.*, 2019). In an attempt to detect the presence of intracellular U(VI), we used TEM to examine osteoclasts grown on synthetic or biological matrices containing 0 or 1 μg of U(VI). In all osteoclasts examined that have resorbed biological matrix containing U(VI), we observed vesicles that can reach several μm in size with dark needle-like structures inside. Surprisingly, these vesicles exhibit several characteristics of autophagic vesicles (Martinet *et al.*, 2014): some of them are clearly delimited by a double membrane, their content resembles the cytoplasm and sometimes includes membrane debris. Emerging findings indicate that, along with transcytosis, several membrane trafficking pathways that intersect, such as endocytic, secretory, and autophagic pathways are involved in the osteoclast resorption function (Ng *et al.*, 2019). Based on these results, it is tempting to speculate that U(VI) conditioned in vesicles crosses osteoclasts to be secreted by the functional domain with other degradation products. To date, we have planned STXM analyses to verify that the needle-shaped structures correspond to U(VI), though we have yet to determine the nature of the vesicles observed.

These vesicles have not been observed in osteoclasts that have resorbed synthetic matrix. This could be explained by the nature of this matrix, which is so thin that osteoclasts are very quickly found on a plastic surface during resorption. One can assume that in this case, the attachment of the osteoclast to the support becomes loose and that products resulting from resorption are released directly into the extracellular medium.

In conclusion, all our work has shown that pre-osteoclasts and osteoclasts are cells particularly sensitive to U(VI), whose function can be stimulated or inhibited depending on the concentration of U(VI) in the environment. They also show for the first time, at the cellular level, that resorption can contribute to the remobilization of U(VI). We have developed matrices that mimic bone and are contaminated with U(VI). Although improvements are needed in matrices derived from SAOS-2 cells, we believe that this 3D environment model will be very useful for further work on osteoclasts and also to study the effect of U(VI) in a co-culture context, the objective being to get as close as possible to the *in vivo* functioning of a bone remodeling unit.

8. References

- Abdelmagid, S.M., Sondag, G.R., Moussa, F.M., Belcher, J.Y., Yu, B., Stinnett, H., Novak, K., Mbimba, T., Khol, M., Hankenson, K.D., *et al.* (2015). Mutation in Osteoactivin Promotes Receptor Activator of NF κ B Ligand (RANKL)-mediated Osteoclast Differentiation and Survival but Inhibits Osteoclast Function. *J. Biol. Chem.* *290*, 20128–20146.
- Ansoborlo, E., Prat, O., Moisy, P., Den Auwer, C., Guilbaud, P., Carriere, M., Gouget, B., Duffield, J., Doizi, D., Vercouter, T., *et al.* (2006). Actinide speciation in relation to biological processes. *Biochimie* *88*, 1605–1618.
- Arey, J.S., Seaman, J.C., and Bertsch, P.M. (1999). Immobilization of Uranium in Contaminated Sediments by Hydroxyapatite Addition. *Environ. Sci. Technol.* *33*, 337–342.
- Arruda-Neto, J.D.T., Guevara, M.V.M., Nogueira, G.P., Saiki, M., Cestari, A.C., Shtejer, K., Deppman, A., Pereira Filho, J.W., Garcia, F., Geraldo, L.P., *et al.* (2004). Long-term accumulation of uranium in bones of Wistar rats as a function of intake dosages. *Radiat. Prot. Dosimetry* *112*, 385–393.
- Arzuaga, X., Gehlhaus, M., and Strong, J. (2015). Modes of action associated with uranium induced adverse effects in bone function and development. *Toxicol. Lett.* *236*, 123–130.
- ATSDR (2013). ATSDR - Toxicological Profile: Uranium.
- Basset, C., Averseng, O., Ferron, P.-J., Richaud, N., Hagège, A., Pible, O., and Vidaud, C. (2013). Revision of the biodistribution of uranyl in serum: is fetuin-A the major protein target? *Chem. Res. Toxicol.* *26*, 645–653.
- Boskey, A., and Robey, P. (2013). The Composition of Bone. In *Primer on the Metabolic Bone Diseases and Disorders of Mineral Metabolism: Seventh Edition*, pp. 49–58.
- Bostick, W.D., Jarabek, R.J., and Conca, J.L. (1999). Phosphate-induced metal stabilization: Use of apatite and bone char for the removal of soluble radionuclides in authentic and simulated DOE groundwater. *Air Waste 92nd Annu. Meet. Exhib. Proc.*
- Bourgeois, D., Burt-Pichat, B., Le Goff, X., Garrevoet, J., Tack, P., Falkenberg, G., Van Hoorebeke, L., Vincze, L., Denecke, M.A., Meyer, D., *et al.* (2015). Micro-distribution of uranium in bone after contamination: new insight into its mechanism of accumulation into bone tissue. *Anal. Bioanal. Chem.* *407*, 6619–6625.
- Bozal, C.B., Martinez, A.B., Cabrini, R.L., and Ubios, A.M. (2005). Effect of ethane-1-hydroxy-1,1-bisphosphonate (EHBP) on endochondral ossification lesions induced by a lethal oral dose of uranyl nitrate. *Arch. Toxicol.* *79*, 475–481.
- Brugge, D., and Buchner, V. (2011). Health effects of uranium: new research findings. *Rev. Environ. Health* *26*, 231–249.
- Brylka, L., and Jahnen-Dechent, W. (2013). The role of fetuin-A in physiological and pathological mineralization. *Calcif. Tissue Int.* *93*, 355–364.
- Carrière, M., Avoscan, L., Collins, R., Carrot, F., Khodja, H., Ansoborlo, E., and Gouget, B. (2004). Influence of Uranium Speciation on Normal Rat Kidney (NRK-52^E) Proximal Cell Cytotoxicity. *Chem. Res. Toxicol.* *17*, 446–452.
- Chatelain, G., Bourgeois, D., Ravoux, J., Averseng, O., Vidaud, C., and Meyer, D. (2015). Incorporation of uranium into a biomimetic apatite: physicochemical and biological aspects. *J. Biol. Inorg. Chem. JBIC Publ. Soc. Biol. Inorg. Chem.* *20*, 497–507.
- Díaz Sylvester, P.L., López, R., Ubios, A.M., and Cabrini, R.L. (2002). Exposure to subcutaneously implanted uranium dioxide impairs bone formation. *Arch. Environ. Health* *57*, 320–325.

- Ellender, M., Haines, J.W., and Harrison, J.D. (1995). The distribution and retention of plutonium, americium and uranium in CBA/H mice. *Hum. Exp. Toxicol.* *14*, 38–48.
- Faruqi, A.F., Rao, H., Causer, J., and Beltzer, J.P. (2011). Corning osteo assay surface for the study of bone resorption. p.
- Feng, X., and Teitelbaum, S.L. (2013). Osteoclasts: New Insights. *Bone Res.* *1*, 11–26.
- Fukuda, S., Ikeda, M., Chiba, M., and Kaneko, K. (2006). Clinical diagnostic indicators of renal and bone damage in rats intramuscularly injected with depleted uranium. *Radiat. Prot. Dosimetry* *118*, 307–314.
- Fuller, C.C., Bargar, J.R., Davis, J.A., and Piana, M.J. (2002). Mechanisms of uranium interactions with hydroxyapatite: implications for groundwater remediation. *Environ. Sci. Technol.* *36*, 158–165.
- Fuller, C.C., Bargar, J.R., and Davis, J.A. (2003). Molecular-scale characterization of uranium sorption by bone apatite materials for a permeable reactive barrier demonstration. *Environ. Sci. Technol.* *37*, 4642–4649.
- Gigliotti, C.L., Boggio, E., Clemente, N., Shivakumar, Y., Toth, E., Sblattero, D., D'Amelio, P., Isaia, G.C., Dianzani, C., Yagi, J., *et al.* (2016). ICOS-Ligand Triggering Impairs Osteoclast Differentiation and Function In Vitro and In Vivo. *J. Immunol. Baltim. Md 1950* *197*, 3905–3916.
- Gorski, J.P. (2011). Biomineralization of bone: a fresh view of the roles of non-collagenous proteins. *Front. Biosci. Landmark Ed.* *16*, 2598–2621.
- Gritsaenko, T., Pierrefite-Carle, V., Lorivel, T., Breuil, V., Carle, G.F., and Santucci-Darmanin, S. (2017). Natural uranium impairs the differentiation and the resorbing function of osteoclasts. *Biochim. Biophys. Acta Gen. Subj.* *1861*, 715–726.
- Gritsaenko, T., Pierrefite-Carle, V., Creff, G., Vidaud, C., Carle, G., and Santucci-Darmanin, S. (2018). Methods for Analyzing the Impacts of Natural Uranium on In Vitro Osteoclastogenesis. *J. Vis. Exp. JoVE.*
- Guglielmotti, M.B., Ubios, A.M., and Cabrini, R.L. (1985). Alveolar wound healing alteration under uranyl nitrate intoxication. *J. Oral Pathol. Med.* *14*, 565–572.
- Guglielmotti, M.B., Ubios, A.M., de Rey, B.M., and Cabrini, R.L. (1984). Effects of acute intoxication with uranyl nitrate on bone formation. *Experientia* *40*, 474–476.
- Hurault, L., Creff, G., Hagège, A., Santucci-Darmanin, S., Pagnotta, S., Farlay, D., Den Auwer, C., Pierrefite-Carle, V., and Carle, G.F. (2019). Uranium Effect on Osteocytic Cells In Vitro. *Toxicol. Sci. Off. J. Soc. Toxicol.* *170*, 199–209.
- Huynh, T.-N.S., Vidaud, C., and Hagège, A. (2016). Investigation of uranium interactions with calcium phosphate-binding proteins using ICP/MS and CE-ICP/MS. *Met. Integr. Biometal Sci.* *8*, 1185–1192.
- Icer, M.A., and Gezmen-Karadag, M. (2018). The multiple functions and mechanisms of osteopontin. *Clin. Biochem.* *59*, 17–24.
- Kurttio, P., Komulainen, H., Leino, A., Salonen, L., Auvinen, A., and Saha, H. (2005). Bone as a possible target of chemical toxicity of natural uranium in drinking water. *Environ. Health Perspect.* *113*, 68–72.
- Larivière, D., Tolmachev, S.Y., Kochermin, V., and Johnson, S. (2013). Uranium bone content as an indicator of chronic environmental exposure from drinking water. *J. Environ. Radioact.* *121*, 98–103.
- Leggett, R.W. (1994). Basis for the ICRP's age-specific biokinetic model for uranium. *Health Phys.* *67*, 589–610.

- Leggett, R.W., and Harrison, J.D. (1995). Fractional absorption of ingested uranium in humans. *Health Phys.* 68, 484–498.
- Locock, A.J., and Burns, P.C. (2003). The crystal structure of synthetic autunite, $\text{Ca}[(\text{UO}_2)(\text{PO}_4)]_2(\text{H}_2\text{O})_{11}$. *Am. Mineral.* 88, 240–244.
- Lutter, A.-H., Hempel, U., Wolf-Brandstetter, C., Garbe, A.I., Goetsch, C., Hofbauer, L.C., Jessberger, R., and Dieter, P. (2010). A novel resorption assay for osteoclast functionality based on an osteoblast-derived native extracellular matrix. *J. Cell. Biochem.* 109, 1025–1032.
- Martinet, W., Timmermans, J.-P., and De Meyer, G.R.Y. (2014). Methods to assess autophagy in situ—transmission electron microscopy versus immunohistochemistry. *Methods Enzymol.* 543, 89–114.
- Mehta, V.S., Maillot, F., Wang, Z., Catalano, J.G., and Giammar, D.E. (2016). Effect of Reaction Pathway on the Extent and Mechanism of Uranium(VI) Immobilization with Calcium and Phosphate. *Environ. Sci. Technol.* 50, 3128–3136.
- Milgram, S., Carrière, M., Malaval, L., and Gouget, B. (2008a). Cellular accumulation and distribution of uranium and lead in osteoblastic cells as a function of their speciation. *Toxicology* 252, 26–32.
- Milgram, S., Carrière, M., Thiebault, C., Malaval, L., and Gouget, B. (2008b). Cytotoxic and phenotypic effects of uranium and lead on osteoblastic cells are highly dependent on metal speciation. *Toxicology* 250, 62–69.
- Neuman, W.F., and Neuman, M.W. (1949). The deposition of uranium in bone; adsorption studies in vitro. *J. Biol. Chem.* 179, 325–333.
- Ng, P.Y., Brigitte Patricia Ribet, A., and Pavlos, N.J. (2019). Membrane trafficking in osteoclasts and implications for osteoporosis. *Biochem. Soc. Trans.* 47, 639–650.
- Ochotny, N., Voronov, I., Owen, C., Aubin, J.E., and Manolson, M.F. (2013). The R740S mutation in the V-ATPase $\alpha 3$ subunit results in osteoclast apoptosis and defective early-stage autophagy. *J. Cell. Biochem.* 114, 2823–2833.
- Ohnuki, T., Kozai, N., Samadifam, M., Yasuda, R., Yamamoto, S., Narumi, K., Naramoto, H., and Murakami, T. (2004). The formation of autunite ($\text{Ca}(\text{UO}_2)_2(\text{PO}_4)_2 \cdot n\text{H}_2\text{O}$) within the leached layer of dissolving apatite: Incorporation mechanism of uranium by apatite. *Chem. Geol.* 211, 1–14.
- Pierrefite-Carle, V., Santucci-Darmanin, S., Breuil, V., Gritsaenko, T., Vidaud, C., Creff, G., Solari, P.L., Pagnotta, S., Al-Sahlane, R., Auwer, C.D., *et al.* (2016). Effect of natural uranium on the UMR-106 osteoblastic cell line: impairment of the autophagic process as an underlying mechanism of uranium toxicity. *Arch. Toxicol.*
- Priest, N.D., Howells, G.R., Green, D., and Haines, J.W. (1982). Uranium in bone: metabolic and autoradiographic studies in the rat. *Hum. Toxicol.* 1, 97–114.
- Qi, L., Basset, C., Averseng, O., Quéméneur, E., Hagège, A., and Vidaud, C. (2014). Characterization of $\text{UO}_2(2+)$ binding to osteopontin, a highly phosphorylated protein: insights into potential mechanisms of uranyl accumulation in bones. *Met. Integr. Biometal Sci.* 6, 166–176.
- Ravel, B., and Newville, M. (2005). ATHENA, ARTEMIS, HEPHAESTUS: data analysis for X-ray absorption spectroscopy using IFEFFIT. *J. Synchrotron Radiat.* 12, 537–541.
- Rehr, J.J., Kas, J.J., Vila, F.D., Prange, M.P., and Jorissen, K. (2010). Parameter-free calculations of X-ray spectra with FEFF9. *Phys. Chem. Chem. Phys.* PCCP 12, 5503–5513.

- Rodrigues, G., Arruda-Neto, J.D.T., Pereira, R.M.R., Kleeb, S.R., Geraldo, L.P., Primi, M.C., Takayama, L., Rodrigues, T.E., Cavalcante, G.T., Genofre, G.C., *et al.* (2013). Uranium deposition in bones of Wistar rats associated with skeleton development. *Appl. Radiat. Isot.* 82, 105–110.
- Simon, F., Biermann, V., and Peplinski, B. (2008). Uranium removal from groundwater using hydroxyapatite. p.
- Sitaud, B., Solari, P.L., Schlutig, S., Llorens, I., and Hermange, H. (2012). Characterization of radioactive materials using the MARS beamline at the synchrotron SOLEIL. *J. Nucl. Mater.* 425, 238–243.
- Tasat, D.R., Orona, N.S., Mandalunis, P.M., Cabrini, R.L., and Ubios, A.M. (2007). Ultrastructural and metabolic changes in osteoblasts exposed to uranyl nitrate. *Arch. Toxicol.* 81, 319–326.
- Thakur, P., Moore, R.C., and Choppin, G.R. (2009). Sorption of U(VI) species on hydroxyapatite. *Radiochim. Acta* 93, 385–391.
- Triffitt, J.T., Gebauer, U., Ashton, B.A., Owen, M.E., and Reynolds, J.J. (1976). Origin of plasma alpha₂HSGlycoprotein and its accumulation in bone. *Nature* 262, 226–227.
- Ubios, A.M., Guglielmotti, M.B., Steimetz, T., and Cabrini, R.L. (1991). Uranium inhibits bone formation in physiologic alveolar bone modeling and remodeling. *Environ. Res.* 54, 17–23.
- Väänänen, H.K., Zhao, H., Mulari, M., and Halleen, J.M. (2000). The cell biology of osteoclast function. *J. Cell Sci.* 113 (Pt 3), 377–381.
- Vidaud, C., Bourgeois, D., and Meyer, D. (2012). Bone as target organ for metals: the case of f-elements. *Chem. Res. Toxicol.* 25, 1161–1175.
- Wade-Gueye, N.M., Delissen, O., Gourmelon, P., Aigueperse, J., Dublineau, I., and Souidi, M. (2012). Chronic exposure to natural uranium via drinking water affects bone in growing rats. *Biochim. Biophys. Acta BBA - Gen. Subj.* 1820, 1121–1127.
- Yue, Y.-C., Li, M.-H., Wang, H.-B., Zhang, B.-L., and He, W. (2018). The toxicological mechanisms and detoxification of depleted uranium exposure. *Environ. Health Prev. Med.* 23, 18.
- Zhao, H., Lazarenko, O.P., and Chen, J.-R. (2020). Hippuric acid and 3-(3-hydroxyphenyl) propionic acid inhibit murine osteoclastogenesis through RANKL-RANK independent pathway. *J. Cell. Physiol.* 235, 599–610

Conclusion

CONCLUSION

This dissertation presents results of two projects, seemingly very different: (1) the characterization of a murine model corresponding to a rare human progeroid disease with pathological bone alterations and (2) the study of the effect of uranium on osteoclasts. Both, however, are related to the exploration of the modified bone extracellular matrices and the consequences of these modifications on bone cells. Thereby, the general study design was the same for both projects: the *in vitro* production of the mineralized ECMs, their characterization and their use as a culture support for bone cells.

The two projects have progressed at different tempos. While in the first one we have thoroughly characterized the ECM, in the second, we have focused more on the effect of ECM modifications on osteoclasts behaviors. Nonetheless, we have developed three different three-dimensional bone cell culture systems that mimic normal or defective bone microenvironments. These are: (1) the synthetic inorganic resorbable substrates containing varying amounts of adsorbed uranium, (2) “biological” matrices into which uranium is incorporated through biomineralization (3) the matrices synthesized by *Recql4*^{-/-} primary mouse osteoblasts, which have abnormal stiffness and modified protein composition. The last two models are of particular interest because, used in co-culture experiments (osteoclasts + osteoblasts), they would allow to approach the physiological conditions of a bone remodeling unit.

With RECQL4-deficient mice, we have described a new murine model of premature bone aging and determined possible mechanisms underlying this

phenotype. On the basis of proteomic data, several non-exclusive hypotheses can be proposed. Accumulation of decorin in the bone ECM, combined with the increased number of collagen cross-links produced by LOXL4, could stiffen the organic matrix, thereby enhancing osteoclastic resorption. At the same time, the lack of pleiotrophin and SLIT3, two chemoattractant molecules of osteoblasts, could affect the recruitment of these cells at remodeling sites, and thus alter mineralization. Experiments to validate these hypotheses are currently being programmed. Additionally, we have identified YB1 as another protein that might participate in the establishment of bone phenotype induced by RECQL4 deficiency. It has not been associated previously with bone physiology and therefore seems an interesting research subject. Taken together our results suggest that alterations in bone ECM are involved in accelerated bone loss associated with RECQL4 dysfunction.

With regard to uranium, we provide the first evidence of a biphasic effect of this metal on osteoclasts, whose function can be stimulated or inhibited depending on the U(VI) concentration in the environment. We have also shown that osteoclasts are able to remobilize the uranium incorporated in the ECM, which had never been formally demonstrated before.

In conclusion, this work illustrates the importance of bone matrix alterations on bone cell function. In addition, the development of three-dimensional bone cell culture systems will be useful in identifying new mechanisms essential to bone health.

REFERENCES

1. Karaplis, A. C. Chapter 3 - Embryonic Development of Bone and Regulation of Intramembranous and Endochondral Bone Formation. in *Principles of Bone Biology (Third Edition)* (eds. Bilezikian, J. P., Raisz, L. G. & Martin, T. J.) 53–84 (Academic Press, 2008). doi:10.1016/B978-0-12-373884-4.00025-2.
2. Franz-Odenaal, T., A. Induction and patterning of intramembranous bone. *Front. Biosci.* **16**, 2734 (2011).
3. Provot, S., Schipani, E., Wu, J. Y. & Kronenberg, H. Chapter 6 - Development of the Skeleton. in *Osteoporosis (Fourth Edition)* (eds. Marcus, R., Feldman, D., Dempster, D. W., Luckey, M. & Cauley, J. A.) 97–126 (Academic Press, 2013). doi:10.1016/B978-0-12-415853-5.00006-6.
4. Gentili, C. & Cancedda, R. Cartilage and bone extracellular matrix. *Curr. Pharm. Des.* **15**, 1334–1348 (2009).
5. Jilka, R. L. The Relevance of Mouse Models for Investigating Age-Related Bone Loss in Humans. *J. Gerontol. A. Biol. Sci. Med. Sci.* **68**, 1209–1217 (2013).
6. Bouxsein, M. L. *et al.* Guidelines for assessment of bone microstructure in rodents using micro-computed tomography. *J. Bone Miner. Res.* **25**, 1468–1486 (2010).
7. Clarke, B. Normal Bone Anatomy and Physiology. *Clin. J. Am. Soc. Nephrol. CJASN* **3**, S131–S139 (2008).
8. Squier, C. A., Ghoneim, S. & Kremenak, C. R. Ultrastructure of the periosteum from membrane bone. *J. Anat.* **171**, 233–239 (1990).
9. Martin, R. B., Burr, D. B., Sharkey, N. A. & Fyhrie, D. P. Skeletal Biology. in *Skeletal Tissue Mechanics* (eds. Martin, R. B., Burr, D. B., Sharkey, N. A. & Fyhrie, D. P.) 35–93 (Springer New York, 2015). doi:10.1007/978-1-4939-3002-9_2.
10. Skedros, J. G., Holmes, J. L., Vajda, E. G. & Bloebaum, R. D. Cement lines of secondary osteons in human bone are not mineral-deficient: New data in a historical perspective. *Anat. Rec. A. Discov. Mol. Cell. Evol. Biol.* **286A**, 781–803 (2005).
11. Jee, W. S. S. Integrated Bone Tissue Physiology. in *Bone mechanics handbook* 1-1–68 (CRC Press, 2001).
12. Ramasamy, S. K. Structure and Functions of Blood Vessels and Vascular Niches in Bone. *Stem Cells Int.* **2017**, 5046953 (2017).
13. Grüneboom, A. *et al.* A network of trans-cortical capillaries as mainstay for blood circulation in long bones. *Nat. Metab.* **1**, 236 (2019).
14. Gorelashvili, M. G., Heinze, K. G. & Stegner, D. Optical Clearing of Murine Bones to Study Megakaryocytes in Intact Bone Marrow Using Light-Sheet Fluorescence Microscopy. *Methods Mol. Biol. Clifton NJ* **1812**, 233–253 (2018).
15. Qiu, S., Rao, D. S., Palnitkar, S. & Parfitt, A. M. Age and distance from the surface but not menopause reduce osteocyte density in human cancellous bone. *Bone* **31**, 313–318 (2002).
16. Tiede-Lewis, L. M. *et al.* Degeneration of the osteocyte network in the C57BL/6 mouse model of aging. *Aging* **9**, 2190–2208 (2017).

17. D'Ippolito, G., Schiller, P. C., Ricordi, C., Roos, B. A. & Howard, G. A. Age-Related Osteogenic Potential of Mesenchymal Stromal Stem Cells from Human Vertebral Bone Marrow. *J. Bone Miner. Res.* **14**, 1115–1122 (1999).
18. Muschler, G. F., Nitto, H., Boehm, C. A. & Easley, K. A. Age- and gender-related changes in the cellularity of human bone marrow and the prevalence of osteoblastic progenitors. *J. Orthop. Res.* **19**, 117–125 (2001).
19. Nishida, S., Endo, N., Yamagiwa, H., Tanizawa, T. & Takahashi, H. E. Number of osteoprogenitor cells in human bone marrow markedly decreases after skeletal maturation. *J. Bone Miner. Metab.* **17**, 171–177 (1999).
20. Brazill, J. M., Beeve, A. T., Craft, C. S., Ivanusic, J. J. & Scheller, E. L. Nerves in Bone: Evolving Concepts in Pain and Anabolism. *J. Bone Miner. Res. Off. J. Am. Soc. Bone Miner. Res.* (2019) doi:10.1002/jbmr.3822.
21. Hill, E. L., Turner, R. & Elde, R. Effects of neonatal sympathectomy and capsaicin treatment on bone remodeling in rats. *Neuroscience* **44**, 747–755 (1991).
22. He, H. *et al.* CGRP may regulate bone metabolism through stimulating osteoblast differentiation and inhibiting osteoclast formation. *Mol. Med. Rep.* **13**, 3977–3984 (2016).
23. Villa, I., Mrak, E., Rubinacci, A., Ravasi, F. & Guidobono, F. CGRP inhibits osteoprotegerin production in human osteoblast-like cells via cAMP/PKA-dependent pathway. *Am. J. Physiol. Cell Physiol.* **291**, C529–537 (2006).
24. Wang, L. *et al.* Substance P stimulates bone marrow stromal cell osteogenic activity, osteoclast differentiation, and resorption activity in vitro. *Bone* **45**, 309–320 (2009).
25. Hayashi, M. *et al.* Osteoprotection by semaphorin 3A. *Nature* **485**, 69–74 (2012).
26. Kim, B.-J. *et al.* Osteoclast-secreted SLIT3 coordinates bone resorption and formation. *J. Clin. Invest.* **128**, 1429–1441 (2018).
27. Weiner, S. & Wagner, H.D. The material bone: Structure-Mechanical Function Relations. *Annu. Rev. Mater. Sci.* **28**, 271–298 (1998).
28. Reznikov, N., Shahar, R. & Weiner, S. Three-dimensional structure of human lamellar bone: The presence of two different materials and new insights into the hierarchical organization. *Bone* **59**, 93–104 (2014).
29. Reznikov, N., Bilton, M., Lari, L., Stevens, M. M. & Kröger, R. Fractal-like hierarchical organization of bone begins at the nanoscale. *Science* **360**, (2018).
30. Orgel, J. P. R. O., Irving, T. C., Miller, A. & Wess, T. J. Microfibrillar structure of type I collagen in situ. *Proc. Natl. Acad. Sci.* **103**, 9001–9005 (2006).
31. Giraud-Guille, M. M. Twisted plywood architecture of collagen fibrils in human compact bone osteons. *Calcif. Tissue Int.* **42**, 167–180 (1988).
32. Weiner, S., Arad, T., Sabanay, I. & Traub, W. Rotated plywood structure of primary lamellar bone in the rat: Orientations of the collagen fibril arrays. *Bone* **20**, 509–514 (1997).
33. Atkins, A. *et al.* The three-dimensional structure of anosteocytic lamellated bone of fish. *Acta Biomater.* **13**, 311–323 (2015).
34. Faingold, A., Cohen, S. R., Reznikov, N. & Wagner, H. D. Osteonal lamellae elementary units: Lamellar microstructure, curvature and mechanical properties. *Acta Biomater.* **9**, 5956–5962 (2013).
35. Reznikov, N., Almany-Magal, R., Shahar, R. & Weiner, S. Three-dimensional imaging of collagen fibril organization in rat circumferential lamellar bone using a dual beam electron microscope reveals ordered and disordered sub-lamellar structures. *Bone* **52**, 676–683 (2013).

36. Reznikov, N., Chase, H., Brumfeld, V., Shahar, R. & Weiner, S. The 3D structure of the collagen fibril network in human trabecular bone: Relation to trabecular organization. *Bone* **71**, 189–195 (2015).
37. Reznikov, N., Shahar, R. & Weiner, S. Bone hierarchical structure in three dimensions. *Acta Biomater.* **10**, 3815–3826 (2014).
38. Fuchs, R. K., Thompson, W. R. & Warden, S. J. 2 - Bone biology. in *Bone Repair Biomaterials (Second Edition)* (eds. Pawelec, K. M. & Planell, J. A.) 15–52 (Woodhead Publishing, 2019). doi:10.1016/B978-0-08-102451-5.00002-0.
39. Kiel, M. J. *et al.* SLAM Family Receptors Distinguish Hematopoietic Stem and Progenitor Cells and Reveal Endothelial Niches for Stem Cells. *Cell* **121**, 1109–1121 (2005).
40. Nakamura, Y. *et al.* Isolation and characterization of endosteal niche cell populations that regulate hematopoietic stem cells. *Blood* **116**, 1422–1432 (2010).
41. Zhang, J. *et al.* Identification of the haematopoietic stem cell niche and control of the niche size. *Nature* **425**, 836–841 (2003).
42. Bowers, M. *et al.* Osteoblast ablation reduces normal long-term hematopoietic stem cell self-renewal but accelerates leukemia development. *Blood* **125**, 2678–2688 (2015).
43. Calvi, L. M. *et al.* Osteoblastic cells regulate the haematopoietic stem cell niche. *Nature* **425**, 841–846 (2003).
44. Burr, D. B. Chapter 1 - Bone Morphology and Organization. in *Basic and Applied Bone Biology (Second Edition)* (eds. Burr, D. B. & Allen, M. R.) 3–26 (Academic Press, 2019). doi:10.1016/B978-0-12-813259-3.00001-4.
45. Saidak, Z., Le Henaff, C., Azzi, S., Marty, C. & Marie, P. J. Low-dose PTH increases osteoblast activity via decreased Mef2c/Sost in senescent osteopenic mice. *J. Endocrinol.* **223**, 25–33 (2014).
46. Brown, E. M. & Hebert, S. C. Calcium-receptor-regulated parathyroid and renal function. *Bone* **20**, 303–309 (1997).
47. Shaker, J. L. & Deftos, L. Calcium and Phosphate Homeostasis. in *Endotext* (eds. Feingold, K. R. *et al.*) (MDText.com, Inc., 2000).
48. Han, Y., You, X., Xing, W., Zhang, Z. & Zou, W. Paracrine and endocrine actions of bone—the functions of secretory proteins from osteoblasts, osteocytes, and osteoclasts. *Bone Res.* **6**, (2018).
49. Feng, J. Q. *et al.* Loss of DMP1 causes rickets and osteomalacia and identifies a role for osteocytes in mineral metabolism. *Nat. Genet.* **38**, 1310–1315 (2006).
50. Liu, S. *et al.* Pathogenic role of Fgf23 in Hyp mice. *Am. J. Physiol. Endocrinol. Metab.* **291**, E38-49 (2006).
51. Jonsson, K. B. *et al.* Fibroblast growth factor 23 in oncogenic osteomalacia and X-linked hypophosphatemia. *N. Engl. J. Med.* **348**, 1656–1663 (2003).
52. Yamazaki, Y. *et al.* Increased Circulatory Level of Biologically Active Full-Length FGF-23 in Patients with Hypophosphatemic Rickets/Osteomalacia. *J. Clin. Endocrinol. Metab.* **87**, 4957–4960 (2002).
53. Segawa, H. *et al.* Effect of hydrolysis-resistant FGF23-R179Q on dietary phosphate regulation of the renal type-II Na/Pi transporter. *Pflüg. Arch.* **446**, 585–592 (2003).
54. Shimada, T. *et al.* Cloning and characterization of FGF23 as a causative factor of tumor-induced osteomalacia. *Proc. Natl. Acad. Sci. U. S. A.* **98**, 6500–6505 (2001).
55. Shimada, T. *et al.* FGF-23 Is a Potent Regulator of Vitamin D Metabolism and Phosphate Homeostasis. *J. Bone Miner. Res.* **19**, 429–435 (2004).

56. Shimada, T. *et al.* Vitamin D receptor-independent FGF23 actions in regulating phosphate and vitamin D metabolism. *Am. J. Physiol. Renal Physiol.* **289**, F1088-1095 (2005).
57. Au, W. Y. Inhibition by 1,25 dihydroxycholecalciferol of hormonal secretion of rat parathyroid gland in organ culture. *Calcif. Tissue Int.* **36**, 384–391 (1984).
58. Andrukhova, O. *et al.* FGF23 promotes renal calcium reabsorption through the TRPV5 channel. *EMBO J.* **33**, 229–246 (2014).
59. Andrukhova, O. *et al.* FGF23 regulates renal sodium handling and blood pressure. *EMBO Mol. Med.* **6**, 744–759 (2014).
60. Hauschka, P. V., Lian, J. B., Cole, D. E. & Gundberg, C. M. Osteocalcin and matrix Gla protein: vitamin K-dependent proteins in bone. *Physiol. Rev.* **69**, 990–1047 (1989).
61. Lee, N. K. *et al.* Endocrine regulation of energy metabolism by the skeleton. *Cell* **130**, 456–469 (2007).
62. Ferron, M. *et al.* Insulin signaling in osteoblasts integrates bone remodeling and energy metabolism. *Cell* **142**, 296–308 (2010).
63. Lacombe, J., Karsenty, G. & Ferron, M. In vivo analysis of the contribution of bone resorption to the control of glucose metabolism in mice. *Mol. Metab.* **2**, 498–504 (2013).
64. Oury, F. *et al.* Endocrine regulation of male fertility by the skeleton. *Cell* **144**, 796–809 (2011).
65. Oury, F. *et al.* Maternal and offspring pools of osteocalcin influence brain development and functions. *Cell* **155**, (2013).
66. Friedenstein, A. J., Chailakhjan, R. K. & Lalykina, K. S. The development of fibroblast colonies in monolayer cultures of guinea-pig bone marrow and spleen cells. *Cell Tissue Kinet.* **3**, 393–403 (1970).
67. Friedenstein, A. J., Gorskaja, J. F. & Kulagina, N. N. Fibroblast precursors in normal and irradiated mouse hematopoietic organs. *Exp. Hematol.* **4**, 267–274 (1976).
68. Grigoriadis, A. E., Heersche, J. N. & Aubin, J. E. Differentiation of muscle, fat, cartilage, and bone from progenitor cells present in a bone-derived clonal cell population: effect of dexamethasone. *J. Cell Biol.* **106**, 2139–2151 (1988).
69. Pittenger, M. F. *et al.* Multilineage potential of adult human mesenchymal stem cells. *Science* **284**, 143–147 (1999).
70. Guo, Z. *et al.* In vitro characteristics and in vivo immunosuppressive activity of compact bone-derived murine mesenchymal progenitor cells. *Stem Cells Dayt. Ohio* **24**, 992–1000 (2006).
71. Bari, C. D., Dell’Accio, F. & Luyten, F. P. Human periosteum-derived cells maintain phenotypic stability and chondrogenic potential throughout expansion regardless of donor age. *Arthritis Rheum.* **44**, 85–95 (2001).
72. Bari, C. D. *et al.* Mesenchymal multipotency of adult human periosteal cells demonstrated by single-cell lineage analysis. *Arthritis Rheum.* **54**, 1209–1221 (2006).
73. Nakahara, H. *et al.* In vitro differentiation of bone and hypertrophic cartilage from periosteal-derived cells. *Exp. Cell Res.* **195**, 492–503 (1991).
74. Zuk, P. A. *et al.* Human Adipose Tissue Is a Source of Multipotent Stem Cells. *Mol. Biol. Cell* **13**, 4279–4295 (2002).
75. Kuznetsov, S. A. *et al.* Single-colony derived strains of human marrow stromal fibroblasts form bone after transplantation in vivo. *J. Bone Miner. Res. Off. J. Am. Soc. Bone Miner. Res.* **12**, 1335–1347 (1997).

76. Gronthos, S. *et al.* Differential cell surface expression of the STRO-1 and alkaline phosphatase antigens on discrete developmental stages in primary cultures of human bone cells. *J. Bone Miner. Res. Off. J. Am. Soc. Bone Miner. Res.* **14**, 47–56 (1999).
77. Rider, D. A., Nalathamby, T., Nurcombe, V. & Cool, S. M. Selection using the alpha-1 integrin (CD49a) enhances the multipotentiality of the mesenchymal stem cell population from heterogeneous bone marrow stromal cells. *J. Mol. Histol.* **38**, 449–458 (2007).
78. Zhang, S., Chan, M. & Aubin, J. E. Pleiotropic effects of the steroid hormone 1,25-dihydroxyvitamin D3 on the recruitment of mesenchymal lineage progenitors in fetal rat calvaria cell populations. *J. Mol. Endocrinol.* **36**, 425–433 (2006).
79. Gimble, J. M., Zvonic, S., Floyd, Z. E., Kassem, M. & Nuttall, M. E. Playing with bone and fat. *J. Cell. Biochem.* **98**, 251–266 (2006).
80. Karystinou, A. *et al.* Distinct mesenchymal progenitor cell subsets in the adult human synovium. *Rheumatol. Oxf. Engl.* **48**, 1057–1064 (2009).
81. Meury, T., Verrier, S. & Alini, M. Human endothelial cells inhibit BMSC differentiation into mature osteoblasts in vitro by interfering with osterix expression. *J. Cell. Biochem.* **98**, 992–1006 (2006).
82. Park, Y.-E., Musson, D. S., Naot, D. & Cornish, J. Cell–cell communication in bone development and whole-body homeostasis and pharmacological avenues for bone disorders. *Curr. Opin. Pharmacol.* **34**, 21–35 (2017).
83. Villars, F. *et al.* Effect of HUVEC on human osteoprogenitor cell differentiation needs heterotypic gap junction communication. *Am. J. Physiol. Cell Physiol.* **282**, C775–785 (2002).
84. Wang, Y.-K. & Chen, C. S. Cell adhesion and mechanical stimulation in the regulation of mesenchymal stem cell differentiation. *J. Cell. Mol. Med.* **17**, 823–832 (2013).
85. Falconi, D. & Aubin, J. E. LIF inhibits osteoblast differentiation at least in part by regulation of HAS2 and its product hyaluronan. *J. Bone Miner. Res. Off. J. Am. Soc. Bone Miner. Res.* **22**, 1289–1300 (2007).
86. Aubin, J. E. Chapter 4 - Mesenchymal Stem Cells and Osteoblast Differentiation. in *Principles of Bone Biology (Third Edition)* (eds. Bilezikian, J. P., Raisz, L. G. & Martin, T. J.) 85–107 (Academic Press, 2008). doi:10.1016/B978-0-12-373884-4.00026-4.
87. Komori, T. *et al.* Targeted Disruption of Cbfa1 Results in a Complete Lack of Bone Formation owing to Maturational Arrest of Osteoblasts. *Cell* **89**, 755–764 (1997).
88. Fakhry, M., Hamade, E., Badran, B., Buchet, R. & Magne, D. Molecular mechanisms of mesenchymal stem cell differentiation towards osteoblasts. *World J. Stem Cells* **5**, 136–148 (2013).
89. Geoffroy, V., Kneissel, M., Fournier, B., Boyde, A. & Matthias, P. High Bone Resorption in Adult Aging Transgenic Mice Overexpressing Cbfa1/Runx2 in Cells of the Osteoblastic Lineage. *Mol. Cell. Biol.* **22**, 6222–6233 (2002).
90. Kanatani, N. *et al.* Cbf beta regulates Runx2 function isoform-dependently in postnatal bone development. *Dev. Biol.* **296**, 48–61 (2006).
91. Liu, W. *et al.* Overexpression of Cbfa1 in osteoblasts inhibits osteoblast maturation and causes osteopenia with multiple fractures. *J. Cell Biol.* **155**, 157–166 (2001).
92. Maruyama, Z. *et al.* Runx2 determines bone maturity and turnover rate in postnatal bone development and is involved in bone loss in estrogen deficiency. *Dev. Dyn. Off. Publ. Am. Assoc. Anat.* **236**, 1876–1890 (2007).
93. Liu, F., Malaval, L. & Aubin, J. E. Global amplification polymerase chain reaction reveals novel transitional stages during osteoprogenitor differentiation. *J. Cell Sci.* **116**, 1787–1796 (2003).

94. Malaval, L., Modrowski, D., Gupta, A. K. & Aubin, J. E. Cellular expression of bone-related proteins during in vitro osteogenesis in rat bone marrow stromal cell cultures. *J. Cell. Physiol.* **158**, 555–572 (1994).
95. Malaval, L., Liu, F., Roche, P. & Aubin, J. E. Kinetics of osteoprogenitor proliferation and osteoblast differentiation in vitro. *J. Cell. Biochem.* **74**, 616–627 (1999).
96. Strecker, S., Fu, Y., Liu, Y. & Maye, P. Generation and Characterization of Osterix-Cherry Reporter Mice. *Genes. N. Y. N 2000* **51**, 246–258 (2013).
97. Zhu, F., Friedman, M. S., Luo, W., Woolf, P. & Hankenson, K. D. The transcription factor osterix (SP7) regulates BMP6-induced human osteoblast differentiation. *J. Cell. Physiol.* **227**, 2677–2685 (2012).
98. Rucci, N. & Teti, A. Bone Cells: Osteoblast/Osteoclast/Osteocyte. in *Encyclopedia of Endocrine Diseases (Second Edition)* (eds. Huhtaniemi, I. & Martini, L.) 1–9 (Academic Press, 2019). doi:10.1016/B978-0-12-801238-3.64347-7.
99. Jilka, R. L., Weinstein, R. S., Bellido, T., Parfitt, A. M. & Manolagas, S. C. Osteoblast programmed cell death (apoptosis): modulation by growth factors and cytokines. *J. Bone Miner. Res. Off. J. Am. Soc. Bone Miner. Res.* **13**, 793–802 (1998).
100. Manolagas, S. C. Birth and death of bone cells: basic regulatory mechanisms and implications for the pathogenesis and treatment of osteoporosis. *Endocr. Rev.* **21**, 115–137 (2000).
101. Cong, F., Schweizer, L. & Varmus, H. Wnt signals across the plasma membrane to activate the beta-catenin pathway by forming oligomers containing its receptors, Frizzled and LRP. *Dev. Camb. Engl.* **131**, 5103–5115 (2004).
102. Takada, I., Kouzmenko, A. P. & Kato, S. Wnt and PPARgamma signaling in osteoblastogenesis and adipogenesis. *Nat. Rev. Rheumatol.* **5**, 442–447 (2009).
103. Kim, J.-B. *et al.* Bone regeneration is regulated by wnt signaling. *J. Bone Miner. Res. Off. J. Am. Soc. Bone Miner. Res.* **22**, 1913–1923 (2007).
104. van Bezooijen, R. L. *et al.* Sclerostin Is an Osteocyte-expressed Negative Regulator of Bone Formation, But Not a Classical BMP Antagonist. *J. Exp. Med.* **199**, 805–814 (2004).
105. Ahn, V. E. *et al.* Structural basis of Wnt signaling inhibition by Dickkopf binding to LRP5/6. *Dev. Cell* **21**, 862–873 (2011).
106. Li, X. *et al.* Sclerostin binds to LRP5/6 and antagonizes canonical Wnt signaling. *J. Biol. Chem.* **280**, 19883–19887 (2005).
107. Almeida, M., Han, L., Bellido, T., Manolagas, S. C. & Kousteni, S. Wnt proteins prevent apoptosis of both uncommitted osteoblast progenitors and differentiated osteoblasts by beta-catenin-dependent and -independent signaling cascades involving Src/ERK and phosphatidylinositol 3-kinase/AKT. *J. Biol. Chem.* **280**, 41342–41351 (2005).
108. Honasoge, M., Rao, A. D. & Rao, S. D. Sclerostin: recent advances and clinical implications. *Curr. Opin. Endocrinol. Diabetes Obes.* **21**, 437–446 (2014).
109. Guo, X. & Wang, X.-F. Signaling cross-talk between TGF- β /BMP and other pathways. *Cell Res.* **19**, 71–88 (2009).
110. Chen, G., Deng, C. & Li, Y.-P. TGF- β and BMP Signaling in Osteoblast Differentiation and Bone Formation. *Int. J. Biol. Sci.* **8**, 272–288 (2012).
111. Bandyopadhyay, A. *et al.* Genetic Analysis of the Roles of BMP2, BMP4, and BMP7 in Limb Patterning and Skeletogenesis. *PLoS Genet.* **2**, (2006).

112. Shen, B. *et al.* The role of BMP-7 in chondrogenic and osteogenic differentiation of human bone marrow multipotent mesenchymal stromal cells in vitro. *J. Cell. Biochem.* **109**, 406–416 (2010).
113. Kamiya, N. *et al.* Wnt Inhibitors Dkk1 and Sost Are Downstream Targets of BMP Signaling Through the Type IA Receptor (BMPRIA) in Osteoblasts. *J. Bone Miner. Res.* **25**, 200–210 (2010).
114. Tang, N. *et al.* BMP-9-induced osteogenic differentiation of mesenchymal progenitors requires functional canonical Wnt/ β -catenin signalling. *J. Cell. Mol. Med.* **13**, 2448–2464 (2009).
115. Franz-Odenaal, T. A., Hall, B. K. & Witten, P. E. Buried alive: how osteoblasts become osteocytes. *Dev. Dyn. Off. Publ. Am. Assoc. Anat.* **235**, 176–190 (2006).
116. Chen, H., Senda, T. & Kubo, K. The osteocyte plays multiple roles in bone remodeling and mineral homeostasis. *Med. Mol. Morphol.* **48**, 61–68 (2015).
117. Holtrop, M. E. The ultrastructure of bone. *Ann. Clin. Lab. Sci.* **5**, 264–271 (1975).
118. Weinger, J. M. & Holtrop, M. E. An ultrastructural study of bone cells: the occurrence of microtubules, microfilaments and tight junctions. *Calcif. Tissue Res.* **14**, 15–29 (1974).
119. Krempien, B., Manegold, C., Ritz, E. & Bommer, J. The influence of immobilization on osteocyte morphology: osteocyte differential count and electron microscopical studies. *Virchows Arch. A Pathol. Anat. Histol.* **370**, 55–68 (1976).
120. Steinberg, B., Singh, I. J. & Mitchell, O. G. The effects of cold-stress. Hibernation, and prolonged inactivity on bone dynamics in the golden hamster, *Mesocricetus auratus*. *J. Morphol.* **167**, 43–51 (1981).
121. Tazawa, K. *et al.* Osteocytic osteolysis observed in rats to which parathyroid hormone was continuously administered. *J. Bone Miner. Metab.* **22**, 524–529 (2004).
122. Palumbo, C., Palazzini, S., Zaffe, D. & Marotti, G. Osteocyte differentiation in the tibia of newborn rabbit: an ultrastructural study of the formation of cytoplasmic processes. *Acta Anat. (Basel)* **137**, 350–358 (1990).
123. Mullen, C. A., Haugh, M. G., Schaffler, M. B., Majeska, R. J. & McNamara, L. M. Osteocyte differentiation is regulated by extracellular matrix stiffness and intercellular separation. *J. Mech. Behav. Biomed. Mater.* **28**, 183–194 (2013).
124. Weinreb, M., Shinar, D. & Rodan, G. A. Different pattern of alkaline phosphatase, osteopontin, and osteocalcin expression in developing rat bone visualized by in situ hybridization. *J. Bone Miner. Res. Off. J. Am. Soc. Bone Miner. Res.* **5**, 831–842 (1990).
125. Candelieri, G. A., Liu, F. & Aubin, J. E. Individual osteoblasts in the developing calvaria express different gene repertoires. *Bone* **28**, 351–361 (2001).
126. Zhang, K. *et al.* E11/gp38 Selective Expression in Osteocytes: Regulation by Mechanical Strain and Role in Dendrite Elongation. *Mol. Cell. Biol.* **26**, 4539–4552 (2006).
127. Westbroek, I., De Rooij, K. E. & Nijweide, P. J. Osteocyte-specific monoclonal antibody MAb OB7.3 is directed against Phex protein. *J. Bone Miner. Res. Off. J. Am. Soc. Bone Miner. Res.* **17**, 845–853 (2002).
128. Poole, K. E. S. *et al.* Sclerostin is a delayed secreted product of osteocytes that inhibits bone formation. *FASEB J. Off. Publ. Fed. Am. Soc. Exp. Biol.* **19**, 1842–1844 (2005).
129. Feng, J. Q. *et al.* The Dentin matrix protein 1 (Dmp1) is specifically expressed in mineralized, but not soft, tissues during development. *J. Dent. Res.* **82**, 776–780 (2003).
130. Rios, H. F. *et al.* DMP1 is essential for osteocyte formation and function. *J. Musculoskelet. Neuronal Interact.* **5**, 325–327 (2005).

131. Shapiro, F. Variable conformation of GAP junctions linking bone cells: a transmission electron microscopic study of linear, stacked linear, curvilinear, oval, and annular junctions. *Calcif. Tissue Int.* **61**, 285–293 (1997).
132. Burger, E. H., Klein-Nulend, J. & Smit, T. H. Strain-derived canalicular fluid flow regulates osteoclast activity in a remodelling osteon—a proposal. *J. Biomech.* **36**, 1453–1459 (2003).
133. Knothe Tate, M. L., Adamson, J. R., Tami, A. E. & Bauer, T. W. The osteocyte. *Int. J. Biochem. Cell Biol.* **36**, 1–8 (2004).
134. Simonet, W. S. *et al.* Osteoprotegerin: a novel secreted protein involved in the regulation of bone density. *Cell* **89**, 309–319 (1997).
135. Cardoso, L. *et al.* Osteocyte Apoptosis Controls Activation of Intracortical Resorption in Response to Bone Fatigue. *J. Bone Miner. Res.* **24**, 597–605 (2009).
136. Emerton, K. *et al.* Osteocyte apoptosis and control of bone resorption following ovariectomy in mice. *Bone* **46**, 577–583 (2010).
137. Komori, T. Cell Death in Chondrocytes, Osteoblasts, and Osteocytes. *Int. J. Mol. Sci.* **17**, (2016).
138. Verborgt, O., Gibson, G. J. & Schaffler, M. B. Loss of osteocyte integrity in association with microdamage and bone remodeling after fatigue in vivo. *J. Bone Miner. Res. Off. J. Am. Soc. Bone Miner. Res.* **15**, 60–67 (2000).
139. Tatsumi, S. *et al.* Targeted ablation of osteocytes induces osteoporosis with defective mechanotransduction. *Cell Metab.* **5**, 464–475 (2007).
140. Tondravi, M. M. *et al.* Osteopetrosis in mice lacking haematopoietic transcription factor PU.1. *Nature* **386**, 81–84 (1997).
141. DeKoter, R. P., Walsh, J. C. & Singh, H. PU.1 regulates both cytokine-dependent proliferation and differentiation of granulocyte/macrophage progenitors. *EMBO J.* **17**, 4456–4468 (1998).
142. Harris, S. E. *et al.* Meox2Cre-mediated Disruption of CSF-1 Leads to Osteopetrosis and Osteocyte Defects. *Bone* **50**, 42–53 (2012).
143. Nakashima, T. *et al.* Evidence for osteocyte regulation of bone homeostasis through RANKL expression. *Nat. Med.* **17**, 1231–1234 (2011).
144. Xiong, J. *et al.* Osteocytes, not Osteoblasts or Lining Cells, are the Main Source of the RANKL Required for Osteoclast Formation in Remodeling Bone. *PLoS ONE* **10**, (2015).
145. Biskobing, D. M., Fan, X. & Rubin, J. Characterization of MCSF-induced proliferation and subsequent osteoclast formation in murine marrow culture. *J. Bone Miner. Res. Off. J. Am. Soc. Bone Miner. Res.* **10**, 1025–1032 (1995).
146. Chen, W., Zhu, G., Tang, J., Zhou, H.-D. & Li, Y.-P. C/ebp α controls osteoclast terminal differentiation, activation, function, and postnatal bone homeostasis through direct regulation of Nfatc1. *J. Pathol.* **244**, 271–282 (2018).
147. Jules, J., Chen, W. & Li, Y.-P. C/EBP α and PU.1 Exhibit Different Responses to RANK Signaling for Osteoclastogenesis. *Bone* **107**, 104–114 (2018).
148. Baud'huin, M. *et al.* Interleukin-34 is expressed by giant cell tumours of bone and plays a key role in RANKL-induced osteoclastogenesis. *J. Pathol.* **221**, 77–86 (2010).
149. Chen, Z., Buki, K., Vääräniemi, J., Gu, G. & Väänänen, H. K. The Critical Role of IL-34 in Osteoclastogenesis. *PLoS ONE* **6**, (2011).
150. Adamopoulos, I. E., Xia, Z., Lau, Y. S. & Athanasou, N. A. Hepatocyte growth factor can substitute for M-CSF to support osteoclastogenesis. *Biochem. Biophys. Res. Commun.* **350**, 478–483 (2006).

151. Lean, J. M., Fuller, K. & Chambers, T. J. FLT3 ligand can substitute for macrophage colony-stimulating factor in support of osteoclast differentiation and function. *Blood* **98**, 2707–2713 (2001).
152. Taylor, R. M., Kashima, T. G., Knowles, H. J. & Athanasou, N. A. VEGF, FLT3 ligand, PlGF and HGF can substitute for M-CSF to induce human osteoclast formation: implications for giant cell tumour pathobiology. *Lab. Investig. J. Tech. Methods Pathol.* **92**, 1398–1406 (2012).
153. Hwang, S.-J. *et al.* Interleukin-34 produced by human fibroblast-like synovial cells in rheumatoid arthritis supports osteoclastogenesis. *Arthritis Res. Ther.* **14**, R14 (2012).
154. Feng, X. & Teitelbaum, S. L. Osteoclasts: New Insights. *Bone Res.* **1**, 11–26 (2013).
155. Suda, T. *et al.* Modulation of osteoclast differentiation and function by the new members of the tumor necrosis factor receptor and ligand families. *Endocr. Rev.* **20**, 345–357 (1999).
156. Kramer, I. *et al.* Osteocyte Wnt/ β -Catenin Signaling Is Required for Normal Bone Homeostasis. *Mol. Cell. Biol.* **30**, 3071–3085 (2010).
157. Grigoriadis, A. E. *et al.* c-Fos: a key regulator of osteoclast-macrophage lineage determination and bone remodeling. *Science* **266**, 443–448 (1994).
158. Ikeda, T., Utsuyama, M. & Hirokawa, K. Expression profiles of receptor activator of nuclear factor kappaB ligand, receptor activator of nuclear factor kappaB, and osteoprotegerin messenger RNA in aged and ovariectomized rat bones. *J. Bone Miner. Res. Off. J. Am. Soc. Bone Miner. Res.* **16**, 1416–1425 (2001).
159. Takayanagi, H. *et al.* Induction and Activation of the Transcription Factor NFATc1 (NFAT2) Integrate RANKL Signaling in Terminal Differentiation of Osteoclasts. *Dev. Cell* **3**, 889–901 (2002).
160. Koga, T. *et al.* Costimulatory signals mediated by the ITAM motif cooperate with RANKL for bone homeostasis. *Nature* **428**, 758–763 (2004).
161. Kim, K., Lee, S.-H., Ha Kim, J., Choi, Y. & Kim, N. NFATc1 Induces Osteoclast Fusion Via Up-Regulation of Atp6v0d2 and the Dendritic Cell-Specific Transmembrane Protein (DC-STAMP). *Mol. Endocrinol.* **22**, 176–185 (2008).
162. Song, I. *et al.* Regulatory mechanism of NFATc1 in RANKL-induced osteoclast activation. *FEBS Lett.* **583**, 2435–2440 (2009).
163. Verma, S. K. *et al.* Cell-surface phosphatidylserine regulates osteoclast precursor fusion. *J. Biol. Chem.* **293**, 254–270 (2018).
164. Yagi, M. *et al.* DC-STAMP is essential for cell–cell fusion in osteoclasts and foreign body giant cells. *J. Exp. Med.* **202**, 345–351 (2005).
165. Miyamoto, H. *et al.* Osteoclast stimulatory transmembrane protein and dendritic cell–specific transmembrane protein cooperatively modulate cell–cell fusion to form osteoclasts and foreign body giant cells. *J. Bone Miner. Res. Off. J. Am. Soc. Bone Miner. Res.* **27**, 1289–1297 (2012).
166. Lee, S.-H. *et al.* v-ATPase V0 subunit d2-deficient mice exhibit impaired osteoclast fusion and increased bone formation. *Nat. Med.* **12**, 1403–1409 (2006).
167. McHugh, K. P. *et al.* Mice lacking beta3 integrins are osteosclerotic because of dysfunctional osteoclasts. *J. Clin. Invest.* **105**, 433–440 (2000).
168. Teitelbaum, S. L. Osteoclasts and integrins. *Ann. N. Y. Acad. Sci.* **1068**, 95–99 (2006).
169. Horne, W. C. *et al.* Osteoclasts express high levels of pp60c-src in association with intracellular membranes. *J. Cell Biol.* **119**, 1003–1013 (1992).
170. Soriano, P., Montgomery, C., Geske, R. & Bradley, A. Targeted disruption of the c-src proto-oncogene leads to osteopetrosis in mice. *Cell* **64**, 693–702 (1991).

171. Sanjay, A. *et al.* Cbl Associates with Pyk2 and Src to Regulate Src Kinase Activity, $\alpha\beta 3$ Integrin-Mediated Signaling, Cell Adhesion, and Osteoclast Motility. *J. Cell Biol.* **152**, 181–196 (2001).
172. Holtrop, M. E. & King, G. J. The Ultrastructure of the Osteoclast and its Functional Implications. *Clin. Orthop. Relat. Res.* **123**, 177 (1977).
173. Salo, J., Lehenkari, P., Mulari, M., Metsikkö, K. & Väänänen, H. K. Removal of osteoclast bone resorption products by transcytosis. *Science* **276**, 270–273 (1997).
174. Lakkakorpi, P., Tuukkanen, J., Hentunen, T., Järvelin, K. & Väänänen, K. Organization of osteoclast microfilaments during the attachment to bone surface in vitro. *J. Bone Miner. Res. Off. J. Am. Soc. Bone Miner. Res.* **4**, 817–825 (1989).
175. Zou, W. *et al.* Syk, c-Src, the $\alpha\beta 3$ integrin, and ITAM immunoreceptors, in concert, regulate osteoclastic bone resorption. *J. Cell Biol.* **176**, 877–888 (2007).
176. Alford, A. I., Kozloff, K. M. & Hankenson, K. D. Extracellular matrix networks in bone remodeling. *Int. J. Biochem. Cell Biol.* **65**, 20–31 (2015).
177. Blair, H. C., Teitelbaum, S. L., Ghiselli, R. & Gluck, S. Osteoclastic bone resorption by a polarized vacuolar proton pump. *Science* **245**, 855–857 (1989).
178. Sundquist, K., Lakkakorpi, P., Wallmark, B. & Väänänen, K. Inhibition of osteoclast proton transport by bafilomycin A1 abolishes bone resorption. *Biochem. Biophys. Res. Commun.* **168**, 309–313 (1990).
179. Väänänen, H. K. *et al.* Evidence for the presence of a proton pump of the vacuolar H(+)-ATPase type in the ruffled borders of osteoclasts. *J. Cell Biol.* **111**, 1305–1311 (1990).
180. Kornak, U. *et al.* Loss of the ClC-7 chloride channel leads to osteopetrosis in mice and man. *Cell* **104**, 205–215 (2001).
181. Gay, C. V. & Mueller, W. J. Carbonic Anhydrase and Osteoclasts: Localization by Labeled Inhibitor Autoradiography. *Science* **183**, 432–434 (1974).
182. Laitala, T. & Väänänen, H. K. Inhibition of bone resorption in vitro by antisense RNA and DNA molecules targeted against carbonic anhydrase II or two subunits of vacuolar H(+)-ATPase. *J. Clin. Invest.* **93**, 2311–2318 (1994).
183. Lindsey, A. E. *et al.* Functional expression and subcellular localization of an anion exchanger cloned from choroid plexus. *Proc. Natl. Acad. Sci. U. S. A.* **87**, 5278–5282 (1990).
184. Teti, A. *et al.* Cytoplasmic pH regulation and chloride/bicarbonate exchange in avian osteoclasts. *J. Clin. Invest.* **83**, 227–233 (1989).
185. Wu, J., Glimcher, L. H. & Aliprantis, A. O. HCO₃⁻/Cl⁻ anion exchanger SLC4A2 is required for proper osteoclast differentiation and function. *Proc. Natl. Acad. Sci.* **105**, 16934–16939 (2008).
186. Parikka, V. *et al.* Estrogen Reduces the Depth of Resorption Pits by Disturbing the Organic Bone Matrix Degradation Activity of Mature Osteoclasts. *Endocrinology* **142**, 5371–5378 (2001).
187. Drake, F. H. *et al.* Cathepsin K, but not cathepsins B, L, or S, is abundantly expressed in human osteoclasts. *J. Biol. Chem.* **271**, 12511–12516 (1996).
188. Inui, T. *et al.* Cathepsin K antisense oligodeoxynucleotide inhibits osteoclastic bone resorption. *J. Biol. Chem.* **272**, 8109–8112 (1997).
189. Xia, L. *et al.* Localization of rat cathepsin K in osteoclasts and resorption pits: inhibition of bone resorption and cathepsin K-activity by peptidyl vinyl sulfones. *Biol. Chem.* **380**, 679–687 (1999).
190. Brömme, D., Okamoto, K., Wang, B. B. & Biroc, S. Human Cathepsin O2, a Matrix Protein-degrading Cysteine Protease Expressed in Osteoclasts: functional expression of human cathepsin

- O₂ in *spodoptera frugiperda* and characterization of the enzyme. *J. Biol. Chem.* **271**, 2126–2132 (1996).
191. Garnero, P. *et al.* The collagenolytic activity of cathepsin K is unique among mammalian proteinases. *J. Biol. Chem.* **273**, 32347–32352 (1998).
 192. Kafienah, W., Brömme, D., Buttle, D. J., Croucher, L. J. & Hollander, A. P. Human cathepsin K cleaves native type I and II collagens at the N-terminal end of the triple helix. *Biochem. J.* **331**, 727–732 (1998).
 193. Nesbitt, S. A. & Horton, M. A. Trafficking of matrix collagens through bone-resorbing osteoclasts. *Science* **276**, 266–269 (1997).
 194. Halleen, J. M., Räsänen, S. R., Alatalo, S. L. & Väänänen, H. K. Potential function for the ROS-generating activity of TRACP. *J. Bone Miner. Res. Off. J. Am. Soc. Bone Miner. Res.* **18**, 1908–1911 (2003).
 195. Hughes, D. E. & Boyce, B. F. Apoptosis in bone physiology and disease. *Mol. Pathol.* **50**, 132–137 (1997).
 196. Bentolila, V. *et al.* Intracortical remodeling in adult rat long bones after fatigue loading. *Bone* **23**, 275–281 (1998).
 197. Mori, S. & Burr, D. B. Increased intracortical remodeling following fatigue damage. *Bone* **14**, 103–109 (1993).
 198. Hattner, R., Epker, B. N. & Frost, H. M. Suggested sequential mode of control of changes in cell behaviour in adult bone remodelling. *Nature* **206**, 489–490 (1965).
 199. Parfitt, A. M. Osteonal and hemi-osteonal remodeling: The spatial and temporal framework for signal traffic in adult human bone. *J. Cell. Biochem.* **55**, 273–286 (1994).
 200. Agerbaek, M. O., Eriksen, E. F., Kragstrup, J., Mosekilde, L. & Melsen, F. A reconstruction of the remodelling cycle in normal human cortical iliac bone. *Bone Miner.* **12**, 101–112 (1991).
 201. Weinstein, R. S., Jilka, R. L., Parfitt, A. M. & Manolagas, S. C. Inhibition of osteoblastogenesis and promotion of apoptosis of osteoblasts and osteocytes by glucocorticoids. Potential mechanisms of their deleterious effects on bone. *J. Clin. Invest.* **102**, 274–282 (1998).
 202. Kotani, M. *et al.* Systemic circulation and bone recruitment of osteoclast precursors tracked by using fluorescent imaging techniques. *J. Immunol. Baltim. Md 1950* **190**, 605–612 (2013).
 203. Muto, A. *et al.* Lineage-committed osteoclast precursors circulate in blood and settle down into bone. *J. Bone Miner. Res. Off. J. Am. Soc. Bone Miner. Res.* **26**, 2978–2990 (2011).
 204. Ferrier, J., Xia, S. L., Lagan, E., Aubin, J. E. & Heersche, J. N. Displacement and translocation of osteoblast-like cells by osteoclasts. *J. Bone Miner. Res. Off. J. Am. Soc. Bone Miner. Res.* **9**, 1397–1405 (1994).
 205. Perez-Amodio, S., Beertsen, W. & Everts, V. (Pre-)osteoclasts induce retraction of osteoblasts before their fusion to osteoclasts. *J. Bone Miner. Res. Off. J. Am. Soc. Bone Miner. Res.* **19**, 1722–1731 (2004).
 206. Hauge, E. M., Qvesel, D., Eriksen, E. F., Mosekilde, L. & Melsen, F. Cancellous Bone Remodeling Occurs in Specialized Compartments Lined by Cells Expressing Osteoblastic Markers. *J. Bone Miner. Res.* **16**, 1575–1582 (2001).
 207. Allen, M. R. & Burr, D. B. Chapter 5 - Bone Growth, Modeling, and Remodeling. in *Basic and Applied Bone Biology (Second Edition)* (eds. Burr, D. B. & Allen, M. R.) 85–100 (Academic Press, 2019). doi:10.1016/B978-0-12-813259-3.00005-1.

208. Everts, V. *et al.* The bone lining cell: its role in cleaning Howship's lacunae and initiating bone formation. *J. Bone Miner. Res. Off. J. Am. Soc. Bone Miner. Res.* **17**, 77–90 (2002).
209. McKee, M. D. & Nanci, A. Osteopontin at mineralized tissue interfaces in bone, teeth, and osseointegrated implants: ultrastructural distribution and implications for mineralized tissue formation, turnover, and repair. *Microsc. Res. Tech.* **33**, 141–164 (1996).
210. Zhou, H., Chernecky, R. & Davies, J. E. Deposition of cement at reversal lines in rat femoral bone. *J. Bone Miner. Res. Off. J. Am. Soc. Bone Miner. Res.* **9**, 367–374 (1994).
211. Kim, B.-J. & Koh, J.-M. Coupling factors involved in preserving bone balance. *Cell. Mol. Life Sci. CMLS* **76**, 1243–1253 (2019).
212. Howard, G. A., Bottemiller, B. L., Turner, R. T., Rader, J. I. & Baylink, D. J. Parathyroid hormone stimulates bone formation and resorption in organ culture: evidence for a coupling mechanism. *Proc. Natl. Acad. Sci. U. S. A.* **78**, 3204–3208 (1981).
213. Mayr-Wohlfart, U. *et al.* Vascular endothelial growth factor stimulates chemotactic migration of primary human osteoblasts. *Bone* **30**, 472–477 (2002).
214. Tang, Y. *et al.* TGF- β 1-induced Migration of Bone Mesenchymal Stem Cells Couples Bone Resorption and Formation. *Nat. Med.* **15**, 757–765 (2009).
215. Bonucci, E. Bone mineralization. *Front. Biosci. Landmark Ed.* **17**, 100–128 (2012).
216. Boskey, A. L. Bone composition: relationship to bone fragility and antiosteoporotic drug effects. *BoneKEy Rep.* **2**, (2013).
217. Kenkre, J. S. & Bassett, J. The bone remodelling cycle. *Ann. Clin. Biochem.* **55**, 308–327 (2018).
218. Fleisch, H. & Bisaz, S. Mechanism of calcification: inhibitory role of pyrophosphate. *Nature* **195**, 911 (1962).
219. Omelon, S. *et al.* Control of Vertebrate Skeletal Mineralization by Polyphosphates. *PLOS ONE* **4**, e5634 (2009).
220. Bailey, S., Karsenty, G., Gundberg, C. & Vashishth, D. Osteocalcin and osteopontin influence bone morphology and mechanical properties. *Ann. N. Y. Acad. Sci.* **1409**, 79–84 (2017).
221. Gajjeraman, S., Narayanan, K., Hao, J., Qin, C. & George, A. Matrix Macromolecules in Hard Tissues Control the Nucleation and Hierarchical Assembly of Hydroxyapatite. *J. Biol. Chem.* **282**, 1193–1204 (2007).
222. George, A. & Veis, A. Phosphorylated Proteins and Control Over Apatite Nucleation, Crystal Growth and Inhibition. *Chem. Rev.* **108**, 4670–4693 (2008).
223. Gorski, J. P. Biomineralization of bone: a fresh view of the roles of non-collagenous proteins. *Front. Biosci. Landmark Ed.* **16**, 2598–2621 (2011).
224. Ishii, M. & Kikuta, J. Sphingosine-1-phosphate signaling controlling osteoclasts and bone homeostasis. *Biochim. Biophys. Acta* **1831**, 223–227 (2013).
225. Ishii, M., Kikuta, J., Shimazu, Y., Meier-Schellersheim, M. & Germain, R. N. Chemorepulsion by blood S1P regulates osteoclast precursor mobilization and bone remodeling in vivo. *J. Exp. Med.* **207**, 2793–2798 (2010).
226. Ishii, T., Shimazu, Y., Nishiyama, I., Kikuta, J. & Ishii, M. The Role of Sphingosine 1-Phosphate in Migration of Osteoclast Precursors; an Application of Intravital Two-Photon Microscopy. *Mol. Cells* **31**, 399–403 (2011).
227. Binder, N. B. *et al.* Estrogen-dependent and C-C chemokine receptor-2-dependent pathways determine osteoclast behavior in osteoporosis. *Nat. Med.* **15**, 417–424 (2009).

228. Yang, M. *et al.* Chemokine and chemokine receptor expression during colony stimulating factor-1–induced osteoclast differentiation in the toothless osteopetrotic rat: a key role for CCL9 (MIP-1 γ) in osteoclastogenesis in vivo and in vitro. *Blood* **107**, 2262–2270 (2006).
229. Onan, D. *et al.* The chemokine Cxcl1 is a novel target gene of parathyroid hormone (PTH)/PTH-related protein in committed osteoblasts. *Endocrinology* **150**, 2244–2253 (2009).
230. Gronthos, S. & Zannettino, A. C. W. The role of the chemokine CXCL12 in osteoclastogenesis. *Trends Endocrinol. Metab. TEM* **18**, 108–113 (2007).
231. Delaisse, J.-M. The reversal phase of the bone-remodeling cycle: cellular prerequisites for coupling resorption and formation. *BoneKEy Rep.* **3**, (2014).
232. Karsdal, M. A., Neutzsky-Wulff, A. V., Dziegiel, M. H., Christiansen, C. & Henriksen, K. Osteoclasts secrete non-bone derived signals that induce bone formation. *Biochem. Biophys. Res. Commun.* **366**, 483–488 (2008).
233. Duong, L. T. Therapeutic inhibition of cathepsin K—reducing bone resorption while maintaining bone formation. *BoneKEy Rep.* **1**, (2012).
234. Kidd, T., Bland, K. S. & Goodman, C. S. Slit is the midline repellent for the robo receptor in *Drosophila*. *Cell* **96**, 785–794 (1999).
235. Matsuoka, K. *et al.* WAIF1 Is a Cell-Surface CTHRC1 Binding Protein Coupling Bone Resorption and Formation. *J. Bone Miner. Res. Off. J. Am. Soc. Bone Miner. Res.* **33**, 1500–1512 (2018).
236. Takeshita, S. *et al.* Osteoclast-secreted CTHRC1 in the coupling of bone resorption to formation. *J. Clin. Invest.* **123**, 3914–3924 (2013).
237. Hirschberg, A. *et al.* Gene Deletion Mutants Reveal a Role for Semaphorin Receptors of the Plexin-B Family in Mechanisms Underlying Corticogenesis. *Mol. Cell. Biol.* **30**, 764–780 (2010).
238. Negishi-Koga, T. *et al.* Suppression of bone formation by osteoclastic expression of semaphorin 4D. *Nat. Med.* **17**, 1473–1480 (2011).
239. Negishi-Koga, T. & Takayanagi, H. Bone cell communication factors and Semaphorins. *BoneKEy Rep.* **1**, (2012).
240. Seeman, E. Age- and menopause-related bone loss compromise cortical and trabecular microstructure. *J. Gerontol. A. Biol. Sci. Med. Sci.* **68**, 1218–1225 (2013).
241. Cooper, D. M. L. *et al.* Age-dependent change in the 3D structure of cortical porosity at the human femoral midshaft. *Bone* **40**, 957–965 (2007).
242. Glatt, V., Canalis, E., Stadmeier, L. & Bouxsein, M. L. Age-Related Changes in Trabecular Architecture Differ in Female and Male C57BL/6J Mice. *J. Bone Miner. Res.* **22**, 1197–1207 (2007).
243. Halloran, B. P. *et al.* Changes in Bone Structure and Mass With Advancing Age in the Male C57BL/6J Mouse. *J. Bone Miner. Res.* **17**, 1044–1050 (2002).
244. Hemmatian, H. *et al.* Age-related changes in female mouse cortical bone microporosity. *Bone* **113**, 1–8 (2018).
245. Piemontese, M. *et al.* Old age causes de novo intracortical bone remodeling and porosity in mice. *JCI Insight* **2**, (2017).
246. Khosla, S. & Monroe, D. G. Regulation of Bone Metabolism by Sex Steroids. *Cold Spring Harb. Perspect. Med.* **8**, (2018).
247. Almeida, M. *et al.* Skeletal Involution by Age-associated Oxidative Stress and Its Acceleration by Loss of Sex Steroids. *J. Biol. Chem.* **282**, 27285–27297 (2007).

248. Tomkinson, A., Reeve, J., Shaw, R. W. & Noble, B. S. The death of osteocytes via apoptosis accompanies estrogen withdrawal in human bone. *J. Clin. Endocrinol. Metab.* **82**, 3128–3135 (1997).
249. Bellido, T. Osteocyte-Driven Bone Remodeling. *Calcif. Tissue Int.* **94**, 25–34 (2014).
250. Jilka, R. L., Weinstein, R. S., Takahashi, K., Parfitt, A. M. & Manolagas, S. C. Linkage of decreased bone mass with impaired osteoblastogenesis in a murine model of accelerated senescence. *J. Clin. Invest.* **97**, 1732–1740 (1996).
251. Stolzing, A., Jones, E., McGonagle, D. & Scutt, A. Age-related changes in human bone marrow-derived mesenchymal stem cells: consequences for cell therapies. *Mech. Ageing Dev.* **129**, 163–173 (2008).
252. Bethel, M., Chitteti, B. R., Srour, E. F. & Kacena, M. A. The changing balance between osteoblastogenesis and adipogenesis in aging and its impact on hematopoiesis. *Curr. Osteoporos. Rep.* **11**, 99–106 (2013).
253. Kim, M. *et al.* Age-related alterations in mesenchymal stem cells related to shift in differentiation from osteogenic to adipogenic potential: implication to age-associated bone diseases and defects. *Mech. Ageing Dev.* **133**, 215–225 (2012).
254. Paccou, J., Penel, G., Chauveau, C., Cortet, B. & Hardouin, P. Marrow adiposity and bone: Review of clinical implications. *Bone* **118**, 8–15 (2019).
255. Kassem, M. & Marie, P. J. Senescence-associated intrinsic mechanisms of osteoblast dysfunctions. *Aging Cell* **10**, 191–197 (2011).
256. Stenderup, K., Justesen, J., Clausen, C. & Kassem, M. Aging is associated with decreased maximal life span and accelerated senescence of bone marrow stromal cells. *Bone* **33**, 919–926 (2003).
257. Zhou, S. *et al.* Age-Related Intrinsic Changes in Human Bone Marrow-Derived Mesenchymal Stem Cells and Their Differentiation to Osteoblasts. *Aging Cell* **7**, 335–343 (2008).
258. Kanis, J. A. *et al.* Ten Year Probabilities of Osteoporotic Fractures According to BMD and Diagnostic Thresholds. *Osteoporos. Int.* **12**, 989–995 (2001).
259. Burr, D. B. Changes in bone matrix properties with aging. *Bone* **120**, 85–93 (2019).
260. Hui, S. L., Slemenda, C. W. & Johnston, C. C. Age and bone mass as predictors of fracture in a prospective study. *J. Clin. Invest.* **81**, 1804–1809 (1988).
261. Piez, K. A. History of extracellular matrix: A personal view. *Matrix Biol.* **16**, 85–92 (1997).
262. Lin, H., Yang, G., Tan, J. & Tuan, R. S. Influence of decellularized matrix derived from human mesenchymal stem cells on their proliferation, migration and multi-lineage differentiation potential. *Biomaterials* **33**, 4480–4489 (2012).
263. Patabhi, S. rao, Martinez, J. S. & Keller, T. C. S. Decellularized ECM Effects on Human Mesenchymal Stem Cell Stemness and Differentiation. *Differ. Res. Biol. Divers.* **88**, 131–143 (2014).
264. Rakian, R. *et al.* Native extracellular matrix preserves mesenchymal stem cell “stemness” and differentiation potential under serum-free culture conditions. *Stem Cell Res. Ther.* **6**, (2015).
265. Krivacic, K. A. & Levine, A. D. Extracellular Matrix Conditions T Cells for Adhesion to Tissue Interstitium. *J. Immunol.* **170**, 5034–5044 (2003).
266. Underwood, P. A., Bean, P. A. & Cubeddu, L. Human endothelial cells grow poorly on vitronectin: role of PAI-1. *J. Cell. Biochem.* **82**, 98–109 (2001).
267. Koshikawa, N., Giannelli, G., Cirulli, V., Miyazaki, K. & Quaranta, V. Role of Cell Surface Metalloprotease Mt1-Mmp in Epithelial Cell Migration over Laminin-5. *J. Cell Biol.* **148**, 615–624 (2000).

268. Powell, R. J., Carruth, J. A., Basson, M. D., Bloodgood, R. & Sumpio, B. E. Matrix-specific effect of endothelial control of smooth muscle cell migration. *J. Vasc. Surg.* **24**, 51–57 (1996).
269. Hutter, R. *et al.* The Novel Small Leucine-Rich Repeat Protein Podocan is a Negative Regulator of Migration and Proliferation of Smooth Muscle Cells, Modulates Neointima Formation and is Expressed in Human Atheroma. *Circulation* **128**, 2351–2363 (2013).
270. Yamaguchi, Y. & Ruoslahti, E. Expression of human proteoglycan in Chinese hamster ovary cells inhibits cell proliferation. *Nature* **336**, 244–246 (1988).
271. Bi, Y. *et al.* Extracellular Matrix Proteoglycans Control the Fate of Bone Marrow Stromal Cells. *J. Biol. Chem.* **280**, 30481–30489 (2005).
272. Dike, L. E. *et al.* Geometric control of switching between growth, apoptosis, and differentiation during angiogenesis using micropatterned substrates. *In Vitro Cell. Dev. Biol. Anim.* **35**, 441–448 (1999).
273. McLean, F. C. & Urist, M. R. *Bone: fundamentals of the physiology of skeletal tissue.* (The University of Chicago Press, 1968).
274. Cai, X. *et al.* Homogenization of cortical bone reveals that the organization and shape of pores marginally affect elasticity. *J. R. Soc. Interface* **16**, 20180911 (2019).
275. Granke, M. *et al.* Change in porosity is the major determinant of the variation of cortical bone elasticity at the millimeter scale in aged women. *Bone* **49**, 1020–1026 (2011).
276. Granke, M., Makowski, A. J., Uppuganti, S., Does, M. D. & Nyman, J. S. Identifying Novel Clinical Surrogates to Assess Human Bone Fracture Toughness. *J. Bone Miner. Res.* **30**, 1290–1300 (2015).
277. McCalden, R. W., McGeough, J. A., Barker, M. B. & Court-Brown, C. M. Age-related changes in the tensile properties of cortical bone. The relative importance of changes in porosity, mineralization, and microstructure. *J. Bone Joint Surg. Am.* **75**, 1193–1205 (1993).
278. Nyman, J. S. *et al.* Partial removal of pore and loosely bound water by low-energy drying decreases cortical bone toughness in young and old donors. *J. Mech. Behav. Biomed. Mater.* **22**, 136–145 (2013).
279. Lazarev, Y. A., Grishkovsky, B. A., Khromova, T. B., Lazareva, A. A. & Grechishko, V. S. Bound water in the collagen-like triple-helical structure. *Biopolymers* **32**, 189–195 (1992).
280. Okuyama, K., Okuyama, K., Arnott, S., Takayanagi, M. & Kakudo, M. Crystal and molecular structure of a collagen-like polypeptide (Pro-Pro-Gly)₁₀. *J. Mol. Biol.* **152**, 427–443 (1981).
281. Brodsky, B. & Persikov, A. V. Molecular Structure of the Collagen Triple Helix. in *Advances in Protein Chemistry* vol. 70 301–339 (Academic Press, 2005).
282. Leikin, S., Parsegian, V. A., Yang, W.-H. & Walrafen, G. E. Raman spectral evidence for hydration forces between collagen triple helices. *Proc. Natl. Acad. Sci.* **94**, 11312–11317 (1997).
283. Granke, M., Does, M. D. & Nyman, J. S. The Role of Water Compartments in the Material Properties of Cortical Bone. *Calcif. Tissue Int.* **97**, 292–307 (2015).
284. Wilson, E. E. *et al.* Highly Ordered Interstitial Water Observed in Bone by Nuclear Magnetic Resonance. *J. Bone Miner. Res.* **20**, 625–634 (2005).
285. Davies, E. *et al.* Citrate bridges between mineral platelets in bone. *Proc. Natl. Acad. Sci.* **111**, E1354–E1363 (2014).
286. Wilson, E. E. *et al.* Three Structural Roles for Water in Bone Observed by Solid-State NMR. *Biophys. J.* **90**, 3722–3731 (2006).

287. Bhowmik Rahul, Katti Kalpana S. & Katti Dinesh R. Mechanisms of Load-Deformation Behavior of Molecular Collagen in Hydroxyapatite-Tropocollagen Molecular System: Steered Molecular Dynamics Study. *J. Eng. Mech.* **135**, 413–421 (2009).
288. Eberhardsteiner, L., Hellmich, C. & Scheiner, S. Layered water in crystal interfaces as source for bone viscoelasticity: arguments from a multiscale approach. *Comput. Methods Biomech. Biomed. Engin.* **17**, 48–63 (2014).
289. Bertinetti, L. *et al.* Surface Structure, Hydration, and Cationic Sites of Nanohydroxyapatite: UHR-TEM, IR, and Microgravimetric Studies. *J. Phys. Chem. C* **111**, 4027–4035 (2007).
290. Zahn, D. & Hochrein, O. Computational study of interfaces between hydroxyapatite and water. *Phys. Chem. Chem. Phys.* **5**, 4004–4007 (2003).
291. Nyman, J. S., Ni, Q., Nicoletta, D. P. & Wang, X. MEASUREMENTS OF MOBILE AND BOUND WATER BY NUCLEAR MAGNETIC RESONANCE CORRELATE WITH MECHANICAL PROPERTIES OF BONE. *Bone* **42**, 193–199 (2008).
292. Fritsch, A., Hellmich, C. & Dormieux, L. Ductile sliding between mineral crystals followed by rupture of collagen crosslinks: Experimentally supported micromechanical explanation of bone strength. *J. Theor. Biol.* **260**, 230–252 (2009).
293. Zhao, W., Byrne, M. H., Wang, Y. & Krane, S. M. Osteocyte and osteoblast apoptosis and excessive bone deposition accompany failure of collagenase cleavage of collagen. *J. Clin. Invest.* **106**, 941–949 (2000).
294. Lynch, M. P., Stein, J. L., Stein, G. S. & Lian, J. B. The Influence of Type I Collagen on the Development and Maintenance of the Osteoblast Phenotype in Primary and Passaged Rat Calvarial Osteoblasts: Modification of Expression of Genes Supporting Cell Growth, Adhesion, and Extracellular Matrix Mineralization. *Exp. Cell Res.* **216**, 35–45 (1995).
295. Green, J., Schotland, S., Stauber, D. J., Kleeman, C. R. & Clemens, T. L. Cell-matrix interaction in bone: type I collagen modulates signal transduction in osteoblast-like cells. *Am. J. Physiol.-Cell Physiol.* **268**, C1090–C1103 (1995).
296. Beck, K. *et al.* Destabilization of osteogenesis imperfecta collagen-like model peptides correlates with the identity of the residue replacing glycine. *Proc. Natl. Acad. Sci. U. S. A.* **97**, 4273–4278 (2000).
297. Long, C. G. *et al.* Characterization of collagen-like peptides containing interruptions in the repeating Gly-X-Y sequence. *Biochemistry* **32**, 11688–11695 (1993).
298. Hongo, C., Noguchi, K., Okuyama, K., Tanaka, Y. & Nishino, N. Repetitive interactions observed in the crystal structure of a collagen-model peptide, [(Pro-Pro-Gly)₉]₃. *J. Biochem. (Tokyo)* **138**, 135–144 (2005).
299. Yamauchi, M. & Sricholpech, M. Lysine post-translational modifications of collagen. *Essays Biochem.* **52**, 113–133 (2012).
300. Eyre, D. R. & Ann Weis, M. Bone Collagen: New Clues to its Mineralization Mechanism From Recessive Osteogenesis Imperfecta. *Calcif. Tissue Int.* **93**, 338–347 (2013).
301. Giraud-Guille, M.-M., Besseau, L. & Martin, R. Liquid crystalline assemblies of collagen in bone and in vitro systems. *J. Biomech.* **36**, 1571–1579 (2003).
302. Hulmes, D. J. & Miller, A. Quasi-hexagonal molecular packing in collagen fibrils. *Nature* **282**, 878–880 (1979).
303. Hulmes, D. J., Wess, T. J., Prockop, D. J. & Fratzl, P. Radial packing, order, and disorder in collagen fibrils. *Biophys. J.* **68**, 1661–1670 (1995).

304. Orgel, J. P. R. O. *et al.* The In Situ Supermolecular Structure of Type I Collagen. *Structure* **9**, 1061–1069 (2001).
305. Orgel, J. P. R. O., San Antonio, J. D. & Antipova, O. Molecular and structural mapping of collagen fibril interactions. *Connect. Tissue Res.* **52**, 2–17 (2011).
306. Kuypers, R., Tyler, M., Kurth, L. B., Jenkins, I. D. & Horgan, D. J. Identification of the loci of the collagen-associated Ehrlich chromogen in type I collagen confirms its role as a trivalent cross-link. *Biochem. J.* **283**, 129–136 (1992).
307. Bank, R. A. *et al.* Defective collagen crosslinking in bone, but not in ligament or cartilage, in Bruck syndrome: Indications for a bone-specific telopeptide lysyl hydroxylase on chromosome 17. *Proc. Natl. Acad. Sci. U. S. A.* **96**, 1054–1058 (1999).
308. Schwarze, U. *et al.* Mutations in FKBP10, which result in Bruck syndrome and recessive forms of osteogenesis imperfecta, inhibit the hydroxylation of telopeptide lysines in bone collagen. *Hum. Mol. Genet.* **22**, 1–17 (2013).
309. Lindert, U. *et al.* Molecular Consequences of the SERPINH1/HSP47 Mutation in the Dachshund Natural Model of Osteogenesis Imperfecta. *J. Biol. Chem.* **290**, 17679–17689 (2015).
310. Grillo, M. A. & Colombatto, S. Advanced glycation end-products (AGEs): involvement in aging and in neurodegenerative diseases. *Amino Acids* **35**, 29–36 (2008).
311. Robins, S. P. & Bailey, A. J. Age-related changes in collagen: The identification of reducible lysine-carbohydrate condensation products. *Biochem. Biophys. Res. Commun.* **48**, 76–84 (1972).
312. Nagai, R. *et al.* Detection of AGEs as markers for carbohydrate metabolism and protein denaturation. *J. Clin. Biochem. Nutr.* **55**, 1–6 (2014).
313. Saito, M. & Marumo, K. Effects of Collagen Crosslinking on Bone Material Properties in Health and Disease. *Calcif. Tissue Int.* **97**, 242–261 (2015).
314. Silva, M. J. *et al.* Type 1 Diabetes in Young Rats Leads to Progressive Trabecular Bone Loss, Cessation of Cortical Bone Growth, and Diminished Whole Bone Strength and Fatigue Life. *J. Bone Miner. Res.* **24**, 1618–1627 (2009).
315. Viguet-Carrin, S. *et al.* Contribution of the advanced glycation end product pentosidine and of maturation of type I collagen to compressive biomechanical properties of human lumbar vertebrae. *Bone* **39**, 1073–1079 (2006).
316. Willett, T. L., Suttly, S., Gaspar, A., Avery, N. & Grynblas, M. In vitro non-enzymatic ribation reduces post-yield strain accommodation in cortical bone. *Bone* **52**, 611–622 (2013).
317. Alikhani, M. *et al.* Advanced Glycation Endproducts Stimulate Osteoblast Apoptosis Via the MAP Kinase and Cytosolic Apoptotic Pathways. *Bone* **40**, 345–353 (2007).
318. Liu, J. *et al.* AGEs Induce Apoptosis in Rat Osteoblast Cells by Activating the Caspase-3 Signaling Pathway Under a High-Glucose Environment In Vitro. *Appl. Biochem. Biotechnol.* **178**, 1015–1027 (2016).
319. Ogawa, N. *et al.* The combination of high glucose and advanced glycation end-products (AGEs) inhibits the mineralization of osteoblastic MC3T3-E1 cells through glucose-induced increase in the receptor for AGEs. *Horm. Metab. Res. Horm. Stoffwechselforschung Horm. Metab.* **39**, 871–875 (2007).
320. Valcourt, U. *et al.* Non-enzymatic Glycation of Bone Collagen Modifies Osteoclastic Activity and Differentiation. *J. Biol. Chem.* **282**, 5691–5703 (2007).
321. Bornstein, P. & Sage, E. H. Matricellular proteins: extracellular modulators of cell function. *Curr. Opin. Cell Biol.* **14**, 608–616 (2002).

322. Takagi, J. Structural basis for ligand recognition by RGD (Arg-Gly-Asp)-dependent integrins. *Biochem. Soc. Trans.* **32**, 403–406 (2004).
323. Fisher, L. W. & Fedarko, N. S. Six genes expressed in bones and teeth encode the current members of the SIBLING family of proteins. *Connect. Tissue Res.* **44 Suppl 1**, 33–40 (2003).
324. Staines, K. A., MacRae, V. E. & Farquharson, C. The importance of the SIBLING family of proteins on skeletal mineralisation and bone remodelling. *J. Endocrinol.* **214**, 241–255 (2012).
325. Price, P. A., Otsuka, A. A., Poser, J. W., Kristaponis, J. & Raman, N. Characterization of a gamma-carboxyglutamic acid-containing protein from bone. *Proc. Natl. Acad. Sci. U. S. A.* **73**, 1447–1451 (1976).
326. Price, P. A., Urist, M. R. & Otawara, Y. Matrix Gla protein, a new gamma-carboxyglutamic acid-containing protein which is associated with the organic matrix of bone. *Biochem. Biophys. Res. Commun.* **117**, 765–771 (1983).
327. Maillard, C., Berruyer, M., Serre, C. M., Dechavanne, M. & Delmas, P. D. Protein-S, a vitamin K-dependent protein, is a bone matrix component synthesized and secreted by osteoblasts. *Endocrinology* **130**, 1599–1604 (1992).
328. Luo, G. *et al.* Spontaneous calcification of arteries and cartilage in mice lacking matrix GLA protein. *Nature* **386**, 78–81 (1997).
329. Murshed, M., Schinke, T., McKee, M. D. & Karsenty, G. Extracellular matrix mineralization is regulated locally; different roles of two gla-containing proteins. *J. Cell Biol.* **165**, 625–630 (2004).
330. Poundarik, A. A., Boskey, A., Gundberg, C. & Vashishth, D. Biomolecular regulation, composition and nanoarchitecture of bone mineral. *Sci. Rep.* **8**, 1–8 (2018).
331. Iozzo, R. V. & Schaefer, L. Proteoglycan form and function: A comprehensive nomenclature of proteoglycans. *Matrix Biol. J. Int. Soc. Matrix Biol.* **42**, 11–55 (2015).
332. Kalamajski, S. & Oldberg, A. The role of small leucine-rich proteoglycans in collagen fibrillogenesis. *Matrix Biol. J. Int. Soc. Matrix Biol.* **29**, 248–253 (2010).
333. Chen, S. & Birk, D. E. The regulatory roles of small leucine-rich proteoglycans in extracellular assembly. *FEBS J.* **280**, 2120–2137 (2013).
334. Prince, C. W., Rahemtulla, F. & Butler, W. T. Metabolism of rat bone proteoglycans in vivo. *Biochem. J.* **216**, 589–596 (1983).
335. Hoshi, K., Kemmotsu, S., Takeuchi, Y., Amizuka, N. & Ozawa, H. The Primary Calcification in Bones Follows Removal of Decorin and Fusion of Collagen Fibrils. *J. Bone Miner. Res.* **14**, 273–280 (1999).
336. Mochida, Y., Duarte, W. R., Tanzawa, H., Paschalis, E. P. & Yamauchi, M. Decorin modulates matrix mineralization in vitro. *Biochem. Biophys. Res. Commun.* **305**, 6–9 (2003).
337. Bianco, P., Fisher, L. W., Young, M. F., Termine, J. D. & Robey, P. G. Expression and localization of the two small proteoglycans biglycan and decorin in developing human skeletal and non-skeletal tissues. *J. Histochem. Cytochem. Off. J. Histochem. Soc.* **38**, 1549–1563 (1990).
338. Danielson, K. G. *et al.* Targeted Disruption of Decorin Leads to Abnormal Collagen Fibril Morphology and Skin Fragility. *J. Cell Biol.* **136**, 729–743 (1997).
339. Mochida, Y. *et al.* Decorin modulates collagen matrix assembly and mineralization. *Matrix Biol. J. Int. Soc. Matrix Biol.* **28**, 44–52 (2009).
340. Vogel, K. G. & Trotter, J. A. The effect of proteoglycans on the morphology of collagen fibrils formed in vitro. *Coll. Relat. Res.* **7**, 105–114 (1987).

341. Zhu, W., Robey, P. G. & Boskey, A. L. The Regulatory Role of Matrix Proteins in Mineralization of Bone. in *Osteoporosis* 191–240 (Elsevier, 2008). doi:10.1016/B978-012370544-0.50011-2.
342. Ciancaglini, P. *et al.* Kinetic Analysis of Substrate Utilization by Native and TNAP-, NPP1-, or PHOSPHO1-Deficient Matrix Vesicles. *J. Bone Miner. Res.* **25**, 716–723 (2010).
343. Bradshaw, A. D. & Sage, E. H. SPARC, a matricellular protein that functions in cellular differentiation and tissue response to injury. *J. Clin. Invest.* **107**, 1049–1054 (2001).
344. Delany, A. M., Kalajzic, I., Bradshaw, A. D., Sage, E. H. & Canalis, E. Osteonectin-null mutation compromises osteoblast formation, maturation, and survival. *Endocrinology* **144**, 2588–2596 (2003).
345. Midwood, K. S. & Schwarzbauer, J. E. Tenascin-C Modulates Matrix Contraction via Focal Adhesion Kinase- and Rho-mediated Signaling Pathways. *Mol. Biol. Cell* **13**, 3601–3613 (2002).
346. Mackie, E. J. & Ramsey, S. Modulation of osteoblast behaviour by tenascin. *J. Cell Sci.* **109 (Pt 6)**, 1597–1604 (1996).
347. Velling, T., Risteli, J., Wennerberg, K., Mosher, D. F. & Johansson, S. Polymerization of Type I and III Collagens Is Dependent On Fibronectin and Enhanced By Integrins $\alpha 1\beta 1$ and $\alpha 2\beta 1$. *J. Biol. Chem.* **277**, 37377–37381 (2002).
348. Sottile, J. & Hocking, D. C. Fibronectin Polymerization Regulates the Composition and Stability of Extracellular Matrix Fibrils and Cell-Matrix Adhesions. *Mol. Biol. Cell* **13**, 3546–3559 (2002).
349. Moursi, A. M. *et al.* Fibronectin regulates calvarial osteoblast differentiation. *J. Cell Sci.* **109 (Pt 6)**, 1369–1380 (1996).
350. Moursi, A. M., Globus, R. K. & Damsky, C. H. Interactions between integrin receptors and fibronectin are required for calvarial osteoblast differentiation in vitro. *J. Cell Sci.* **110 (Pt 18)**, 2187–2196 (1997).
351. Bentmann, A. *et al.* Circulating fibronectin affects bone matrix, whereas osteoblast fibronectin modulates osteoblast function. *J. Bone Miner. Res.* **25**, 706–715 (2010).
352. Rohanizadeh, R. *et al.* Apatite precipitation after incubation of biphasic calcium-phosphate ceramic in various solutions: Influence of seed species and proteins. *J. Biomed. Mater. Res.* **42**, 530–539 (1998).
353. Grzesik, W. J. & Robey, P. G. Bone matrix RGD glycoproteins: immunolocalization and interaction with human primary osteoblastic bone cells in vitro. *J. Bone Miner. Res. Off. J. Am. Soc. Bone Miner. Res.* **9**, 487–496 (1994).
354. Davies, J. *et al.* The osteoclast functional antigen, implicated in the regulation of bone resorption, is biochemically related to the vitronectin receptor. *J. Cell Biol.* **109**, 1817–1826 (1989).
355. Carron, J. A., Wagstaff, S. C., Gallagher, J. A. & Bowler, W. B. A CD36-binding peptide from thrombospondin-1 can stimulate resorption by osteoclasts in vitro. *Biochem. Biophys. Res. Commun.* **270**, 1124–1127 (2000).
356. Adams, J. C. Thrombospondin-1. *Int. J. Biochem. Cell Biol.* **29**, 861–865 (1997).
357. Adams, J. C. & Lawler, J. The thrombospondins. *Int. J. Biochem. Cell Biol.* **36**, 961–968 (2004).
358. Bornstein, P., Kyriakides, T. R., Yang, Z., Armstrong, L. C. & Birk, D. E. Thrombospondin 2 modulates collagen fibrillogenesis and angiogenesis. *J. Investig. Dermatol. Symp. Proc.* **5**, 61–66 (2000).
359. Hankenson, K. D. & Bornstein, P. The secreted protein thrombospondin 2 is an autocrine inhibitor of marrow stromal cell proliferation. *J. Bone Miner. Res. Off. J. Am. Soc. Bone Miner. Res.* **17**, 415–425 (2002).

360. Hankenson, K. D. *et al.* Increased marrow-derived osteoprogenitor cells and endosteal bone formation in mice lacking thrombospondin 2. *J. Bone Miner. Res. Off. J. Am. Soc. Bone Miner. Res.* **15**, 851–862 (2000).
361. Boskey, A. L. *et al.* Osteopontin-hydroxyapatite interactions in vitro: inhibition of hydroxyapatite formation and growth in a gelatin-gel. *Bone Miner.* **22**, 147–159 (1993).
362. Hunter, G. K. Role of osteopontin in modulation of hydroxyapatite formation. *Calcif. Tissue Int.* **93**, 348–354 (2013).
363. Steitz, S. A. *et al.* Osteopontin inhibits mineral deposition and promotes regression of ectopic calcification. *Am. J. Pathol.* **161**, 2035–2046 (2002).
364. Fantner, G. E. *et al.* Nanoscale ion mediated networks in bone: osteopontin can repeatedly dissipate large amounts of energy. *Nano Lett.* **7**, 2491–2498 (2007).
365. Giachelli, C. M. & Steitz, S. Osteopontin: a versatile regulator of inflammation and biomineralization. *Matrix Biol. J. Int. Soc. Matrix Biol.* **19**, 615–622 (2000).
366. Suzuki, K. *et al.* Colocalization of intracellular osteopontin with CD44 is associated with migration, cell fusion, and resorption in osteoclasts. *J. Bone Miner. Res. Off. J. Am. Soc. Bone Miner. Res.* **17**, 1486–1497 (2002).
367. Baht, G. S., Hunter, G. K. & Goldberg, H. A. Bone sialoprotein-collagen interaction promotes hydroxyapatite nucleation. *Matrix Biol. J. Int. Soc. Matrix Biol.* **27**, 600–608 (2008).
368. Hunter, G. K. & Goldberg, H. A. Nucleation of hydroxyapatite by bone sialoprotein. *Proc. Natl. Acad. Sci. U. S. A.* **90**, 8562–8565 (1993).
369. Bouleffour, W. *et al.* The role of the SIBLING, Bone Sialoprotein in skeletal biology — Contribution of mouse experimental genetics. *Matrix Biol.* **52–54**, 60–77 (2016).
370. Gordon, J. A. R. *et al.* Bone sialoprotein expression enhances osteoblast differentiation and matrix mineralization in vitro. *Bone* **41**, 462–473 (2007).
371. Boudiffa, M. *et al.* Bone sialoprotein deficiency impairs osteoclastogenesis and mineral resorption in vitro. *J. Bone Miner. Res. Off. J. Am. Soc. Bone Miner. Res.* **25**, 2669–2679 (2010).
372. Malaval, L. *et al.* Bone sialoprotein plays a functional role in bone formation and osteoclastogenesis. *J. Exp. Med.* **205**, 1145–1153 (2008).
373. Yang, W. *et al.* Dentin matrix protein 1 gene cis-regulation: use in osteocytes to characterize local responses to mechanical loading in vitro and in vivo. *J. Biol. Chem.* **280**, 20680–20690 (2005).
374. Martin, A. *et al.* Bone proteins PHEX and DMP1 regulate fibroblastic growth factor Fgf23 expression in osteocytes through a common pathway involving FGF receptor (FGFR) signaling. *FASEB J.* **25**, 2551–2562 (2011).
375. Ducy, P. *et al.* Increased bone formation in osteocalcin-deficient mice. *Nature* **382**, 448–452 (1996).
376. Liggett, W. H., Lian, J. B., Greenberger, J. S. & Glowacki, J. Osteocalcin promotes differentiation of osteoclast progenitors from murine long-term bone marrow cultures. *J. Cell. Biochem.* **55**, 190–199 (1994).
377. Gehron Robey, P. Chapter 17 - Noncollagenous Bone Matrix Proteins. in *Principles of Bone Biology (Third Edition)* (eds. Bilezikian, J. P., Raisz, L. G. & Martin, T. J.) 335–349 (Academic Press, 2008). doi:10.1016/B978-0-12-373884-4.00036-7.
378. Du, W. W. *et al.* The role of versican G3 domain in regulating breast cancer cell motility including effects on osteoblast cell growth and differentiation in vitro - evaluation towards understanding breast cancer cell bone metastasis. *BMC Cancer* **12**, 341 (2012).

379. Hedbom, E. & Heinegård, D. Binding of fibromodulin and decorin to separate sites on fibrillar collagens. *J. Biol. Chem.* **268**, 27307–27312 (1993).
380. Asawa, Y., Aoki, K., Ohya, K., Ohshima, H. & Takano, Y. Appearance of electron-dense segments: indication of possible conformational changes of pre-mineralizing collagen fibrils in the osteoid of rat bones. *J. Electron Microsc. (Tokyo)* **53**, 423–433 (2004).
381. Svensson, L. *et al.* Fibromodulin-null Mice Have Abnormal Collagen Fibrils, Tissue Organization, and Altered Lumican Deposition in Tendon. *J. Biol. Chem.* **274**, 9636–9647 (1999).
382. Boskey, A. L., Spevak, L., Doty, S. B. & Rosenberg, L. Effects of Bone CS-Proteoglycans, DS-Decorin, and DS-Biglycan on Hydroxyapatite Formation in a Gelatin Gel. *Calcif. Tissue Int.* **61**, 298–305 (1997).
383. Corsi, A. *et al.* Phenotypic effects of biglycan deficiency are linked to collagen fibril abnormalities, are synergized by decorin deficiency, and mimic Ehlers-Danlos-like changes in bone and other connective tissues. *J. Bone Miner. Res. Off. J. Am. Soc. Bone Miner. Res.* **17**, 1180–1189 (2002).
384. Chen, X.-D., Fisher, L. W., Robey, P. G. & Young, M. F. The small leucine-rich proteoglycan biglycan modulates BMP-4-induced osteoblast differentiation. *FASEB J. Off. Publ. Fed. Am. Soc. Exp. Biol.* **18**, 948–958 (2004).
385. Parisuthiman, D., Mochida, Y., Duarte, W. R. & Yamauchi, M. Biglycan modulates osteoblast differentiation and matrix mineralization. *J. Bone Miner. Res. Off. J. Am. Soc. Bone Miner. Res.* **20**, 1878–1886 (2005).
386. Buraschi, S. *et al.* Decorin causes autophagy in endothelial cells via Peg3. *Proc. Natl. Acad. Sci. U. S. A.* **110**, E2582–E2591 (2013).
387. Elliott, J. C. Calcium Phosphate Biominerals. *Rev. Mineral. Geochem.* **48**, 427–453 (2002).
388. Fujisawa, R. & Tamura, M. Acidic bone matrix proteins and their roles in calcification. *Front. Biosci. Landmark Ed.* **17**, 1891–1903 (2012).
389. Kafak-Hachulska, A., Samoson, A. & Kolodziejewski, W. ¹H MAS and ¹H → ³¹P CP/MAS NMR study of human bone mineral. *Calcif. Tissue Int.* **73**, 476–486 (2003).
390. Landi, E. *et al.* Biomimetic Mg- and Mg, CO₃-substituted hydroxyapatites: synthesis characterization and in vitro behaviour. *J. Eur. Ceram. Soc.* **26**, 2593–2601 (2006).
391. Rude, R. K. & Gruber, H. E. Magnesium deficiency and osteoporosis: animal and human observations. *J. Nutr. Biochem.* **15**, 710–716 (2004).
392. Dani, S. U. Osteoresorptive arsenic intoxication. *Bone* **53**, 541–545 (2013).
393. Chappard, D. *et al.* Aluminum and iron can be deposited in the calcified matrix of bone exostoses. *J. Inorg. Biochem.* **152**, 174–179 (2015).
394. Li, X. *et al.* Effects of Aluminum Exposure on Bone Mineral Density, Mineral, and Trace Elements in Rats. *Biol. Trace Elem. Res.* **143**, 378–385 (2011).
395. Silbergeld, E. K. *et al.* Lead in bone: storage site, exposure source, and target organ. *Neurotoxicology* **14**, 225–236 (1993).
396. Neuman, W. F. & Neuman, M. W. The deposition of uranium in bone; ion competition studies. *J. Biol. Chem.* **179**, 341–348 (1949).
397. Glimcher, M. J. 8. Bone: Nature of the Calcium Phosphate Crystals and Cellular, Structural, and Physical Chemical Mechanisms in Their Formation. in *Medical Mineralogy and Geochemistry* vol. 64 223–282 (De Gruyter, 2006).
398. Fratzi-Zelman, N. *et al.* CRTAP deficiency leads to abnormally high bone matrix mineralization in a murine model and in children with Osteogenesis Imperfecta type VII. *Bone* **46**, 820–826 (2010).

399. Chatterji, S., Wall, J. C. & Jeffery, J. W. Age-related changes in the orientation and particle size of the mineral phase in human femoral cortical bone. *Calcif. Tissue Int.* **33**, 567–574 (1981).
400. Posner, A. S., Harper, R. A., Muller, S. A. & Menczel, J. Age Changes in the Crystal Chemistry of Bone Apatite*. *Ann. N. Y. Acad. Sci.* **131**, 737–742 (1965).
401. Chambers, T. J. & Fuller, K. Bone cells predispose bone surfaces to resorption by exposure of mineral to osteoclastic contact. *J. Cell Sci.* **76**, 155–165 (1985).
402. Chambers, T. J., Thomson, B. M. & Fuller, K. Effect of substrate composition on bone resorption by rabbit osteoclasts. *J. Cell Sci.* **70**, 61–71 (1984).
403. Nakamura, I. *et al.* Chemical and physical properties of the extracellular matrix are required for the actin ring formation in osteoclasts. *J. Bone Miner. Res. Off. J. Am. Soc. Bone Miner. Res.* **11**, 1873–1879 (1996).
404. Geblinger, D., Addadi, L. & Geiger, B. Nano-topography sensing by osteoclasts. *J. Cell Sci.* **123**, 1503–1510 (2010).
405. Shemesh, M., Addadi, L. & Geiger, B. Surface microtopography modulates sealing zone development in osteoclasts cultured on bone. *J. R. Soc. Interface* **14**, (2017).
406. Geblinger, D., Zink Christian, Spencer Nicholas D., Addadi Lia & Geiger Benjamin. Effects of surface microtopography on the assembly of the osteoclast resorption apparatus. *J. R. Soc. Interface* **9**, 1599–1608 (2012).
407. Faia-Torres, A. B. *et al.* Osteogenic differentiation of human mesenchymal stem cells in the absence of osteogenic supplements: A surface-roughness gradient study. *Acta Biomater.* **28**, 64–75 (2015).
408. Juignet, L. *et al.* Macrotopographic closure promotes tissue growth and osteogenesis in vitro. *Acta Biomater.* **53**, 536–548 (2017).
409. Urquia Edreira, E. R. *et al.* Effect of calcium phosphate ceramic substrate geometry on mesenchymal stromal cell organization and osteogenic differentiation. *Biofabrication* **8**, 025006 (2016).
410. Engler, A. J., Sen, S., Sweeney, H. L. & Discher, D. E. Matrix Elasticity Directs Stem Cell Lineage Specification. *Cell* **126**, 677–689 (2006).
411. Franceschi, R. T. & Iyer, B. S. Relationship between collagen synthesis and expression of the osteoblast phenotype in MC3T3-E1 cells. *J. Bone Miner. Res. Off. J. Am. Soc. Bone Miner. Res.* **7**, 235–246 (1992).
412. Franceschi, R. T., Iyer, B. S. & Cui, Y. Effects of ascorbic acid on collagen matrix formation and osteoblast differentiation in murine MC3T3-E1 cells. *J. Bone Miner. Res.* **9**, 843–854 (1994).
413. Xiao, G., Cui, Y., Ducey, P., Karsenty, G. & Franceschi, R. T. Ascorbic Acid-Dependent Activation of the Osteocalcin Promoter in MC3T3-E1 Preosteoblasts: Requirement for Collagen Matrix Synthesis and the Presence of an Intact OSE2 Sequence. *Mol. Endocrinol.* **11**, 1103–1113 (1997).
414. Xiao, G. *et al.* Bone morphogenetic proteins, extracellular matrix, and mitogen-activated protein kinase signaling pathways are required for osteoblast-specific gene expression and differentiation in MC3T3-E1 cells. *J. Bone Miner. Res. Off. J. Am. Soc. Bone Miner. Res.* **17**, 101–110 (2002).
415. Jikko, A., Harris, S. E., Chen, D., Mendrick, D. L. & Damsky, C. H. Collagen integrin receptors regulate early osteoblast differentiation induced by BMP-2. *J. Bone Miner. Res. Off. J. Am. Soc. Bone Miner. Res.* **14**, 1075–1083 (1999).
416. Takeuchi, Y. *et al.* Differentiation and transforming growth factor-beta receptor down-regulation by collagen-alpha2beta1 integrin interaction is mediated by focal adhesion kinase and its downstream signals in murine osteoblastic cells. *J. Biol. Chem.* **272**, 29309–29316 (1997).

417. Zhang, M. *et al.* Osteoblast-specific Knockout of the Insulin-like Growth Factor (IGF) Receptor Gene Reveals an Essential Role of IGF Signaling in Bone Matrix Mineralization. *J. Biol. Chem.* **277**, 44005–44012 (2002).
418. Xian, L. *et al.* Matrix IGF-1 regulates bone mass by activation of mTOR in mesenchymal stem cells. *Nat. Med.* **18**, 1095–1101 (2012).
419. Verron, E. *et al.* Gallium modulates osteoclastic bone resorption in vitro without affecting osteoblasts. *Br. J. Pharmacol.* **159**, 1681–1692 (2010).
420. Luckman, S. P. *et al.* Nitrogen-containing bisphosphonates inhibit the mevalonate pathway and prevent post-translational prenylation of GTP-binding proteins, including Ras. *J. Bone Miner. Res. Off. J. Am. Soc. Bone Miner. Res.* **13**, 581–589 (1998).
421. Odvina, C. V. *et al.* Severely suppressed bone turnover: a potential complication of alendronate therapy. *J. Clin. Endocrinol. Metab.* **90**, 1294–1301 (2005).
422. Sillence, D. O., Senn, A. & Danks, D. M. Genetic heterogeneity in osteogenesis imperfecta. *J. Med. Genet.* **16**, 101–116 (1979).
423. Theocharis, A. D., Manou, D. & Karamanos, N. K. The extracellular matrix as a multitasking player in disease. *FEBS J.* **286**, 2830–2869 (2019).
424. Marini, J. C. *et al.* Consortium for Osteogenesis Imperfecta Mutations in the Helical Domain of Type I Collagen: Regions Rich in Lethal Mutations Align with Collagen Binding Sites for Integrins and Proteoglycans. *Hum. Mutat.* **28**, 209–221 (2007).
425. Bateman, J. F., Boot-Handford, R. P. & Lamandé, S. R. Genetic diseases of connective tissues: cellular and extracellular effects of ECM mutations. *Nat. Rev. Genet.* **10**, 173–183 (2009).
426. Seeliger, F. *et al.* Osteogenesis imperfecta in two litters of dachshunds. *Vet. Pathol.* **40**, 530–539 (2003).
427. Fitzgerald, J., Lamandé, S. R. & Bateman, J. F. Proteasomal degradation of unassembled mutant type I collagen pro- α 1(I) chains. *J. Biol. Chem.* **274**, 27392–27398 (1999).
428. Lamandé, S. R. *et al.* Endoplasmic reticulum-mediated quality control of type I collagen production by cells from osteogenesis imperfecta patients with mutations in the pro α 1 (I) chain carboxyl-terminal propeptide which impair subunit assembly. *J. Biol. Chem.* **270**, 8642–8649 (1995).
429. Lisse, T. S. *et al.* ER stress-mediated apoptosis in a new mouse model of osteogenesis imperfecta. *PLoS Genet.* **4**, e7 (2008).
430. Smaldone, S. & Ramirez, F. Fibrillin microfibrils in bone physiology. *Matrix Biol. J. Int. Soc. Matrix Biol.* **52–54**, 191–197 (2016).
431. Jensen, S. A. & Handford, P. A. New insights into the structure, assembly and biological roles of 10-12 nm connective tissue microfibrils from fibrillin-1 studies. *Biochem. J.* **473**, 827–838 (2016).
432. Sengle, G. & Sakai, L. Y. The fibrillin microfibril scaffold: A niche for growth factors and mechanosensation? *Matrix Biol. J. Int. Soc. Matrix Biol.* **47**, 3–12 (2015).
433. Nistala, H. *et al.* Fibrillin-1 and -2 differentially modulate endogenous TGF- β and BMP bioavailability during bone formation. *J. Cell Biol.* **190**, 1107–1121 (2010).
434. Tiedemann, K. *et al.* Fibrillin-1 directly regulates osteoclast formation and function by a dual mechanism. *J. Cell Sci.* **126**, 4187–4194 (2013).
435. Boivin, G. & Meunier, P. J. The degree of mineralization of bone tissue measured by computerized quantitative contact microradiography. *Calcif. Tissue Int.* **70**, 503–511 (2002).
436. Akkus, O., Adar, F. & Schaffler, M. B. Age-related changes in physicochemical properties of mineral crystals are related to impaired mechanical function of cortical bone. *Bone* **34**, 443–453 (2004).

437. Handschin, R. G. & Stern, W. B. X-ray diffraction studies on the lattice perfection of human bone apatite (Crista Iliaca). *Bone* **16**, S355–S363 (1995).
438. Rey, C., Renugopalakrishnan, V., Collins, B. & Glimcher, M. J. Fourier transform infrared spectroscopic study of the carbonate ions in bone mineral during aging. *Calcif. Tissue Int.* **49**, 251–258 (1991).
439. Ishimoto, T., Nakano, T., Umakoshi, Y., Yamamoto, M. & Tabata, Y. Degree of biological apatite c-axis orientation rather than bone mineral density controls mechanical function in bone regenerated using recombinant bone morphogenetic protein-2. *J. Bone Miner. Res. Off. J. Am. Soc. Bone Miner. Res.* **28**, 1170–1179 (2013).
440. Currey, J. D. Tensile yield in compact bone is determined by strain, post-yield behaviour by mineral content. *J. Biomech.* **37**, 549–556 (2004).
441. Bailey, A. J. Molecular mechanisms of ageing in connective tissues. *Mech. Ageing Dev.* **122**, 735–755 (2001).
442. Eyre, D. R., Dickson, I. R. & Van Ness, K. Collagen cross-linking in human bone and articular cartilage. Age-related changes in the content of mature hydroxypyridinium residues. *Biochem. J.* **252**, 495–500 (1988).
443. Knott, L. & Bailey, A. J. Collagen cross-links in mineralizing tissues: a review of their chemistry, function, and clinical relevance. *Bone* **22**, 181–187 (1998).
444. Sparke, A. J. *et al.* Differences in composition of avian bone collagen following genetic selection for resistance to osteoporosis. *Br. Poult. Sci.* **43**, 127–134 (2002).
445. Dyer, D. G., Blackledge, J. A., Thorpe, S. R. & Baynes, J. W. Formation of pentosidine during nonenzymatic browning of proteins by glucose. Identification of glucose and other carbohydrates as possible precursors of pentosidine in vivo. *J. Biol. Chem.* **266**, 11654–11660 (1991).
446. Nyman, J. S. *et al.* Age-related effect on the concentration of collagen crosslinks in human osteonal and interstitial bone tissue. *Bone* **39**, 1210–1217 (2006).
447. Odetti, P. *et al.* Advanced glycation end products and bone loss during aging. *Ann. N. Y. Acad. Sci.* **1043**, 710–717 (2005).
448. Thomas, C. J., Cleland, T. P., Sroga, G. E. & Vashishth, D. Accumulation of carboxymethyl-lysine (CML) in human cortical bone. *Bone* **110**, 128–133 (2018).
449. Hernandez, C. J. *et al.* Trabecular microfracture and the influence of pyridinium and non-enzymatic glycation mediated collagen cross-links. *Bone* **37**, 825–832 (2005).
450. Wang, X., Shen, X., Li, X. & Mauli Agrawal, C. Age-related changes in the collagen network and toughness of bone. *Bone* **31**, 1–7 (2002).
451. Zimmermann, E. A. *et al.* Age-related changes in the plasticity and toughness of human cortical bone at multiple length scales. *Proc. Natl. Acad. Sci.* **108**, 14416–14421 (2011).
452. Okazaki, K. *et al.* Advanced glycation end products (AGEs), but not high glucose, inhibit the osteoblastic differentiation of mouse stromal ST2 cells through the suppression of osterix expression, and inhibit cell growth and increasing cell apoptosis. *Calcif. Tissue Int.* **91**, 286–296 (2012).
453. Katayama, Y., Celic, S., Nagata, N., Martin, T. J. & Findlay, D. M. Nonenzymatic glycation of type I collagen modifies interaction with UMR 201-10B preosteoblastic cells. *Bone* **21**, 237–242 (1997).
454. Plotkin, L. I., Essex, A. L. & Davis, H. M. RAGE Signaling in Skeletal Biology. *Curr. Osteoporos. Rep.* **17**, 16–25 (2019).

455. McCarthy, A. D., Uemura, T., Etcheverry, S. B. & Cortizo, A. M. Advanced glycation endproducts interfere with integrin-mediated osteoblastic attachment to a type-I collagen matrix. *Int. J. Biochem. Cell Biol.* **36**, 840–848 (2004).
456. Takagi, M. *et al.* Advanced glycation endproducts stimulate interleukin-6 production by human bone-derived cells. *J. Bone Miner. Res. Off. J. Am. Soc. Bone Miner. Res.* **12**, 439–446 (1997).
457. Zhou, Z. *et al.* Regulation of osteoclast function and bone mass by RAGE. *J. Exp. Med.* **203**, 1067–1080 (2006).
458. McCarthy, A. D. *et al.* Non-enzymatic glycosylation of a type I collagen matrix: effects on osteoblastic development and oxidative stress. *BMC Cell Biol.* **2**, 16 (2001).
459. Iyer, S. *et al.* FOXOs attenuate bone formation by suppressing Wnt signaling. *J. Clin. Invest.* **123**, 3409–3419 (2013).
460. Manolagas, S. C. The Quest for Osteoporosis Mechanisms and Rational Therapies: How Far We've Come, How Much Further We Need to Go. *J. Bone Miner. Res. Off. J. Am. Soc. Bone Miner. Res.* **33**, 371–385 (2018).
461. Ha, H. *et al.* Reactive oxygen species mediate RANK signaling in osteoclasts. *Exp. Cell Res.* **301**, 119–127 (2004).
462. Lee, N. K. *et al.* A crucial role for reactive oxygen species in RANKL-induced osteoclast differentiation. *Blood* **106**, 852–859 (2005).
463. Wang, X. *et al.* Age-Related Deterioration of Bone Toughness Is Related to Diminishing Amount of Matrix Glycosaminoglycans (GAGs). *JBMR Plus* **2**, 164–173 (2018).
464. Wang, X., Xu, H., Huang, Y., Gu, S. & Jiang, J. X. Coupling effect of water and proteoglycans on the in situ toughness of bone. *J. Bone Miner. Res. Off. J. Am. Soc. Bone Miner. Res.* **31**, 1026–1029 (2016).
465. Salbach-Hirsch, J. *et al.* Structural and functional insights into sclerostin-glycosaminoglycan interactions in bone. *Biomaterials* **67**, 335–345 (2015).
466. Sroga, G. E. & Vashishth, D. Phosphorylation of Extracellular Bone Matrix Proteins and Its Contribution to Bone Fragility. *J. Bone Miner. Res. Off. J. Am. Soc. Bone Miner. Res.* **33**, 2214–2229 (2018).
467. Fantner, G. E. *et al.* Sacrificial bonds and hidden length dissipate energy as mineralized fibrils separate during bone fracture. *Nat. Mater.* **4**, 612–616 (2005).
468. Bronner, F. Chapter 22 - Metals in Bone: Aluminum, Boron, Cadmium, Chromium, Lead, Silicon, and Strontium. in *Principles of Bone Biology (Second Edition)* (eds. Bilezikian, J. P., Raisz, L. G. & Rodan, G. A.) 359–369 (Academic Press, 2002).
469. Anissian, L. *et al.* Cobalt ions influence proliferation and function of human osteoblast-like cells. *Acta Orthop. Scand.* **73**, 369–374 (2002).
470. Beier, E. E. *et al.* Heavy metal lead exposure, osteoporotic-like phenotype in an animal model, and depression of Wnt signaling. *Environ. Health Perspect.* **121**, 97–104 (2013).
471. Chen, X., Zhu, G., Gu, S., Jin, T. & Shao, C. Effects of cadmium on osteoblasts and osteoclasts in vitro. *Environ. Toxicol. Pharmacol.* **28**, 232–236 (2009).
472. Hu, Y.-C. *et al.* Arsenic trioxide affects bone remodeling by effects on osteoblast differentiation and function. *Bone* **50**, 1406–1415 (2012).
473. Miyahara, T. *et al.* Inhibitory effects of cadmium on in vitro calcification of a clonal osteogenic cell, MC3T3-E1. *Toxicol. Appl. Pharmacol.* **96**, 52–59 (1988).

474. Queally, J. M. *et al.* Cobalt ions induce chemokine secretion in primary human osteoblasts. *J. Orthop. Res. Off. Publ. Orthop. Res. Soc.* **27**, 855–864 (2009).
475. Bernhardt, A., Schamel, M., Gbureck, U. & Gelinsky, M. Osteoclastic differentiation and resorption is modulated by bioactive metal ions Co^{2+} , Cu^{2+} and Cr^{3+} incorporated into calcium phosphate bone cements. *PLoS ONE* **12**, (2017).
476. Bhattacharyya, M. H., Whelton, B. D., Stern, P. H. & Peterson, D. P. Cadmium accelerates bone loss in ovariectomized mice and fetal rat limb bones in culture. *Proc. Natl. Acad. Sci. U. S. A.* **85**, 8761–8765 (1988).
477. Patntirapong, S., Habibovic, P. & Hauschka, P. V. Effects of soluble cobalt and cobalt incorporated into calcium phosphate layers on osteoclast differentiation and activation. *Biomaterials* **30**, 548–555 (2009).
478. Rousselle, A. V. *et al.* Influence of metal ion solutions on rabbit osteoclast activities in vitro. *Histol. Histopathol.* **17**, 1025–1032 (2002).
479. Roy, M., Fielding, G. A., Bandyopadhyay, A. & Bose, S. Effects of zinc and strontium substitution in tricalcium phosphate on osteoclast differentiation and resorption. *Biomater Sci* **1**, 74–82 (2013).
480. Yamada, Y. *et al.* Inhibitory effect of Zn^{2+} in zinc-containing β -tricalcium phosphate on resorbing activity of mature osteoclasts. *J. Biomed. Mater. Res. A* **84A**, 344–352 (2008).
481. Bourgeois, D. *et al.* Micro-distribution of uranium in bone after contamination: new insight into its mechanism of accumulation into bone tissue. *Anal. Bioanal. Chem.* **407**, 6619–6625 (2015).
482. Dermience, M., Lognay, G., Mathieu, F. & Goyens, P. Effects of thirty elements on bone metabolism. *J. Trace Elem. Med. Biol.* **32**, 86–106 (2015).
483. Krewski, D. *et al.* Human Health Risk Assessment for Aluminium, Aluminium Oxide, and Aluminium Hydroxide. *J. Toxicol. Environ. Health Part B* **10**, 1–269 (2007).
484. Blumenthal, N. C. & Posner, A. S. In vitro model of aluminum-induced osteomalacia: Inhibition of hydroxyapatite formation and growth. *Calcif. Tissue Int.* **36**, 439–441 (1984).
485. Meyer, J. L. & Thomas, W. C. Trace metal-citric acid complexes as inhibitors of calcification and crystal growth. I. Effects of Fe(III) , Cr(III) and Al(III) complexes on calcium phosphate crystal growth. *J. Urol.* **128**, 1372–1375 (1982).
486. Degeratu, C. N., Mabillean, G., Cincu, C. & Chappard, D. Aluminum inhibits the growth of hydroxyapatite crystals developed on a biomimetic methacrylic polymer. *J. Trace Elem. Med. Biol. Organ Soc. Miner. Trace Elem. GMS* **27**, 346–351 (2013).
487. Faugere, M. C., Arnala, I. O., Ritz, E. & Malluche, H. H. Loss of bone resulting from accumulation of aluminum in bone of patients undergoing dialysis. *J. Lab. Clin. Med.* **107**, 481–487 (1986).
488. Baba, H., Tsuneyama, K., Kumada, T., Aoshima, K. & Imura, J. Histopathological analysis for osteomalacia and tubulopathy in itai-itai disease. *J. Toxicol. Sci.* **39**, 91–96 (2014).
489. Blumenthal, N. C., Cosma, V., Skyler, D., LeGeros, J. & Walters, M. The effect of cadmium on the formation and properties of hydroxyapatite in vitro and its relation to cadmium toxicity in the skeletal system. *Calcif. Tissue Int.* **56**, 316–322 (1995).
490. Galicka, A., Brzóska, M. M., Sredzińska, K. & Gindziński, A. Effect of cadmium on collagen content and solubility in rat bone. *Acta Biochim. Pol.* **51**, 825–829 (2004).
491. Iguchi, H. & Sano, S. Effect of cadmium on the bone collagen metabolism of rat. *Toxicol. Appl. Pharmacol.* **62**, 126–136 (1982).
492. Sredzińska, K., Galicka, A., Brzóska, M. M. & Gindziński, A. Effect of cadmium on glycosaminoglycans in the bone of rats. *Bull. Environ. Contam. Toxicol.* **73**, 437–442 (2004).

493. Barry, P. S. A comparison of concentrations of lead in human tissues. *Br. J. Ind. Med.* **32**, 119–139 (1975).
494. Vig, E. K. & Hu, H. Lead toxicity in older adults. *J. Am. Geriatr. Soc.* **48**, 1501–1506 (2000).
495. Monir, A. U. *et al.* The Effect of Lead on Bone Mineral Properties From Female Adult C57/BL6 Mice. *Bone* **47**, 888–894 (2010).
496. Dowd, T. L., Rosen, J. F., Mints, L. & Gundberg, C. M. The effect of Pb²⁺ on the structure and hydroxyapatite binding properties of osteocalcin. *Biochim. Biophys. Acta BBA - Mol. Basis Dis.* **1535**, 153–163 (2001).
497. Gruber, H. E. *et al.* Osteopenia induced by long-term, low- and high-level exposure of the adult rat to lead. *Miner. Electrolyte Metab.* **23**, 65–73 (1997).
498. Escribano, A. *et al.* Effect of lead on bone development and bone mass: a morphometric, densitometric, and histomorphometric study in growing rats. *Calcif. Tissue Int.* **60**, 200–203 (1997).
499. Cunniff, C., Bassetti, J. A. & Ellis, N. A. Bloom's Syndrome: Clinical Spectrum, Molecular Pathogenesis, and Cancer Predisposition. *Mol. Syndromol.* **8**, 4–23 (2017).
500. Shamanna, R. A., Croteau, D. L., Lee, J.-H. & Bohr, V. A. Recent Advances in Understanding Werner Syndrome. *F1000Research* **6**, (2017).
501. Yokote, K. *et al.* WRN Mutation Update: Mutation Spectrum, Patient Registries, and Translational Prospects. *Hum. Mutat.* **38**, 7–15 (2017).
502. Kitao, S., Lindor, N. M., Shiratori, M., Furuichi, Y. & Shimamoto, A. Rothmund-thomson syndrome responsible gene, RECQL4: genomic structure and products. *Genomics* **61**, 268–276 (1999).
503. Siitonen, H. A. *et al.* Molecular defect of RAPADILINO syndrome expands the phenotype spectrum of RECQL diseases. *Hum. Mol. Genet.* **12**, 2837–2844 (2003).
504. Van Maldergem, L. *et al.* Revisiting the craniosynostosis-radial ray hypoplasia association: Baller-Gerold syndrome caused by mutations in the RECQL4 gene. *J. Med. Genet.* **43**, 148–152 (2006).
505. Larizza, L., Roversi, G. & Volpi, L. Rothmund-Thomson syndrome. *Orphanet J. Rare Dis.* **5**, 2 (2010).
506. Dietschy, T., Shevelev, I. & Stajlar, I. The molecular role of the Rothmund-Thomson-, RAPADILINO- and Baller-Gerold-gene product, RECQL4: recent progress. *Cell. Mol. Life Sci. CMLS* **64**, 796–802 (2007).
507. Vennos, E. M., Collins, M. & James, W. D. Rothmund-Thomson syndrome: review of the world literature. *J. Am. Acad. Dermatol.* **27**, 750–762 (1992).
508. Mehollin-Ray, A. R., Kozinetz, C. A., Schlesinger, A. E., Guillerman, R. P. & Wang, L. L. Radiographic abnormalities in Rothmund-Thomson syndrome and genotype-phenotype correlation with RECQL4 mutation status. *AJR Am. J. Roentgenol.* **191**, W62-66 (2008).
509. Wang, L. L. *et al.* Clinical manifestations in a cohort of 41 Rothmund-Thomson syndrome patients. *Am. J. Med. Genet.* **102**, 11–17 (2001).
510. Cao, F. *et al.* Generalized metabolic bone disease and fracture risk in Rothmund-Thomson syndrome. *Hum. Mol. Genet.* **26**, 3046–3055 (2017).
511. Wang, L. L. *et al.* Association between osteosarcoma and deleterious mutations in the RECQL4 gene in Rothmund-Thomson syndrome. *J. Natl. Cancer Inst.* **95**, 669–674 (2003).
512. Siitonen, H. A. *et al.* The mutation spectrum in RECQL4 diseases. *Eur. J. Hum. Genet. EJHG* **17**, 151–158 (2009).

513. Jin, W. *et al.* Sensitivity of RECQL4-deficient fibroblasts from Rothmund-Thomson syndrome patients to genotoxic agents. *Hum. Genet.* **123**, 643–653 (2008).
514. Kitao, S. *et al.* Cloning of two new human helicase genes of the RecQ family: biological significance of multiple species in higher eukaryotes. *Genomics* **54**, 443–452 (1998).
515. Liu, Y., El-Naggar, S., Clem, B., Chesney, J. & Dean, D. C. The Rb/E2F pathway and Ras activation regulate RecQ helicase gene expression. *Biochem. J.* **412**, 299–306 (2008).
516. Sengupta, S. *et al.* Tumor suppressor p53 represses transcription of RECQ4 helicase. *Oncogene* **24**, 1738–1748 (2005).
517. Fang, H. *et al.* RecQL4 helicase amplification is involved in human breast tumorigenesis. *PLoS One* **8**, e69600 (2013).
518. Li, J. *et al.* Upregulation of RECQL4 expression predicts poor prognosis in hepatocellular carcinoma. *Oncol. Lett.* **15**, 4248–4254 (2018).
519. Maire, G. *et al.* Recurrent RECQL4 imbalance and increased gene expression levels are associated with structural chromosomal instability in sporadic osteosarcoma. *Neoplasia N. Y. N* **11**, 260–268, 3p following 268 (2009).
520. Su, Y. *et al.* Human RecQL4 helicase plays critical roles in prostate carcinogenesis. *Cancer Res.* **70**, 9207–9217 (2010).
521. Mo, D., Zhao, Y. & Balajee, A. S. Human RecQL4 helicase plays multifaceted roles in the genomic stability of normal and cancer cells. *Cancer Lett.* **413**, 1–10 (2018).
522. Im, J.-S. *et al.* RecQL4 is required for the association of Mcm10 and Ctf4 with replication origins in human cells. *Cell Cycle Georget. Tex* **14**, 1001–1009 (2015).
523. Masai, H. RecQL4: a helicase linking formation and maintenance of a replication fork. *J. Biochem. (Tokyo)* **149**, 629–631 (2011).
524. Sangrithi, M. N. *et al.* Initiation of DNA replication requires the RECQL4 protein mutated in Rothmund-Thomson syndrome. *Cell* **121**, 887–898 (2005).
525. Bruck, I. & Kaplan, D. L. The replication initiation protein Sld2 regulates helicase assembly. *J. Biol. Chem.* **289**, 1948–1959 (2014).
526. Abe, T. *et al.* The N-terminal region of RECQL4 lacking the helicase domain is both essential and sufficient for the viability of vertebrate cells: Role of the N-terminal region of RECQL4 in cells. *Biochim. Biophys. Acta BBA - Mol. Cell Res.* **1813**, 473–479 (2011).
527. Fu, W., Ligabue, A., Rogers, K. J., Akey, J. M. & Monnat, R. J. Human RECQ Helicase Pathogenic Variants, Population Variation and “Missing” Diseases. *Hum. Mutat.* **38**, 193–203 (2017).
528. Siitonen, H. A. *et al.* The mutation spectrum in RECQL4 diseases. *Eur. J. Hum. Genet. EJHG* **17**, 151–158 (2009).
529. Lu, H. *et al.* Cell cycle-dependent phosphorylation regulates RECQL4 pathway choice and ubiquitination in DNA double-strand break repair. *Nat. Commun.* **8**, (2017).
530. Mann, M. B. *et al.* Defective sister-chromatid cohesion, aneuploidy and cancer predisposition in a mouse model of type II Rothmund–Thomson syndrome. *Hum. Mol. Genet.* **14**, 813–825 (2005).
531. Kaiser, S., Sauer, F. & Kisker, C. The structural and functional characterization of human RecQ4 reveals insights into its helicase mechanism. *Nat. Commun.* **8**, 15907 (2017).
532. Rossi, M. L., Ghosh, A. K., Kulikowicz, T., Croteau, D. L. & Bohr, V. A. Conserved helicase domain of human RecQ4 is required for strand annealing-independent DNA unwinding. *DNA Repair* **9**, 796–804 (2010).

533. Suzuki, T., Kohno, T. & Ishimi, Y. DNA helicase activity in purified human RECQL4 protein. *J. Biochem. (Tokyo)* **146**, 327–335 (2009).
534. Xu, X. & Liu, Y. Dual DNA unwinding activities of the Rothmund-Thomson syndrome protein, RECQ4. *EMBO J.* **28**, 568–577 (2009).
535. Croteau, D. L., Singh, D. K., Ferrarelli, L. H., Lu, H. & Bohr, V. A. RECQL4 in genomic instability and aging. *Trends Genet. TIG* **28**, 624–631 (2012).
536. Lu, L., Jin, W. & Wang, L. L. Aging in Rothmund-Thomson syndrome and related RECQL4 genetic disorders. *Ageing Res. Rev.* **33**, 30–35 (2017).
537. Ferrarelli, L. K. *et al.* The RECQL4 protein, deficient in Rothmund–Thomson syndrome is active on telomeric D-loops containing DNA metabolism blocking lesions. *DNA Repair* **12**, 518–528 (2013).
538. Ghosh, A. K. *et al.* RECQL4, the Protein Mutated in Rothmund-Thomson Syndrome, Functions in Telomere Maintenance. *J. Biol. Chem.* **287**, 196–209 (2012).
539. Croteau, D. L. *et al.* RECQL4 LOCALIZES TO MITOCHONDRIA AND PRESERVES MITOCHONDRIAL DNA INTEGRITY. *Aging Cell* **11**, 456–466 (2012).
540. Gupta, S. *et al.* RECQL4 and p53 potentiate the activity of polymerase γ and maintain the integrity of the human mitochondrial genome. *Carcinogenesis* **35**, 34–45 (2014).
541. Kumari, J. *et al.* Mitochondrial functions of RECQL4 are required for the prevention of aerobic glycolysis-dependent cell invasion. *J. Cell Sci.* **129**, 1312–1318 (2016).
542. Fang, H. *et al.* RecQL4-Aurora B kinase axis is essential for cellular proliferation, cell cycle progression, and mitotic integrity. *Oncogenesis* **7**, 68 (2018).
543. Yokoyama, H. *et al.* Chromosome alignment maintenance requires the MAP RECQL4, mutated in the Rothmund-Thomson syndrome. *Life Sci. Alliance* **2**, (2019).
544. Davis, T. *et al.* Activation of p38 MAP kinase and stress signalling in fibroblasts from the progeroid Rothmund-Thomson syndrome. *Age Dordr. Neth.* **35**, 1767–1783 (2013).
545. Lu, H. *et al.* Senescence induced by RECQL4 dysfunction contributes to Rothmund–Thomson syndrome features in mice. *Cell Death Dis.* **5**, e1226 (2014).
546. Ohhata, T. *et al.* Cloning, genomic structure and chromosomal localization of the gene encoding mouse DNA helicase RecQ helicase protein-like 4. *Gene* **261**, 251–258 (2000).
547. Cao, F. *et al.* Generalized metabolic bone disease and fracture risk in Rothmund-Thomson syndrome. *Hum. Mol. Genet.* **26**, 3046–3055 (2017).
548. Lu, L. *et al.* RECQL4 Regulates p53 Function In Vivo During Skeletogenesis. *J. Bone Miner. Res.* **30**, 1077–1089 (2015).
549. Ng, A. J. M. *et al.* The DNA helicase recql4 is required for normal osteoblast expansion and osteosarcoma formation. *PLoS Genet.* **11**, e1005160 (2015).
550. Arias, C. F., Herrero, M. A., Echeverri, L. F., Oleaga, G. E. & López, J. M. Bone remodeling: A tissue-level process emerging from cell-level molecular algorithms. *PLOS ONE* **13**, e0204171 (2018).
551. Sims, N. A. & Martin, T. J. Coupling Signals between the Osteoclast and Osteoblast: How are Messages Transmitted between These Temporary Visitors to the Bone Surface? *Front. Endocrinol.* **6**, (2015).
552. Coppé, J.-P. *et al.* Senescence-Associated Secretory Phenotypes Reveal Cell-Nonautonomous Functions of Oncogenic RAS and the p53 Tumor Suppressor. *PLoS Biol.* **6**, (2008).

553. Alves, R. D. A. M., Eijken, M., Bezstarosti, K., Demmers, J. A. A. & van Leeuwen, J. P. T. M. Activin A Suppresses Osteoblast Mineralization Capacity by Altering Extracellular Matrix (ECM) Composition and Impairing Matrix Vesicle (MV) Production. *Mol. Cell. Proteomics MCP* **12**, 2890–2900 (2013).
554. Eijken, M. *et al.* The activin A-follistatin system: potent regulator of human extracellular matrix mineralization. *FASEB J. Off. Publ. Fed. Am. Soc. Exp. Biol.* **21**, 2949–2960 (2007).
555. Urtasun, R., Cubero, F. J., Vera, M. & Nieto, N. Reactive nitrogen species switch on early extracellular matrix remodeling via induction of MMP1 and TNFalpha. *Gastroenterology* **136**, 1410–1422, e1-4 (2009).
556. WHO, W. H. O. Depleted uranium: sources, exposure and health effects (WHO/SDE/PHE/01.1). (2001).
557. Bernhard, G. *et al.* Uranyl(VI) carbonate complex formation: Validation of the $\text{Ca}_2\text{UO}_2(\text{CO}_3)_3(\text{aq})$ species. *Radiochim. Acta* **89**, (2001).
558. Durbin, P. Actinides in animals and man. in *The chemistry of the actinide and transactinide elements* vol. 5 3339–3440 (Springer, 2006).
559. Sutton, M. & Burastero, S. R. Uranium(VI) solubility and speciation in simulated elemental human biological fluids. *Chem. Res. Toxicol.* **17**, 1468–1480 (2004).
560. Carrière, M. *et al.* Influence of Uranium Speciation on Normal Rat Kidney (NRK-52 E) Proximal Cell Cytotoxicity. *Chem. Res. Toxicol.* **17**, 446–452 (2004).
561. Milgram, S., Carrière, M., Thiebault, C., Malaval, L. & Gouget, B. Cytotoxic and phenotypic effects of uranium and lead on osteoblastic cells are highly dependent on metal speciation. *Toxicology* **250**, 62–69 (2008).
562. Mirto, H. *et al.* Influence of uranium(VI) speciation for the evaluation of in vitro uranium cytotoxicity on LLC-PK1 cells. *Hum. Exp. Toxicol.* **18**, 180–187 (1999).
563. Melo, D. & Burkart, W. Uranium. in *Elements and Their Compounds in the Environment* (eds. Merian, E., Anke, M., Ihnat, M. & Stoepler, M.) 1157–1164 (Wiley-VCH Verlag GmbH, 2004). doi:10.1002/9783527619634.ch47b.
564. Huikuri, P. & Salonen, L. Removal of Uranium from Finnish Groundwaters in Domestic Use with a Strong Base Anion Resin. *J. Radioanal. Nucl. Chem.* **245**, 385–393 (2000).
565. Al Kaddissi, S. *et al.* Are antioxidant and transcriptional responses useful for discriminating between chemo- and radiotoxicity of uranium in the crayfish *Procambarus clarkii*? *Ecotoxicol. Environ. Saf.* **80**, 266–272 (2012).
566. Vidaud, C., Bourgeois, D. & Meyer, D. Bone as target organ for metals: the case of f-elements. *Chem. Res. Toxicol.* **25**, 1161–1175 (2012).
567. Neuman, W. F. & Neuman, M. W. The deposition of uranium in bone; adsorption studies in vitro. *J. Biol. Chem.* **179**, 325–333 (1949).
568. Amprino, R. Observations on the fixation in vitro of uranium to sections of bone. *Experientia* **9**, 291–293 (1953).
569. Igarashi, Y., Yamakawa, A. & Ikeda, N. Distribution of uranium in human bones. *Radioisotopes* **36**, 563–567 (1987).
570. Rowland, R. E. & Farnham, J. E. The Deposition of Uranium in Bone. *Health Phys.* **17**, 139 (1969).
571. Priest, N. D., Howells, G. R., Green, D. & Haines, J. W. Uranium in bone: metabolic and autoradiographic studies in the rat. *Hum. Toxicol.* **1**, 97–114 (1982).

572. López, R., Díaz Sylvester, P. L., Ubios, A. M. & Cabrini, R. L. Percutaneous toxicity of uranyl nitrate: its effect in terms of exposure area and time. *Health Phys.* **78**, 434–437 (2000).
573. Leggett, R. W. & Pellmar, T. C. The biokinetics of uranium migrating from embedded DU fragments. *J. Environ. Radioact.* **64**, 205–225 (2003).
574. Tasat, D. R., Orona, N. S., Mandalunis, P. M., Cabrini, R. L. & Ubios, A. M. Ultrastructural and metabolic changes in osteoblasts exposed to uranyl nitrate. *Arch. Toxicol.* **81**, 319–326 (2007).
575. Wade-Gueye, N. M. *et al.* Chronic exposure to natural uranium via drinking water affects bone in growing rats. *Biochim. Biophys. Acta BBA - Gen. Subj.* **1820**, 1121–1127 (2012).
576. Kurttio, P. *et al.* Bone as a possible target of chemical toxicity of natural uranium in drinking water. *Environ. Health Perspect.* **113**, 68–72 (2005).
577. Milgram, S., Carrière, M., Malaval, L. & Gouget, B. Cellular accumulation and distribution of uranium and lead in osteoblastic cells as a function of their speciation. *Toxicology* **252**, 26–32 (2008).
578. Pierrefite-Carle, V. *et al.* Effect of natural uranium on the UMR-106 osteoblastic cell line: impairment of the autophagic process as an underlying mechanism of uranium toxicity. *Arch. Toxicol.* (2016) doi:10.1007/s00204-016-1833-5.
579. Arzuaga, X., Gehlhaus, M. & Strong, J. Modes of action associated with uranium induced adverse effects in bone function and development. *Toxicol. Lett.* **236**, 123–130 (2015).
580. Ubios, A. M., Guglielmotti, M. B., Steimetz, T. & Cabrini, R. L. Uranium inhibits bone formation in physiologic alveolar bone modeling and remodeling. *Environ. Res.* **54**, 17–23 (1991).
581. Bozal, C. B., Martinez, A. B., Cabrini, R. L. & Ubios, A. M. Effect of ethane-1-hydroxy-1,1-bisphosphonate (EHBP) on endochondral ossification lesions induced by a lethal oral dose of uranyl nitrate. *Arch. Toxicol.* **79**, 475–481 (2005).
582. Fukuda, S., Ikeda, M., Chiba, M. & Kaneko, K. Clinical diagnostic indicators of renal and bone damage in rats intramuscularly injected with depleted uranium. *Radiat. Prot. Dosimetry* **118**, 307–314 (2006).
583. WHO. Uranium in Drinking Water, Background document for development of WHO Guidelines for Drinking-water Quality (WHO/SDE/WSH/03.04/118). (2004).
584. Prewitz, M. C. *et al.* Tightly anchored tissue-mimetic matrices as instructive stem cell microenvironments. *Nat. Methods* **10**, 788–794 (2013).
585. Riggs, B. L. *et al.* Population-based study of age and sex differences in bone volumetric density, size, geometry, and structure at different skeletal sites. *J. Bone Miner. Res. Off. J. Am. Soc. Bone Miner. Res.* **19**, 1945–1954 (2004).
586. McHugh, D. & Gil, J. Senescence and aging: Causes, consequences, and therapeutic avenues. *J. Cell Biol.* **217**, 65–77 (2018).
587. Farr, J. N. & Khosla, S. Cellular senescence in bone. *Bone* **121**, 121–133 (2019).
588. Schumacher, B., Garinis, G. A. & Hoeijmakers, J. H. J. Age to survive: DNA damage and aging. *Trends Genet.* **24**, 77–85 (2008).
589. Wu, Z. *et al.* Differential stem cell aging kinetics in Hutchinson-Gilford progeria syndrome and Werner syndrome. *Protein Cell* **9**, 333–350 (2018).
590. Goldman, R. D. *et al.* Accumulation of mutant lamin A causes progressive changes in nuclear architecture in Hutchinson-Gilford progeria syndrome. *Proc. Natl. Acad. Sci. U. S. A.* **101**, 8963–8968 (2004).
591. Osorio, F. G. *et al.* Splicing-directed therapy in a new mouse model of human accelerated aging. *Sci. Transl. Med.* **3**, 106ra107 (2011).

592. Varela, I. *et al.* Accelerated ageing in mice deficient in Zmpste24 protease is linked to p53 signalling activation. *Nature* **437**, 564–568 (2005).
593. Zhang, J. *et al.* A human iPSC model of Hutchinson Gilford Progeria reveals vascular smooth muscle and mesenchymal stem cell defects. *Cell Stem Cell* **8**, 31–45 (2011).
594. Du, X. *et al.* Telomere Shortening Exposes Functions for the Mouse Werner and Bloom Syndrome Genes. *Mol. Cell. Biol.* **24**, 8437–8446 (2004).
595. Chang, S. *et al.* Essential role of limiting telomeres in the pathogenesis of Werner syndrome. *Nat. Genet.* **36**, 877–882 (2004).
596. Benson, E. K., Lee, S. W. & Aaronson, S. A. Role of progerin-induced telomere dysfunction in HGPS premature cellular senescence. *J. Cell Sci.* **123**, 2605–2612 (2010).
597. Sharpless, N. E. & Sherr, C. J. Forging a signature of *in vivo* senescence. *Nat. Rev. Cancer* **15**, 397–408 (2015).
598. Bursuker, I., Rhodes, J. M. & Goldman, R. Beta-galactosidase—an indicator of the maturational stage of mouse and human mononuclear phagocytes. *J. Cell. Physiol.* **112**, 385–390 (1982).
599. Kopp, H.-G., Hooper, A. T., Shmelkov, S. V. & Rafii, S. Beta-galactosidase staining on bone marrow. The osteoclast pitfall. *Histol. Histopathol.* **22**, 971–976 (2007).
600. Itahana, K., Campisi, J. & Dimri, G. P. Methods to Detect Biomarkers of Cellular Senescence. in *Biological Aging: Methods and Protocols* (ed. Tollefsbol, T. O.) 21–31 (Humana Press, 2007). doi:10.1007/978-1-59745-361-5_3.
601. Goldstein, S., Moerman, E. J., Fujii, S. & Sobel, B. E. Overexpression of plasminogen activator inhibitor type-1 in senescent fibroblasts from normal subjects and those with Werner syndrome. *J. Cell. Physiol.* **161**, 571–579 (1994).
602. Kortlever, R. M., Higgins, P. J. & Bernards, R. Plasminogen activator inhibitor-1 is a critical downstream target of p53 in the induction of replicative senescence. *Nat. Cell Biol.* **8**, 877–884 (2006).
603. Elzi, D. J. *et al.* Plasminogen activator inhibitor 1–insulin-like growth factor binding protein 3 cascade regulates stress-induced senescence. *Proc. Natl. Acad. Sci. U. S. A.* **109**, 12052–12057 (2012).
604. Goldstein, S., Moerman, E. J. & Baxter, R. C. Accumulation of insulin-like growth factor binding protein-3 in conditioned medium of human fibroblasts increases with chronologic age of donor and senescence *in vitro*. *J. Cell. Physiol.* **156**, 294–302 (1993).
605. Farr, J. N. *et al.* Independent Roles of Estrogen Deficiency and Cellular Senescence in the Pathogenesis of Osteoporosis: Evidence in Young Adult Mice and Older Humans. *J. Bone Miner. Res. Off. J. Am. Soc. Bone Miner. Res.* **34**, 1407–1418 (2019).
606. Wiley, C. D. *et al.* Analysis of individual cells identifies cell-to-cell variability following induction of cellular senescence. *Aging Cell* **16**, 1043–1050 (2017).
607. Kim, J.-H. *et al.* Matrix cross-linking–mediated mechanotransduction promotes posttraumatic osteoarthritis. *Proc. Natl. Acad. Sci. U. S. A.* **112**, 9424–9429 (2015).
608. Cribb, A. M. & Scott, J. E. Tendon response to tensile stress: an ultrastructural investigation of collagen: proteoglycan interactions in stressed tendon. *J. Anat.* **187 (Pt 2)**, 423–428 (1995).
609. Iwasaki, S. *et al.* The modulation of collagen fibril assembly and its structure by decorin: an electron microscopic study. *Arch. Histol. Cytol.* **71**, 37–44 (2008).
610. Sharma, C., Kaur, A., Thind, S. S., Singh, B. & Raina, S. Advanced glycation End-products (AGEs): an emerging concern for processed food industries. *J. Food Sci. Technol.* **52**, 7561–7576 (2015).

611. Nowotny, K., Jung, T., Höhn, A., Weber, D. & Grune, T. Advanced Glycation End Products and Oxidative Stress in Type 2 Diabetes Mellitus. *Biomolecules* **5**, 194–222 (2015).
612. Panwar, P. *et al.* Changes in Structural-Mechanical Properties and Degradability of Collagen during Aging-associated Modifications. *J. Biol. Chem.* **290**, 23291–23306 (2015).
613. Yang, X. *et al.* Induction of Human Osteoprogenitor Chemotaxis, Proliferation, Differentiation, and Bone Formation by Osteoblast Stimulating Factor-1/Pleiotrophin: Osteoconductive Biomimetic Scaffolds for Tissue Engineering. *J. Bone Miner. Res.* **18**, 47–57 (2003).
614. Lyabin, D. N., Eliseeva, I. A. & Ovchinnikov, L. P. YB-1 protein: functions and regulation. *Wiley Interdiscip. Rev. RNA* **5**, 95–110 (2014).
615. Mo, D. *et al.* Human Helicase RECQL4 Drives Cisplatin Resistance in Gastric Cancer by Activating an AKT–YB1–MDR1 Signaling Pathway. *Cancer Res.* **76**, 3057–3066 (2016).
616. Kretov, D. A. *et al.* mRNA and DNA selection via protein multimerization: YB-1 as a case study. *Nucleic Acids Res.* **43**, 9457–9473 (2015).
617. Sorokin, A. V. *et al.* Proteasome-mediated cleavage of the Y-box-binding protein 1 is linked to DNA-damage stress response. *EMBO J.* **24**, 3602–3612 (2005).
618. Kang, S. *et al.* Differential Control of Interleukin-6 mRNA Levels by Cellular Distribution of YB-1. *PLoS ONE* **9**, (2014).
619. Tacke, F. *et al.* Y-box protein-1/p18 fragment identifies malignancies in patients with chronic liver disease. *BMC Cancer* **11**, 185 (2011).
620. Kim, E. R. *et al.* The proteolytic YB-1 fragment interacts with DNA repair machinery and enhances survival during DNA damaging stress. *Cell Cycle* **12**, 3791–3803 (2013).
621. van Roeyen, C. R. *et al.* Cold shock Y-box protein-1 proteolysis autoregulates its transcriptional activities. *Cell Commun. Signal.* **11**, 63 (2013).
622. Kim, E. R. *et al.* The proteolytic YB-1 fragment interacts with DNA repair machinery and enhances survival during DNA damaging stress. *Cell Cycle* **12**, 3791–3803 (2013).
623. Evdokimova, V. *et al.* Translational Activation of Snail1 and Other Developmentally Regulated Transcription Factors by YB-1 Promotes an Epithelial-Mesenchymal Transition. *Cancer Cell* **15**, 402–415 (2009).
624. Guarino, A. M. *et al.* Oxidative Stress Causes Enhanced Secretion of YB-1 Protein that Restrains Proliferation of Receiving Cells. *Genes* **9**, (2018).
625. Kossinova, O. A. *et al.* Cytosolic YB-1 and NSUN2 are the only proteins recognizing specific motifs present in mRNAs enriched in exosomes. *Biochim. Biophys. Acta Proteins Proteomics* **1865**, 664–673 (2017).
626. Frye, B. C. *et al.* Y-box protein-1 is actively secreted through a non-classical pathway and acts as an extracellular mitogen. *EMBO Rep.* **10**, 783–789 (2009).